Title
ON THE PERIODIC ELECTRODEPOSITION OF ALLOYS

Authors
Verbrugge, M.W.
Tobias, C.W.

Publication Date
1985-11-01

Lawrence Berkeley Laboratory
UNIVERSITY OF CALIFORNIA

Materials & Molecular Research Division

ON THE PERIODIC ELECTRODEPOSITION OF ALLOYS

M.W. Verbrugge* and C.W. Tobias

(*Ph.D. Thesis)

November 1985

Prepared for the U.S. Department of Energy under Contract DE-AC03-76SF00098

DISCLAIMER

LBL-20500

ON THE PERIODIC ELECTRODEPOSITION OF ALLOYS

Mark W. Verbrugge
(Ph.D. Thesis)

and

Charles W. Tobias

Department of Chemical Engineering
and Lawrence Berkeley Laboratory
University of California
Berkeley, California 94720

November 1985

This work was supported by the Director, Office of Energy Research, Office of Basic Energy Sciences, Materials Sciences Division of the Office of the U.S. Department of Energy, under contract no. DE-AC03-76SF00098.

Contents

On the Periodic Electrodeposition of Alloys

Mark W. Verbrugge and Charles W. Tobias

Department of Chemical Engineering
and Lawrence Berkeley Laboratory
University of California
Berkeley, California 94720

Abstract

The increased demand for thin films of alloyed materials with known chemical composition, phase structure, and morphology has stimulated alloy-electrodeposition research. An experimental and theoretical investigation of periodic alloy electrodeposition is presented. A mathematical model is developed for the electrodeposition of alloys by an arbitrarily specified cell-current or electrode-potential waveform. Transient, convective mass transfer, Butler-Volmer electrode kinetics, and individual component activities in the electrodeposit are considered. The model can be used to calculate current-potential relationships, ionic concentration profiles, and electrodeposit composition. The theoretical predictions are compared with experimental results for the electrodeposition of cadmium telluride onto a rotating disk electrode. A number of *in situ* and *ex situ* analytical techniques that were used to characterize the thin film, alloy electrodeposits clearly illustrated the effect of the cell-current waveform on the electrodeposit morphology and physical properties.

In order to gain fundamental insight into metal deposition processes, a convenient series solution is presented for the evaluation of ionic concentrations during triangular current-sweep chronopotentiometry at a rotating

disk electrode, and at a stationary, planar electrode in the absence of free convection. The treatment is valid for electrode processes with one electrochemical reaction of uniform rate along the electrode surface. The advantages of controlled-current processes, relative to controlled-potential processes, for obtaining kinetic, thermodynamic, and transport information are elucidated. Theoretical predictions are compared with results obtained for the deposition of cadmium from a dilute, aqueous, cadmium-sulfate/potassium-sulfate electrolyte.

The cadmium telluride material electrodeposited in the alloy study is photovoltaic and semiconducting. Description of the semiconductor-electrolyte interface is addressed mathematically by extending existing steady-state models to account for variable illumination. Analytic solutions for the minority-carrier concentration in the semiconductor phase are presented for pulse, step, sinusoidal, and periodic square-pulse illumination. The periodic illumination of the semiconductor-electrolyte interface can be used as a means to evaluate transport and kinetic coefficients of photoelectrochemical systems with widely varying time constants, particularly since the system reaches a uniform and sustained periodic state when subjected to a periodic light flux.

Acknowledgment

During the past four years, I have had the good fortune to interact with a number of fine people, and I take this opportunity to recognize some of the friends I have associated with during my stay in Berkeley. I will always remember, and strive to assimilate, Professor Tobias' inquisitive and philosophical nature, which spans a phenomenally large number of subjects. Professor Newman has taught me the meaning of diligence, and how it can greatly simplify seemingly complex situations. Both of these men have given me valuable tools that I shall often use. My fellow coworkers and peers, Dennis Dees (who inspired me to look at periodic alloy electrodeposition), John Dukovic, Vicki Edwards, Tarric El-Sayed, Karrie Hanson, Mike Matlosz, Phil Russell and Gina Whitney, who joined me in my quest for knowledge, provided me with a stimulating environment and have gave me many fond memories. Lastly, I want to thank my family, for they represent my foundation; their continued encouragement and support have helped me through many difficult times. My wife, Dawn, is my greatest source of happiness and I look forward to our life together.

This work was supported by the Director, Office of Energy Research, Office of Basic Energy Sciences Division of the Office of the U.S. Department of Energy, under Contract No. DE-AC03-76SF00098.

Chapter 1.

Thesis Introduction

To be accepted, a new approach must pass through the danger zone of exaggerated expectations and yield physically realistic, discernible results. This is the present state of multicomponent electrodeposition modeling. A large amount of literature is devoted to the study of alloy electrodeposition. At times, however, workers in this field still find themselves part of a gambling fraternity. The objective of this research was to provide a new framework for the rational description of periodic alloy electrodeposition based on previous fundamental work relevant to this study, and to develop new concepts necessary to advance the understanding of these processes.

In the analysis of periodic, alloy electrodeposition, two developing areas of research are condensed into one. Alloy-electrodeposition research is stimulated by the unique advantages electrodeposition offers for alloy formation: the control of alloy composition, the ability to prepare thin films, and the relatively low cost of electrodeposition process technology. Periodic-electrodeposition processes, which have been analyzed quantitively for single-component electrodeposition processes, represent the second developing area of research integrated into this study. Although a general and fundamental treatment explaining the effect of a periodic current or potential source on electrodeposit properties has yet to be developed, investigations have clearly shown that a periodic current or potential source can be used to produce superior electrodeposits for many metal/metal ion systems.

In Chapter 2 of this thesis, a literature review of experimental and

theoretical periodic alloy-electrodeposition studies is presented. Following this, a mathematical model is developed which allows for the calculation of electrodeposit composition, ionic surface concentrations in the liquid phase, and the cell-current/electrode-potential relationship during a periodic alloy-electrodeposition process. A three-component system, with physicochemical parameters characteristic of metal/metal ion systems, was chosen to analyze the effects of various cell-current and electrode-potential waveforms for a periodic alloy-electrodeposition process.

In Chapter 3, the model developed in Chapter 2 is applied to the periodic electrodeposition of cadmium telluride. Results of the simulation are compared with experimental data obtained in the deposition of the alloy from an acid sulfate bath. The present applications of cadmium telluride are reviewed briefly, and literature concerning cadmium-telluride electrodeposition is referenced. Both *in situ* and *ex situ* analytical techniques are employeed to characterize the electrodeposited cadmium-tellurium materials.

In the cadmium telluride electrodeposition investigation, it was found that the kinetics of the cadmium-cation reduction strongly influence the cadmium-telluride electrodeposition process. An expermental and theoretical investigation of the cadmium electrodeposition process from an aqueous, sulfate bath, similar to that used in the cadmium-telluride electrodeposition process, is described in Chapter 4. The bulk of the analysis addresses the ionic mass transport, since charge-transfer kinetic equations require the knowledge of the ionic surface concentrations, cell-current density, and electrode potential.

A particularly useful characterization technique for the evaluation of

cadmium telluride electrodeposits is to measure the transient photoresponse of the resulting deposits. Since cadmium telluride is a semiconducting photovoltaic material, photoresponse analysis can be used to estimate electrodeposit composition and address electrodeposit quality. In Chapter 5, theoretical work is presented for the study of transient and periodic illumination of a semiconductor-electrolyte interface. This treatment is analogous to work in Chapter 4, in which standard, cyclic chronopotentiometric techniques are used to study a metal-electrolyte interface. Analytic solutions are presented for the evaluation of charge-carrier concentrations in the semiconductor electrode.

Chapters 4 and 5, neither of which directly address alloy-electrodeposition processes, grew out of results obtained in the cadmium-telluride study of Chapter 3. As much as possible, the chapters in this thesis have been written so that they may be read independently. A list of nomenclature, a list of references, and an appendix is provided for each chapter. It is hoped that this will make the reading of this thesis more straightforward and more interesting.

Chapter 2.

A Mathematical Model for the Periodic Electrodeposition of Alloys

The properties of alloys vary over a wider range than those of their parent metals, and thus can often be designed to fulfill better the mechanical and chemical requirements of our civilization. Electrodeposition offers several unique advantages for the formation of alloys. The superior control of the alloy composition, including the formation of non-equilibrium alloys, and the ability to prepare thin films are well documented. Brenner's encyclopedic monograph (1) reviews some practical methods for the electrodeposition of various alloys and Gorbunova and Polukarov's treatment (2) outlines the fundamental principles involved. Srivastava and Mukerjee (3) review developments in the electrodeposition of binary alloys.

It has long been known that pulsing the current can profoundly affect the nature of single-component electrodeposits. Although the pulse plating of alloys has received comparatively little attention, it has been observed that the phase structure and morphology of alloy deposits can be altered by changing the characteristics of the pulse-current waveform. This work presents a model for predicting the current-potential relationship and the composition profiles in the electrodeposit and the electrolyte.

Wan *et al.* (4) have presented a literature review dealing with the application of pulse-plating techniques for single-component metal deposition. Avila and Brown (5) have cited the following advantages of pulse plating over dc electroplating: 1) extremely dense and highly conductive deposits, 2) a reduced need for plating additives, and 3) increased plating rates. In refer-

ence to the last advantage, Cheh (6) has shown analytically that pulse-current plating can never attain a higher average plating rate than dc plating at the diffusion-limited current. However, a higher average current density is often used in pulse plating, relative to dc plating, since poor quality electrodeposits are often formed under dc conditions near the diffusion-limiting current. Lamb (7) has investigated the mechanical properties of single-component copper and silver electrodeposits obtained by current pulses in the microsecond range. Puippe and Ibl (8) studied the morphology of pulse-plated cadmium, copper, and gold electrodeposits. The influence of the off-time, the pulse-current density, and the length of the pulse time were analyzed. Different morphological trends were observed and discussed for the different chemical systems. Ismail (9) investigated the periodic, reverse-current electroplating of copper from an alkaline-cyanide bath. The maximum brightness occurred at 0.27 Hertz with a cathodic-current to anodic-current ratio of two. Despic and Popov (10) examined the effect of a pulsating potential on the morphology of copper and zinc electrodeposits. Typical results illustrated that increasing the frequency led to a progressively smoother deposit. Popov (11) also has reviewed some approaches to the quantitative modeling of the surface-roughness amplification during an electrodeposition process. Sullivan (12) has reported that high-current-density pulse-plating of cobalt results in significantly stronger and harder electrodeposits.

The pulse plating of multicomponent electrodeposits has received less attention than pure-component electrodeposition. Gelchinski et al. (13) electroplated chromium-cobalt alloys using a pulse-potential source. Mirror bright electrodeposits containing supersaturated solid solutions were

obtained. It has been observed that the structure and the physical properties of the electrodeposited alloys can be very different from the thermally prepared alloys of similar composition. Gelchinski et al. also found that a change in the electrodeposition conditions can cause a marked change in the phase structure of the electrodeposit, even for those deposits of identical chemical composition. Burrus (14) has described various conditions where the pulse plating of different metals and metal mixtures can be used advantageously. Leidheiser and Ghuman (15) used a pulse-current setup to electrodeposit silver-tin alloys which could be easily polished to a high luster. Cohen et al. (16) have electroplated cyclic, multilayered, alloy-coatings of varying silver and palladium composition with square-pulse and triangular current waveforms. They also report on periodic-potential plating studies of various multicomponent electrodeposits.

Mathematical Analysis

In considering the mathematical modeling for the electrodeposition of multicomponent alloys, it is convenient to divide the problem into three interrelated parts: the liquid phase containing the discharging ions, the electrolyte-electrodeposit interface, and the electrodeposited alloy.

The Liquid Phase

One of the goals of this work is to predict quantitatively the ionic surface-concentrations throughout the electrodeposition process. It has been well established that the ionic surface concentrations can greatly influence the electrodeposit composition and morphology (17,18).

A theoretical analysis for single-component mass transfer in pulsed electrolysis was recently published by Chin (19). A stagnant (Nernst)

diffusion layer was assumed to be valid in order to develop a comprehensive theory for pulsed electrolysis. Chin's paper includes a brief review of previous theoretical studies in single-component pulsed electrolysis.

Since our treatment uses a current-step solution and the method of superposition to derive a model for multicomponent mass transfer, we shall review some current-step solutions which can be used with this technique. The method of superposition is computationally very efficient, although the differential equations describing the process must be linear for this method to be applied. Thus migration effects are not included in this model. Double layer charging is also not considered. Since practical plating baths usually contain an excess of supporting electrolyte, migration effects can often be neglected. Double layer charging effects can become important in an electrodeposition process if microsecond current cycles are used (20). Before proceeding, it should be mentioned that attempts have been made to describe multicomponent, pulse-current processes qualitatively. (21–24). Also, Cheng and Cheh have presented finite-difference models for the pulse-current electrodeposition of copper with hydrogen evolution (25) and of lead-tin alloys (26).

The convective diffusion equation for the one-dimensional mass transport of species i is

$$\frac{\partial c_i}{\partial t} + v_y \frac{\partial c_i}{\partial y} = D_i \frac{\partial^2 c_i}{\partial y^2} \quad . \qquad [2\text{-}1]$$

For high Schmidt numbers, the appropriate expression for the normal component of the fluid velocity to a rotating disk electrode (RDE) is (27,28)

$$v_y = -0.51023\, \omega^{3/2} \nu^{-1/2} y^2 \quad . \qquad [2\text{-}2]$$

The radial variation of the ionic surface concentration is neglected in this treatment, as it would considerably complicate the problem (29–31). In a rigorous treatment for the RDE system incorporating both radial and axial variations, dimensionless groups arise which include the disk radius. (29,30) For small disks, it is appropriate to neglect radial variations in concentration and potential. Nanis and Klein (32) qualitatively address this assumption in their one-dimensional treatment for transient mass transfer to an RDE in the absence of kinetic resistance.

For the current-step problem, the initial condition and boundary conditions are

$$c_i(0,y) = c_i^b \ , \qquad [2\text{-}3]$$

$$c_i(t,\infty) = c_i^b \ , \qquad [2\text{-}4]$$

and

$$\frac{\partial c_i(t,0)}{\partial y} = -\frac{i(0)}{n_i F D_i} \ ; \qquad [2\text{-}5]$$

where the electrode reaction for metal deposition is

$$M_i^{n_i+} + n_i e^- \underset{k_{a,i}}{\overset{k_{c,i}}{\rightleftarrows}} M_i \ . \qquad [2\text{-}6]$$

Krylov and Babak (33) have obtained an analytic series solution for the current-step problem stated by Eqs. [2-1] through [2-5]. However, the solution does not converge for long times (34). Nisancioglu and Newman (35) numerically calculated an alternate series solution which is valid for long times and can be used in conjunction with a short-time, asymptotic series representation of Krylov and Babak's solution.

Nisancioglu and Newman's long-time solution is

$$c_i = c_i^b + \qquad [2\text{-}7]$$

$$\frac{i_i \delta_i}{n_i F D_i \Gamma(4/3)} \left\{ \int_{\frac{\Gamma(4/3)y}{\delta_i}}^{\infty} e^{-x^3} dx - \sum_{k=1}^{\infty} B_k Z_k \left[\frac{y\Gamma(4/3)}{\delta_i} \right] e^{-\lambda_k D_i t \left[\frac{\Gamma(4/3)}{\delta_i} \right]^2} \right\} .$$

The values of B_k, Z_k, and λ_k are given in Refs. (20) and (35).

The first few terms of the short-time, asymptotic series representation of Krylov and Babak's surface-concentration solution are:

$$c_i^s = c_i^b + \qquad [2\text{-}8]$$

$$\frac{2i_i\sqrt{t}}{n_i F \sqrt{\pi D_i}} \left\{ 1 - \frac{\sqrt{\pi}}{16} \left[\frac{D_i t}{\left(\frac{\delta_i}{3^{1/3}\Gamma(4/3)} \right)^2} \right]^{3/2} + \frac{1}{420} \left[\frac{D_i t}{\left(\frac{\delta_i}{3^{1/3}\Gamma(4/3)} \right)^2} \right]^3 + \cdots \right\}$$

In Eqs. [2-7] and [2-8], δ_i is the Levich diffusion layer thickness (36)

$$\delta_i = 1.612 \left(\frac{D_i}{\nu} \right)^{1/3} \left(\frac{\nu}{\omega} \right)^{1/2} , \qquad [2\text{-}9]$$

which is the characteristic distance for long times.

More approximate representations for the current-step problem have also yielded relatively accurate results. In a classic treatment, Rosebrugh and Lash Miller (37) derived an analytic solution for the current-step problem by replacing Eq. [2-1] with the equation representing Fick's second law of diffusion and Eq. [2-4] by

$$c_i(t,\delta_i) = c_i^b \quad . \qquad [2\text{-}10]$$

This solution is presented in the appendix.

Rosebrugh and Lash Miller used the method of superposition on their current-step solution to describe single-component mass transfer with a periodic current source (37). Cheh et al. (6,38,39) have made use of this solution by comparing it with some experimental results. Visawanathan and Cheh (40) and Hale (41) have presented numerical solutions to Eqs. [2-1] through [2-5] and compared their solutions to that of Rosebrugh and Lash Miller. (Hale actually compared his solution to Siver's solution (42), which Siver had in turn referenced to Rosebrugh and Lash Miller.) The error was always less than 4 percent. Visawanathan et al. (43) numerically solved the system of Eqs. [2-1] through [2-4], with a pulse-current boundary condition in place of Eq. [2-5], and compared this to Rosebrugh and Lash Miller's analytic solution for a pulse-current source. The agreement between the two solutions was excellent.

For the problem we address in this work, we require a current-step solution for short and long times. There is very little extra numerical effort involved in using Eqs. [2-7] instead of Eq. [2A-2], especially if only the surface concentrations of the discharging ions are required. For this reason, we have chosen to use Eqs. [2-7] and [2-8], along with the method of superposition, to model the ionic mass transfer. This restricts our treatment to an RDE. The procedure to be used for other systems which can be modeled accurately with a Nernst diffusion layer is presented in the appendix. A comparison between the two methods is shown in Fig. 2-2 for the RDE system.

The method of superposition can be used with Eq. [2-7] to obtain an expression for the ionic concentration during controlled potential or cell-

current processes:

$$c_i = i_{i,n}\,\Theta_{i,n} + \Psi_{i,n} \quad , \qquad [2\text{-}11]$$

where

$$\Theta_{i,n} = \frac{\delta_i}{n_i F D_i \Gamma(4/3)} \left\{ \int_{\frac{y\Gamma(4/3)}{\delta_i}}^{\infty} e^{-x^3} dx - \sum_{k=1}^{\infty} B_k Z_k e^{-\lambda_k D_i \left[\frac{\Gamma(4/3)}{\delta_i}\right]^2 (t - t_{n-1})} \right\} \qquad [2\text{-}12]$$

and

$$\Psi_{i,n} = c_i^b + \qquad [2\text{-}13]$$

$$\frac{\delta_i}{n_i F D_i \Gamma(4/3)} \left\{ \sum_{j=1}^{n-1} i_{i\,j} \sum_{k=1}^{\infty} B_k Z_k \left[e^{-\lambda_k D_i \left[\frac{\Gamma(4/3)}{\delta_i}\right]^2 (t - t_{j-1})} - e^{-\lambda_k D_i \left[\frac{\Gamma(4/3)}{\delta_i}\right]^2 (t - t_j)} \right] \right\} .$$

The current source has been expressed as n discrete current steps. The method of superposition has been used previously for single-component, pulse-current chronopotentiometry by Andricacos and Cheh (44), and there are a number of references in the literature which can be consulted to derive Eqs. [2-11], [2-12], and [2-13]. (37,45,46)

For short times, the series in Eqs. [2-12] and [2-13] will not converge. Equation [2-8] can then be used to express $\Theta_{i,n}$ and $\Psi_{i,n}$. For very short times, only the first term in Eq. [2-8] need be retained. Equation [2-8] then becomes the familiar Sand equation and δ_i drops out of the problem since there is no characteristic length for the semi-infinite linear diffusion problem. Equations [2-12] and [13] are then replaced by

$$\Theta^{s}_{i,n} = \frac{2\sqrt{t - t_{n-1}}}{n_i F \sqrt{\pi D_i}} \qquad [2\text{-}14]$$

and

$$\Psi^{s}_{i,n} = c^{b}_{i} + \frac{2}{n_i F \sqrt{\pi D_i}} \sum_{j=1}^{n} i_j \left[\sqrt{t - t_{j-1}} - \sqrt{t - t_j} \right] . \qquad [2\text{-}15]$$

Equations [2-14] and [2-15] can also be used to solve the analogous problem of multicomponent mass transfer to a stationary electrode.

The Liquid-Electrodeposit Interface

While a relatively accurate liquid-phase transport model can be developed, such an exacting and general approach is not as easily accomplished for the interface. In multicomponent electrolysis, the potential distribution across the double layer will be affected by the various discharging ions. However, in well supported solutions, the discharging ions will not significantly influence the double-layer structure. The crystallization kinetics can also be changed, although this will not be considered in this paper. An excellent treatment of this problem can be found in the work of Fleischmann and Thirsk (47).

For the electrode reaction of component i, given by Eq. [2-6], a Bulter-Volmer expression will be used to describe the electrode kinetics. Specific adsorption and chemisorption are not taken into account. Thus (48)

$$\frac{i_{i,n}}{n_i F} = k_{a,i} a_{i,n} e^{(1-\beta_i) n_i f V_n} - k_{c,i} \frac{c^{s}_{i,n}}{\rho_o} e^{-\beta_i n_i f V_n} , \qquad [2\text{-}16]$$

where

$$V_n = E_n + \left[U^{\theta}_{re} - \frac{1}{n_{re} f} \sum_i s_{i,re} \ln \frac{c_{i,re}}{\rho_o} \right] - i_n r \quad . \qquad [2\text{-}17]$$

The bracketed term in Eq [2-17] represents the open-circuit potential difference between the reference electrode and a standard hydrogen electrode. The potential difference between the working electrode and the reference electrode is E_n. The last term in Eq. [2-17] accounts for the ohmic drop between the reference electrode and the working electrode. Hence, V_n is the potential difference between the working electrode and a standard hydrogen electrode, corrected for ohmic drop.

The individual currents can be obtained by substituting for $c^s_{i,n}$ in Eq. [2-16] using Eq. [2-11], evaluated at the surface, and solving for $i_{i,n}$:

$$i_{i,n} = \frac{k_{a,i} \alpha_{i,n} e^{(1-\beta_i) n_i f V_n} - \frac{1}{\rho_o} k_{c,i} \Psi^s_{i,n} e^{-\beta_i n_i f V_n}}{\frac{1}{n_i F} + \frac{1}{\rho_o} k_{c,i} \Theta^s_{i,n} e^{-\beta_i n_i f V_n}} \qquad [2\text{-}18]$$

The total imposed current must equal the sum of the m individual currents:

$$\left(\sum_{i=1}^{m} i_{i,n} \right) - i_n = 0 \qquad [2\text{-}19]$$

Equations [2-18] and [2-19] can be combined to yield a nonlinear equation in V_n. The second order Newton-Raphson algorithm (49) is used to solve the resulting equation for V_n in the case of controlled current processes, and for i_n in the case of controlled potential processes.

Using Eqs. [2-18] and [2-19], for the controlled current mode of operation, the function H_n is defined as

$$H_n = \left(\sum_{i=1}^{m} i_{i,n}\right) - i_n \quad . \qquad [2\text{-}20]$$

For the correct value of the electrode potential, H_n will be equal to zero. H_n is given by

$$H_n = \left[\sum_{i=1}^{m} \frac{k_{a,i} a_{i,n} e^{(1-\beta_i) n_i f V_n} - \frac{1}{\rho_o} k_{c,i} \Psi_{i,n}^{s} e^{-\beta_i n_i f V_n}}{\frac{1}{n_i F} + \frac{1}{\rho_o} k_{c,i} \Theta_{i,n}^{s} e^{-\beta_i n_i f V_n}}\right] - i_n \quad . \qquad [2\text{-}21]$$

The value of V_n is found by iteration:

$$(V_n)_{new} = (V_n)_{old} - \left[\frac{H_n}{\left(\frac{\partial H_n}{\partial V_n}\right)}\right]_{old} \quad . \qquad [2\text{-}22]$$

The value of the derivative in Eq. [2-22] is

$$\frac{\partial H_n}{\partial V_n} = \sum_{i=1}^{m} \frac{\frac{k_{a,i} a_{i,n} (1-\beta_i)}{RT} e^{(1-\beta_i) n_i f V_n} + \frac{k_{c,i} \Psi_i^{s} \beta_i}{\rho_o RT} e^{-\beta_i n_i f V_n}}{\left(\frac{1}{n_i F} + \frac{1}{\rho_o} k_{c,i} \Theta_i^{s} e^{-\beta_i n_i f V_n}\right)^2}$$

$$+ \frac{\frac{1}{\rho_o} k_{c,i} \Theta_{i,n}^{s} k_{a,i} a_{i,n} n_i f e^{(1-2\beta_i) n_i f V_n}}{\left(\frac{1}{n_i F} + \frac{1}{\rho_o} k_{c,i} \Theta_i^{s} e^{-\beta_i n_i f V_n}\right)^2} \quad . \qquad [2\text{-}23]$$

For each time step, the iteration scheme outlined in Eqs. [2-20] through [2-23] must be completed. However, when the previous time step's value of V_n is used to start the iteration in Eq. [2-22], convergence is generally obtained within 3 or 4 iterations.

It should be noted that the partial currents can be obtained explicitly in terms of V_n in Eq. [2-18] because the electrochemical reaction was

assumed to be first order in the concentration of the discharging metal ion. This is usually the case in the electrodeposition of metals. If the reaction were not first order, it would still be relatively easy to solve numerically for the electrode potential and the partial currents.

Equation [2-18] is also valid for controlled potential electrolysis. If the ohmic drop is neglected in Eq. [2-17], Eq. [2-18] yields the partial current explicitly for controlled potential electrolysis. For the controlled electrode-potential mode of operation with ohmic resistance ($r \neq 0$), Eqs. [2-18] and [2-19] can be combined to form a function I_n, analogous to H_n

$$I_n = -i_n + \sum_{i=1}^{m} \frac{k_{a,i} a_{i,n} e^{(1-\beta_i) n_i f \epsilon_n} e^{-(1-\beta_i) n_i f r i_n} - \frac{1}{\rho_o} k_{c,i} \Psi^s_{i,n} e^{-\beta_i n_i f \epsilon_n} e^{\beta_i n_i f r i_n}}{\frac{1}{n_i F} + \frac{1}{\rho_o} k_{c,i} \Theta^s_{i,n} e^{-\beta_i n_i f \epsilon_n} e^{\beta_i n_i f r i_n}} \qquad [2\text{-}24]$$

where $\epsilon_n = E_n + \left[U^\theta_{re} - \frac{1}{n_{re} f} \sum_i s_{i,re} \ln \left(\frac{c_{i,re}}{\rho_o} \right) \right]$. The value of the cell-current density can be found by iteration:

$$(i_n)_{new} = (i_n)_{old} - \left[\frac{I_n}{\left(\frac{\partial I_n}{\partial i_n} \right)} \right]_{old} \qquad [2\text{-}25]$$

where

$$\frac{\partial I_n}{\partial i_n} = -1 - \sum_{i=1}^{m} \frac{\dfrac{k_{a,i}\alpha_{i,n}e^{(1-\beta_i)n_i f\epsilon_n}(1-\beta_i)r}{RT}e^{-(1-\beta_i)n_i fri_n} + \dfrac{k_{c,i}\Psi^s_{i,n}e^{-\beta_i n_i f\epsilon_n}\beta_i r}{\rho_o RT}e^{\beta_i n_i fri_n}}{\left(\dfrac{1}{n_i F} + \dfrac{1}{\rho_o}k_{c,i}\Theta^s_{i,n}e^{-\beta_i n_i f\epsilon_n}e^{\beta_i n_i fri_n}\right)^2} + \frac{\dfrac{1}{\rho_o}k_{c,i}\Theta^s_{i,n}k_{a,i}\alpha_{i,n}e^{(1-2\beta_i)n_i f\epsilon_n}n_i fre^{-(1-2\beta_i)n_i fri_n}}{\left(\dfrac{1}{n_i F} + \dfrac{1}{\rho_o}k_{c,i}\Theta^s_{i,n}e^{-\beta_i n_i f\epsilon_n}e^{\beta_i n_i fri_n}\right)^2}. \quad [2\text{-}26]$$

The model we have provided for the liquid-phase mass transfer and kinetics could also be used to describe processes for the electrosynthesis of compounds by a periodic current or potential source. Alkire and Tsai (50) have listed a number of references for the synthesis of compounds by a periodic current source.

The Electrodeposit

Two problems must be treated for a complete description of the solid-state alloy. The first problem concerns the dependence of the surface activity on the alloy composition. When experimental data are combined with the judicious choice of an activity model, the activities of the alloy components can be obtained. The second problem involves the actual number of monolayers in the electrodeposit which affect the surface activity, or the relevant surface-activity thickness (*RSAT*).

The first step in determining component activity coefficients is to choose a model for the molar excess Gibbs energy G^E. The excess properties are taken with reference to an ideal solution wherein the standard state for each component is the pure solid at the temperature and pressure of the

mixture. Once the molar excess Gibbs energy is expressed, the activity coefficients γ_i can be found by (51)

$$RT \ln \gamma_i = \left[\frac{\partial (N_T G^E)}{\partial N_i}\right] . \qquad [2\text{-}27]$$

Since no general treatment has yet been developed to consider repulsion between ion cores or the interaction among cores and electrons at the Fermi surface, a useful approach is to treat the interaction between ions in a mixture by a pairwise model. The properties of such a system are represented by the sum of interactions between neighboring pairs of ion cores and the complications due to higher-order interactions are ignored. This quasichemical (or lattice theory) approach is outlined by Swalin (52) for regular solutions in which there is no excess entropy creation upon mixing, and any nonideality is considered in an enthalpy of mixing term. For the quasichemical approach, the activity coefficients for a binary, regular solution are given by (52,53)

$$\ln \gamma_A = \frac{(1 - x_A)^2 \Omega}{RT} \qquad [2\text{-}28]$$

$$\ln \gamma_B = \frac{(1 - x_B)^2 \Omega}{RT} \qquad [2\text{-}29]$$

where Ω is an adjustable parameter.

Equations [2-28] and [29] bear close resemblance to the two-suffix Margules equation. Guggenheim (54) has extended the quasichemical approach to model systems which exhibit considerable deviation from randomness. For this case, the excess entropy of mixing is no longer zero and a short-range order parameter is introduced which may be determined in some cases by x-ray and neutron diffraction techniques (52).

Two other informative treatments of solid-state thermodynamics should be mentioned before presenting the theoretical aspects for the activity model we have chosen to use in this paper. Darken and Gurry's text (55) contains a large number of references with tabular thermodynamic data for numerous metal systems, as well as an informative description of solid-state physical chemistry. Lumsden's (56) monograph illustrates the usefulness of thermodynamics for the accurate correlation of various equilibrium properties in alloy systems.

Electrodeposited metals usually have a more fine-grained, amorphous structure than their pyrometallurgical counterparts. Hence, the simple quasichemical lattice model does not generally represent the true thermodynamic nature of electrodeposited alloys. The activity model proposed by Renon and Prausnitz (57,58) is well suited to such a morphology. The authors define a local mole fraction x_{ij} representing the mole fraction of i in the vicinity of j. In a treatment similar to Guggenheim's extension of the quasichemical lattice theory, the local mole fractions are related to the overall mole fractions through Boltzmann factors:

$$\frac{x_{ji}}{x_{ki}} = \frac{x_j}{x_k} \frac{\exp(-\alpha_{ij} g_{ji}/RT)}{\exp(-\alpha_{ik} g_{ki}/RT)} \qquad [2\text{-}30]$$

The parameter α_{ij} ($\alpha_{ij} = \alpha_{ji}$) characterizes the tendency of components i and j to mix in a nonrandom fashion. The parameter g_{ik} ($g_{ik} = g_{ki}$) represents the energy of interaction between an $i-k$ molecular pair. Scott's theory (59) is used to relate the extensive excess properties to the interaction energies and the local mole fractions. For a solution of m components, the molar excess Gibbs energy is

$$\frac{G^E}{RT} = \sum_{i=1}^{m} x_i \frac{\sum_{j=1}^{m} \tau_{ji} G_{ji} x_j}{\sum_{k=1}^{i} G_{ki} x_k} \qquad [2\text{-}31]$$

where

$$\tau_{ji} = \frac{(g_{ji} - g_{ii})}{RT} \qquad [2\text{-}32]$$

and

$$G_{ji} = \exp(-\alpha_{ji} \tau_{ji}) \quad . \qquad [2\text{-}33]$$

Using Eqs. [2-27] and [2-31], the activity coefficient of component i can be calculated (57):

$$\ln \gamma_i = \frac{\sum_{j=1}^{m} \tau_{ji} G_{ji} x_j}{\sum_{k=1}^{m} G_{ki} x_k} + \sum_{j=1}^{m} \frac{x_j G_{ij}}{\sum_{k=1}^{m} G_{kj} x_k} \left(\tau_{ij} - \frac{\sum_{l=1}^{m} x_l \tau_{lj} G_{lj}}{\sum_{k=1}^{m} G_{kj} x_k} \right) . \qquad [2\text{-}34]$$

One of the advantages of this activity model is that it can be extended to as many components as desired without any additional assumptions and without adding any constants other than those obtained from binary data. This treatment is applicable to partially miscible as well as completely miscible systems.

For some alloy systems, the simpler quasichemical treatment may represent the activity data quite well. This approach, outlined by Eqs. [2-28] and [2-29], can also be extended to model multicomponent systems. When Eqs. [2-28] and [2-29] cannot be used to fit the data, the computer programs listed in appendix K of Ref. 60 can be used to fit the parameters of Eq. [2-34].

For this general treatment, we have chosen to use Eqs. [2-30] through [2-34] to describe the electrodeposit thermodynamics. However, the overall

mole fractions in Eq. [2-30] must be adjusted to represent the surface, rather than bulk, composition. Though the activity model accounts for local composition, no characteristic length is associated with the range of applicability. Even for single-component electrodeposition systems, the surface plays a major role in the kinetics. Wranglen (61) observed that metals of low overvoltage grow by the lateral extension of layers, 0.1–1 μm thick. It was also observed that changing the current density changes the relative growth rates between crystal faces as well as where the deposited layers begin to grow on the respective crystal faces. Wranglen's microphotographic study of growth layers contains results for a periodic current source although no high-frequency results are reported.

Underpotential deposition studies can yield some information about the *RSAT*. Kolb et al. (62) correlated the underpotential shift between the bulk deposit stripping peak and the first deposited monolayer stripping peak as a function of the difference in work functions between the substrate and the deposited material. The authors conclude that the work function of the first deposited monolayer may not differ greatly from that of the bulk electrodeposit, although the optical properties of such a monolayer are usually far from those of the bulk. Adzic et al. studied the underpotential deposition of Zn on Ag (63) and Zn on Cu and Au (64). For these reversible systems, the results support the work of Kolb et al. Approximately one monolayer of zinc was formed on the polycrystalline substrates prior to bulk deposition.

All of the work mentioned above indicates that the *RSAT* is about one monolayer. However, this may not be the case for all systems. Cadle and Bruckenstein (65) found that although only one monolayer of Bi is deposited on Pt by underpotential deposition, it is not until approximately 5 mono-

layers have been deposited that bulk deposition is occurring.

Takamura and Kozawa (66) have reviewed a great deal of literature concerned with the use of optical reflectance methods to investigate an electrode-electrolyte interface *in situ*. They have found that for a number of systems, the first few atomic layers do not have the same reflectance properties (67).

In general, higher current densities will shorten the *RSAT*. Setty and Wilman (68) have shown by electron diffraction experiments that high current densities promote the growth of a random, polycrystalline deposit growth which does not reflect the original electrode structure even during the initial stages of electrodeposition. Since most pulse-plating processes make use of unusually high current densities, a highly random (or amorphous), polycrystalline deposit typically results. It has also been observed that the influence of a polycrystalline substrate with small crystallite grains ceases to exist at much earlier stages of deposition than that of the surface of a large single crystal substrate (69).

Though there is a wealth of literature concentrating on epitaxy and morphology of electrodeposits, there is no clear *a priori* approach to estimate the *RSAT*. The work reviewed in this paper dealt only with the early stages of electrodeposition. In a pulse-plating processes, the deposit usually has a random, polycrystalline structure, and the *RSAT* is probably much less than that of the initially deposited monolayer.

Optical studies seem to indicate that the *RSAT* can be greater than a monolayer. Conversely, the high current-density pulses often used in practical plating operations may lower the *RSAT* to about a monolayer. In light of the above considerations, it may be advantageous to weight the substrate's

influence on the newly forming surface with a function that decays with depth (70,71). For the purposes of this work, the following heuristic treatment will be used in estimating a relevant surface composition x_i:

$$x_i = \frac{\sum_{ml} \left[1 - \exp\left(-\sigma \frac{RSAT - d_{ml}}{RSAT} \right) \right] x_{i,ml}}{\sum_{ml} \left[1 - \exp\left(-\sigma \frac{RSAT - d_{ml}}{RSAT} \right) \right]} \qquad [2\text{-}35]$$

where $d_{ml} \leq RSAT$.

In Eq. [2-35], the subscript ml refers to a monolayer, d_{ml} is the monolayer's distance from the surface, σ is a system-specific proportionality constant, $x_{i,ml}$ refers to the monolayer mole fraction of component i, and the bracketed terms are weighting functions for each monolayer. Monolayers that are deep below the surface make only a small contribution to the relevant surface composition. For $d_{ml} > RSAT$, no effect on the surface composition is taken in account. Equation [2-35] assures that the sum of the overall mole fractions is unity. It can also be seen that if σ is set to a very high value, then the weighting function for each monolayer within the $RSAT$ will essentially be unity.

We can now formalize in the following algorithm the procedure for the implementation of the mathematical model.

For $t = t_1, t_2, \cdots t_n$

1. Obtain $\{i_n \mid E_n\}$
2. Solve for $\Theta^s_{i,n}$ and $\Psi^s_{i,n}$ (Eqs. [2-12] through [2-15]).
3. Solve for $\{H_n \mid I_n\}$ (Eq. {[2-21] | [2-24]}).

4. Solve for $\{(\partial H_n/\partial V_n) \mid (\partial I_n/\partial i_n)\}$ (Eq. {[2-23] | [2-26]}).
5. solve for $\{V_n \mid i_n\}$ by iteration (Eq. {[2-22] | [2-25]}).
6. Obtain the new surface composition from the individual currents according to Faraday's law (Eqs. [2-18] and [2-35]).
7. Determine the new surface activity (Eq. [2-34]).

The quantities in brackets, { }, separated by a bar, |, refer to the controlled current mode of operation (first quantity in the brackets), or the controlled potential mode of operation (second quantity in brackets). Appendix 2 contains the computer program and data file used to implement the mathematical algorithm.

Results

We have chosen to model a three-component system to illustrate the flexibility of the algorithm. It is not possible to obtain the necessary parameters required for the model from the literature; for this reason, we are presently working on experiments that should yield the necessary data. We will discuss the experimental investigation and make a model comparison in a future publication.

The model inputs are listed in Table 1. The values of the standard electrode potentials U_i^θ can be calculated from the rate constants. The values of U_i^θ are 0.3, 0.1, and -0.1 volts, for components 1, 2, and 3, respectively. For each reaction, the rate constants have been chosen to yield an exchange-current density of 2 ma/cm^2 for $\alpha_i = 1$ and $(c_i/\rho_o) = 1$ mol/kg . The transport properties for all components are equivalent since the diffusion coefficient and the characteristic length δ_i , which has been used to nondimensionalize the mass-transfer problem, were set equal for all ionic species.

For the base case, the current is pulsed to the total dc limiting current of the system. This current program is displayed in Fig. 2-1. In Fig. 2-2, the

Table 1. Model inputs.[†]

Quantity				Units
c_i^b	1×10^{-6}	1×10^{-5}	1×10^{-4}	mol/cm^3
d_m	3			Å
$k_{s,i}$	8.741×10^{-14}	2.109×10^{-10}	5.091×10^{-7}	mol/cm^2–s
$k_{c,i}$	1.229×10^{-3}	5.092×10^{-7}	2.110×10^{-10}	kg/cm^2–s
n_i	2	2	2	---
r	0			ohm –cm^2
RSAT	9			Å
x_i^g	1.0	0.0	0.0	mol i/mol
β_i	0.5	0.5	0.5	---
γ_i	1.0	1.0	1.0	---
δ_i	0.001014	0.001014	0.001014	cm
ρ_o	0.001			kg/cm^3
ρ_i	0.073	0.073	0.073	mol/cm^3
σ	1.0			---

[†]For component entries, component 1 is at the far left, followed by components 2 and 3 respectively.

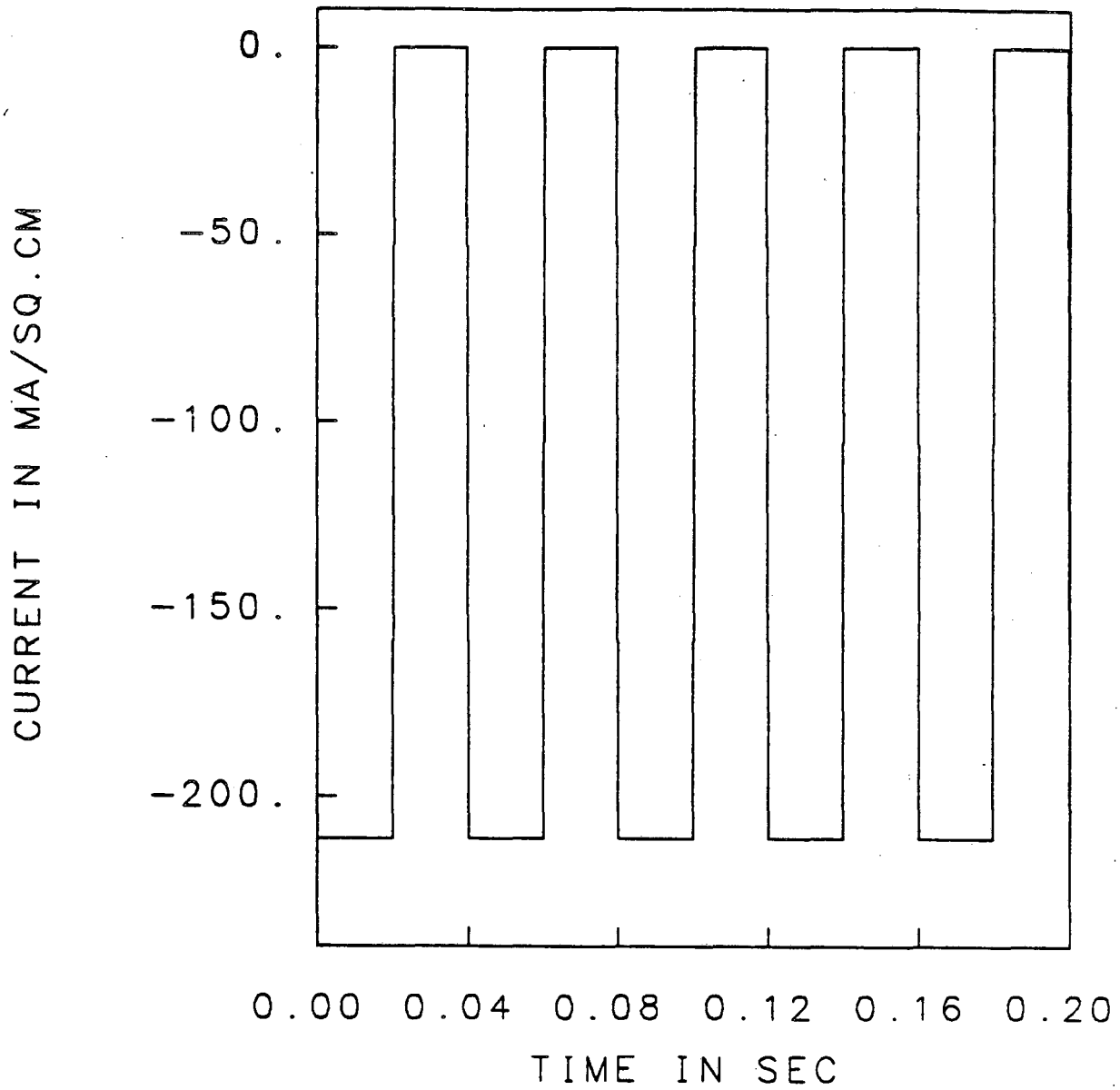

Figure 2-1. Current source for the base case. The maximum cathodic current is the sum of the dc limiting currents of the discharging ions (−211 mA/sq·cm).

dimensionless surface concentrations are plotted for a system in which a Nernst diffusion layer is applicable (the dotted curves) and for the more rigorous solution outlined by Eqs. [2-12] and [2-13] (the unbroken curves). It can be seen that the two solution techniques yield very similar answers, as would be expected from the close agreement of the respective current-step solutions. Due to the low bulk concentration and more noble character of component one, its surface concentration remains negligible throughout the electrodeposition process. The least noble component 3 has the highest bulk and surface concentration. Figure 2-2 illustrates that the process reaches a uniform and sustained periodic state after about the fourth cycle.

The electrode-potential profile is portrayed in Fig. 2-3. The lower portions of the curve correspond to the on-time. While deposition is occurring, the electrode potential is forced to more cathodic (negative) values since the discharging ion concentrations are decreasing. During the off-times, the potential drifts in the anodic direction as corrosion reactions take place and metal ions are transported to the electrode surface by convection and diffusion.

One of the more practical aims of this work is to obtain the electrodeposit composition. A plot of the deposit composition is shown in Fig. 2-4. Though component 1 is the most noble component, its low bulk concentration limits its rate of mass transfer thereby suppressing its deposit concentration. The opposite is true for component 3. About 10 monolayers are deposited during the on-time; thus, there is a considerable variation in the electrodeposit concentration during the on-time. The corrosion currents also cause a change in the deposit mole fractions during the off-time. At higher frequencies, there would be less variation in the deposit composition during a pulse.

In order to obtain the deposit mole fractions, the partial currents must be known. A plot of partial currents is shown in Fig. 2-5 for a pulse-reversal

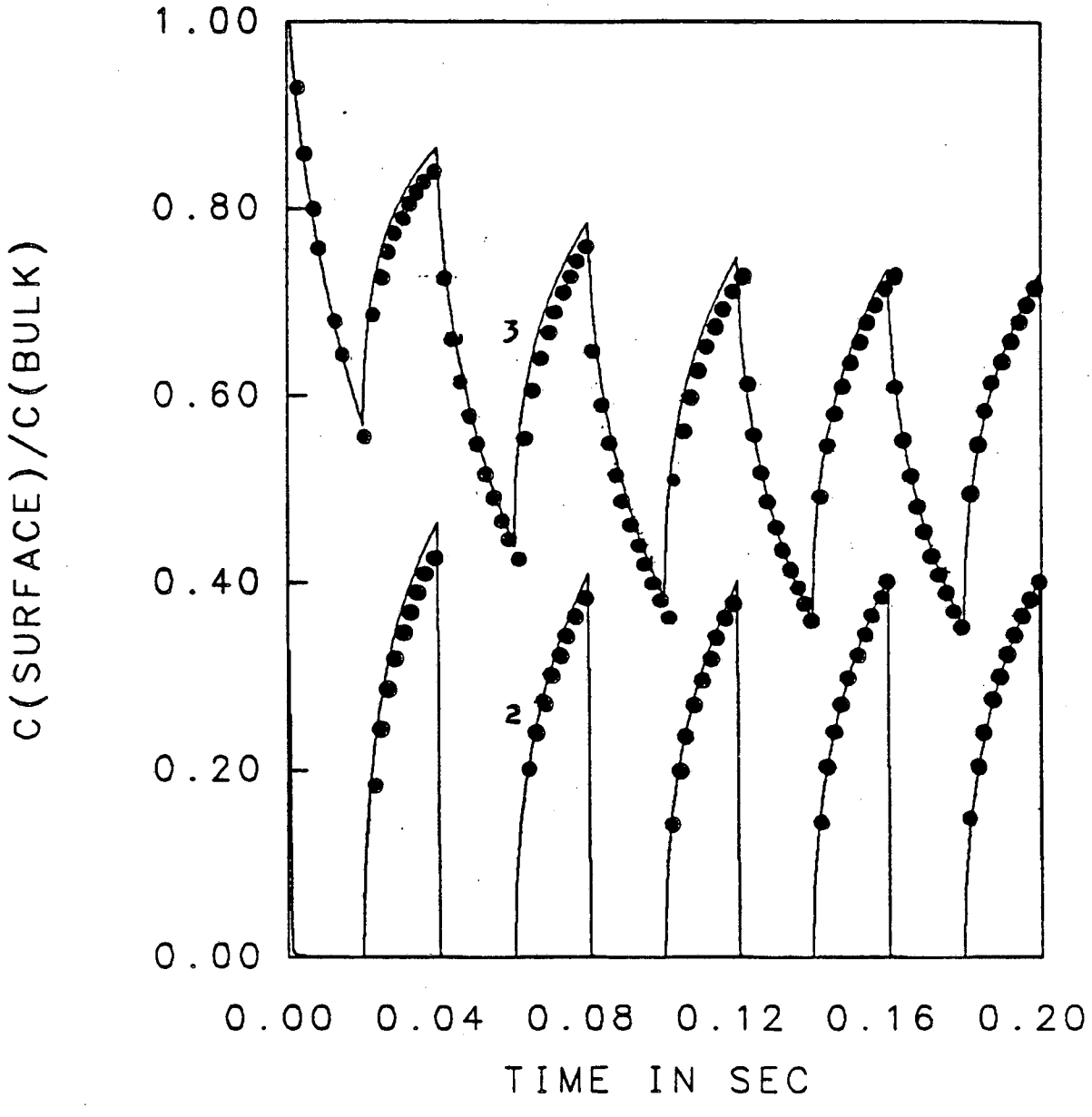

Figure 2-2. Dimensionless surface concentrations for the first five cycles. The current source is shown in Fig. 2-1. The dotted curve was obtained using the Nernst diffusion layer approximation. The surface concentration of component 1 remains near zero throughout the deposition process.

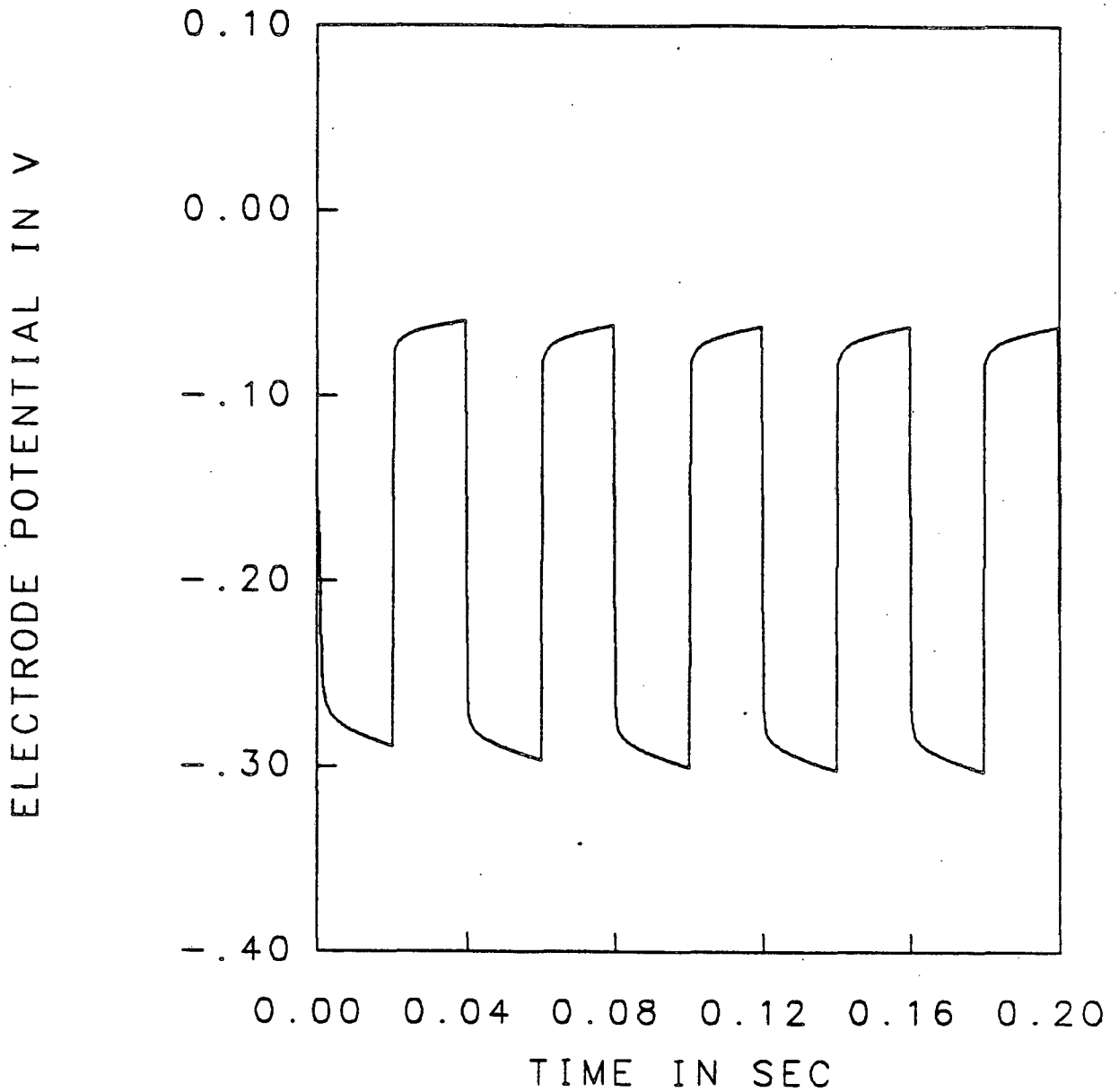

Figure 2-3. Electrode potential relative to a SHE for the base case. The lower portion of the curve represents the on-time.

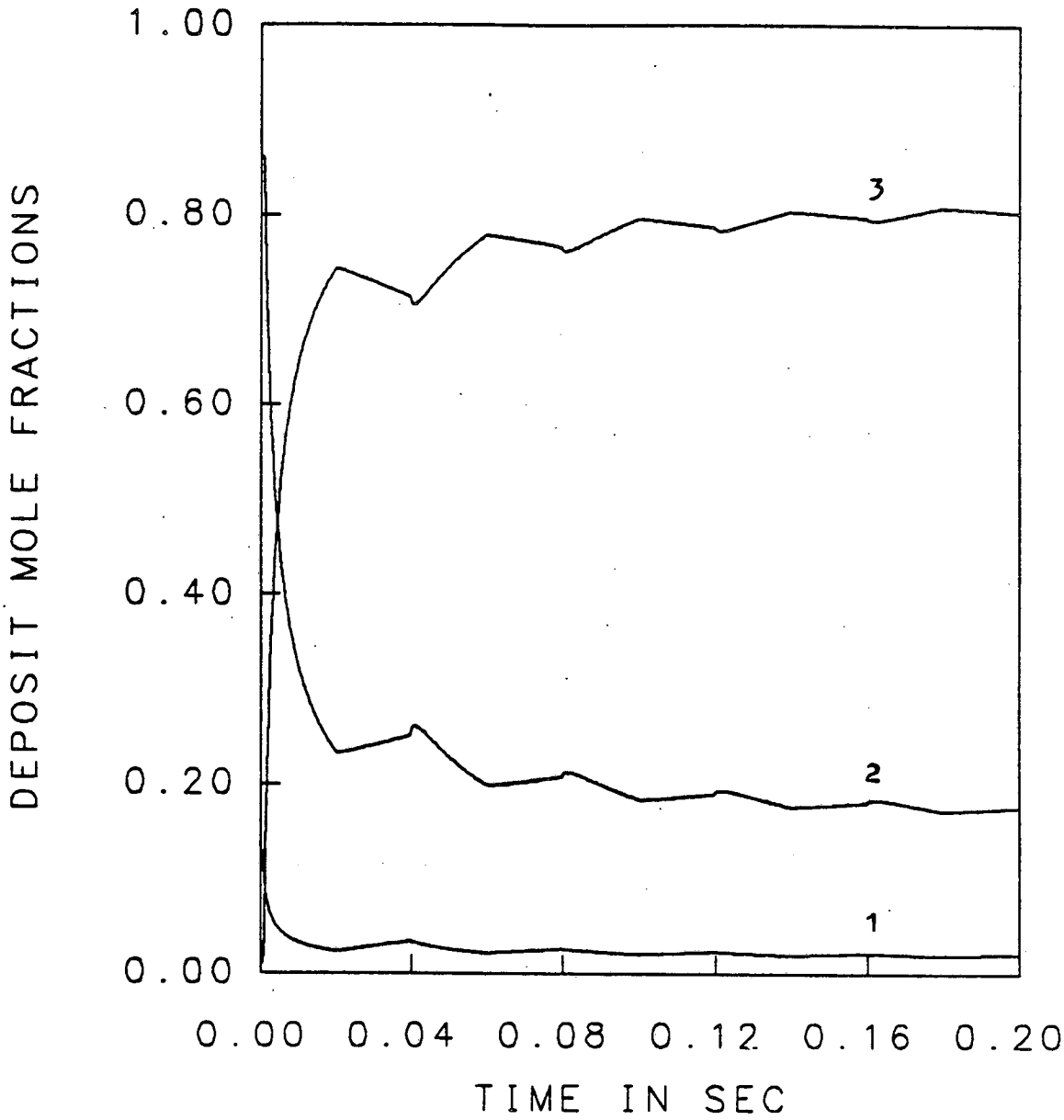

Figure 2-4. Deposit mole fraction variation for the base case. Uppermost curve: component 3. Middle curve: component 2. Lowestmost curve: component 1. At time zero, the electrode is pure 1.

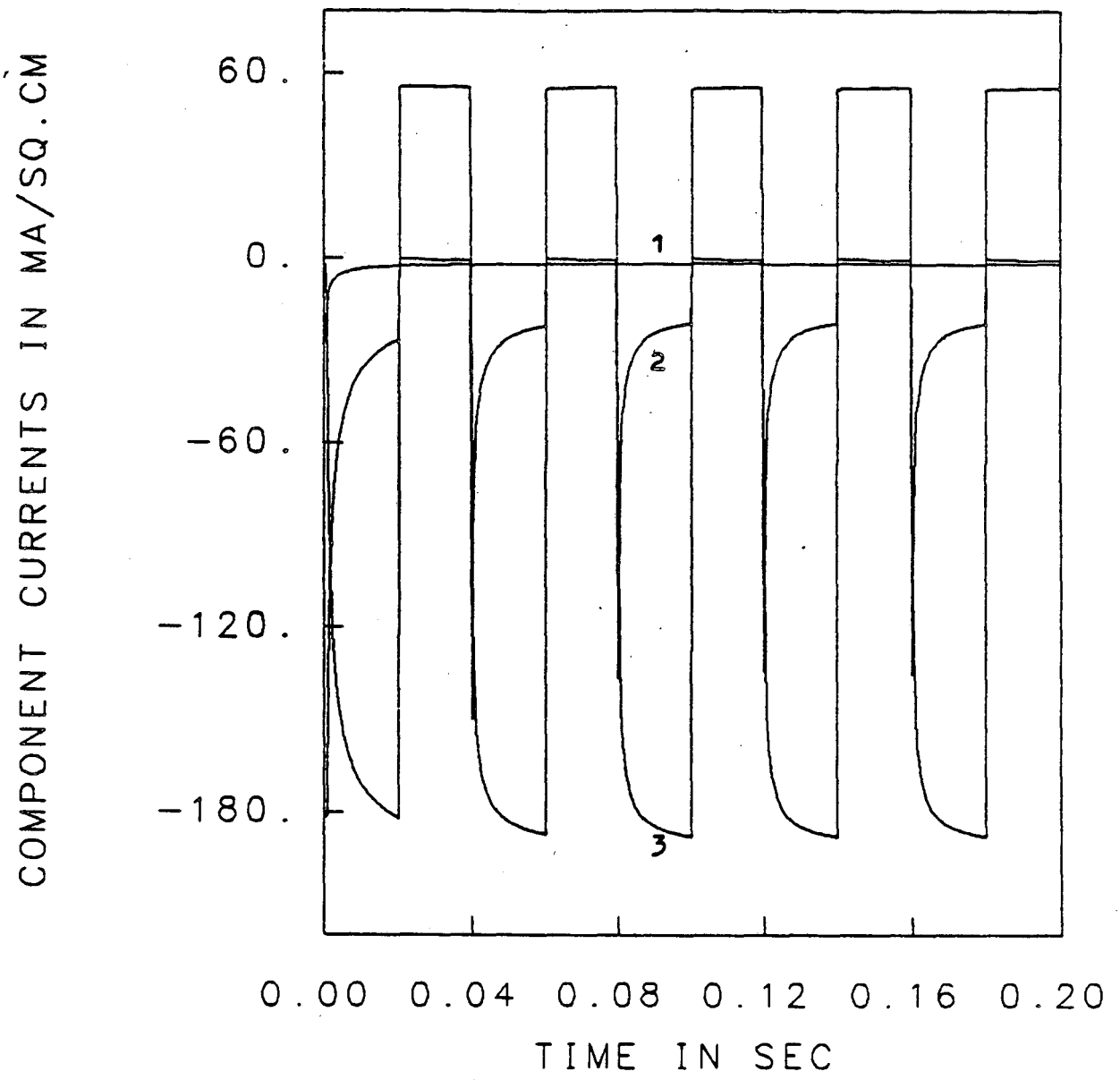

Figure 2-5. Component currents for a pulse-reversal current source. The current is reversed to 52.8 mA/sq·cm. The maximum cathodic current is the same as that shown in Fig. 2-1 (211.2 mA/sq·cm).

current source. A pulse-reversal current source is often used to produce smooth deposits, and it has a significant effect on the alloy composition and ionic surface concentrations. Due to the high bulk concentration of component 3, it carries most of the cathodic current. Figure 2-5 shows that components 1 and 2 incur mass-transport limitations during the on-time. Component 3 also carries most of the anodic current due to its more negative standard electrode potential. At the end of the fifth cycle, the total deposit mole fractions are 0.028, 0.222, and 0.750 for components 1, 2, and 3, respectively. For the base case (Figs. 2-1 through 2-4) the analogous values are 0.021, 0.175, and 0.804. In addition, the pulse-reversal current source supports higher ionic surface concentrations due to the periodic deposit dissolution. A comparison of Figs. 2-2 and 2-6 illustrates this.

Some insight into multicomponent electrodeposition can be gained by examining the case of a triangular current source. The triangular current waveform in Fig. 2-7 reaches a cathodic current density 1.7 times the total dc limiting current density displayed in Fig. 2-1. The nonlinear nature of the electrode kinetics is manifest in the electrode-potential profile in Fig. 2-8. The waveform in Fig. 2-7 was constructed to disallow the achievement of a periodic state. In Fig. 2-8, it can be seen that the minima reach more cathodic values for each succeeding period. At 0.20 seconds, all three discharging metal ions reach a zero surface concentration. Directly after this another reaction would be forced to take place, such as solvent decomposition.

The influence of the individual solid-state activities is shown by the comparison of Figs. 2-9 and 2-10 for the last off-time displayed in Fig. 2-1. The partial currents for the base case are shown in Fig. 2-9. Component 1 carries its dc limiting current density throughout the process. Component 2 is also depositing during the off-time whereas component 3 dissolves. The partial currents sum to zero during the off-time.

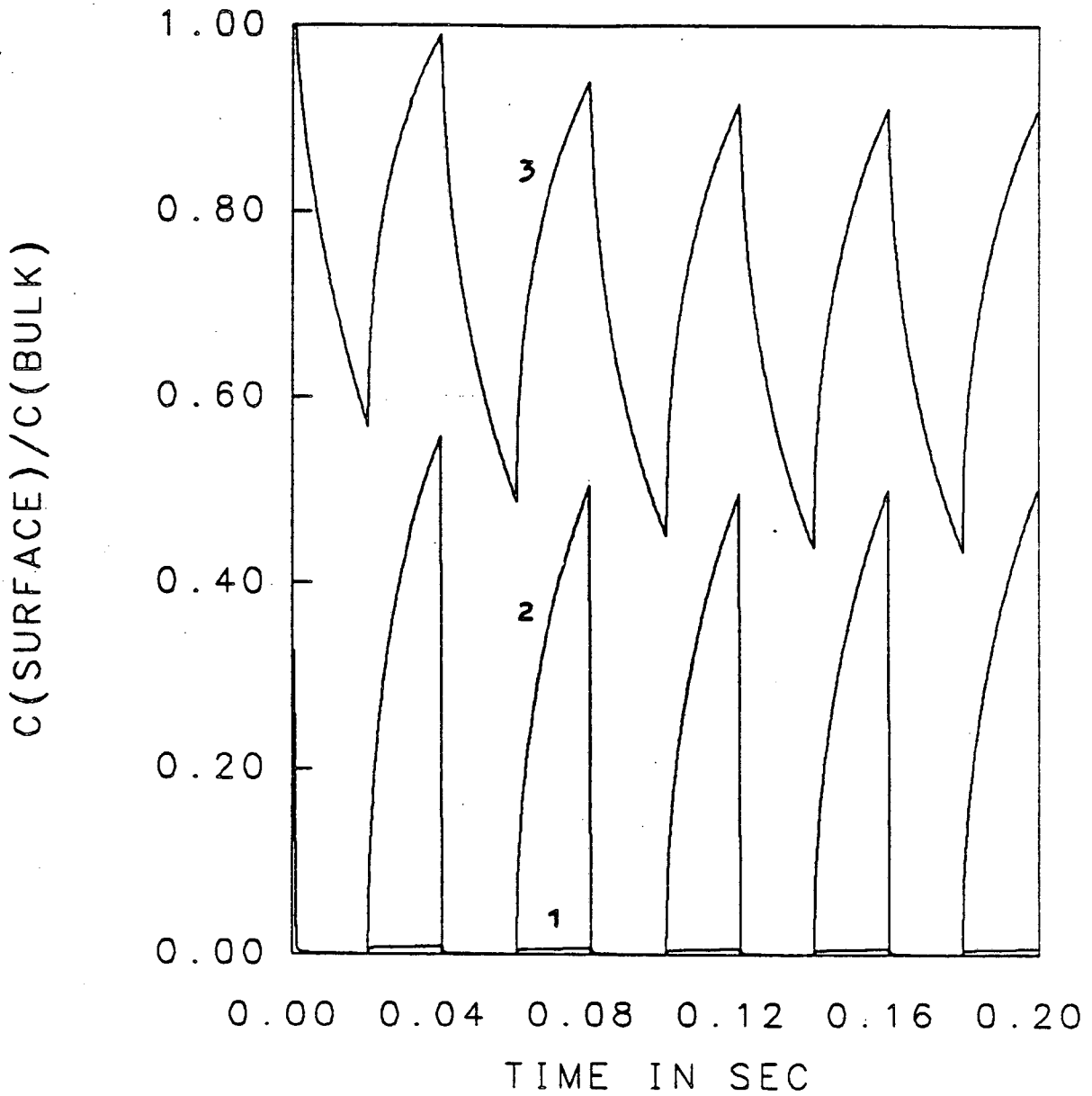

Figure 2-6. Dimensionless surface concentrations for the pulse-reversal current source. The surface concentrations are higher than those for the pulse-current source depicted in Fig. 2-2.

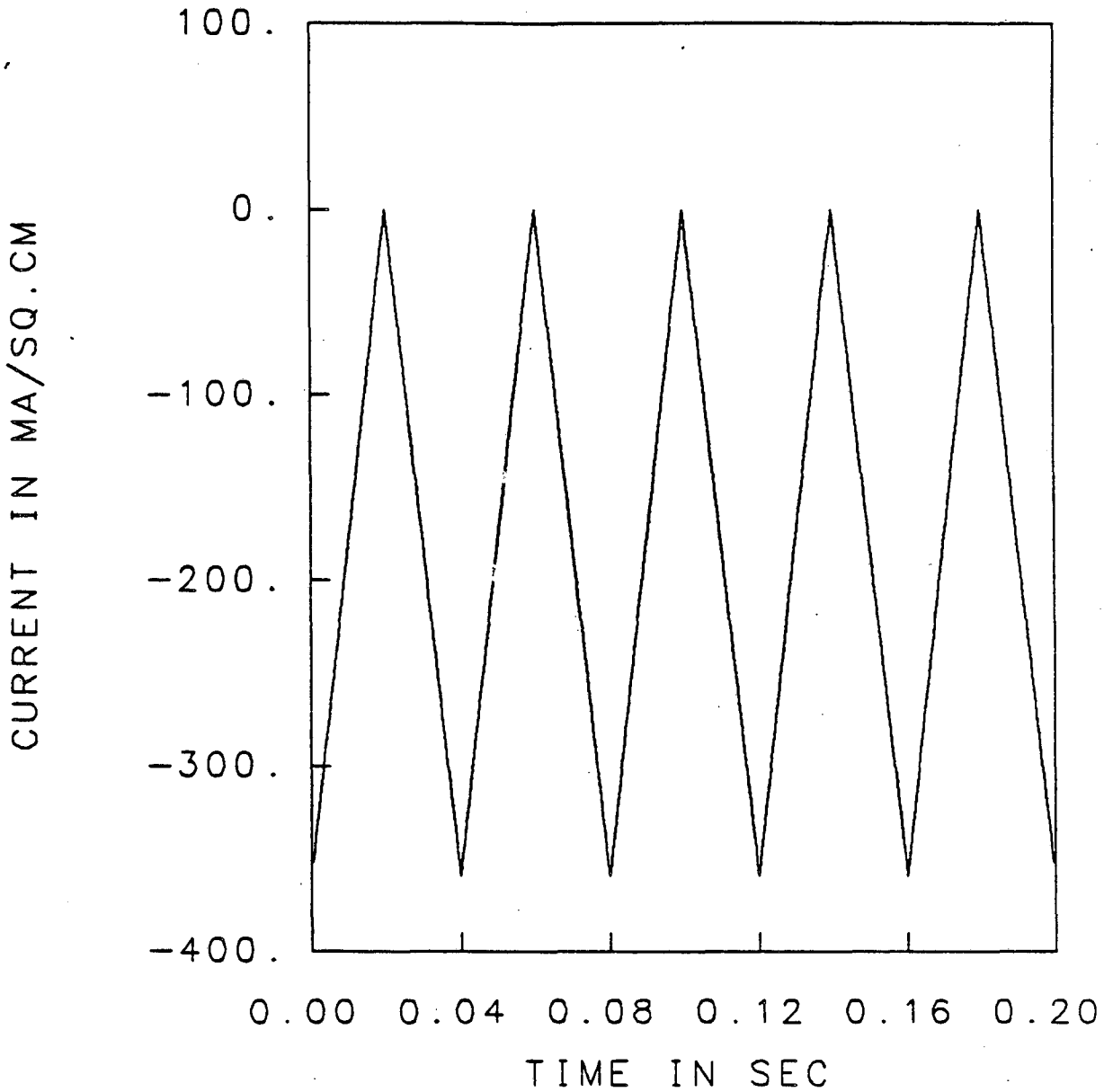

Figure 2-7. Triangular current source. The maximum current is 1.6 times the base case maximum cathodic current source shown in Fig. 2-1.

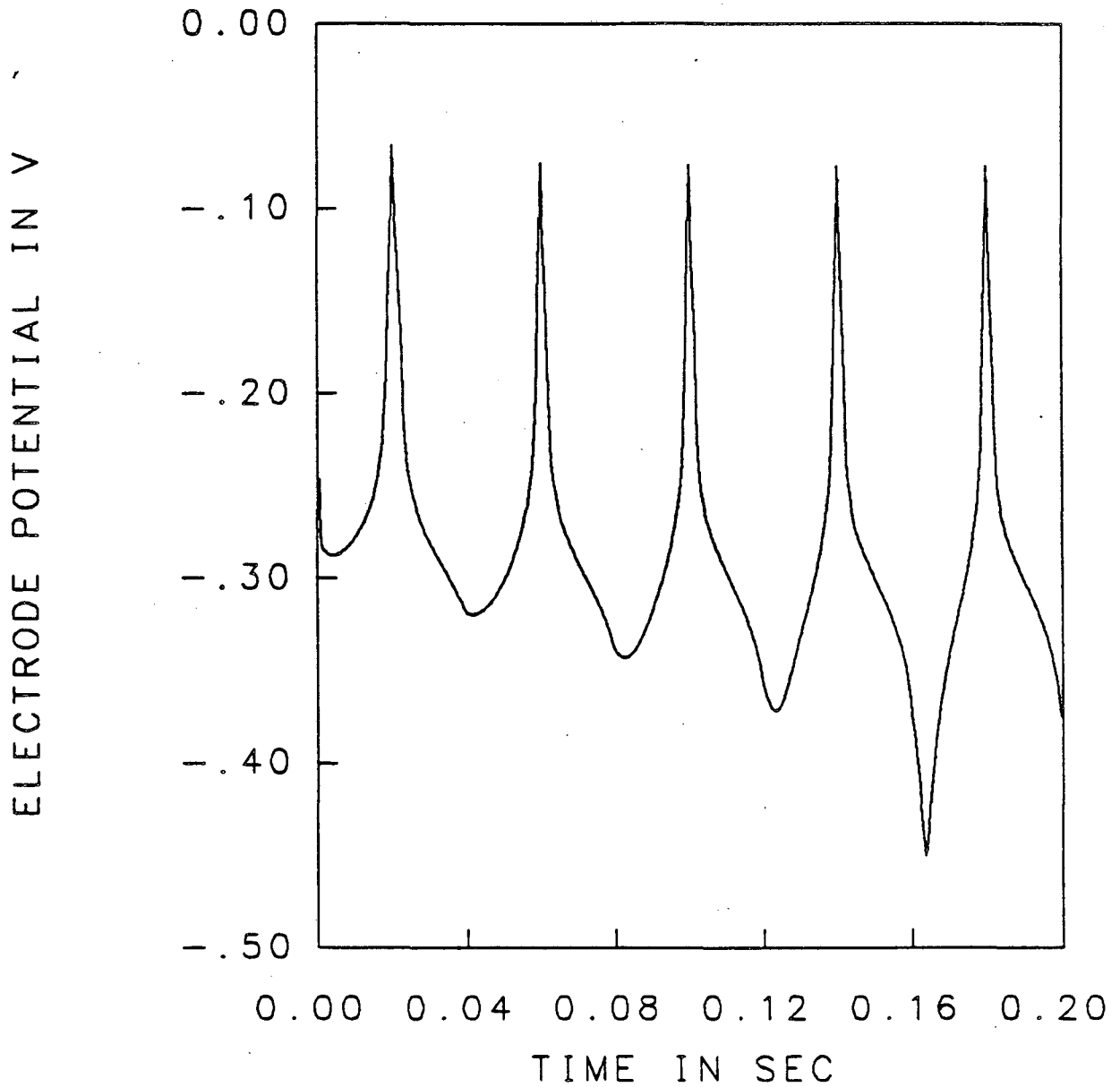

Figure 2-8. Electrode potential relative to the SHE for the triangular current source displayed in Fig. 2-7. For the specified conditions, a periodic state will not be achieved.

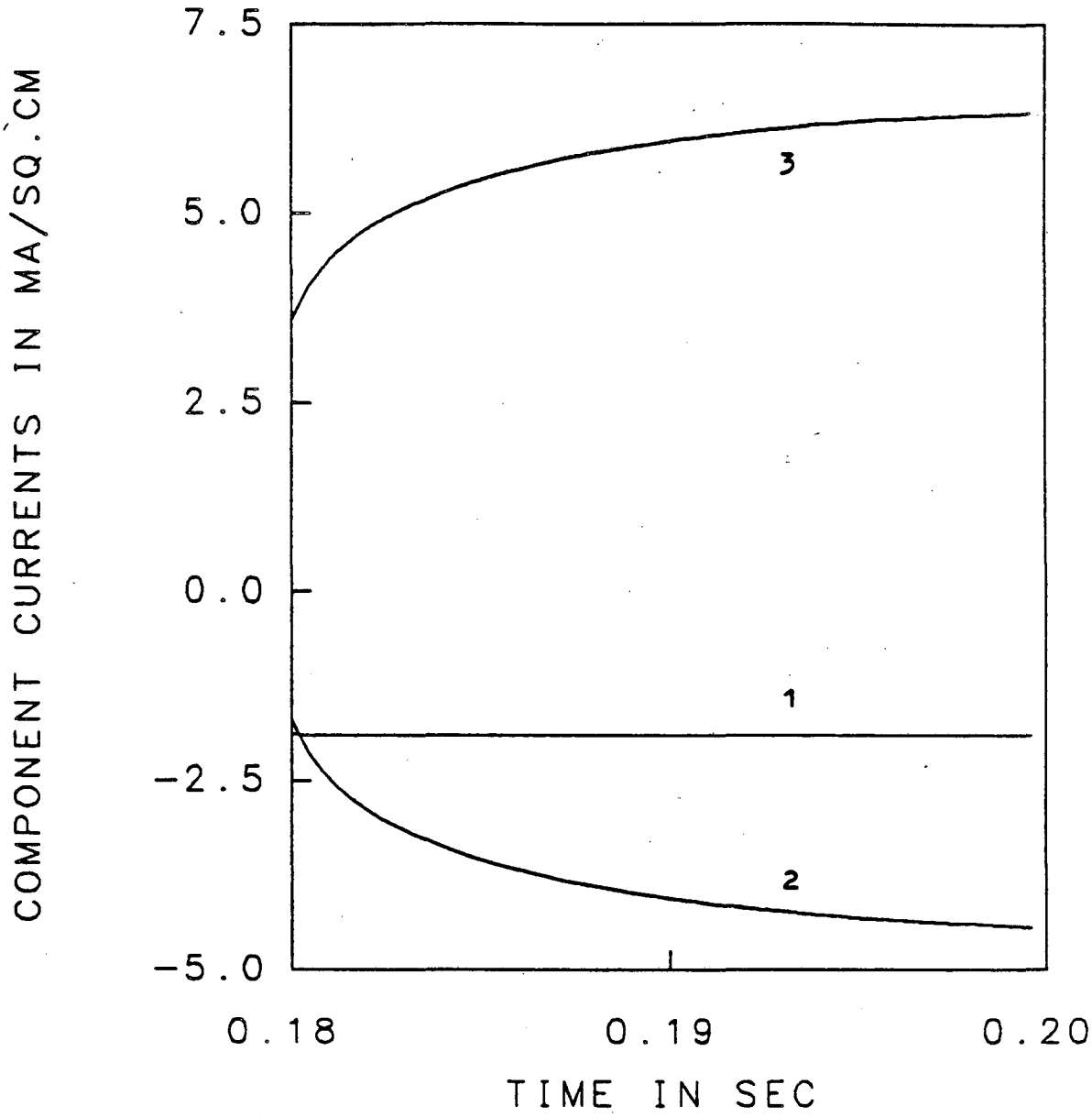

Figure 2-9. Component currents during the fifth off-time for the base case. The activity coefficients are all unity.

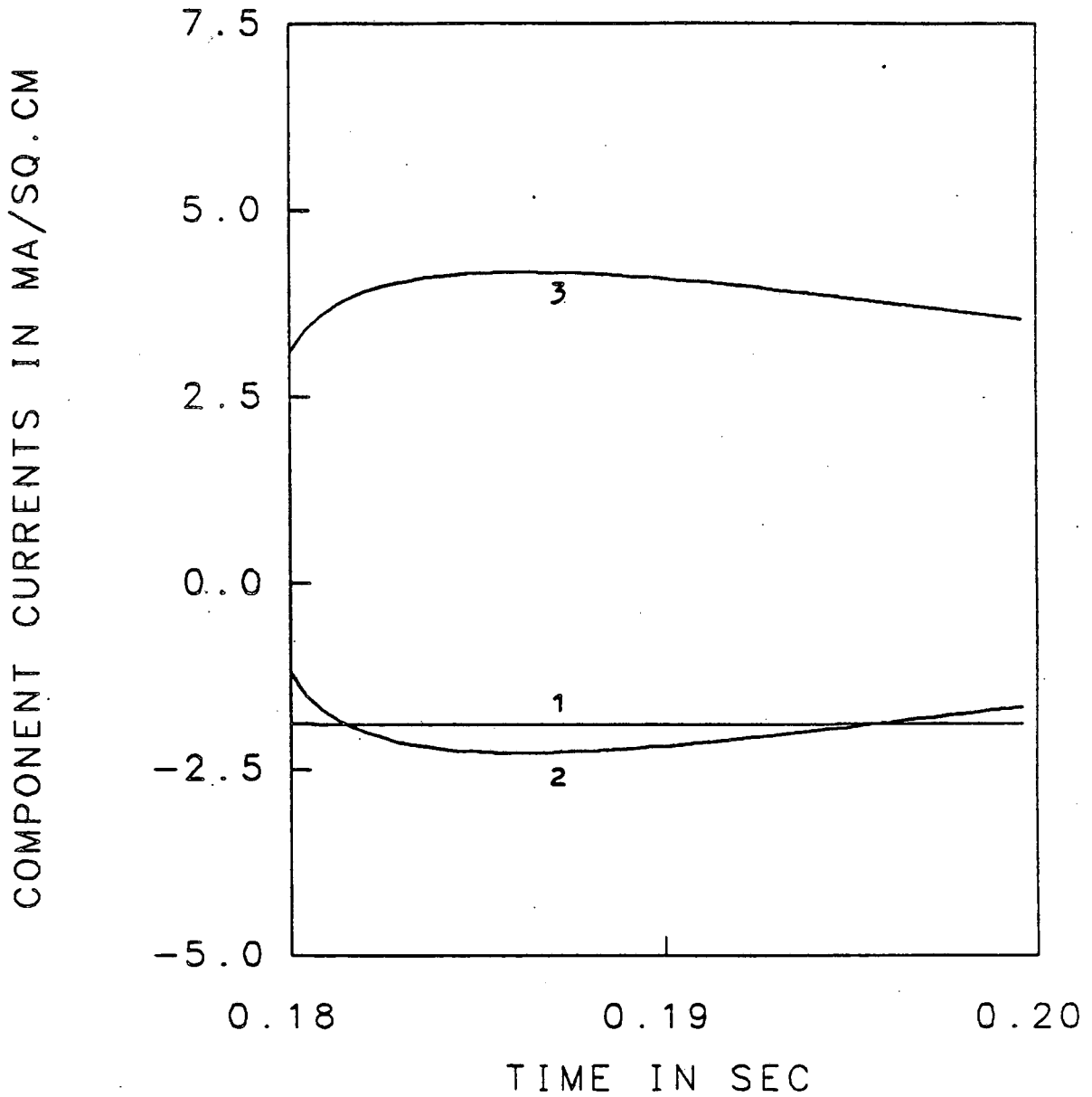

Figure 2-10. Component currents during the fifth off-time of the current source shown in Fig. 2-2. For this case, the activity coefficients deviate from unity. $g_{3,1} - g_{3,3} = g_{3,2} - g_{3,3} = -20{,}000\,J/mol$. Component 3 is attracted to components 1 and 2 in the electrodeposit.

When the energy of interaction between components 1 and 3 and components 2 and 3 is attractive, the corrosion currents are reduced and the deposit is more stable during the off-time. This is depicted in Fig. 2-10. These concepts are important to the understanding of the corrosion of alloys. In particular, elements can be chosen to form a more corrosion resistant alloy. Though the partial currents are relatively low in Figs. 2-9 and 2-10, and the overall deposit composition will not change greatly because of the surface free-energy changes, situations can occur in which the individual solid-state activities could be very important. For instance, in pulse-reversal electrodeposition, where the magnitude of the anodic current is high, the surface activities will play an important role in determining the electrodeposit composition and the ionic surface concentrations.

Thus far, we have investigated controlled current processes. The same equations are used to describe controlled potential processes, although the iteration scheme is slightly altered. For the electrode-potential source shown in Fig. 2-11, the surface-concentration history shown in Fig. 2-12 results. The situation is analogous to that shown in Fig. 2-2; the low concentration and more noble character of component one forces its surface concentration to negligible values throughout the process. Conversely, component three, which has the highest bulk concentration and is least noble, maintains a high dimensionless surface concentration.

The cell-current history is given in Fig. 2-13. The current is initially high during the more negative portion of the electrode potential cycle, and then diminishes due to increasing mass-transport resistance. The partial current densities are shown in Fig. 2-14. The mass-transport and kinetic resistances adjust themselves so that component one maintains its diffusion-limited current density, component two carries the majority of the cell-current density, and component three maintains a low rate of reaction with little mass-transport resistance. The component currents can be

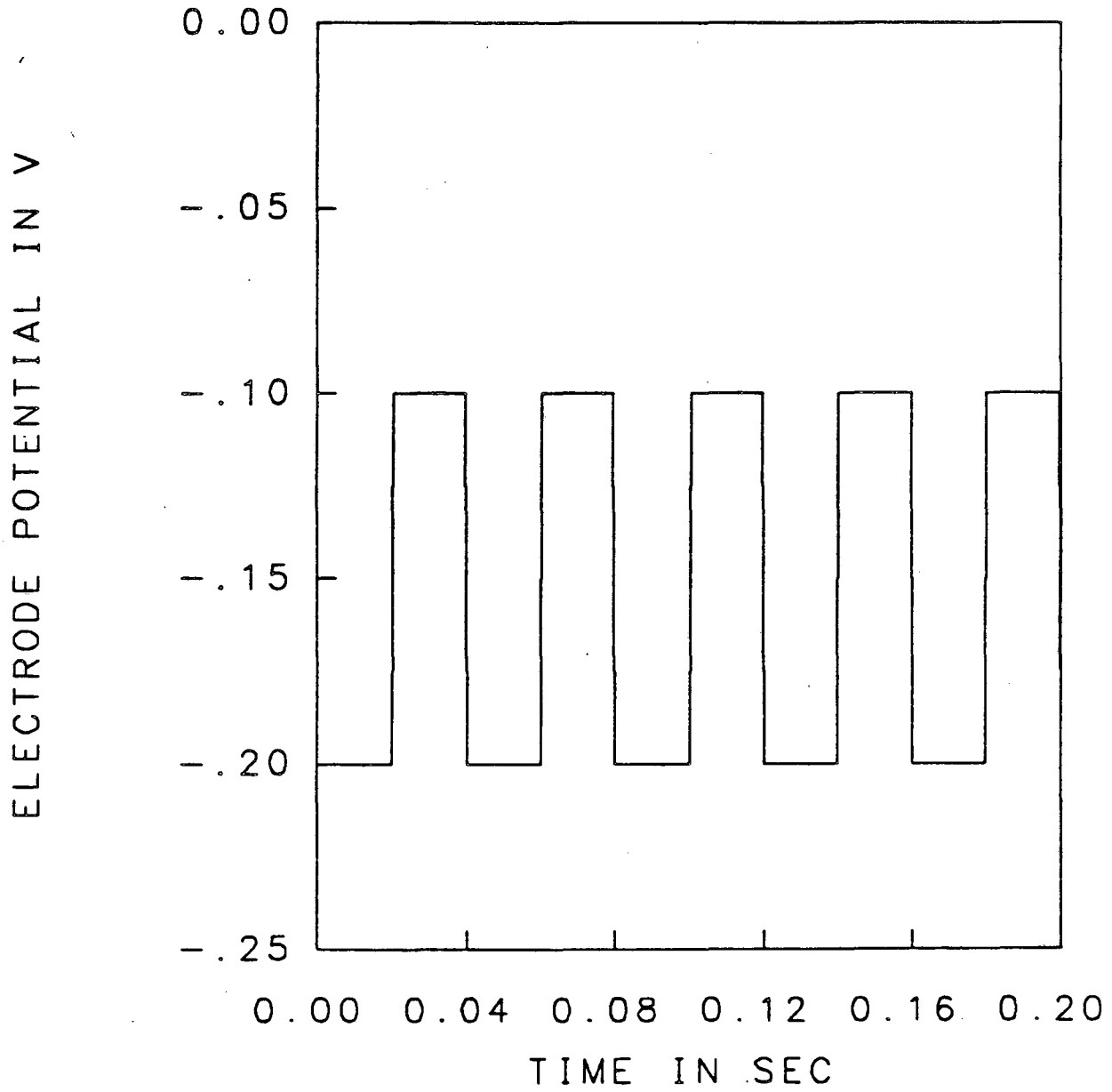

Figure 2-11. Electrode potential source. A SHE is assumed, and there is no ohmic resistance.

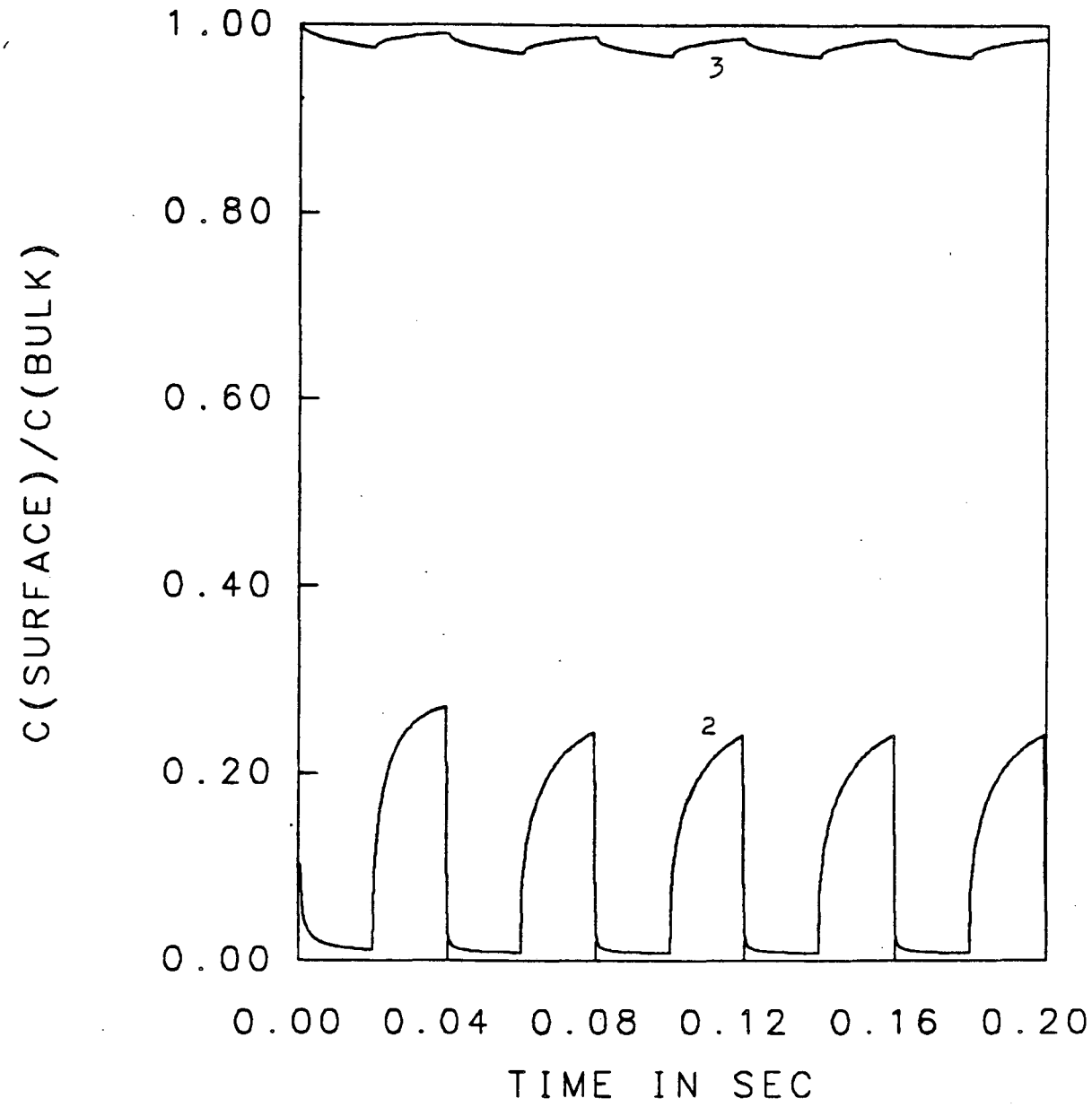

Figure 2-12. Dimensionless surface concentrations for the potential source shown in Fig. 2-11. The surface concentration of component one remains near zero throughout the deposition process.

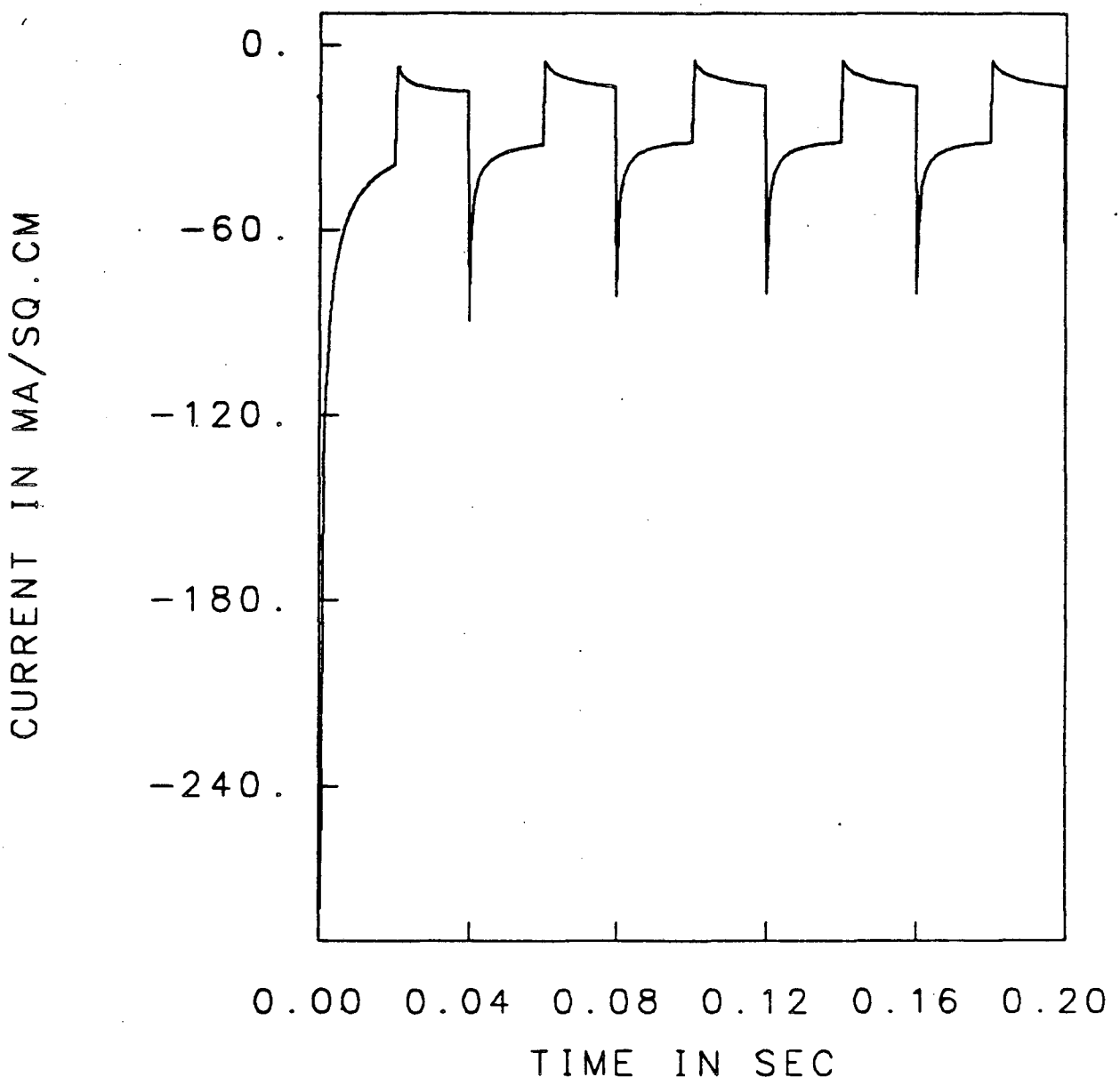

Figure 2-13. Cell-current density for the electrode-potential source shown in Fig. 2-11.

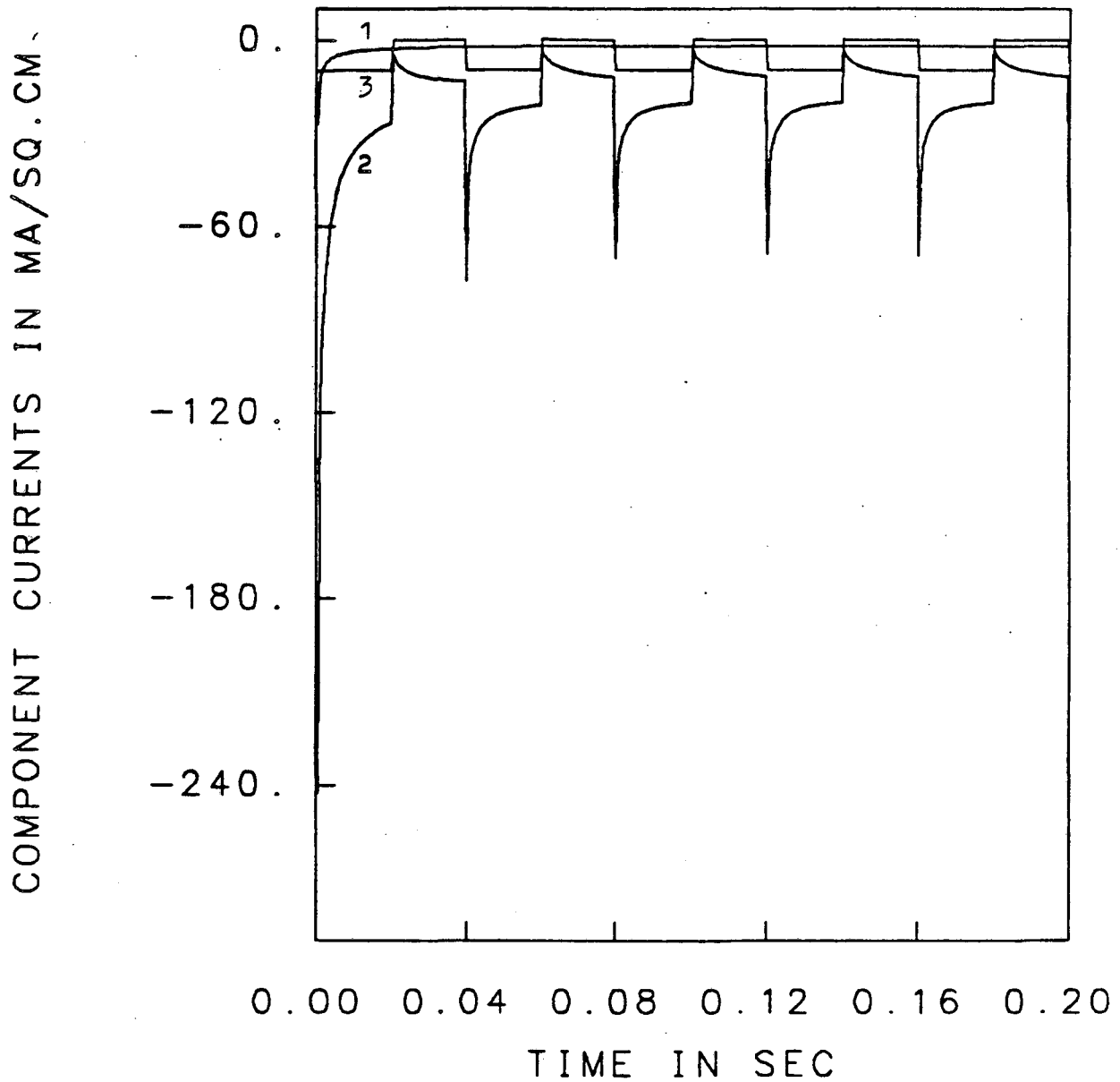

Figure 2-14. Component current densities for the electrode-potential source shown in Fig. 2-11.

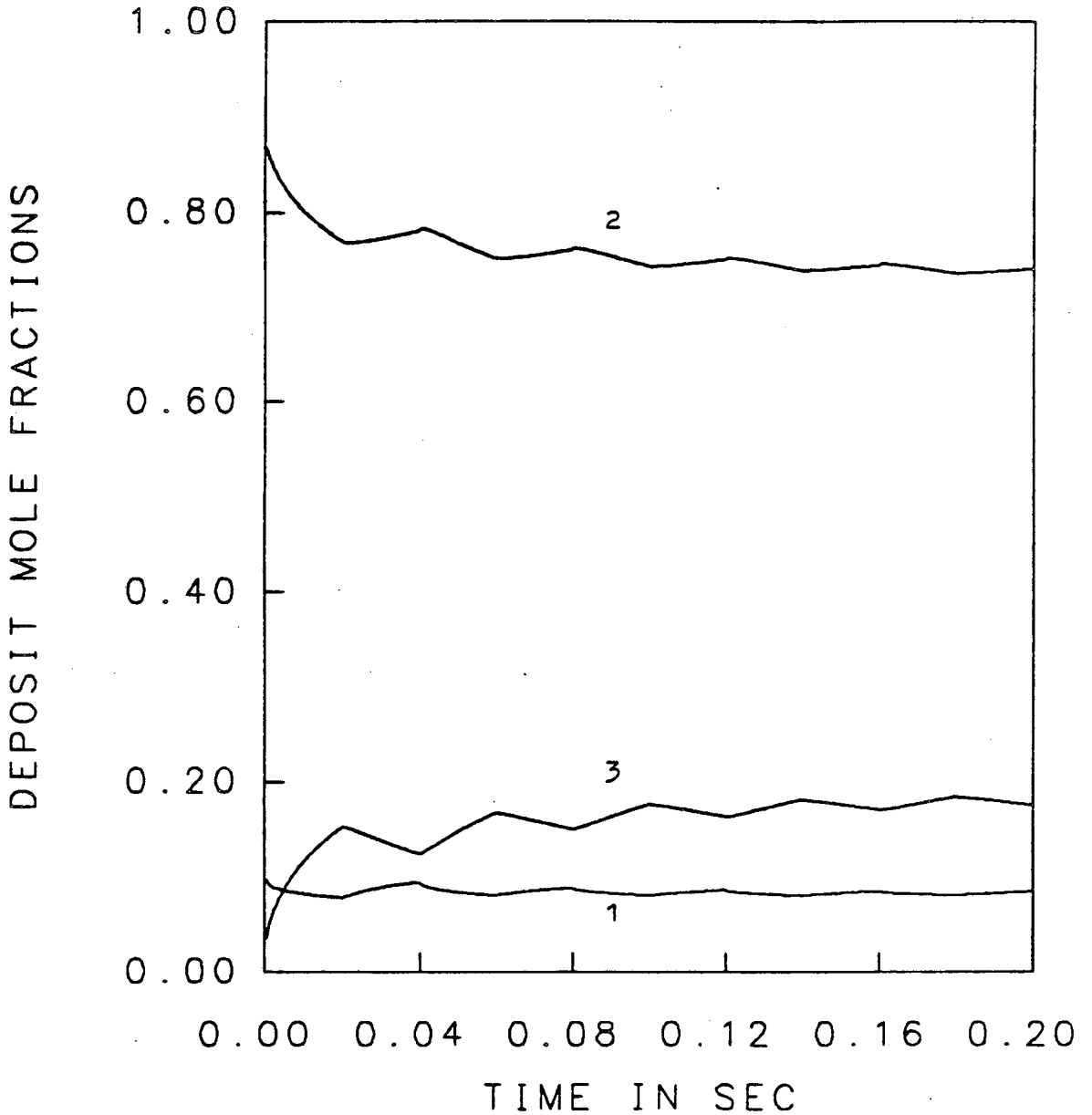

Figure 2-15. Deposit mole fraction history for the electrode-potential source shown in Fig. 2-11. Uppermost curve: component 2. Middle curve: component 3. Lowermost curve: component 1. At time zero, the electrode is pure 1.

integrated to yield the total deposit mole fractions displayed in Fig. 2-15. Since component two carries most of the cell-current density, it has the highest concentration in the deposit, followed by components three and one, respectively. From Fig. 2-15, it can be seen that the concentrations of components one and two increase during the more anodic portion of the electrode-potential cycle, while the concentration of component three decreases. During this time, components one and two contine to deposit, and component three dissolves anodically.

Conclusion

In this chapter, a mathematical model was presented for the periodic electrodeposition of alloys by an arbitrarily specified cell-current density or electrode-potential source. The method of superposition is used to solve this problem with an efficient numerical algorithm. This treatment exposes the large number of parameters the electroplater must consider for obtaining thin alloy films with the desired properties. If an accurate model is used by the electroplater, the different plating parameters can be intelligently varied to assist in manufacturing the desired electrodeposit.

Nomenclature

$a_{i,n}$	surface activity of component i at time step n
$c_{i,n}$	concentration of species i during time step n, mol/cm^3
c_i^b	bulk concentration of species i, mol/cm^3
$c_{i,n}^s$	surface concentration of species i during time step n, mol/cm^3
$c_{i,re}$	reference electrode compartment concentration of species i, mol/cm^3
d_{ml}	monolayer thickness of electrodeposit, cm
D_i	diffusion coefficient of species i, cm^2/s
E_n	electrode potential relative to the reference electrode during time step n, V
f	F/RT, V^{-1}
F	Faraday's constant, 96487 C/equivalent
g_{ij}	energy of interaction between components i and j, J/mol
G^E	molar excess Gibbs energy, J/mol
H_n	zeroing function, mA/cm^2
$i_{i,n}$	current density carried by species i at time step n, mA/cm^2
i_n	total current density at time step n, mA/cm^2
$k_{a,i}$	anodic rate constant of component i, mol/cm^2–s
$k_{c,i}$	cathodic rate constant of species i, kg/cm^2–s
m	number of deposit components
M_i	symbol for chemical formula of species i
n	time step
n_i	number of electrons in the deposition reaction of species i

n_{re}	number of electrons in reference-electrode reaction
N_i	moles of component i
N_T	total moles
r	cell ohmic resistance, Ω–cm^2
R	universal gas constant, 8.314 J/mol–K
$RSAT$	relevant surface-activity thickness, cm
$s_{i,re}$	stoichiometric coefficient of species i in reference electrode reaction
t	time, s
T	absolute temperature, K
U_i^θ	standard electrode potential for reaction involving species i, V
U_{re}^θ	standard electrode potential of the reference electrode reaction, V
v_y	normal velocity component to a rotating disk electrode, cm/s
x_i	mole fraction of component i
y	normal distance from the electrode surface, cm
α_{ij}	species interaction constant characteristic of the nonrandomness of the mixture
β_i	symmetry factor for component i
γ_i	activity coefficient of component i
$\Gamma(4/3)$	0.89298, the gamma function of 4/3
$\Theta_{i,n}$	concentration function, mol/A-cm
$\Theta_{i,n}^s$	surface-concentration function, mol/A-cm
δ_i	Nernst diffusion layer thickness of species i, cm

σ	exponential proportionality constant for the *RSAT* mole fraction
ν	kinematic viscosity, cm^2/s
ρ_o	solvent mass density, kg/cm^3
ρ_i	species i molar density, mol/cm^3
ω	disk rotation speed, radian/s
$\Psi_{i,n}$	concentration function, mol/cm^3
$\Psi^s_{i,n}$	surface concentration function, mol/cm^3

References

1. A. Brenner, *Electrodeposition of Alloys, Principles and Practice*, Academic Press, New York, 1963.
2. K.M. Gorbunova and Yu.M. Polukarov, *Advances in Electrochemistry and Electrochemical Engineering*, Vol. 5, C.W. Tobias, Editor, Interscience, New York, 1967, p. 256.
3. R.D. Srivastava and R.C. Mukerjee, *J. Appl. Electrochem.*, 6(1976)321.
4. C.C. Wan, H.Y. Cheh, and H.B. Linford, *Plating*, 61 (1974) 559.
5. A.J. Avila and M.J. Brown, *Plating*, 57 (1970) 1105.
6. H.Y. Cheh, *J. Electrochem. Soc.*, 118 (1971) 551.
7. V.A. Lamb, *Plating*, 56 (1969) 909.
8. J. Cl. Puippe and N. Ibl, *Plating*, 67 (1980) 68.
9. M.I. Ismail, *J. Appl. Electrochem.*,9(1979)407.
10. A.R. Despic and K.I. Popov, *J. Appl. Electrochem.*, 1 (1971) 275.
11. K.I. Popov, *Modern Aspects of Electrochemistry*, No. 7, B.E. Conway and J. O'M. Bockris, Editors, Plenum Press, New York, 1972, p. 304.
12. W. Sullivan, *Plating*, 62 (1975) 139.
13. M.H. Gelchinski, L. Gal-Or, and J. Yahalom, *J. Electrochem. Soc.*, 129 (1982) 2433.
14. C.A. Burrus, *J. Electrochem. Soc.*, 118 (1971) 833.
15. H. Leidheiser, Jr. and A.R.P. Ghuman, *ibid*, 120 (1973) 484.
16. U. Cohen, F.B. Koch, R. Sard, *ibid*, 130 (1983) 1987.
17. A. Kindler, *Ph.D. Thesis*, University of California, Berkeley (1981).
18. N. Ibl and K. Schadegg, *J. Electrochem. Soc.*, 114 (1967) 54.

19. D-T. Chin, *ibid*, 130 (1983) 1657.

20. K. Nisancioglu, *Ph.D. Thesis*, University of California, Berkeley (1973).

21. R. Haynes, *ibid*, 126 (1979) 881.

22. P. Radhakrishnamurty, *ibid*, 127 (1980) 1320.

23. R. Haynes, *ibid*, 127 (1980) 1321.

24. H.Y. Cheh, *ibid*, 127 (1980) 1321.

25. T. Cheng and H.Y. Cheh, 161'st Electrochemical Society Meeting, Abstract No. 414, Montreal, Canada, 1982.

26. T. Cheng and H.Y. Cheh, 164th Electrochemical Society Meeting, Abstract No. 249, Washington, DC, 1683.

27. W.G. Cochran, *Proceeding of the Cambridge Philosophical Society*, 30 (1934) 365.

28. J.S. Newman, *Electrochemical Systems*, Prentice-Hall, Inc., Englewood Cliffs, NJ, 1973.

29. J.S. Newman, *J. Electrochem. Soc.*, 113 (1966) 1235.

30. J.S. Newman, *ibid.*, 117 (1970) 198.

31. P. Appel, Ph.D. Thesis, University of California, Berkeley (1976).

32. L. Nanis and I. Klein, *J. Electrochem. Soc.*, 119(1972)1683.

33. V.S. Krylov and V.N. Babak, *Sov. Electrochem.*, 7 (1971) 626.

34. D.A. Scherson, P.F. Marconi, J.S. Newman, *J. Electrochem. Soc.*, 127 (1980) 2603.

35. K. Nisancioglu and J.S. Newman, *J. Electroanal. Chem.*, 50 (1974) 23.

36. V.G. Levich, *Physiochemical Hydrodynamics*, Prentice-Hall, Englewood Cliffs, NJ, 1961, p. 69.

37. T.R. Rosebrugh and W. Lash Miller, *J. Phys. Chem.*, 14 (1910) 816.

38. H.Y. Cheh, *J. Electrochem. Soc.*, 118 (1971) 1132.

39. K. Visawanathan and H.Y. Cheh, *ibid*, 125 (1978) 1616.

40. K. Visawanathan and H.Y. Cheh, *J. Appl. Electrochem.*, 9 (1979) 537.

41. J.M. Hale, *J. Electroanal. Chem.*, 6 (1963) 187.

42. Yu.G. Siver, *Russ. J. Phys. Chem.*, 34 (1960) 274.

43. K. Visawanathan, M.A. Farrell, and H.Y. Cheh, *J. Electrochem. Soc.*, 125 (1978) 1772.

44. P.C. Andricacos and H.Y. Cheh, *J. Electroanal. Chem.*, 121 (1981) 133.

45. W.M. Kays and M.E. Crawford, *Convective Heat and Mass Transfer*, McGraw Hill Book Company, 1980, p. 117–129.

46. F.B. Hildebrand, *Advanced Calculus for Applications*, Prentice-Hall, Inc., Englewood Cliffs, New Jersey, 1976, 463–467.

47. M. Fleischmann and H.R. Thirsk, *Advances in Electrochemistry and Electrochemical Engineering*, Vol. 3, P. Delahay, Editor, Interscience, New York, 1963, p. 124.

48. K.J. Vetter, *Electrochemical Kinetics*, S. Bruckenstein and B. Howard, Translation Editors, Academic Press, New York, 1967, p. 140.

49. L. Lapidus, *Digital Computation for Chemical Engineers*, McGraw-Hill Book Company, 1962, p. 288.

50. R.C. Alkire and J.E. Tsai, *J. Electrochem. Soc., 129 (1982) 1157.*

51. E.A. Guggenheim, *Thermodynamics*, North-Holland Publishing Company, Amsterdam, 1959, p. 215.

52. R.A. Swalin, *Thermodynamics of Solids*, John Wiley and Sons, 1972, p. 141–153.

53. J.M. Prausnitz, *Molecular Thermodynamics of Fluid-Phase Equilibria*, Prentic-Hall, Inc., Englewood Cliffs, NJ, p. 279–292.

54. E.A. Guggenheim, *Mixtures*, Oxford Press, London, 1952, p. 215–242.

55. L.S. Darken and R.W. Gurry, *Physical Chemistry of Metals*, R.F. Mehl, consulting editor, McGraw-Hill Book Company, Inc., 1953.

56. J. Lumsden, *Thermodynamics of Alloys*, Institute of Metals, London, 1952.

57. H. Renon and J.M. Prausnitz, *A.I.Ch.E.J.*, 14 (1968) 135.

58. J.M. Prausnitz, *op. cit.*, p. 309–314.

59. R.L. Scott, *J. Chem. Phys.* 25 (1956) 193.

60. H. Renon, Ph.D. Thesis, University of California, Berkeley (1966).

61. G. Wranglen, *Electrochem. Acta*, 2 (1960) 130.

62. D.M. Kolb, M. Prazasnyski, H. Gerischer, *J. Electroanal. Chem.*, 54 (1974) 25.

63. G. Azdic, J. McBreen, and M.G. Chu, *J. Electrochem. Soc.*, 128 (1981) 1691.

64. J. McBreen, M.G. Chu, G. Azdic, *ibid*, 128 (1981) 2281.

65. S.H. Cadle and S. Bruckenstein, *Anal. Chem.*, 44 (1974) 1993.

66. T. Takamura and K. Takamura, *Surface Electrochemistry, Advanced Methods and Concepts*, Japan Scientific Societies Press, T. Takamura and A. Kozawa, Editors, p. 222–234.

67. T. Takamura, F. Watanabe, and K. Takamura, *Electrochem. Acta*, 19 (1974) 933.

68. T.H.V. Setty and H. Wilman, *Trans. Faraday Soc.*, 51 (1955) 984.

69. J.O'M. Bockris and A. Damjanovic, *Modern Aspects of Electrochemistry*, No. 3, J.O'M. Bockris and B.E. Conway, Editors, Butterworth and Co. LTD, London, p. 329.

70. K.H.Z. Brainina, D.P. Synkova, and I.G. Yudelevich, *J. Electroanal. Chem.*, 35 (1972) 165.

71. K.H.Z. Brainina, N.K. Kiva, and V.B. Beliavskaia, *Electrokhimiya*, 1 (1965) 311.

Appendix 2

The use of Rosebrugh and Lash Miller's Solution

Rosebrugh and Lash Miller's solution could be used to derive alternate expressions for Eqs. [2-12] and [2-13]. The current-step solution is first required. Fick's second law,

$$\frac{\partial c_i}{\partial t} = D_i \frac{\partial^2 c_i}{\partial y^2} \quad , \qquad [2A\text{-}1]$$

with the initial condition and the boundary conditions given by Eqs. [2-3], [2-5], and [2-10] outline the current-step problem. The solution is (25)

$$c_i = c_i^b + \frac{i_i \delta_i}{n_i F D_i}\left[1 - \frac{y}{\delta_i} - \frac{8}{\pi^2}\sum_{j=1}^{\infty}\frac{\cos(m g_i y)}{m^2} e^{-m^2 \alpha_i t}\right] \qquad [2A\text{-}2]$$

where $m = 2j - 1$, $g_i = \frac{\pi}{2\delta_i}$, and $\alpha_i = \frac{\pi^2 D_i}{4\delta_i^2}$.

The similarity between Eqs. [2-7] and [2A-2] is evident. Retention of the velocity term in Eq. [2-1], the convective diffusion equation, tends to change slightly the eigenfunctions and the eigenvalues. The form and the behavior of the two current step solutions are very similar.

For short times, Eq. [2A-2] can be reduced to the Sand equation. Thus, Eq. [2-8] bears a close resemblance to the asymptotic expression of Eq. [2A-2] evaluated for short times and at the electrode surface.

When the method of superposition is used to obtain an expression for a varying current source, the concentration can be expressed by Eq. [2-11] and

$$\Theta_{i,n} = \frac{\delta_i}{n_i F D_i}\left[1 - \frac{y}{\delta_i} - \frac{8}{\pi^2}\sum_{j=1}^{\infty}\frac{\cos(m g_i y) e^{-m^2 \alpha_i (t - t_{n-1})}}{m^2}\right] \qquad [2A\text{-}3]$$

and

$$\Psi_{i,n} = c_i^b + \qquad [2A\text{-}4]$$

$$\frac{\delta_i}{n_i F D_i}\left\{\frac{8}{\pi^2}\sum_{j=1}^{n-1} i_{i,j}\sum_{k=1}^{\infty}\frac{\cos(m g_i y)}{m_2}\left[e^{-m^2\alpha_i(t-t_k)} - e^{-m^2\alpha_i(t-t_{k-1})}\right]\right\}.$$

The similarity between Eqs. [2-12], [2-13], [2A-3], and [2A-4] is evident. This is especially true at the electrode surface where Z_k is unity. Equations [2A-3] and [2A-4] and Eqs. [2-14] and [2-15] were used to model the solution-side mass transport in order to obtain the dotted curves in Fig. 2-2.

Computer Program for Periodic Alloy Electrodeposition: Current Controlled Mode of Operation†

```
      program NEWGC (input,output)
c
c     This program models multicomponent electrodeposition
c     by an arbitrarily specified current source.  The con-
c     vective-diffusion equation for one dimension is used
c     to model mass transport to a rotating disk electrode.
c     Butler-Volmer kinetics are used and individual
c     component activities are treated in the electrodeposit.
c
c     Inputs
c     SI units are used.
c       NONRANDOMNESS  FACTOR {alpha(i,j)=alpha(j,i)}..... alpha(i,j)
c       SYMMETRY FACTOR ..................................... b(i)
c       LIQUID BULK CONCENTRATION ........................... c(i)
c       DIFFUSION COEFFICIENT ............................... d(i)
c       SOLID STATE MOLAR DENSITY ........................... den(i)
c       LIQUID SOLVENT MASS DENSITY ......................... densol
c       EQUIVALENTS/MOLE .................................... eq(i)
c       NERNST POTENTIAL OF THE REFERENCE ELECTRODE ....... eref
c       ENERGIES OF INTERACTION {g(i,j)=g(j,i)} ........... g(i,j)
c       FOR LINEAR SWEEP CHRONOPOTENTIOMETRY,   ichose =1 . ichose
c       FOR PULSED CURRENT CHRONOPOTENTIOMETRY, ichose =2 .
c       NUMBER OF COMPONENTS ................................ ncom
c       TOTAL NUMBER OF CYCLES .............................. ncyc
c       MAXIMUM CATHODIC CURRENT ............................ pmax
c       MINIMUM (POSSIBLY ANODIC) CURRENT ................... pmin
c       RSAT PROPORTIONALITY CONSTANT ....................... prop
c       CELL OHMIC RESISTANCE ............................... r
c       ANODIC RATE CONSTANT ................................ rka(i)
c       CATHODIC RATE CONSTANT .............................. rkc(i)
c       RELEVANT SURFACE ACTIVITY THICKNESS (RSAT) ........ rsat
c       DIFFUSION LAYER THICKNESS ........................... s(i)
c       TIME FOR FIRST PORTION OF CYCLE...................... t2
c       TIME FOR SECOND PORTION OF CYCLE .................... t3
c       INITIAL DEPOSIT MOLE FRACTION ....................... xinit(i)
c
      common a(3),ac(3),alpha(3,3),b(3)
      common c(3),capg(3,3),cf(3),cg(3),csf(3)
      common d(3),den(3),densol,depth,dimcsf(3),e,eq(3),eref
      common fa,fitot(3),fr,g(3,3),ichose,n,ncom,op(3)
      common p,pi2,pi(3,1000),pmax,prop,ptest,r,rka(3),rkc(3),rsat
      common s(3),t,tau(3,3),tcyc,thmon,ts
```

†The subroutine used for the potential controlled mode of operation is placed at the end of Appendix 2.

```
      common v,x(3),xinit(3),xitot(3)
c
      read 5, ichose
      read 5, ncom
      read 5, ncyc
    5   format(15x,i10)
c
      read 10, densol
      read 10, eref
      read 10, pmax
      read 10, pmin
      read 10, prop
      read 10, r
      read 10, rsat
      read 10, t2
      read 10, t3
      read 10, thmon
   10   format(15x,e10.3)
c
      read 15, ((alpha(i,j),j=1,ncom),i=1,ncom)
      read 15, (b(i),i=1,ncom)
      read 15, (c(i),i=1,ncom)
      read 15, (d(i),i=1,ncom)
      read 15, (den(i),i=1,ncom)
      read 15, (eq(i),i=1,ncom)
      read 15, ((g(i,j),j=1,ncom),i=1,ncom)
      read 15, (rka(i),i=1,ncom)
      read 15, (rkc(i),i=1,ncom)
      read 15, (s(i),i=1,ncom)
      read 15, (xinit(i),i=1,ncom)
   15   format(15x,e10.3,2x,e10.3,2x,e10.3)
c
      fr=38.9442
      fa=96487.0
      pi2=3.141592654**2
c
c     The deposit mole fractions are set and the diffusion
c     parameters are calculated.
      do 20, i=1,ncom
        x(i)=xinit(i)
        a(i)=d(i)/(s(i)/.89298)**2
   20   continue
c
c     The time step is set.
      ts=amin1(0.02*t2,0.02*t3)
c
ccccccccccccccccccccccccccccccccccccccccccccccccccccccccccccccccccccccc
c     To print out a result similar to Cheh's fig.2, (1971, JES)
c       pmax=-eq(1)*fa*d(1)*c(1)/s(1)
c       pmin=0.0
c       ts=0.1*t3
```

```
c       To print out a result similar to Roseburgh and Lash
c       Miller's,
c         TABLE II
c           a(1)=1.0
c           ncom=1
c           ncyc=5
c           pmax=-0.05*eq(1)*fa*d(1)*c(1)/s(1)
c           pmin=pmax
c           s(1)=sqrt(pi2*d(1)/4.0)
c           t2=0.5
c           t3=0.5
c           ts=0.1
c           xinit(1)=1.0
c         TABLE III
c           pmin=0.0
c           ts=0.01
c   *** Also dimcsf is changed in subroutine genkin. ***
c
ccccccccccccccccccccccccccccccccccccccccccccccccccccccccccccccccccccccc
c
c       The total cycle time t1 is
        t1=t2+t3
c
        n=0
        t=0.0
c
c       Obtain the initial surface activities.
        call act
c
        print 80
   80     format(4x,#n#,6x,#tot cur#,4x,#cur 1#,5x,#cur 2#,5x,#cur 3#,
     1           5x,#csurf1#,4x,#csurf2#,4x,#csurf3#,3x,#rsat x1#,3x,
     2           #rsat x2#,3x,#rsat x3#,5x,#depth#/)
        print 90
   90     format(3x,#time#,4x,#voltage#,3x,#overpot1#,2x,#overpot2#,
     1           2x,#overpot3#,2x,#dimcsf1#,3x,#dimcsf2#,3x,#dimcsf3#,
     2           3x,#total x1#,2x,#total x2#,2x,#total x3#/)
c
        ntot=ncyc*int(t1/ts)
        do 1000 n=1,ntot
          t=float(n)*ts
c
c         The applied current is now obtained.
          tcyc=amod(t,t1)
c         For linear sweep chronopotentiometry (LSC),   ichose=1
c         For pulsed current chronopotentiometry (PCC), ichose=2
          if(ichose.eq.2)go to 150
c
c         LSC
            if(tcyc.le.t2)go to 120
            p=(pmin-pmax)/t3 *(t1-tcyc) + pmax
```

```
              go to 160
  120         p=(pmin-pmax)/t2 *tcyc + pmax
              go to 160
c
c           PCC
  150         continue
              if(tcyc.le.t2)go to 155
              p=pmin
              go to 160
  155         p=pmax
c
  160       continue
c
c           The current independent functions cf(i) and cg(i)
c           are now obtained for both components.
              call conc
c
c           The electrode potential is now found.
              call genkin
c
c           The relevant surface activities, mole fractions, and
c           the deposit thickness are now found.
              call act
c
c             The results are now printed.
          print 200, n,p,(pi(i,n),i=1,ncom),(csf(i),i=1,ncom),
     1               (x(i),i=1,ncom),depth
  200       format(1x,i8,1x,4(f9.1,1x),3(f9.4,1x),3(f9.7,1x),e10.4)
          print 201, t,v,(op(i),i=1,ncom),(dimcsf(i),i=1,ncom),
     1               (xitot(i),i=1,ncom)
  201       format(1x,f8.5,1x,7(f9.6,1x),3(f9.7,1x)/)
c
 1000     continue
c
          stop
          end
c
ccccccccccccccccccccccccccccccccccccccccccccccccccccccccccccccccccccccccccccc
c
          subroutine conc
c
c         This program calculates the concentration functions
c         cf(i) and cg(i).  The surface concentration can then
c         be obtained by c(surface)=cg(i) + pi(i,n)*cf(i).
c         Nisancioglu and Newman's current-step solution
c         and the Sand equation, are used along with
c         the method of superposition to solve for the
c         transient, convective mass transfer.
c         [Nisancioglu and Newman, J. Electroanal. Chem., 50(1974)23-39]
c
          common a(3),ac(3),alpha(3,3),b(3)
```

```
      common c(3),capg(3,3),cf(3),cg(3),csf(3)
      common d(3),den(3),densol,depth,dimcsf(3),e,eq(3),eref
      common fa,fitot(3),fr,g(3,3),ichose,n,ncom,op(3)
      common p,pi2,pi(3,1000),pmax,prop,ptest,r,rka(3),rkc(3),rsat
      common s(3),t,tau(3,3),tcyc,thmon,ts
      common v,x(3),xinit(3),xitot(3)
c
      dimension con(10),eig(10)
c
      pie=3.141592654
c
      con(1)=.663516066
      con(2)=.081564022
      con(3)=.034457046
      con(4)=.01962199
      con(5)=.0123965
      con(6)=.0092267
      con(7)=.0069829
      con(8)=.0055048
      con(9)=.0044645
      con(10)=.0037089
c
      eig(1)=2.58078493
      eig(2)=12.3099728
      eig(3)=24.4331401
      eig(4)=38.3054830
      eig(5)=53.5740271
      eig(6)=70.0220380
      eig(7)=87.5010784
      eig(8)=105.902059
      eig(9)=125.140833
      eig(10)=145.15016
c
      do 500 i=1,ncom
c       The function cf(i) is now obtained.
        w=a(i)*ts
        if(w.ge.0.01)go to 15
        cf(i)=2.0/(eq(i)*fa) *sqrt(ts/(pie*d(i)))
        go to 20
c
   15   cf(i)=0.0
        do 16 j=1,10
          cf(i)=cf(i) + con(j)*exp(-eig(j)*w)
   16     continue
c
        cf(i)=s(i)/(eq(i)*fa*d(i)) *(1.0 - cf(i)/.89298)
   20   continue
c
c       The function cg(i) is obtained here.
        cg(i)=0.0
        if(n.eq.1)go to 110
```

```
c
          do 100 k=1,n-1
            w=a(i)*ts*float(n-k+1)
            if(w.ge.0.01)go to 25
            w=pi2*d(i)/(4*s(i)**2) *ts*float(n-k+1)
            cg1=1.0 - 4.0*sqrt(w)/pie**1.5
            go to 30
c
   25       cg1=0.0
            do 26 j=1,10
              cg1=cg1 + con(j)*exp(-eig(j)*w)
   26         continue
            cg1=cg1/.89298
c
   30       w=a(i)*ts*float(n-k)
            if(w.ge.0.01)go to 35
            w=pi2*d(i)/(4*s(i)**2) *ts*float(n-k)
            cg2=1.0 - 4.0*sqrt(w)/pie**1.5
            go to 40
c
   35       cg2=0.0
            do 36 j=1,10
              cg2=cg2 + con(j)*exp(-eig(j)*w)
   36         continue
            cg2=cg2/.89298
c
   40       cgk=pi(i,k)*(cg1 - cg2)
            cg(i)=cgk + cg(i)
  100       continue
c
  110     cg(i)=c(i) - s(i)*cg(i)/(eq(i)*fa*d(i))
  500     continue
c
        return
        end
c
ccccccccccccccccccccccccccccccccccccccccccccccccccccccccccccccccccccccccccc
c
        subroutine genkin
c
c       This subroutine uses Butler-Volmer kinetics to calculate the
c       electrode potential.  The value of e calculated by this sub-
c       routine is not the electrode potential v.  v=e-eref+p*r
c       where r is the cell resistance.
c
        common a(3),ac(3),alpha(3,3),b(3)
        common c(3),capg(3,3),cf(3),cg(3),csf(3)
        common d(3),den(3),densol,depth,dimcsf(3),e,eq(3),eref
        common fa,fitot(3),fr,g(3,3),ichose,n,ncom,op(3)
        common p,pi2,pi(3,1000),pmax,prop,ptest,r,rka(3),rkc(3),rsat
        common s(3),t,tau(3,3),tcyc,thmon,ts
```

```
      common v,x(3),xinit(3),xitot(3)
c
      dimension q(3,3),z(7,3)
c
      do 20, i=1,ncom
        q(1,i)=(1.0-b(i))*eq(i)*fr
        q(2,i)=-b(i)*eq(i)*fr
        q(3,i)=(1.0 - 2.0*b(i))*eq(i)*fr
c
        z(1,i)=rka(i)*ac(i)
        z(2,i)=rkc(i)*cg(i)/densol
        z(3,i)=1.0/(eq(i)*fa)
        z(4,i)=rkc(i)*cf(i)/densol
        z(5,i)=z(1,i)*(1.0 - b(i))*fr/fa
        z(6,i)=z(2,i)*b(i)*fr/fa
        z(7,i)=z(1,i)*z(4,i)*eq(i)*fr
   20   continue
c
c     If n=1 or the current has just been pulsed to pmax,
c     the bisection method is used to find a bound
c     on e.  Then, the Newton-Raphson is used to obtain e.
      if(n.eq.1)go to 25
      if(ichose.eq.1)go to 45
      if(abs(p).le.abs(ptest))go to 45
   25 el=0.2
      e2=-0.6
      do 41, k=1,50
        em=(el+e2)/2.0
        hbil=-p
        hbim=-p
        do 30, i=1,ncom
          hbil=hbil + (z(1,i)*exp(q(1,i)*el) - z(2,i)*
     1          exp(q(2,i)*el))/(z(3,i) + z(4,i)*exp(q(2,i)*el))
          hbim=hbim + (z(1,i)*exp(q(1,i)*em) - z(2,i)*
     1          exp(q(2,i)*em))/(z(3,i) + z(4,i)*exp(q(2,i)*em))
   30     continue
        if(hbil*hbim.gt.0.0)go to 35
        e2=em
        go to 40
   35   el=em
   40   enew=(el+e2)/2.0
        change=abs((abs(enew) - abs(em))/enew)
        if(change.le.0.1)go to 44
   41   continue
c     If the next statement is executed, convergence was not achieved.
      print 42,em
   42   format(2x,#No convergence. em=#,e10.4)
      stop
c
c     The Newton-Raphson is now started.
   44 e=enew
```

```
   45   do 100, j=1,20
          h=-p
          dh=0.0
          do 50 i=1,ncom
            h=h + (z(1,i)*exp(q(1,i)*e) - z(2,i)*exp(q(2,i)*
     1        e))/(z(3,i) + z(4,i)*exp(q(2,i)*e))
            dh=dh + (z(5,i)*exp(q(1,i)*e) + z(6,i)*exp(q(2,i)*
     1        e) + z(7,i)*exp(q(3,i)*e))/(z(3,i) + z(4,i)*
     2        exp(q(2,i)*e))**2
c
   50       continue
c
          enew=e - h/dh
          change=abs((abs(enew) - abs(e))/enew)
          e=enew
          if(change.le.0.001)go to 110
  100     continue
c
c       If a transfer to 110 was not made, convergence was not
c       achieved.
        print 105, e
  105     format(1x,#No convergence#,2x,f10.5)
        stop
c
c       The individual currents are now obtained.
  110   do 120 i=1,ncom
          pi(i,n)=(z(1,i)*exp(q(1,i)*e) - z(2,i)*exp(q(2,i)*e))/
     1            (z(3,i) + z(4,i)*exp(q(2,i)*e))
  120     continue
c
c       The surface concentration csf(i), the dimensionless
c       surface concentration dimcsf(i), and the surface
c       overpotential op(i) of each species is now calculated.
        do 130 i=1,ncom
          csf(i)=cg(i) + pi(i,n)*cf(i)
          if(c(i).eq.0.0)go to 130
          dimcsf(i)=csf(i)/c(i)
c         The next definition is used if Cheh's or RLM's work
c         is being used as a check.
c         dimcsf(i)=(csf(i)-c(i))*eq(i)*fa*d(i) /(pmax*s(i))
          if(ac(i).ne.0.0)go to 125
          op(i)=-9.999999
          go to 130
  125     op(i)=e - 1.0/(eq(i)*fr)* alog(rkc(i)*csf(i)/(
     1          densol*rka(i)*ac(i)))
  130     continue
c
c       The eletrode potential relative to a specified reference
c       electrode is now obtained.
        v=e - eref + p*r
c
```

```
      ptest=p
c
      return
      end
c
ccccccccccccccccccccccccccccccccccccccccccccccccccccccccccccccccccccccc
c
      subroutine act
c
c     This subroutine determines the surface activities
c     of the components in the electrodeposit.  The NRTL
c     activity model is used on each monolayer of deposit.
c     Each monolayer's influence on the surface composition
c     is exponentially weighted.  Monolayers below the RSAT
c     (relevant surface-activity thickness)  have no influence
c     on the surface composition.
c     [Renon and Prausnitz, AIChE J, 14(1968)135]
c
      common a(3),ac(3),alpha(3,3),b(3)
      common c(3),capg(3,3),cf(3),cg(3),csf(3)
      common d(3),den(3),densol,depth,dimcsf(3),e,eq(3),eref
      common fa,fitot(3),fr,g(3,3),ichose,n,ncom,op(3)
      common p,pi2,pi(3,1000),pmax,prop,ptest,r,rka(3),rkc(3),rsat
      common s(3),t,tau(3,3),tcyc,thmon,ts
      common v,x(3),xinit(3),xitot(3)
c
      dimension flux(3)
c
      rgas=8.314
      temp=298
c
c     Calculate the initial surface activities if t=0.0
      if(n.ge.1)go to 10
c     Initially there has been no current passed.
      depth=0.0
      do 5, i=1,ncom
        fitot(i)=0.0
    5   continue
      go to 180
c
   10 do 15, i=1,ncom
        flux(i)=0.0
        x(i)=0.0
   15   continue
c     Start at the first monolayer.
      m=1
      thick=0.0
      wetot=0.0
      wefun=1.0 - exp(-prop*(rsat-thmon)/rsat)
c
c     Start the weighting of the individual monolayers.
```

```
      do 100, j=1,n
        k=n+1-j
        ftot=0.0
c
c       The deposit thickness is now calculated.  Cathodic
c       currents are negative.
        do 30, i=1,ncom
          flux(i)=pi(i,k)/(eq(i)*fa) + flux(i)
          ftot=ftot + flux(i)
          thick=thick - pi(i,k)*ts/(eq(i)*fa*den(i))
 30       continue
c
c       The activity coefficients are calculated if thick > rsat.
c       The denominator of the weighting function, wetot, cannot be
c       calculated until the very last monolayer has been treated.
        if(thick.lt.rsat)go to 50
        do 40, i=1,ncom
          x(i)=x(i)/wetot
 40       continue
        go to 120
c
 50     continue
c
        if(j.lt.n)go to 70
c       If j=n, the original electrode will influence the surface
c       composition.
c       subfun is the integrated weighting function for the
c       original substate.
        subfun=1.0 - rsat/(prop*(rsat-thick)) *(1.0 - exp(-prop*
     1          (rsat-thick)/rsat))
        wetot=wetot + wefun + subfun
        do 60, i=1,ncom
c         if flux(i)>0, the original electrode dissolved.
          if(flux(i).le.0.0)go to 55
          x(i)=xinit(i)
          go to 60
 55       x(i)=(x(i) + flux(i)/ftot *wefun + xinit(i)*subfun)/wetot
 60       continue
        go to 100
c
 70     continue
        if(thick.le.float(m)*thmon)go to 100
c       A complete and new monolayer has been deposited.
          do 75, i=1,ncom
c           if flux(i)>0, more than a monolayer of i has dissolved.
            if(flux(i).le.0.0)go to 74
            print 72, i,flux(i)
 72           format(1x,#Greater than a monolayer has dissolved, i=#,
     1              i2,#flux(i)=#,e10.4)
            stop
 74         x(i)=wefun*flux(i)/ftot + x(i)
```

```
            flux(i)=0.0
 75         continue
          m=m+1
          wetot=wetot+wefun
          wefun=1.0 - exp(-prop*(rsat-float(m)*thmon)/rsat)
c
 100    continue
c
c      The relevant surface composition has now been obtained.  The
c      total deposit mole fractions and the deposit depth is now
c      obtained.
 120   ftotal=0.0
       do 170, i=1,ncom
         fitot(i)=fitot(i) - pi(i,n)/eq(i)
c        Because of the finite time steps, sometimes a very small
c        negative value of fitot(i) can result.  This is physically
c        unrealistic.
         if(fitot(i).lt.0.0)fitot(i)=0.0
         ftotal=ftotal + fitot(i)
         depth=depth - pi(i,n)*ts/(eq(i)*fa*den(i))
 170     continue
       do 175, i=1,ncom
         xitot(i)=fitot(i)/ftotal
 175     continue
c
c      The relevant surface activity is now calculated.
c      The following constants need only be evaluated once.
 180   continue
       if(n.ge.1)go to 220
       do 210, j=1,ncom
         do 200, i=1,ncom
           tau(j,i)=(g(j,i)-g(i,i))/(rgas*temp)
           capg(j,i)=exp(-alpha(j,i)*tau(j,i))
 200       continue
 210     continue
c
 220   do 400, i=1,ncom
         if(x(i).gt.0.0)go to 222
         ac(i)=0.0
         go to 400
c
 222     serk1=0.0
         do 225, k=1,ncom
           serk1=serk1 + capg(k,i)*x(k)
 225       continue
c
         serj1=0.0
         serj2=0.0
         do 300, j=1,ncom
           serj1=serj1 + tau(j,i)*capg(j,i)*x(j)
c
```

```
            serk2=0.0
            do 230, k=1,ncom
              serk2=serk2 + capg(k,j)*x(k)
  230         continue
c
            serl1=0.0
            do 240, l=1,ncom
              serl1=serl1 + x(l)*tau(l,j)*capg(l,j)
  240         continue
c
            serj2=serj2 + x(j)*capg(i,j)*(tau(i,j) - serl1/serk2)/serk2
  300       continue
c
          ac(i)=x(i)*exp(serj1/serk1 + serj2)
  400     continue
c
        return
        end
c
ccccccccccccccccccccccccccccccccccccccccccccccccccccccccccccccccccccccccccc
```

Data File for Current Controlled Mode of Operation

ichose		2			
ncom		3			
ncyc		5			
densol		1.000e+03			
eref		0.000e+00			
pmax		-2.112e+03			
pmin		0.000e+00			
prop		1.000e+00			
r		0.000e+00			
rsat		9.000e-10			
t2		2.000e-02			
t3		2.000e-02			
thmon		3.000e-10			
alpha	1-1,2,3	1.000e-01	1.000e-01	1.000e-01	note alpha(i,j)=
	2-1,2,3	1.000e-01	1.000e-01	1.000e-01	alpha(j,i)
	3-1,2,3	1.000e-01	1.000e-01	1.000e-01	
b(i)		5.000e-01	5.000e-01	5.000e-01	
c(i)		1.000e+00	1.000e+01	1.000e+02	
d(i)		1.000e-09	1.000e-09	1.000e-09	
den(i)		7.296e+04	7.296e+04	7.296e+04	
eq(i)		2.000e+00	2.000e+00	2.000e+00	
g	1-1,2,3	2.000e+03	2.000e+03	2.000e+03	note g(i,j)=g(j,i)
	2-1,2,3	2.000e+03	2.000e+03	2.000e+03	
	3-1,2,3	2.000e+03	2.000e+03	2.000e+03	
rka(i)		8.741e-10	2.109e-06	5.091e-03	
rkc(i)		1.229e+01	5.092e-03	2.110e-06	
s(i)		1.014e-05	1.014e-05	1.014e-05	
xinit		1.000e+00	0.000e+00	0.000e+00	

Kinetic Subroutine for Potential Controlled Mode of Operation†

```
ccccccccccccccccccccccccccccccccccccccccccccccccccccccccccccccccccccccccc
c
      subroutine genkin
c
c     This subroutine uses Butler-Volmer kinetics to calculate the
c     electrode potential.  The value of e calculated by this sub-
c     routine is not the electrode potential v.  v=e-eref+p*r
c     where r is the cell resistance.
c
      common a(3),ac(3),alpha(3,3),b(3)
      common c(3),capg(3,3),cf(3),cg(3),csf(3)
      common d(3),den(3),densol,depth,dimcsf(3),e,eq(3),eref
      common fa,fitot(3),fr,g(3,3),ichose,n,ncom,op(3)
      common p,pi2,pi(3,1000),prop,ptest,r,rka(3),rkc(3),rsat
      common s(3),t,tau(3,3),tcyc,thmon,ts
      common v,x(3),xinit(3),xitot(3)
c
      dimension q(3,3),z(7,3)
c
      do 20, i=1,ncom
        q(1,i)=(1.0-b(i))*eq(i)*fr
        q(2,i)=-b(i)*eq(i)*fr
        q(3,i)=(1.0 - 2.0*b(i))*eq(i)*fr
c
        z(1,i)=rka(i)*ac(i)*exp(q(1,i)*(v+eref))
        z(2,i)=rkc(i)*cg(i)/densol*exp(q(2,i)*(v+eref))
        z(3,i)=1.0/(eq(i)*fa)
        z(4,i)=rkc(i)*cf(i)/densol*exp(q(2,i)*(v+eref))
        z(5,i)=-z(1,i)*(1.0 - b(i))*fr/fa*r
        z(6,i)=-z(2,i)*b(i)*fr/fa*r
        z(7,i)=-z(1,i)*z(4,i)*eq(i)*fr*r
   20   continue
c
c     If no ohmic drop is taken into account, an explicit
c     solution for the partial currents can be obtained.
      if(r.ne.0.)go to 44
      p=0.0
      do 25 i=1,ncom
        pi(i,n)=(z(1,i) - z(2,i))/(z(3,i) + z(4,i))
        p=p + pi(i,n)
   25   continue
      go to 121
```

†The only major change in the computer program for the potential controlled mode of operation, relative to the current controlled mode, is the different electrode-kinetics subroutine. Because of this, only the kinetics subroutine, subroutine genkin, is listed.

```
c
c       The Newton-Raphson is now started.
   44   if(n.eq.1)p=-50*eq(1)*fa*d(1)*c(1)/s(1)
   45   do 100 j=1,20
          h=-p
          dh=-1.0
          do 50 i=1,ncom
            h=h + (z(1,i)*exp(-q(1,i)*r*p) - z(2,i)*exp(-q(2,i)*
     1        r*p))/(z(3,i) + z(4,i)*exp(-q(2,i)*r*p))
            dh=dh + (z(5,i)*exp(-q(1,i)*r*p) + z(6,i)*exp(-q(2,i)*
     1         r*p) + z(7,i)*exp(-q(3,i)*r*p))/(z(3,i) + z(4,i)*
     2         exp(-q(2,i)*r*p))**2
c
   50       continue
c
          pnew=p - h/dh
          change=abs((abs(pnew) - abs(p))/pnew)
          p=pnew
          if(change.le.0.001)go to 110
  100     continue
c
c       If a transfer to 110 was not made, convergence was not
c       achieved.
        print 105, p
  105     format(1x,#No convergence#,2x,f10.2)
        stop
c
c       The individual currents are now obtained for cases where the
c       ohmic resistance is considered.
  110   do 120 i=1,ncom
          pi(i,n)=(z(1,i)*exp(-q(1,i)*r*p) - z(2,i)*exp(-q(2,i)*r*p))/
     1            (z(3,i) + z(4,i)*exp(-q(2,i)*r*p))
  120     continue
c
c       The surface concentration csf(i), the dimensionless
c       surface concentration dimcsf(i), and the surface
c       overpotential op(i) of each species is now calculated.
  121   do 130 i=1,ncom
          csf(i)=cg(i) + pi(i,n)*cf(i)
          if(c(i).eq.0.0)go to 130
          dimcsf(i)=csf(i)/c(i)
c         The next definition is used if Cheh's or RLM's work
c         is being used as a check.
c         dimcsf(i)=(csf(i)-c(i))*eq(i)*fa*d(i) /(pmax*s(i))
          if(ac(i).ne.0.0)go to 125
          op(i)=-9.999999
          go to 130
  125     op(i)=v - 1.0/(eq(i)*fr)* alog(rkc(i)*csf(i)/(
     1          densol*rka(i)*ac(i))) + eref - p*r
  130     continue
c
```

```
      return
      end
c
ccccccccccccccccccccccccccccccccccccccccccccccccccccccccccccccccccccccccccccccc
```

Chapter 3.

The Periodic Electrodeposition of Cadmium-Tellurium Compounds

The unique physical properties of CdTe are reflected in the numerous devices constructed from this material. A large amount of scientific literature is devoted to the study of CdTe fabrication processes and material characterization. In this work, we investigate the periodic electrodeposition of CdTe and analyze the resulting thin films. Tribbals (1) cites perhaps the earlist study devoted to the production of CdTe, published by Oppenheim in 1857. Cadmium telluride is probably the most extensively studied wide band-gap, II-VI compound. (2) A number of monographs (*eg.* reference 3, and references cited therein) are devoted exclusively to CdTe. Cadmium telluride materials have found applications as gamma-ray and x-ray spectrometers, electrooptic and acoustooptic modulators, optical elements, liquid-crystal imaging devices, and solar cell materials.

Perhaps the most promising application of CdTe lies in the fabrication of photovoltaic devices. In 1956, Loferski (4) presented a theoretical treatment to aid in the selection of the optimum semiconductor for photovoltaic solar-energy conversion. The semiconductor yielding the highest maximum efficiency, defined as the ratio of the maximum electrical power output to the solar power flux incident to the semiconductor surface, was CdTe.

Thin films of CdTe have been prepared by chemical vapor deposition, vacuum evaporation, and electrodeposition processes. As is the case in the present study, most CdTe-electrodeposition processes make use of an aqueous, cadmium-sulfate, tellurium-dioxide, sulfuric acid electrolyte. (5-14)

Thin film electrodeposits have also been formed from nonaqueous solvents (15,16) and from aqueous potassium-cyanide electrolytes. (17) Since the costs associated with thin film electrodeposition processes are generally less than the previously mentioned thin film fabrication techniques, this study is particularly relevant to the fabrication of large area, CdTe solar cells. There are two other notable features concerning the CdTe-electrodeposition process that motivate the selection of this particular system for a study of alloy electrodeposition. First, since the cadmium and tellurium ions are at relatively low concentration in the electrolyte (0.1 molar and 0.001 molar, respectively), dilute solution transport equations can be employeed to model the liquid-phase transport. Secondly, there is a large free energy of reaction in the formation of CdTe from Cd and Te, and the thermodynamics of the solid-state strongly influences the electrodeposition process.

In the following sections, we analyze the electrodeposition of tellurium and cadmium. Following these analyses, the measured physicochemical parameters for tellurium electrodeposition and cadmium electrodeposition will be used to study the codeposition of tellurium and cadmium. The reactions relevant to the study are listed in Table 3-1. In all these deposition studies, 0.3-M-H_2SO_4 was used as supporting electrolyte. The Cd^{2+} species was obtained by adding cadmium sulfate, and the $HTeO_2^+$ species resulted from adding tellurium dioxide to the electrolyte (reaction *vi* of Table 3-1). The experimental equipment used in this work is shown in Fig. 3-1. Glassy-carbon and polycrystalline cadmium rotating disks were used. Standard metallographic polishing techniques were used to remove all projections greater than one micron in height. The electrodes were cleaned with a dilute nitric acid solution before each experiment. The potential of the working

Table 3-1. Reactions

Interfacial Reactions:

Reaction Designation	Standard Electrode Potential (V)	Electrochemical Reaction
i	0.64	$Hg_2SO_4 + 2e^- = 2Hg + SO_4^{2-}$
ii	0.55	$HTeO_2^+ + 3H^+ + 4e^- = Te + 2H_2O$
iii	0.00	$H^+ + e^- = \frac{1}{2}H_2$
iv	-0.40	$Cd^{2+} + 2e^- = Cd$
v	-0.92	$Te + 2e^- = Te^{2-}$

Homogeneous Reactions:

Reaction Designation	Homogeneous Reaction
vi	$TeO_2 + H^+ = HTeO_2^+$
vii	$Cd + Te = CdTe$

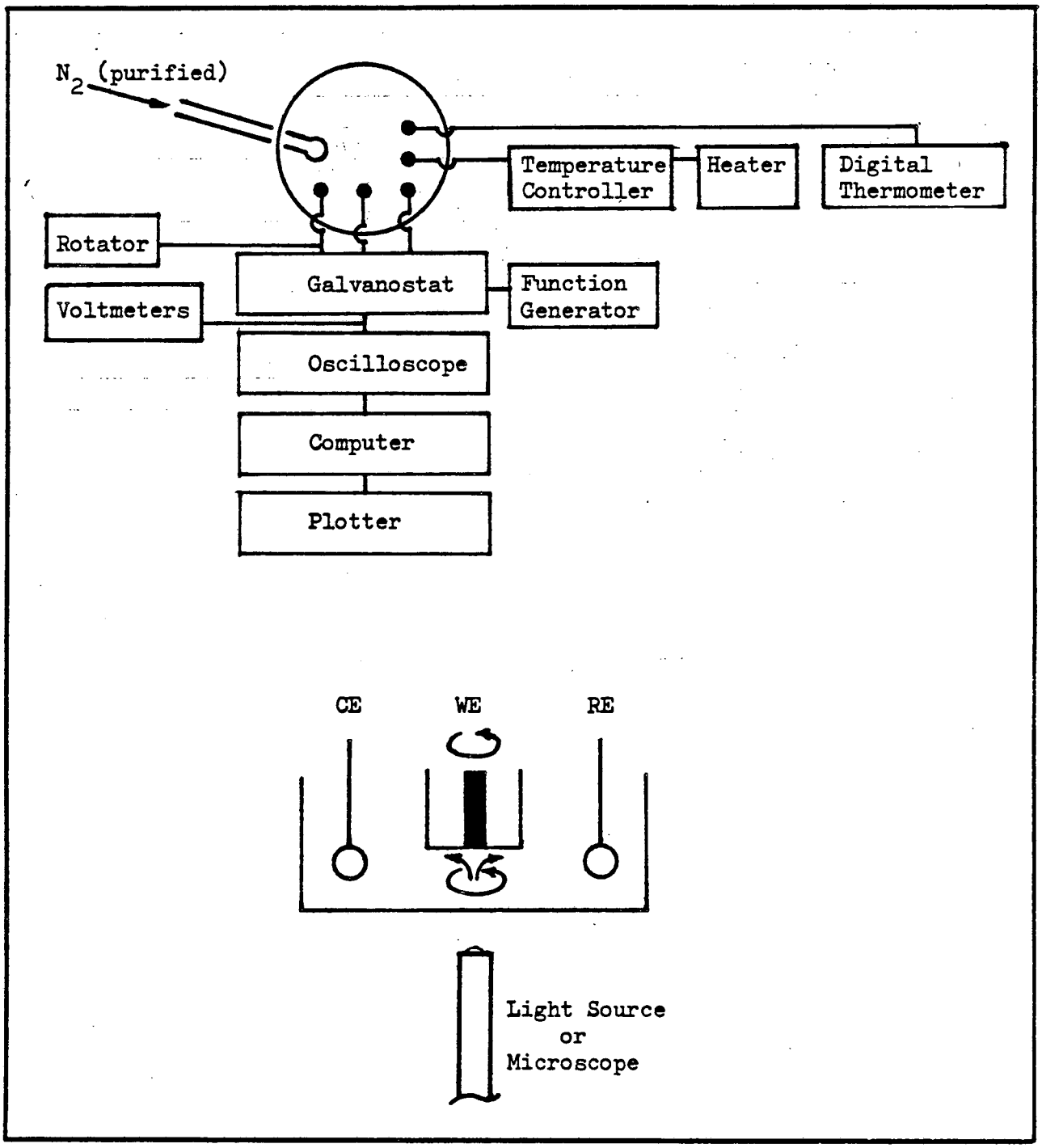

Figure 3-1. Experimental equipment. Upper figure: schematic illustration of the electrochemical cell and peripherals. Lower figure: schematic illustration of the counter electrode (CE), working electrode (WE), and the reference electrode (RE).

electrode was measured against a mercury-mercurous sulfate reference electrode. The morphology of the developing electrodeposit was investigated *in situ* by placing a microscope, equipped with a camera (Polaroid High Speed Land Film, type 47) below the glass bottomed cell. The photoresponse of the electrodeposit was investigated with a chopped light source which was placed below the electrochemical cell, the light beam incident to the working electrode surface. For the RDE experiments, a Pine Instruments ASRP2 rotator was used. The Princeton Applied Research model 173 potentiostat/galvanostat controlled the operation of the cell. An Interstate F77 function generator was used with the potentiostat/galvanostat. The data were stored on a Nicolet 1090A digital oscilloscope and later transferred to an HP9825A computer. A generalized data-acquisition program was written for the Nicolet-1090A/HP9825A-computer/HP9862A-plotter data-acquisition system. The program is listed in Appendix 3. With this system, distinct portions of the oscilloscope memory can be dedicated to the recording of two experimental variables. If the cell current and electrode potential (relative to a reference electrode) are recorded, and other experimental variables requested during the operation of the computer program are entered, the following plots can be generated: cell-current density versus time, electrode potential (relative to a SHE) versus time, integrated charge passed versus time, and cell-current density versus electrode potential (relative to a SHE).

The aqueous, sulfuric acid electrolytes were prepared from analytical reagent grade chemicals and distilled water which was passed through a Culligan water purification unit consisting of an organic trap, a deionizer, and a microfilter. The specific conductance of the treated water was 15 Mohm-cm. Nitrogen, first equilibrated with a similar electrolyte, was bubbled through

the cell solution for 1 hour prior to experiments. A nitrogen atmosphere was maintained above the electrolyte during the experiment.

The Electrodeposition of Tellurium

The primary factor limiting the rate of CdTe electrodeposition is the mass-transfer resistance of the discharging $HTeO_2^+$ ion. This is due to low solubility of TeO_2 in aqueous, sulfuric acid solutions, reaction *vi* in Table 3-1. Since there is very little $HTeO_2^+$ in solution, relative to the concentration of Cd^{2+}, the $HTeO_2^+$ species quickly becomes diffusion limited if a one-to-one ratio (1:1) of cadmium to tellurium is desired in the electrodeposit. If a direct current source is used to form the CdTe electrodeposit, approximately 1:1 CdTe can be produced if the cell-current density is $\frac{3}{2} \times i_{lim,HTeO_2^+}$ where $i_{lim,HTeO_2^+}$ is the steady-state diffusion-limited current density of the $HTeO_2^+$ species:

$$i_{lim,HTeO_2^+} = -\frac{D_{HTeO_2^+} c^b_{HTeO_2^+}}{4F\delta_{HTeO_2^+}} \qquad [3\text{-}1]$$

$\delta_{HTeO_2^+}$ is the Levich diffusion-layer thickness for the $HTeO_2^+$ species,

$$\delta_{HTeO_2^+} = 1.612\left(\frac{D_{HTeO_2^+}}{\nu}\right)^{\frac{1}{3}}\left(\frac{\nu}{\omega}\right)^{\frac{1}{2}} . \qquad [3\text{-}2]$$

The factor of $\frac{3}{2}$ preceding $i_{lim,HTeO_2^+}$ is required since four moles of electrons are reacted per mole of tellurium deposited by reaction *ii*, and two moles of electrons are reacted per mole of cadmium deposited by reaction *iv*.

The tellurium solution chemistry is very complex, and Eq. *ii* of Table 3-1 is only an approximation for the $HTeO_2^+$/Te electrode processes.

Electroanalytical studies of tellurium in the +4 state are presented in the fundamental work of Lingane and Niedrach. (18,19) The chemistry of TeO_2 in sulfuric acid solutions is addressed in the work of Flowers *et al.* (20) The solubility of TeO_2, which limits the rate of CdTe electrodeposition in aqueous, sulfuric-acid solutions, was investigated by Schuhmann (21), who postulated the solution species to be $HTeO_2^+$ and electrode reaction *ii* of Table 3-1. Issa and Awad (22) studied the solubility of TeO_2 in aqueous HCl and buffered solutions. Cheng (23) noted that the sulfate electrolytes yielded a slightly higher solubility than a number of other inorganic salts he studied. Dutton and Cooper (24) have reviewed analytical work on the oxides and oxyacids of tellurium. Later, Cooper (25) produced a treatise on the element tellurium and its unique chemistry.

In the present work, the diffusion coefficient of the $HTeO_2^+$ species, $D_{HTeO_2^+}$, was calculated from the limiting current curves depicted in Fig. 3-2. The cell temperature during the experiment was 20°C, and the calculated diffusion coefficient is $9.4 \times 10^{-6} \frac{cm^2}{s}$. The resulting Levich plot is shown in Fig. 3-3 for the 20°C experiment, as well as for similar experiments conducted at 55, 70, and 85°C.

Knowledge of the temperature dependence of $D_{HTeO_2^+}$ is of value since CdTe is often electrodeposited at higher temperatures to obtain large grain deposits with superior electronic properties. At these higher temperatures, the solubility of TeO_2 is still low relative to $CdSO_4$ (the soluble salt used to place Cd^{2+} in solution), and a direct current-density source equal to $\frac{3}{2} \times i_{lim,HTeO_2^+}$ can still be used to yield approximately 1:1 CdTe. In order to obtain 1:1 CdTe and use the $\frac{3}{2} \times i_{lim,HTeO_2^+}$ estimate for the cell-current

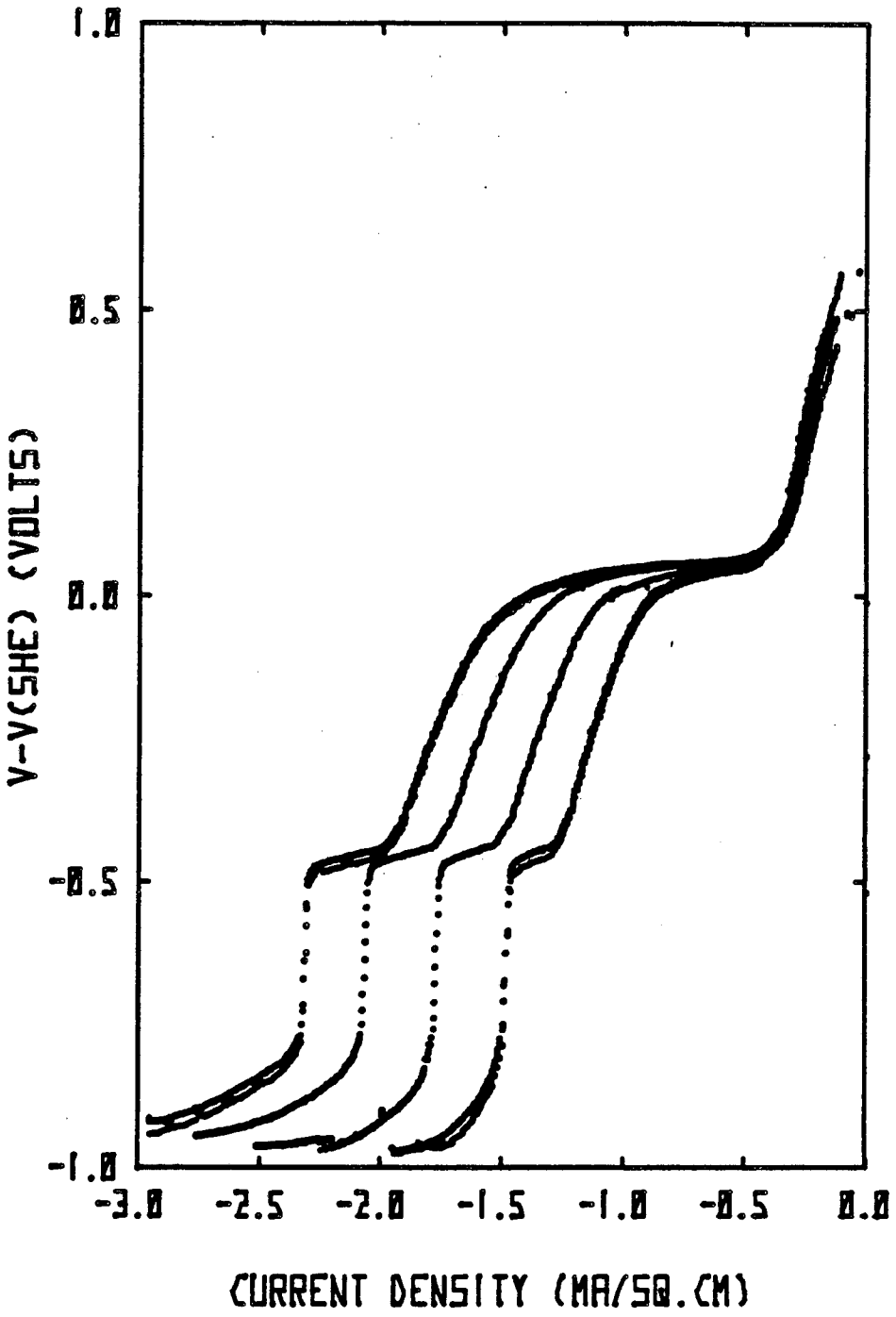

Figure 3-2. Limiting current curves for $HTeO_2^+$. The current density is swept from 0 at a rate of -0.81 mA/cm^2-s. From right to left, the curves represent 392, 588, 784, and 980 rpm. A 5-mm outer diameter, glassy carbon, rotating disk electrode was used.

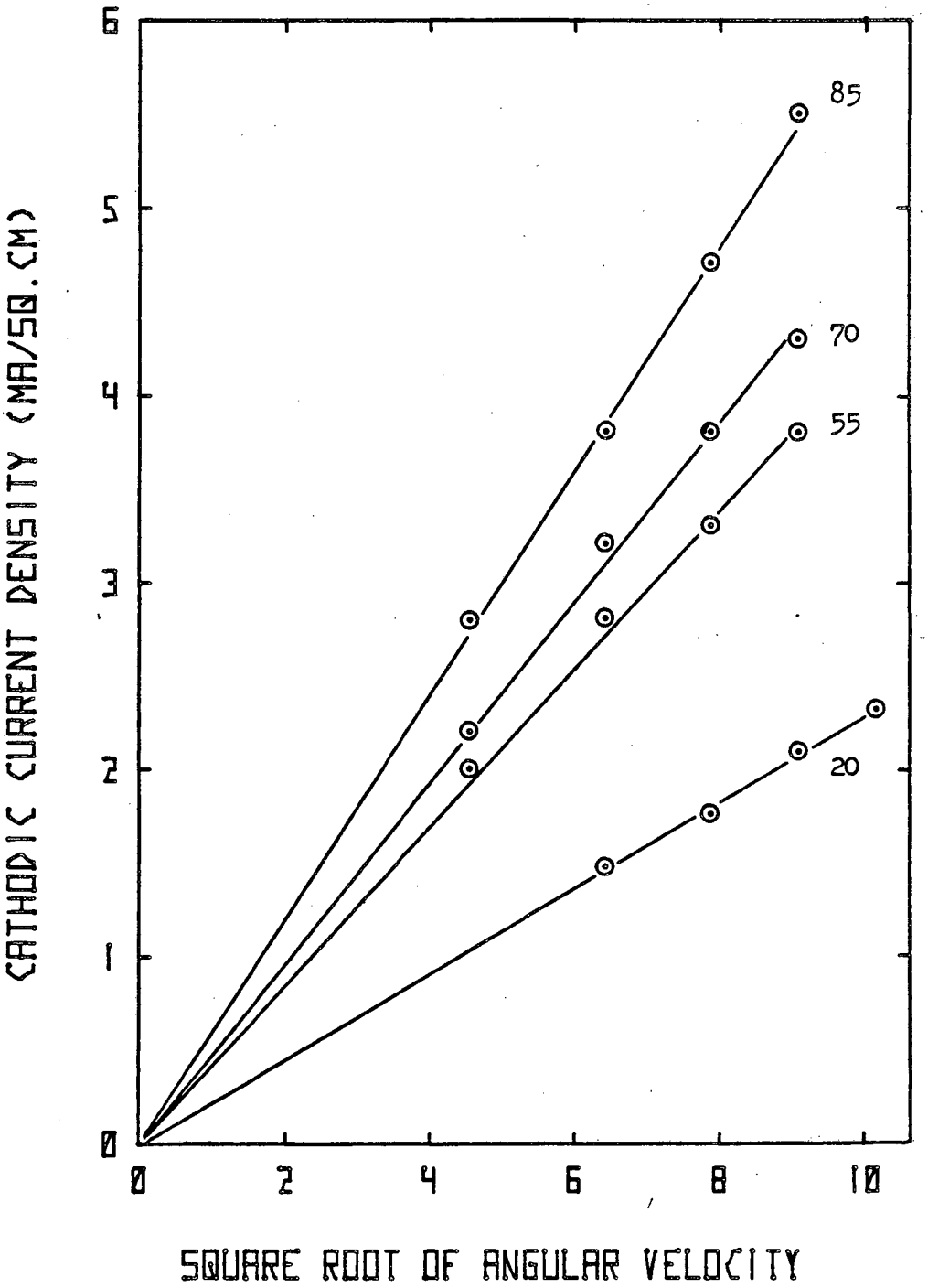

Figure 3-3. Levich plots for $HTeO_2^+$ at various temperatures. The system temperature in °C is listed as a parameter. The diffusion coefficients are listed in Table 3-2.

density, $D_{HTeO_2^+}(T)$ must be known for all temperatures, as can be seen from Eq. [3-1]. Often the relationship (26)

$$\frac{D_i \mu}{T} \approx constant \qquad [3\text{-}3]$$

holds true, where μ is the solution viscosity. For the aqueous H_2SO_4 - $HTeO_2^+$ solutions analyzed in this work, the average value of the constant in Eq. [3-3] was $3.04 \times 10^{-10} \frac{cm - g}{s^2 - K}$ with a standard deviation, weighted over the four temperatures, of $0.014 \times 10^{-10} \frac{cm - g}{s^2 - K}$. Table 3-2 lists the temperature dependence of the solution transport properties. Handbook values were used for the electrolyte viscosity.

Table 3-2. Transport properties of Te-deposition electrolyte.

Temperature (K)	Viscosity $\left(\frac{g}{cm - s}\right)$	Diffusion Coefficient $\left(\frac{cm^2}{s}\right)$	$\frac{D_{HTeO_2^+}\mu}{T}$ $\left(\frac{cm - g}{K - s}\right)$
293	0.010	9.4×10^{-6}	3.21×10^{-10}
328	0.0050	2.0×10^{-5}	3.05×10^{-10}
343	0.0041	2.4×10^{-5}	2.87×10^{-10}
358	0.0034	3.2×10^{-5}	3.04×10^{-10}

Besides providing transport information, Fig. 3-2 shows two apparent half-wave potentials, one near 0 volts and the other near -0.5 volts. Both are independent of rotation rate. This behavior is characteristic of tellurium

deposition on glassy carbon electrodes and has been investigated by Ngac *et al.* (27) They postulate that the initial submonolayer tellurium deposit is poorly conducting and that after a critical amount of tellurium has been deposited, a more conductive solid phase is formed. Our experiments support this theory, since upon subsequent cycling only one half wave near 0 volts was observed, after several atomic layers of tellurium had been deposited.

In Fig. 3-4, the temperature dependence of the potential-time response to the limiting current sweeps used in the construction of the Levich plots in Fig. 3-3 is shown. Two half waves are seen for all potential-time traces. Between 60 and 80 seconds, the cell-current density was reduced to zero. As expected, the open-circuit potential for the $HTeO_2^+$/Te electrode (reaction *ii*, Table 3-1) is near 0.5 volts for the electrolyte used in these experiments. The characteristic time for mass transfer $\frac{\delta_i^2}{D_i}$ is on the order of seconds, yet it takes minutes for this system to reach the calculated open-circuit potential.

The unusually long time required to reach the steady-state open-circuit potential is further investigated in Fig. 3-5. About 100 monolayers of tellurium were deposited at a cathodic current density of $1.0 \frac{mA}{cm^2}$ (1176 rpm, 20°C). After this, the cell-current density was reduced to zero, and the open-circuit potential-time response was recorded. As can be seen from the inset of Fig. 3-5, about 15 minutes were required for the electrode potential to reach its steady-state value near 0.5 volts. Since the liquid-phase transport and composition are well characterized, and the characteristic time for mass transport is orders of magnitude less than 15 minutes, it is apparent that significant interfacial or solid-state changes take place during

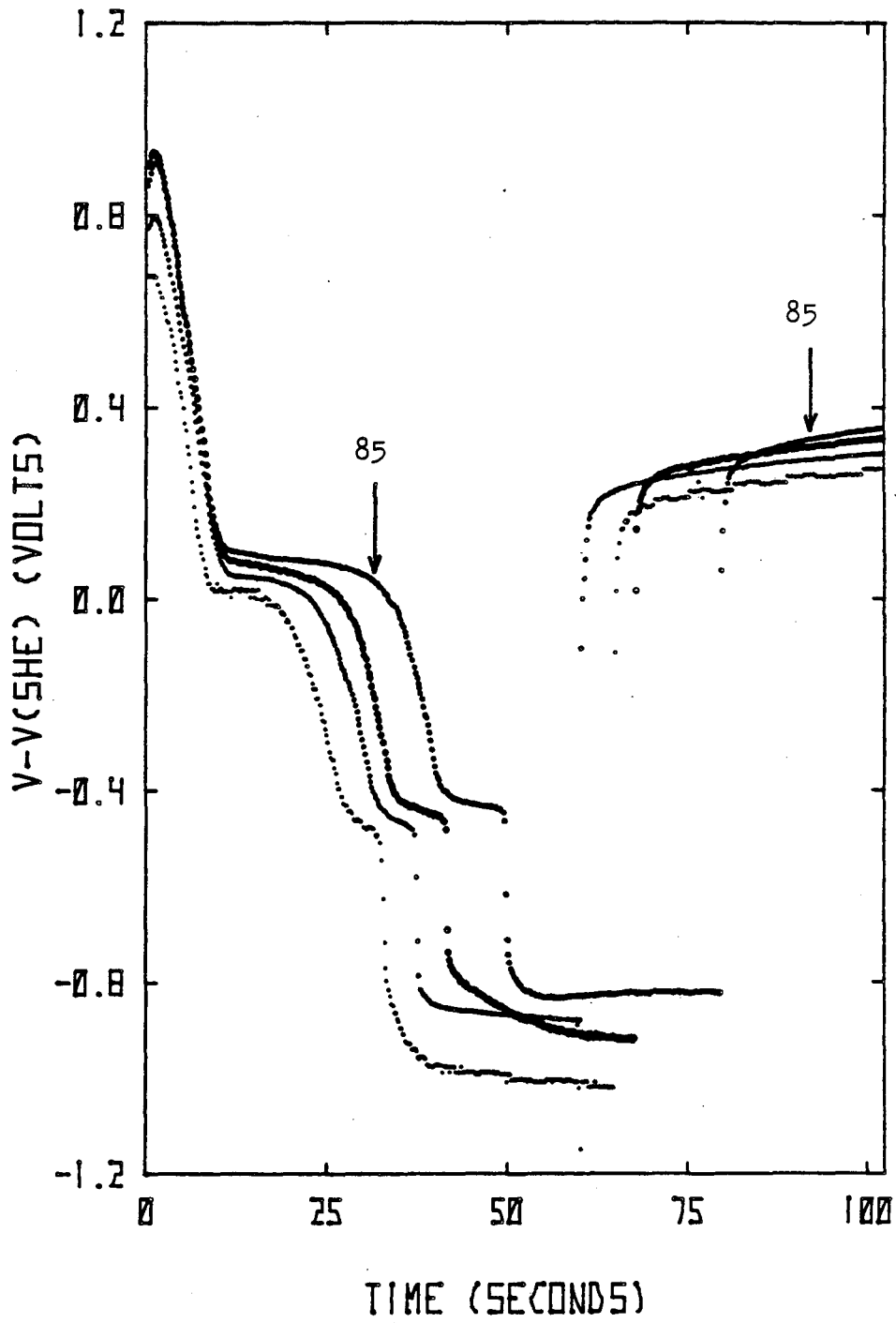

Figure 3-4. Potential-time response for various temperatures. The current was swept from 0 at a rate of -0.76 $mA/cm^2 - s$. The disk rotation rate was 392 rpm. From the uppermost curve to the lowermost curve, the system temperature was 85, 70, 55, and 40°C, respectively. Between 60 and 80 seconds, the cell current density was is zero.

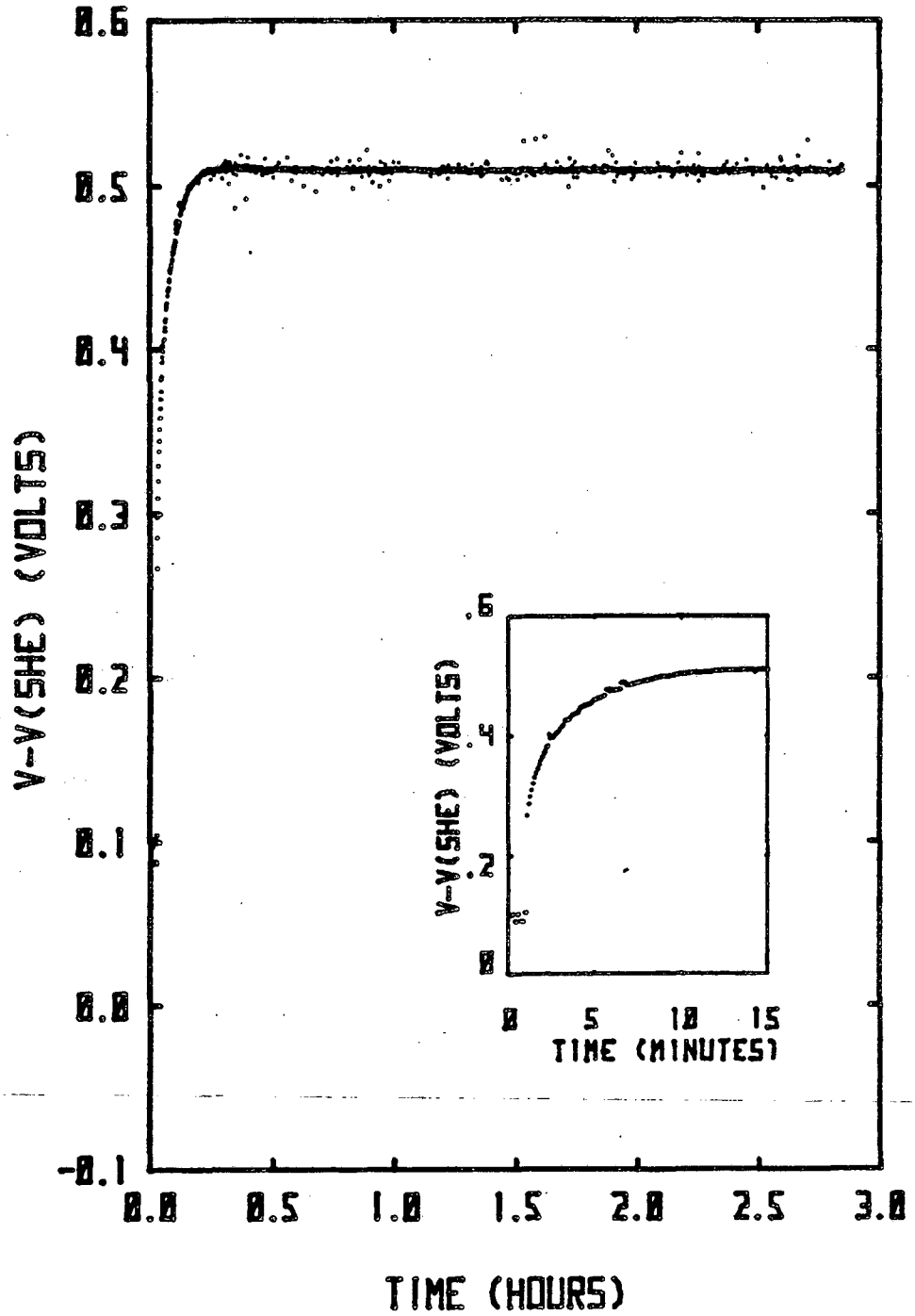

Figure 3-5. Open-circuit potential decay. At time zero, the cell-current density was set to zero. Steady state is reached after about 15 minutes.

the first 15 minutes on open circuit.

The last area of study we describe involves the kinetics of tellurium deposition, reaction *ii* of Table 3-1. Triangular current-sweep chronopotentiometry experiments were conducted on this system; the experimentally recorded potential-time response is represented by the dotted curve in Fig. 3-6. The technique used to construct the theoretical response to the triangular-current sweep, the solid curve in Fig. 3-6, is given in Chapter 4 of this thesis. A cathodic rate constant of $3.16 \times 10^5 \frac{kg^4}{mol^3 - cm^2 - s}$ and a symmetry factor of 0.1 were used to construct the solid curve in Fig. 3-6. Using the standard electrode potential, 0.551 volts, the anodic rate constant can be calculated to be $1.67 \times 10^{-32} \frac{mol}{cm^2 - s}$. The corresponding exchange-current density, based on bulk concentrations and unit activity of the electrodeposit, is $2.0 \frac{mA}{cm^2}$.

To summarize the tellurium electrodeposition study, we have analyzed the mass transport of $HTeO_2^+$, the knowledge of which is integral to characterizing the electrodeposition of cadmium telluride. In addition, we have investigated the kinetics of tellurium electrodeposition. Undoubtedly, a more complex reaction scheme applies than the four-electron transfer reaction listed in Table 3-1; however, this simplified model can be used to represent fairly accurately the experimental behavior of tellurium electrodeposition, as depicted in Fig. 3-6.

The Electrodeposition of Cadmium

The electrode potential at which the cadmium deposition reaction occurs, reaction *iv* of Table 3-1, can be used to approximate the potential at

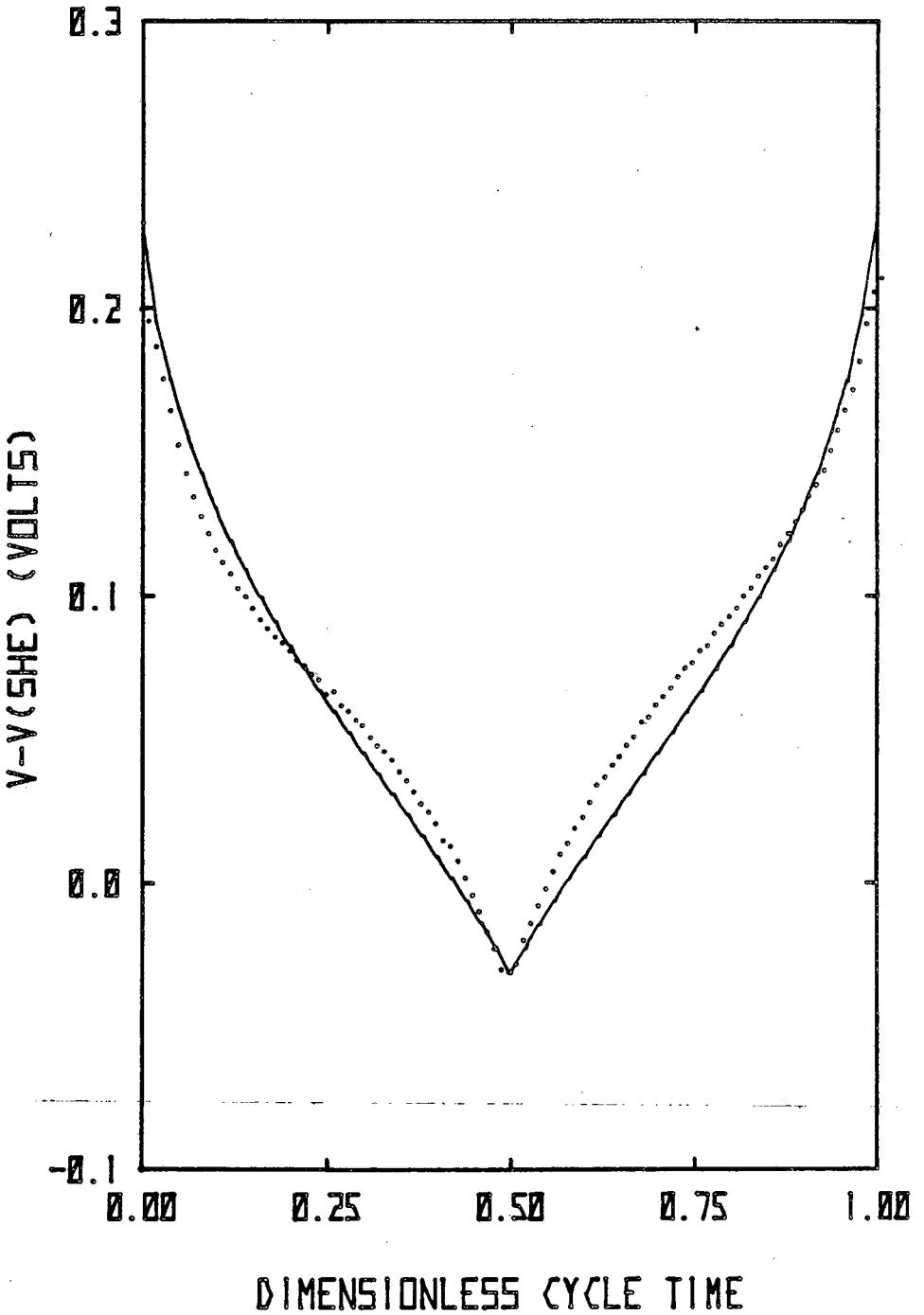

Figure 3-6. Electrode potential. Dotted curve: experimental data (1176 rpm, 20°C, 0.01-Hz current source). Solid curve: theoretical result. The triangular current-density source had minimum cathodic currents of zero at dimensionless cycle times of zero and one. The maximum cathodic current density was -1.62 mA/cm^2 at a dimensionless cycle time of 0.5.

which 1:1 CdTe can be deposited from an aqueous, sulfuric acid electrolyte. As mentioned previously, due to the low solubility of TeO_2, the mass transfer of the $HTeO_2^+$ species usually limits the rate of Te deposition, and has a correspondingly low surface concentration. No matter how much more cathodic the electrode potential is driven, the rate of tellurium deposition is nearly constant, and the added cathodic potential is "used" to increase the rate of cadmium deposition. Knowledge of the electrode-kinetic behavior of reaction *iv* is an important aspect in the understanding of CdTe electrodeposition processes. Also unlike tellurium electrodeposition, coherent films of cadmium can be deposited from an aqueous, sulfuric acid electrolyte. In this section, the effect of a rectangular pulse-current source on the cadmium electrodeposit morphology is investigated.

Before considering the electrode-kinetic behavior of reaction *iv*, we shall address the steady-state polarization curves covering the full potential range of cadmium deposition. The polarization curves in Fig. 3-7 were used to evaluate the diffusion coefficient of Cd^{2+}. The current was swept from 0 at a rate of -1.43 $\frac{mA}{cm^2 - s}$. The cell temperature during the experiment was 23°C and the calculated value for $D_{Cd^{2+}}$ is 3.6×10^{-6} $\frac{cm^2}{s}$. The resulting Levich plot is shown in Fig. 3-8. Since the CdTe-electrodeposition process is less affected by the Cd^{2+} mass transport, relative to the $HTeO_2^+$ mass transport, the temperature dependence of $D_{Cd^{2+}}$ will not be addressed.

In Chapter 4 of this thesis, the diffusion coefficient of the Cd^{2+} species in a 0.0058-M-$CdSO_4$/0.25-M-K_2SO_4 electrolyte was found to be 3.6×10^{-6} $\frac{cm^2}{s}$. Since $D_{Cd^{2+}}$ in the 0.1-M-$CdSO_4$/0.30-M-H_2SO_4 electrolyte is 3.7×10^{-6} $\frac{cm^2}{s}$, we have a strong indication that there are no significant

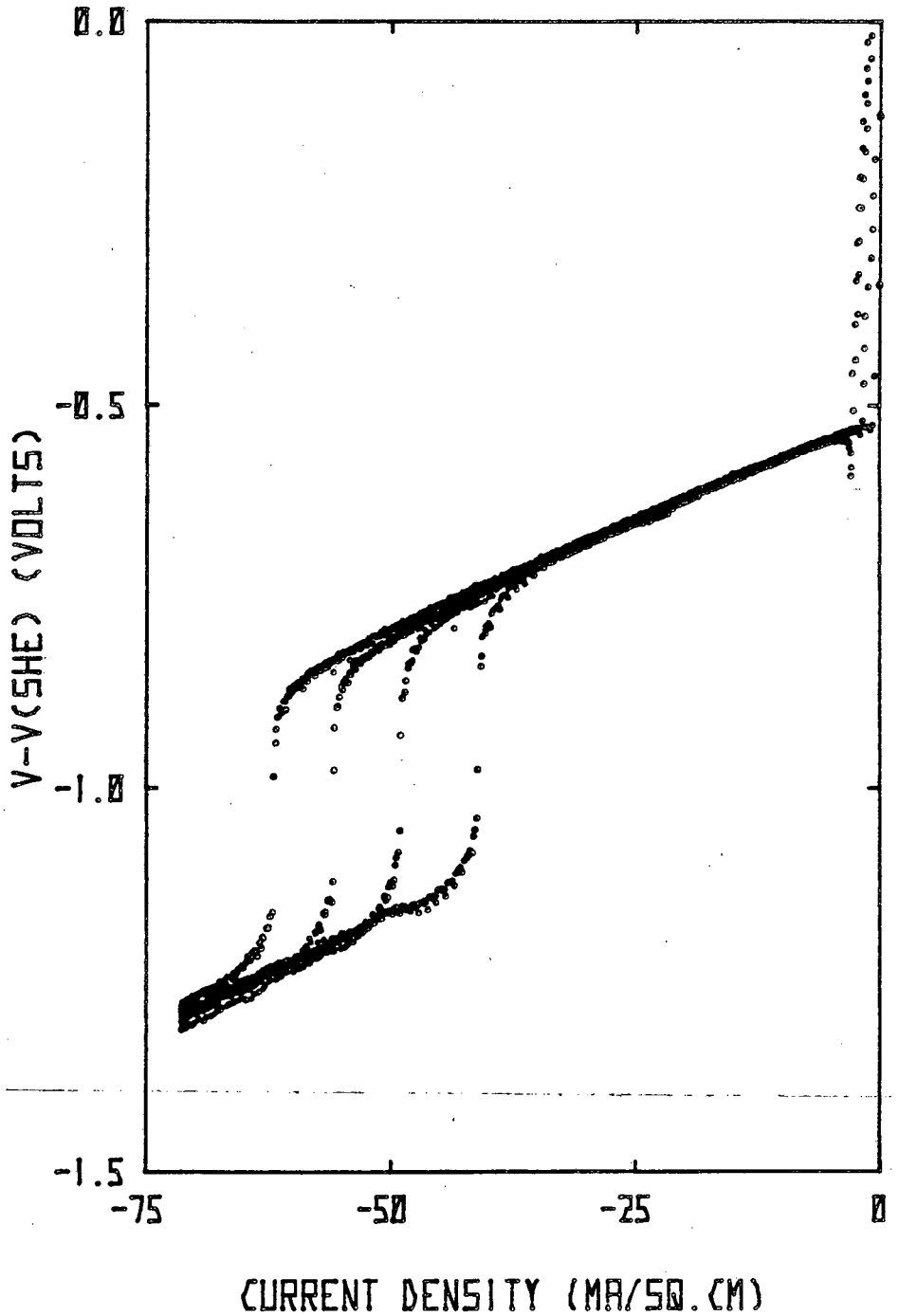

Figure 3-7. Limiting current curves for Cd^{2+}. The current density is swept from 0 at a rate of -1.43 mA/cm^2-s. From right to left, the curves represent 392, 588, 784, and 980 rpm. A 5-mm outer diameter, glassy carbon, rotating disk electrode was used.

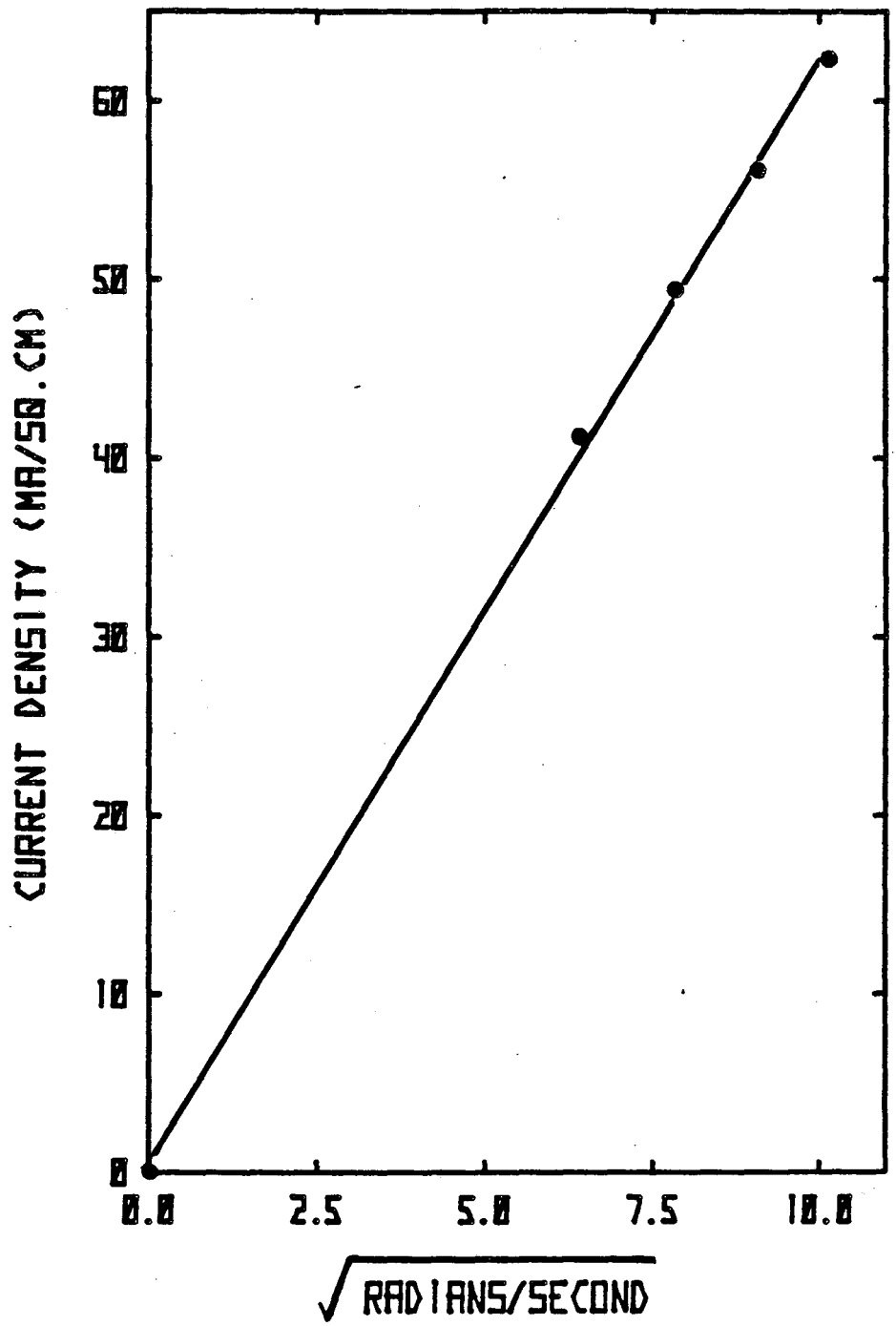

Figure 3-8. Levich plot for Cd^{2+}. These data yield $D_{Cd^{2+}} = 3.6 \times 10^{-6}$ cm^2/s .

ion-ion interactions, only ion-solvent interactions, and that dilute solution transport equations can be used to analyze the experimental systems. In addition, $D_{HTeO_2^+}$ in the aqueous, sulfuric acid electrolyte is $9.6 \times 10^{-6} \frac{cm^2}{s}$, considerably higher than $D_{Cd^{2+}}$. The $HTeO_2^+$ complex is rather large, with only one positive charge spread throughout the ion. Consequently, it is probably less solvated with water molecules and can diffuse faster through the solution than the smaller Cd^{2+} species (the concentration gradient of both species being equal), which probably has a larger hydration shell.

The polarization curves in Fig. 3-7 contain two rather notable features. First, there is a significant amount of underpotential deposition of cadmium on the glassy carbon electrode near zero current, at the start of the linear current sweep. The calculated open-circuit potential for the cadmium electrodeposition reaction is near -0.43 volts for the 0.1 molar Cd^{2+} solution used in these experiments and for unit activity of a cadmium substrate. Secondly, the potential-current relation is quite linear between 0.5 volts, near zero current density, and -0.75 volts, near the beginning of the limiting current for each experiment. In general, the current potential curve is difficult to duplicate theoretically with a Butler-Volmer electrode-kinetic expression. In Chapter 4 of this thesis, we present an investigation of cadmium electrodeposition from an aqueous, sulfate electrolyte. A cathodic rate constant for reaction *iv* of $3.0 \times 10^{-9} \frac{kg}{cm^2 - s}$ and a symmetry factor of 0.15 were found to represent best the current-potential relationship for the discharge of Cd^{2+} from the sulfuric acid electrolye. Using the standard electrode potential of -0.403 volts, the anodic rate constant can be calculated to be $1.29 \times 10^5 \frac{mol}{cm^2 - s}$. The corresponding exchange-current density, based

on bulk concentrations and unit activity of the electrodeposit, is 9.1 $\frac{mA}{cm^2}$.

In Chapter 2 we outlined the motivation for using a pulse-current source. Frequently, the pulse-current electrodeposits contain superior mechanical properties relative to deposits formed with a direct current source. The remainder of this section is devoted to the analysis of the pulse-current cadmium-electrodeposition processes. A 5-*mm* outer diameter, polycrystalline, cadmium, rotating disk electrode was used in these experiments. The cadmium electrodes were etched in a dilute nitric acid solution, the effect of which is shown in Fig. 3-9. Figures 3-10, 3-11, and 3-12 illustrate the pronounced effect of a rectangular pulse-current source on electrodeposit morphology. Two different grains were observed in the cadmium electrodes; for this reason, the pictures of the approximately 1-μm thick cadmium electrodeposits always contained the two grains. In addition, two photos were taken of each electrodeposit, one of the disk center and one of the disk edge; more electrodeposit is formed at the outer edge of the electrode due to the nonuniform current distribution. The mass-transport resistance was not a significant factor as the maximum current density during the pulse on-time was only one-half the Cd^{2+} limiting current density. The on-time was equal to the off-time; no current was passed during the off-time. Due to these conditions, the ratio of the Cd^{2+} surface concentration to the Cd^{2+} bulk concentration oscillated between 0.5 and 1.0. For the direct current electrodeposition process, the cell current was one-fourth the Cd^{2+} limiting current. Using the left photos in Figs. 3-10, 3-11, and 3-12, which represent the disk center, we found that a 100.-Hz rectangular pulse-current source formed the smoothest and most coherent metallic film.

To summarize this section, we have analyzed the mass transport of the

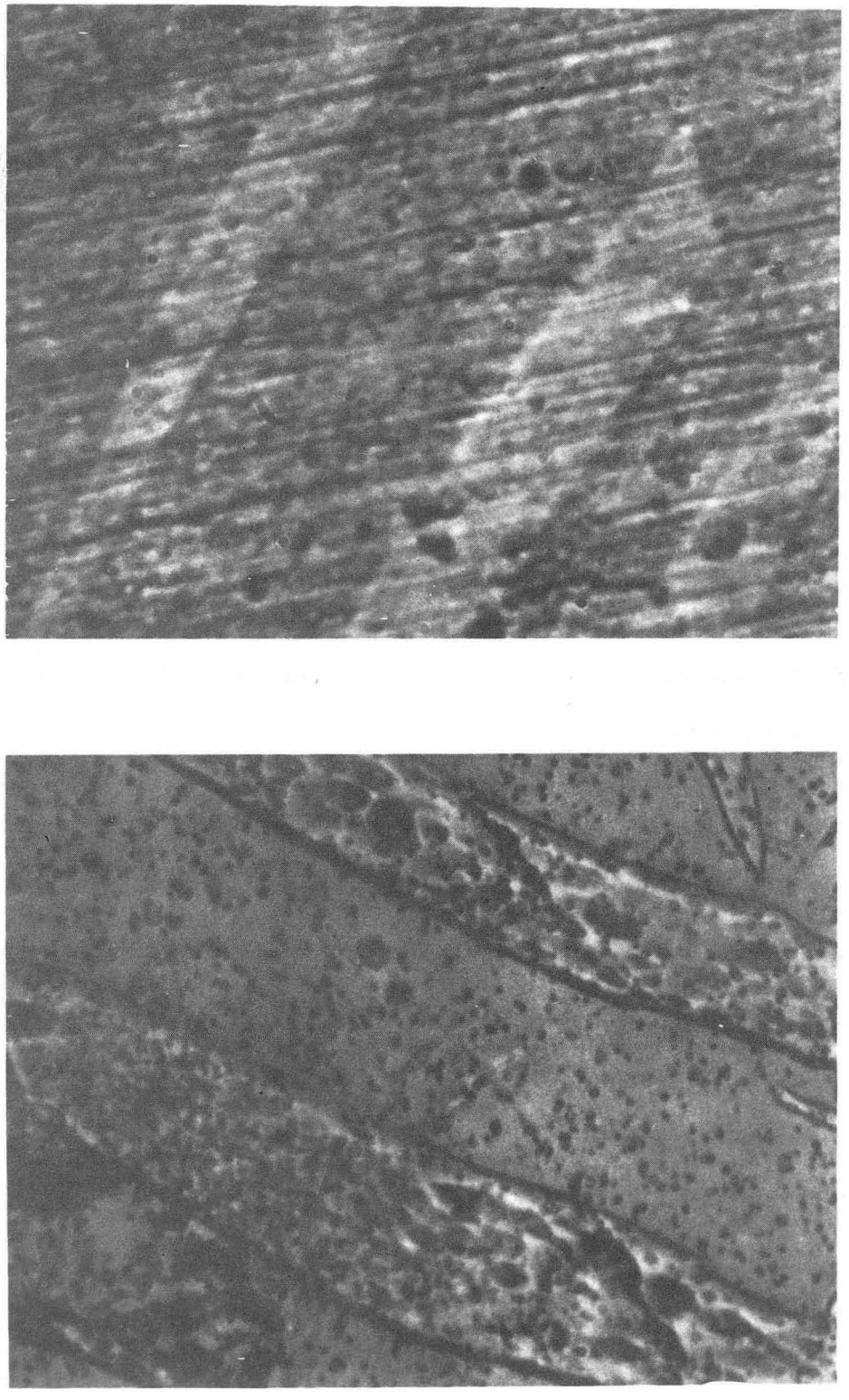

XBB859-7667

Figure 3-9. Cadmium electrode substrate. Upper photo: substrate prior to nitric acid etch. Lower photo: substrate after nitric acid etch. The width of each photo is 80 μm.

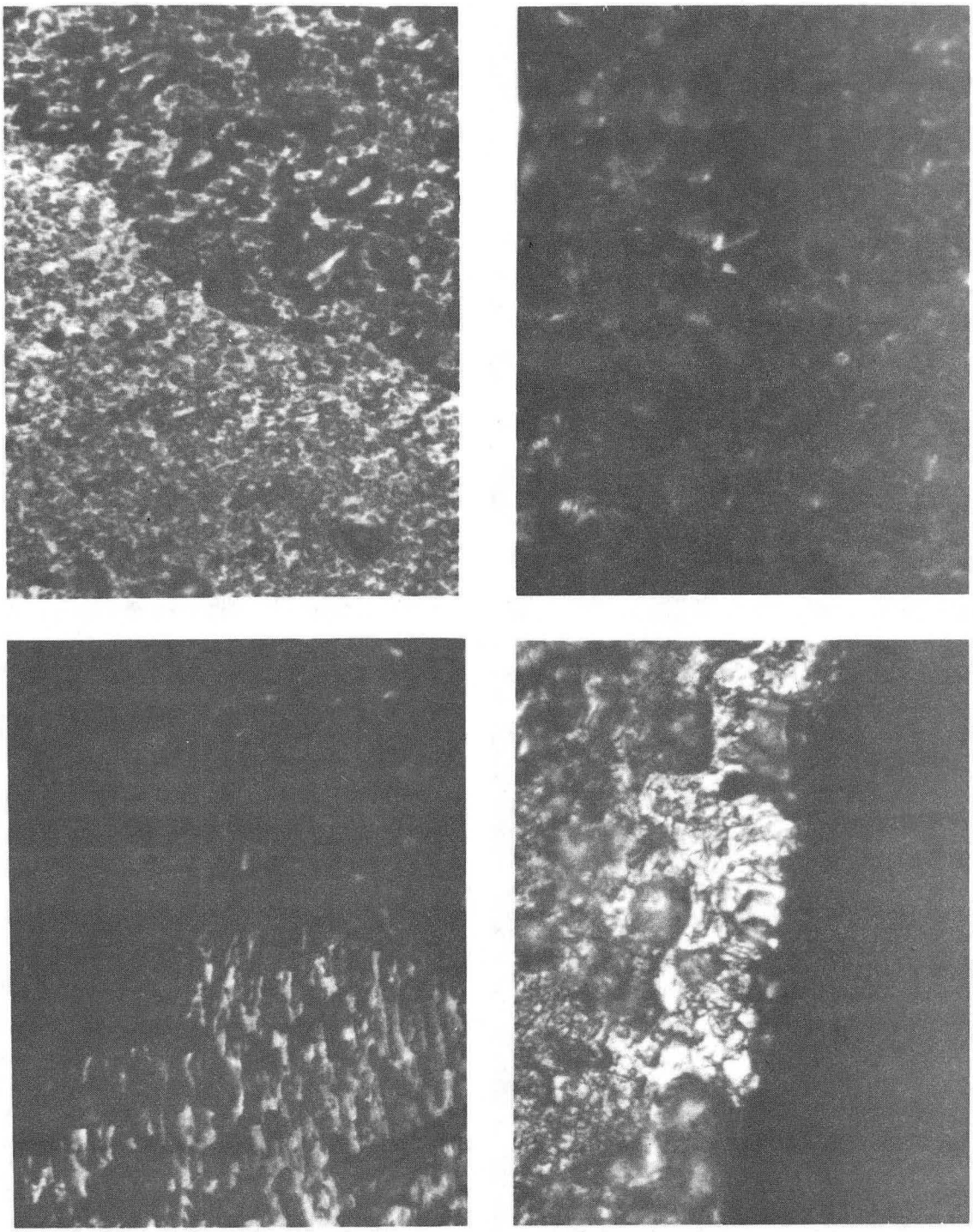

XBB853-2490-A

Figure 3-10. Cadmium electrodeposits. A direct current source was used to form the electrodeposits in the upper photos, and a 0.100-Hz pulse-current source was used to form the electrodeposits in the lower photos. The left photos represent the disk center, and the right photos represent the disk edge. The width of each photo represents 90 μm. A 25°C, 0.3-molal-H_2SO_4, 0.1-molal-$CdSO_4$, aqueous solution was used.

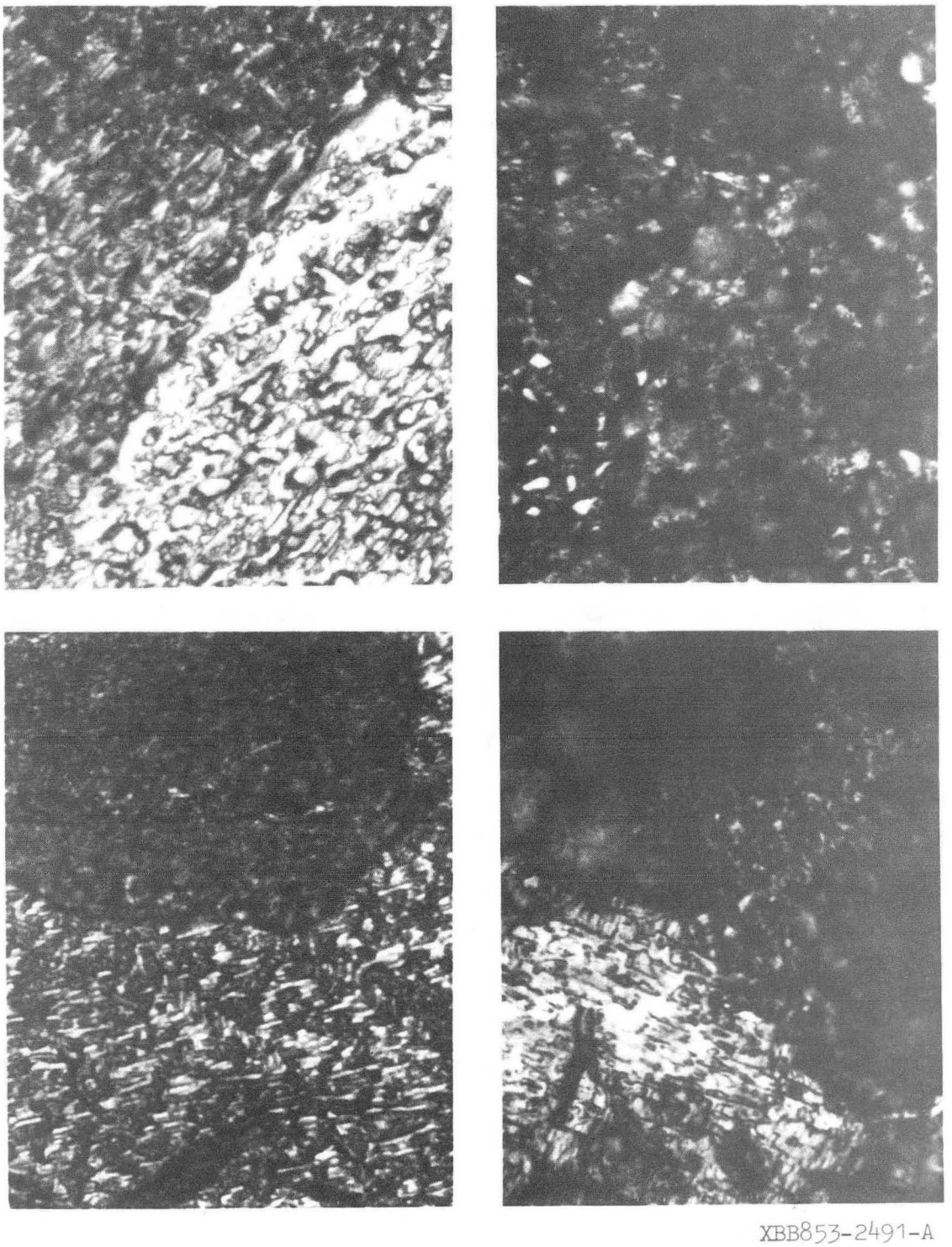

XBB853-2491-A

Figure 3-11. Cadmium electrodeposits. A 1.00-Hz pulse-current source was used to form the electrodeposits in the upper photos, and a 10.0-Hz pulse-current source was used to form the electrodeposits in the lower photos. The left photos, represent the disk center, and the right photos represent the disk edge. The width of each photo represents 90 μm. A 25°C, 0.3-molal-H_2SO_4, 0.1-molal-$CdSO_4$, aqueous solution was used.

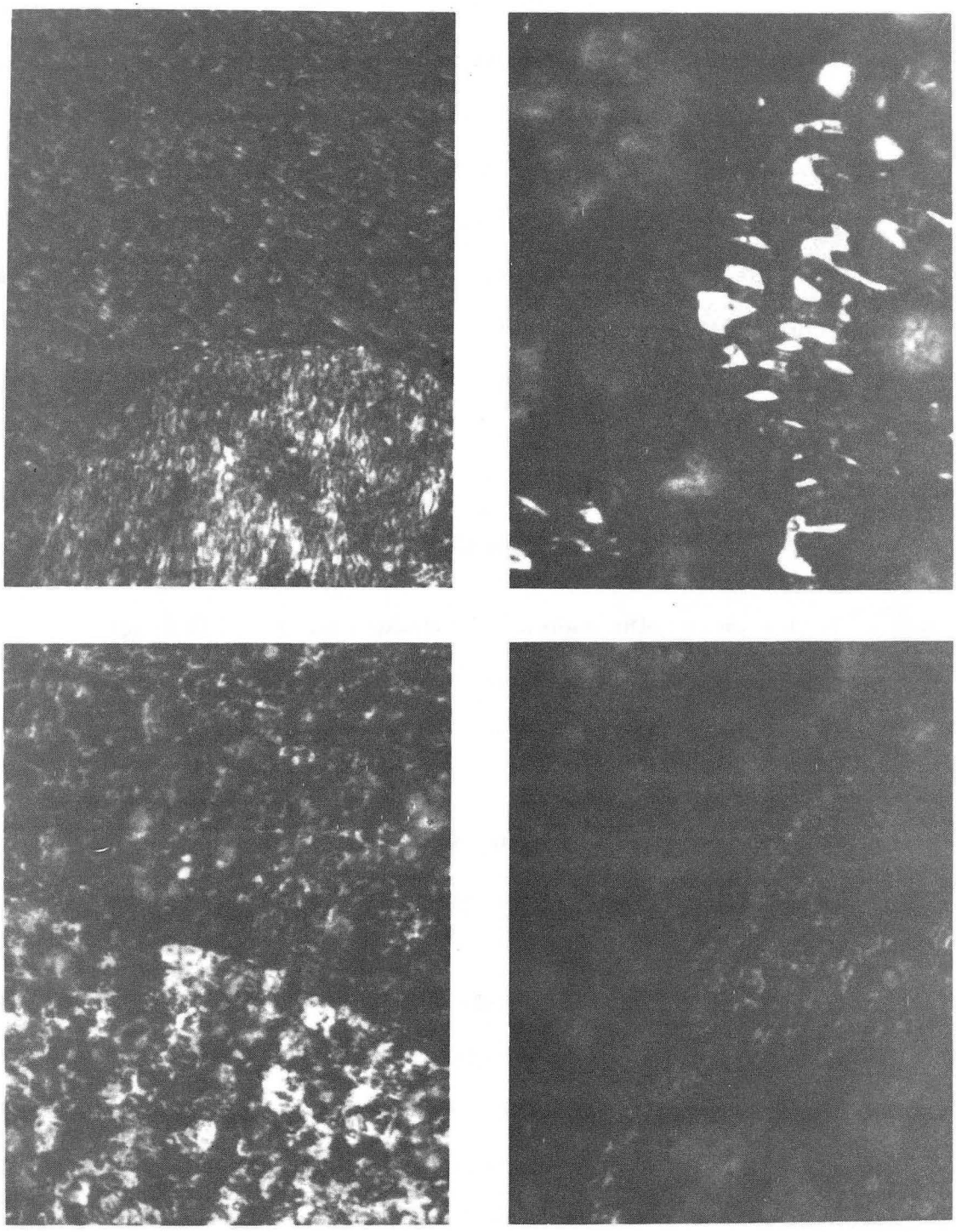

XBB853-2492-A

Figure 3-12. Cadmium electrodeposits. A 100.-Hz pulse-current source was used to form the electrodeposits in the upper photos, and a 1000-Hz pulse-current source was used to form the electrodeposits in the lower photos. The left photos represent the disk center, and the right photos represent the disk edge. The width of each photo represents 90 μm. A 25°C, 0.3-molal-H_2SO_4, 0.1-molal-$CdSO_4$, aqueous solution was used.

Cd^{2+} species. In addition, the effect of a rectangular pulse-current source, with the on-time equal to the off-time, on the cadmium-electrodeposit morphology was investigated. A 100.-Hz current source provided the smoothest and most coherent thin film electrodeposit. The kinetics of the cadmium-electrodeposition process, reaction *iv* of Table 3-1, are briefly addressed; a more thorough study is presented in Chapter 4. With the tellurium and cadmium transport and kinetic analyses complete, the electrodeposition of CdTe can now be addressed.

The Codeposition of Cadmium and Tellurium

In this section, the cadmium electrodeposition and tellurium electrodeposition studies will be combined to analyze cadmium telluride electrodeposition. Specifically, the transport and kinetic parameters measured in the individual component deposition studies can be used to describe the multicomponent electrodeposition process. Furthermore, a solid-state thermodynamic model will be incorporated into the alloy-deposition analysis to describe the activity of the individual components in the electrodeposit.

These thoughts can be clarified with the help of Fig. 3-13. For a dilute liquid phase, there are no ion-ion interactions, and the dilute solution equation of convective diffusion used in Chapter 2 can be applied to evaluate $c_i(t,y)$, the concentration of the reactant or product species in the neutral liquid phase. Nearer the interface, for solutions of high ionic strength and dilute in reacting ions, the diffuse portion of the double layer will not change significantly in structure, and the potential drop across this region of charge separation can be neglected for highly conductive, well supported solutions. The inner edge of the diffuse portion of the double layer is the outer

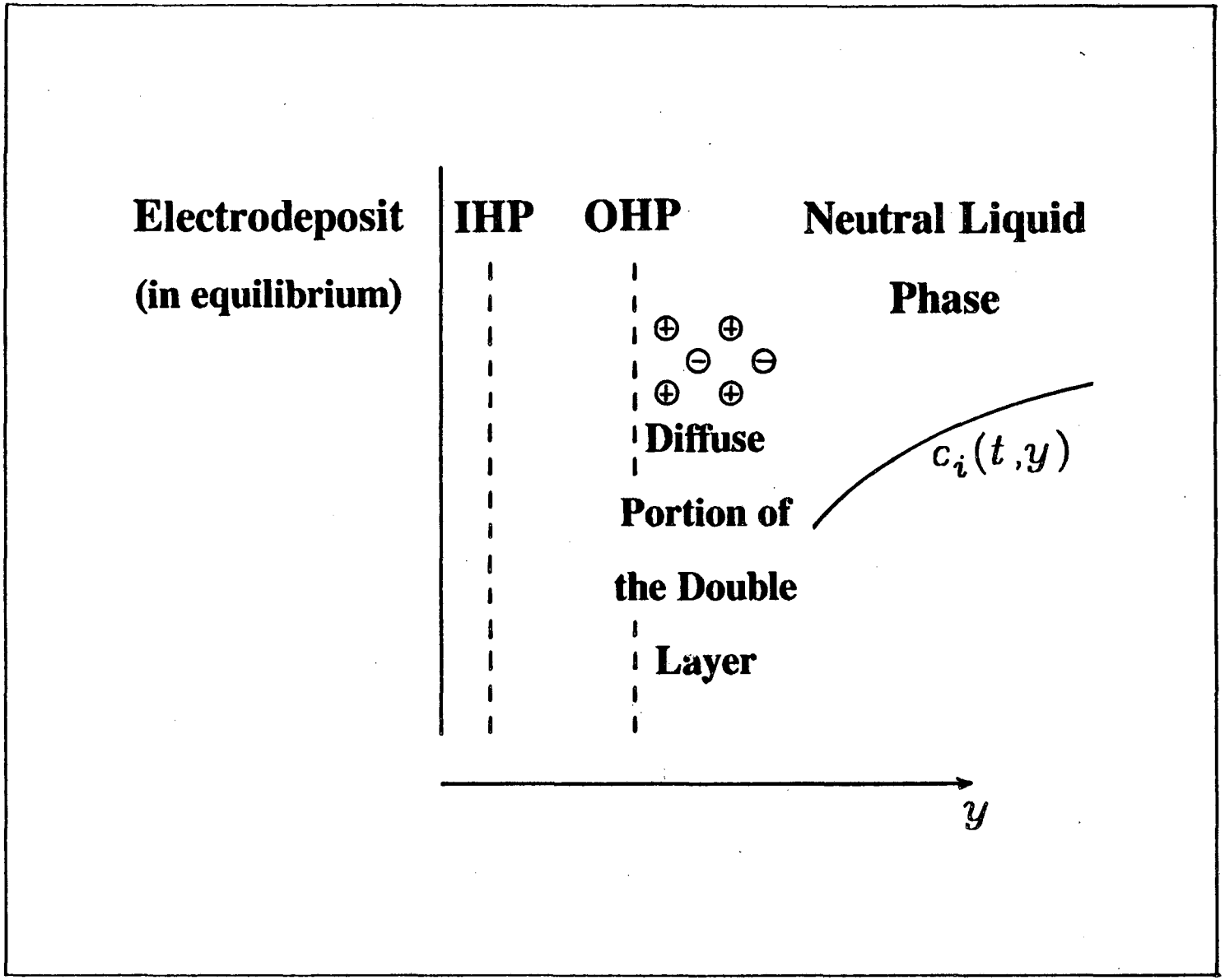

Figure 3-13. Schematic illustration of the electrodeposit, interface, and liquid phase. IHP refers to inner Helmholtz plane, and OHP refers to outer Helmholtz plane.

Helmholtz plane (OHP), which represents the plane of closest approach for the *non-specifically* adsorbed ions. Immediately adjacent to the electrode surface is the inner Helmholtz plane (IHP), where solution species can be *specifically* adsorbed to the electrodeposit surface. Since specific adsorbtion is dependent on the electrodeposit-solution interaction, and since it is not included in our model, the rate constants measured for cadmium and tellurium electrodeposition may have to be altered in an attempt to match experimental and calculated results, as the CdTe surface may specifically adsorb species differently from the cadmium or tellurium electrodes. In general, the inner Helmholtz plane poses a very difficult region to quantify. In this study, the last region of interest, the forming electrodeposit, is assumed to contain three species in equilibrium: Cd, Te, and CdTe.

The most accessible experimental variables are the total cell current and the potential of the working electrode with respect to a suitable reference. For this reason, we shall compare calculated polarization curves with those obtained by experiment. It is also possible to compare the predicted and measured electrodeposit composition, but this is a more difficult task and would probably provide less insight. Too little electrodeposit is formed to allow accurate determination of the composition by quantitative analysis. (Only thin film deposits were formed because thick deposits tend to acquire a roughened surface and affect the fluid flow, thus decreasing the chances for successful experimental-theoretical comparison.) There is a number of other *ex-situ* analysis techniques, although they do not appear as quantitative or convenient as theoretical-experimental comparisons of polarization curves obtained in alloy electrodeposition processes. For instance, in Auger electron spectroscopy analyses, preferential sputtering of components often

takes place (28,29) and electron attenuation within the deposit complicates surface characterization. (30) Brenner (31) reviews some limitations associated with the use of x-rays for structural chacterization of alloy electrodeposits. Swathirajan (32) presents support for the use of *in-situ* acquisition of cell current-potential characteristics and subsequent comparison with theoretical calculations in order to investigate electrochemical stripping experiments of alloy electrodeposits, in lieu of *ex-situ* surface analysis techniques. In this work, all electrodeposit compositions were estimated with a Kevax AMR 1000 x-ray analyzer. The electrodeposit structures were qualitatively analyzed with an x-ray diffractometer. Photoresponse measurements were also employeed to analyze the CdTe semiconducting films.

The next section of this chapter develops the equations governing the electrodeposition of CdTe. The solution technique to this system of equations was addressed in Chapter 2 and will not be repeated in this chapter.

Mathematical Analysis

The liquid phase. The one-dimensional equation of convective diffusion is used to describe the mass transport of species i

$$\frac{\partial c_i}{\partial t} + v_y \frac{\partial c_i}{\partial y} = D_i \frac{\partial^2 c_i}{\partial y^2} \quad . \qquad [3\text{-}4]$$

where

$$v_y = -0.51023\, \omega^{3/2} \nu^{-1/2} y^2 \quad . \qquad [3\text{-}5]$$

The initial condition and boundary conditions are

$$c_i(0,y) = c_i^b \quad , \qquad [3\text{-}6]$$

$$c_i(t,\infty) = c_i^b \quad , \qquad [3\text{-}7]$$

and

$$\frac{\partial c_i(t,0)}{\partial y} = \frac{s_i i_l(t)}{n_l F D_i} \quad ; \qquad [3\text{-}8]$$

The electrode-reaction l is

$$n_l e^- \underset{k_{a,l}}{\overset{k_{c,l}}{\rightleftharpoons}} \sum_i s_i M_i^{z_i} \quad . \qquad [3\text{-}9]$$

Equation [3-9] is a general expression for an electrochemical reaction, by which any of the electrochemical reactions in Table 3-1 can be represented.

Equation [3-4] provides a good representation of the ionic mass transport for systems with large Schmidt numbers, small disk radii, low exchange-current densities, highly conductive electrolytes, and low concentrations of reacting species. For the CdTe electrodeposition process, subscript i refers to $HTeO_2^+$, H^+, Cd^{2+}, and Te^{2-}. Four convective diffusion equations are written for the four species, the solution to this system of equations yields the surface concentrations of the reactant and product species and the partial current densities of reactions *ii*, *iii*, *iv*, and *v*. It should be noted that the hydrogen evolution reaction may have a non-uniform distribution due to the high concentration of H^+. However, the hydrogen evolution reaction is very slow on the electrodeposited material, and the high kinetic resistance tends to promote a uniform reaction distribution. Usually, the CdTe electrodeposition takes place with high current efficiency and little hydrogen evolution occurs.

The liquid-electrodeposit interface. A Butler-Volmer electrode-kinetic

equation is used to relate the partial current density of the electrochemical reaction l, the surface concentrations of the species participating in the reaction, and the electrode potential. The four electrode-kinetic equations represent reactions *ii*, *iii*, *iv*, and *v* of Table 3-1, respectively:

$$\frac{i_{ii}}{4F} = k_{a,ii} e^{(1-\beta_{ii})4fV} a_{Te} - k_{c,ii} e^{-\beta_{ii}4fV} (c_{HTeO_2^+})(c_{H^+})^3 \qquad [3\text{-}10]$$

$$\frac{i_{iii}}{F} = k_{a,iii} e^{(1-\beta_{iii})fV} (p_{H_2})^{1/2} - k_{c,iii} e^{-\beta_{iii}fV} c_{H^+} \qquad [3\text{-}11]$$

$$\frac{i_{iv}}{2F} = k_{a,iv} e^{(1-\beta_{iv})2fV} a_{Cd} - k_{c,iv} e^{-\beta_{iv}2fV} c_{Cd^{2+}} \qquad [3\text{-}12]$$

$$\frac{i_{v}}{2F} = k_{a,v} e^{(1-\beta_{v})2fV} c_{Te^{-2}} - k_{c,v} e^{-\beta_{v}2fV} a_{Te} \qquad [3\text{-}13]$$

In addition, the sum of the partial current densities must equal the cell-current density,

$$\sum_{l=ii}^{v} i_l = i_{cell} \qquad [3\text{-}14]$$

The potential V in Eqs. [3-10]-[3-13] represents the potential difference between the working electrode and a standard hydrogen electrode, corrected for ohmic drop. V is given by

$$V = E + \left[U^{\theta}_{ref} - \frac{1}{n_{ref} f} \sum_i s_{i,ref} \ln c_{i,ref} \right] - i_{cell} r \quad . \qquad [3\text{-}15]$$

where E is the measured cell potential.

The partial current densities in Eqs. [3-10]-[3-13] couple the convective diffusion equations through the boundary condition given by Eq. [3-8]. The activity of the cadmium, a_{Cd}, and tellurium, a_{Te}, will be dealt with in the next

section.

The Electrodeposit. To evaluate the component activities in the electrodeposit, we will make use of Jordan's random associated solution (RAS) theory. (33) Jordan developed this theory in order to describe mathematically the liquidus curve for the Cd-Te and Zn-Te systems. Since the same three species are present in the solid phase, we shall attempt to use the same model. Engelken (8) has used the RAS model to analyze the steady-state electrodeposition of CdTe.

The CdTe-RAS theory assumes that departures from ideal-solution behavior of the Cd-Te-CdTe system are due to short range, nearest neighbor interactions, which are taken into account by identifying the activity coefficients γ_{Cd}, γ_{Te}, and γ_{CdTe}, with those of a regular, ternary solution, making use of *interchange energies* for Cd-Te, Cd-CdTe, and Te-CdTe interactions. These expressions can be combined with the Gibbs energy of formation for CdTe (reaction *vii*, Table 3-1):

$$\Delta G_{CdTe} = -RTln\frac{a_{CdTe}}{a_{Cd}a_{Te}} \qquad [3\text{-}16]$$

If the interchange energies for Cd-CdTe and Te-CdTe interactions are taken equal, the activities can be approximated as

$$a_{Te} = \frac{\bar{x}_{Te} - \bar{x}_{Cd} + P}{1+P}\exp\left[\frac{\alpha(\bar{x}_{Cd})^2}{RT}\right], \qquad [3\text{-}17]$$

$$a_{Cd} = \frac{\bar{x}_{Cd} - \bar{x}_{Te} + P}{1+P}\exp\left[\frac{\alpha(\bar{x}_{Te})^2}{RT}\right], \qquad [3\text{-}18]$$

and

$$a_{CdTe} = \frac{1-P}{1+P}\exp\left[\frac{\alpha}{2RT}(1-4\bar{x}_{Te}\bar{x}_{Cd})\right], \qquad [3\text{-}19]$$

where

$$P = \left[1-\bar{x}_{Te}\bar{x}_{Cd}(1-\beta_{act}^2)\right]^{\frac{1}{2}}. \qquad [3\text{-}20]$$

β_{act} is the degree of dissociation at $\bar{x}_{Cd} = \bar{x}_{Te} = 0.5$; the overbar has been used to denote atomic mole fractions. Equations [3-17]-[3-19] represent a one-parameter model for the electrodeposit thermodynamics, since the Gibbs free energy of formation for CdTe can be used to eliminate α or β_{act}. The behavior of this activity model, using the parameters Jordan used, is displayed in Fig. 3-14. In general, for values of $\bar{x}_{Te}$ or $\bar{x}_{Cd}$ less than 0.5, extremely small activities are registered for cadmium or tellurium, respectively. The a_{CdTe} curve in Fig. 3-14 is asymmetric because Jordan used one value of α for $\bar{x}_{Te} < 0.5$, and another for $\bar{x}_{Te} > 0.5$. In our work, α was eliminated by making use of ΔG_{CdTe} (Eq. [3-16]), hence α remained constant for all values of $\bar{x}_{Te}$.

The atomic mole fractions for tellurium, $\bar{x}_{Te}$, and cadmium, $\bar{x}_{Cd}$, can be obtained by integrating the appropriate partial current densities:

$$\bar{x}_{Cd} = \frac{\int_{t_{RSAT}}^{t} 2i_{iv}\,dt}{\int_{t_{RSAT}}^{t} (i_{ii} + 2i_{iv} - 2i_{v})\,dt}, \qquad [3\text{-}21]$$

and

$$\bar{x}_{Te} = 1 - \bar{x}_{Cd}. \qquad [3\text{-}22]$$

In these expressions, the time interval from t_{RSAT} to t is required to deposit one relative surface-activity thickness ($RSAT$), which was discussed in

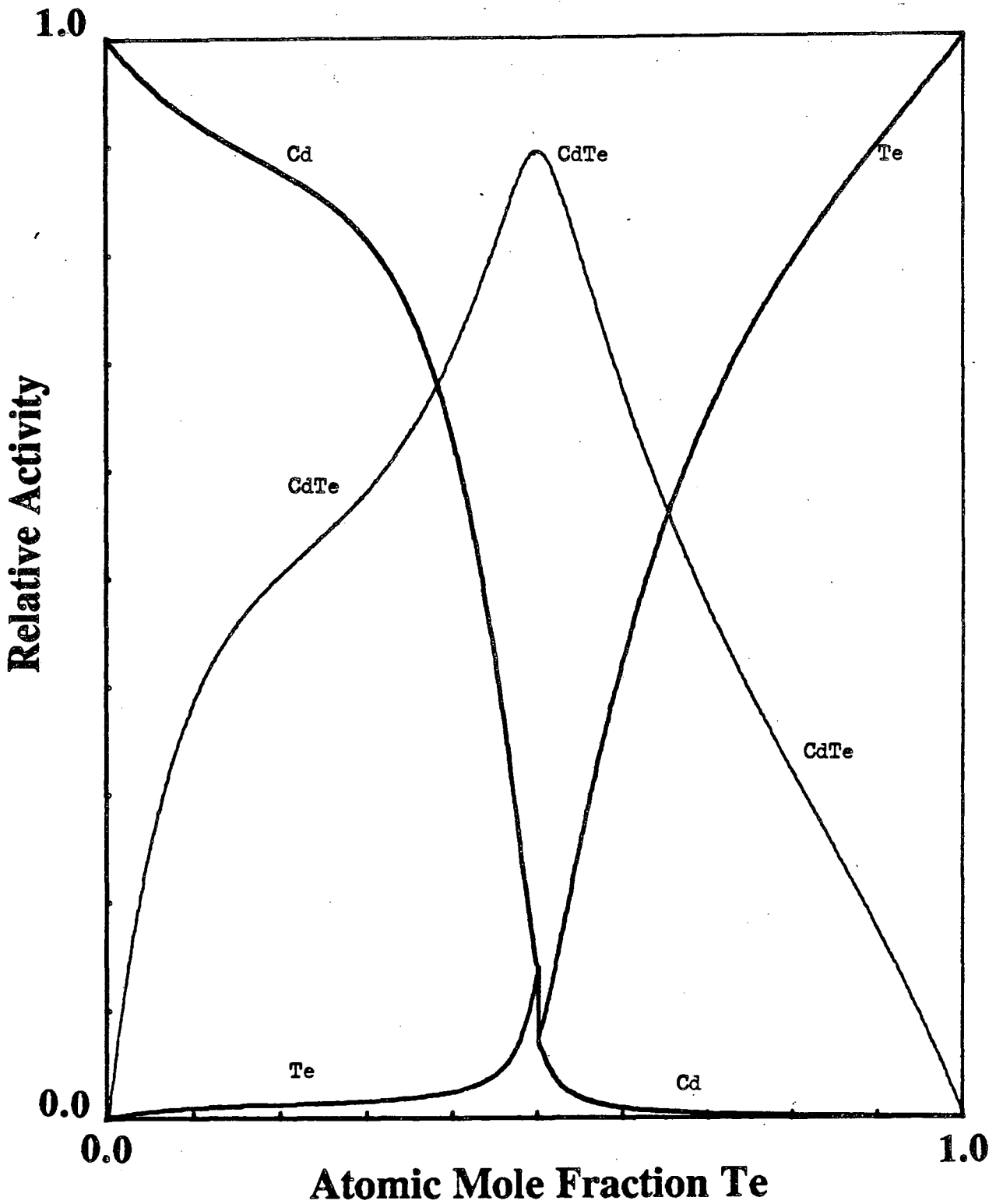

Figure 3-14. Behavior of the RAS model. Equations [3-17] - [3-19] were used to obtain the relative activities a_{Cd}, a_{Te}, and a_{CdTe}. Using Jordan's data at 1400 K, $\beta_{act} = 0.055$, $\alpha = -3.1$ kcal/mol for $x_{Te} < 0.5$, and $\alpha = -10.9$ kcal/mol for $x_{Te} > 0.5$.

Chapter 2.

The *liquid-electrodeposit interface* section and the *electrodeposit* section of this work provide boundary-condition information for the mass-transport problem. In these two sections, there are 10 unknowns: i_{ii}, i_{iii}, i_{iv}, i_v, V, E, a_{Cd}, a_{Te}, x_{Cd}, and x_{Te}. These are balanced by the following 10, independent equations: [3-10], [3-11], [3-12], [3-13], [3-14], [3-15], [3-17], [3-18], [3-21], and [3-22]. The computer program used to solve this system of equations and optimize the appropriate physicochemical parameters is presented in Appendix 3. In the next section of this treatment, we will analyze the CdTe periodic electrodeposition process with model and experimental results.

Results of Proposed Model

The current source used in the theoretical calculations and experimental work is shown in Fig. 3-15. The maximum pulse-current is $1.23 \times i_{lim,HTeO_2^+}$. As previously discussed, $\frac{3}{2} \times i_{lim,HTeO_2^+}$ yields nearly 1:1 CdTe. For the 30 $\frac{A}{m^2}$ (3 $\frac{mA}{cm^2}$) maximum cathodic current source used in this study, we would expect the Te atomic mole fraction to be greater than 0.5. The input parameters to the experimental program are listed in Table 3-3. In the following discussion, we will analyze the base-case behavior and explain how the input kinetic constants and β_{act} were chosen. In Fig. 3-16, a plot of the ionic surface concentrations is shown. A surface-concentration plot is not shown for Te^{2-} since reaction v of Table 3-1 did not take place under these conditions, although the rate constants for this reaction were set to high values. Te^{2-} did not form for two reasons. First, Te is attracted to

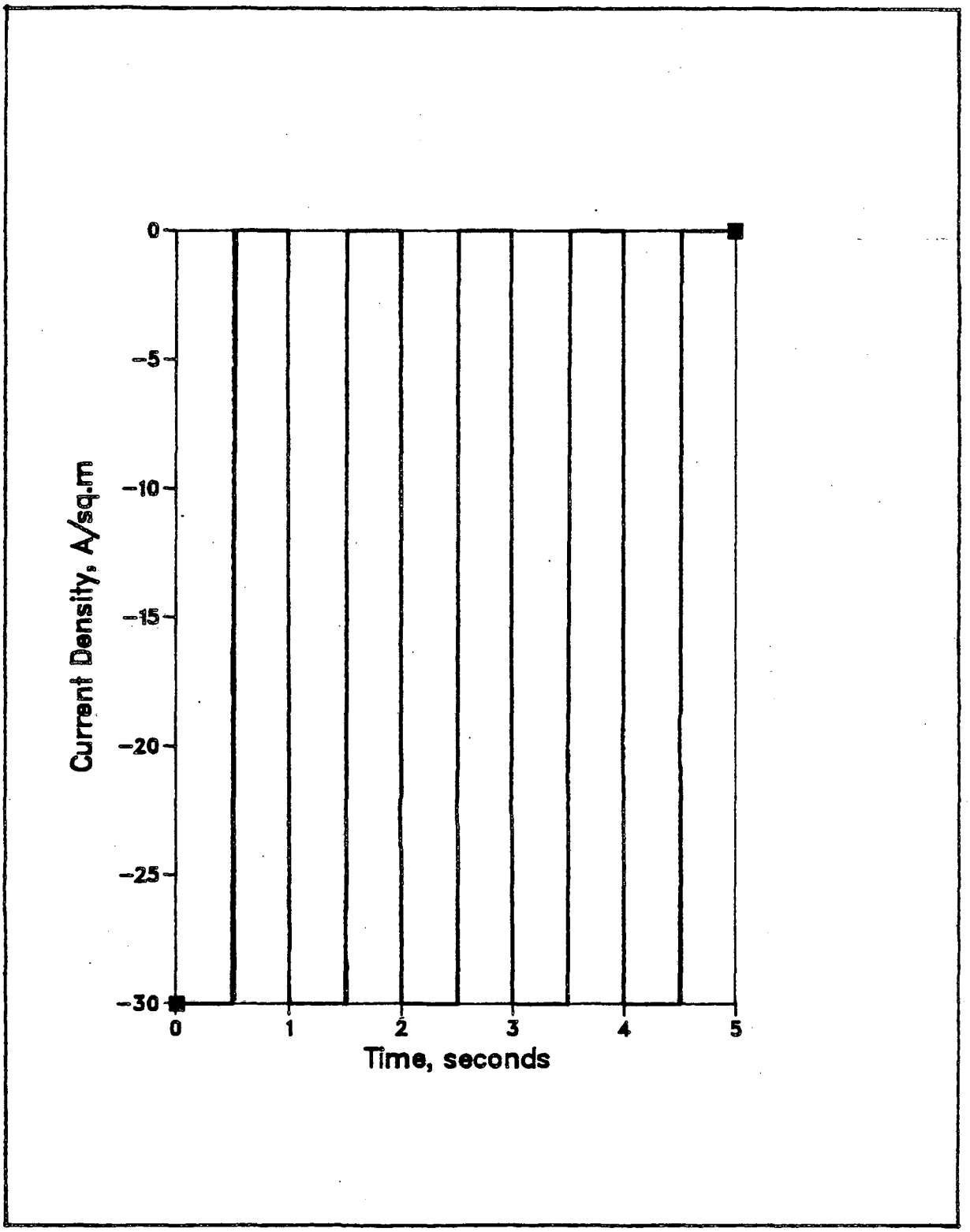

Figure 3-15. Base-case cell-current density.

Table 3-3. Input Parameters. †

Quantity					Units
c_i^b	1.0×10^{-6}	3.0×10^{-4}	1.0×10^{-4}	0.0	$\frac{mol}{cm^3}$
D_i	9.4×10^{-6}	9.3×10^{-5}	3.6×10^{-6}	9.3×10^{-5}	$\frac{cm^2}{s}$
$k_{a,l}$	3.4×10^{-42}	5.0×10^{-12}	7.8×10^{5}	∞	‡
$k_{c,l}$	6.7×10^{-5}	5.0×10^{-12}	1.8×10^{-8}	∞	‡
n_i	4	1	2	2	---
r	0				$\Omega - cm^2$
RSAT	10				Å
α	-1.7×10^{5}				$\frac{J}{mol}$
β_{act}	6.4×10^{-5}				---
β_i	0.26	0.50	0.20		---
δ_i	0.0058	0.0034	0.0011	0.0034	cm
ρ_o	0.0010				$\frac{kg}{cm^3}$
$\hat{\rho}_i$	0.049 (Te)	0.077 (Cd)	0.0025 (CdTe)		$\frac{mol}{cm^3}$

† Optimized results were used for $k_{a,l}$, $k_{c,l}$, α, β_{act}, and β_l. For species entries, denoted by subscript i on the variable quantity, $HTeO_2^+$ is at the far left, followed by H^+, Cd^{2+}, and Te^{2-}, respectively, unless otherwise stated. For reaction entries, denoted by subscript l on the variable quantity, reaction *ii* is at the far left, followed by *iii*, *iv*, and *v*, respectively.

‡ The rate-constant units are reaction dependent. For anodic rate constants, the units are: $mol/[cm^2 - s - \prod_i (\text{anodic reactant concentration units})^{s_i}]$. For cathodic rate constants, the exponent s_i is replaced by $-s_i$.

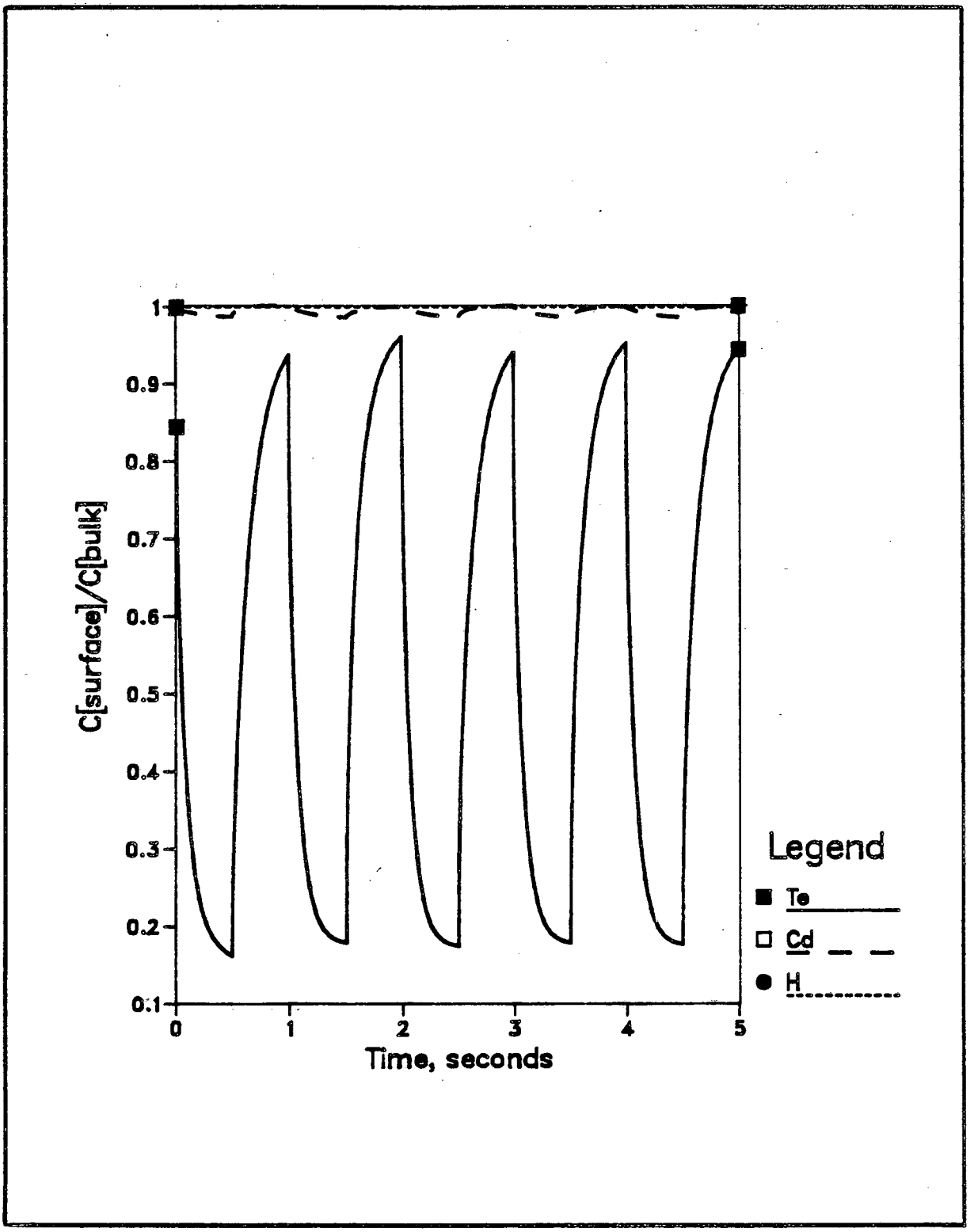

Figure 3-16. Base-case, dimensionless, ionic surface concentrations.

Cd and CdTe in the deposit, thus Te has a supressed deposit activity and the cathodic term in Eq. [3-13] is strongly reduced. Secondly, the electrode potential required to deposit CdTe is significantly more anodic than the -0.92 volts standard electrode potential of reaction *v*. It should be noted that reaction *v* cannot be arbitrarily dropped from the analysis *a priori*. It is commonly observed in the electrodeposition of pure Te (unit deposit activity) that Te^{2-} is formed prior to hydrogen evolution. (34-37) In addition, more cathodic potentials result if larger cathodic currents are used; this could done to create a deposit with higher Cd content. As can be seen in Table 3-3, the bulk concentration of $HTeO_2^+$ is much lower than that of Cd^{2+} or H^+. The $HTeO_2^+$ concentration reaches a low value near the end of the first on-time, where $\frac{c^{surf}_{HTeO_2^+}}{c^{b}_{HTeO_2^+}} = 0.16$ and $t = 0.5$ s. During the following off-time, diffusion and convection resupply the electrode surface with $HTeO_2^+$ ions from the bulk electrolyte, and the concentration of $HTeO_2^+$ increases until the beginning of the next on-time. This process is repeated over the subsequent cycles. The Cd^{2+} and H^+ species incur very little mass-transport resistance, and their surface concentrations do not differ much from their bulk concentrations under these conditions.

The partial current densities for reaction *ii*, *iii*, and *iv* are given in Fig. 3-17. At the beginning of the on-time (0 seconds for the first cycle) reaction *ii* supplies most of the current and the $HTeO_2^+$ surface concentration is reduced. As the $HTeO_2^+$ ion becomes mass-transfer limited, reaction *iv* increases in rate and more Cd is deposited. During the off-time, Cd dissolves and Te continues to electrodeposit. For these conditions, there is very little hydrogen evolution. The electrodeposition process takes about 5 cycles to

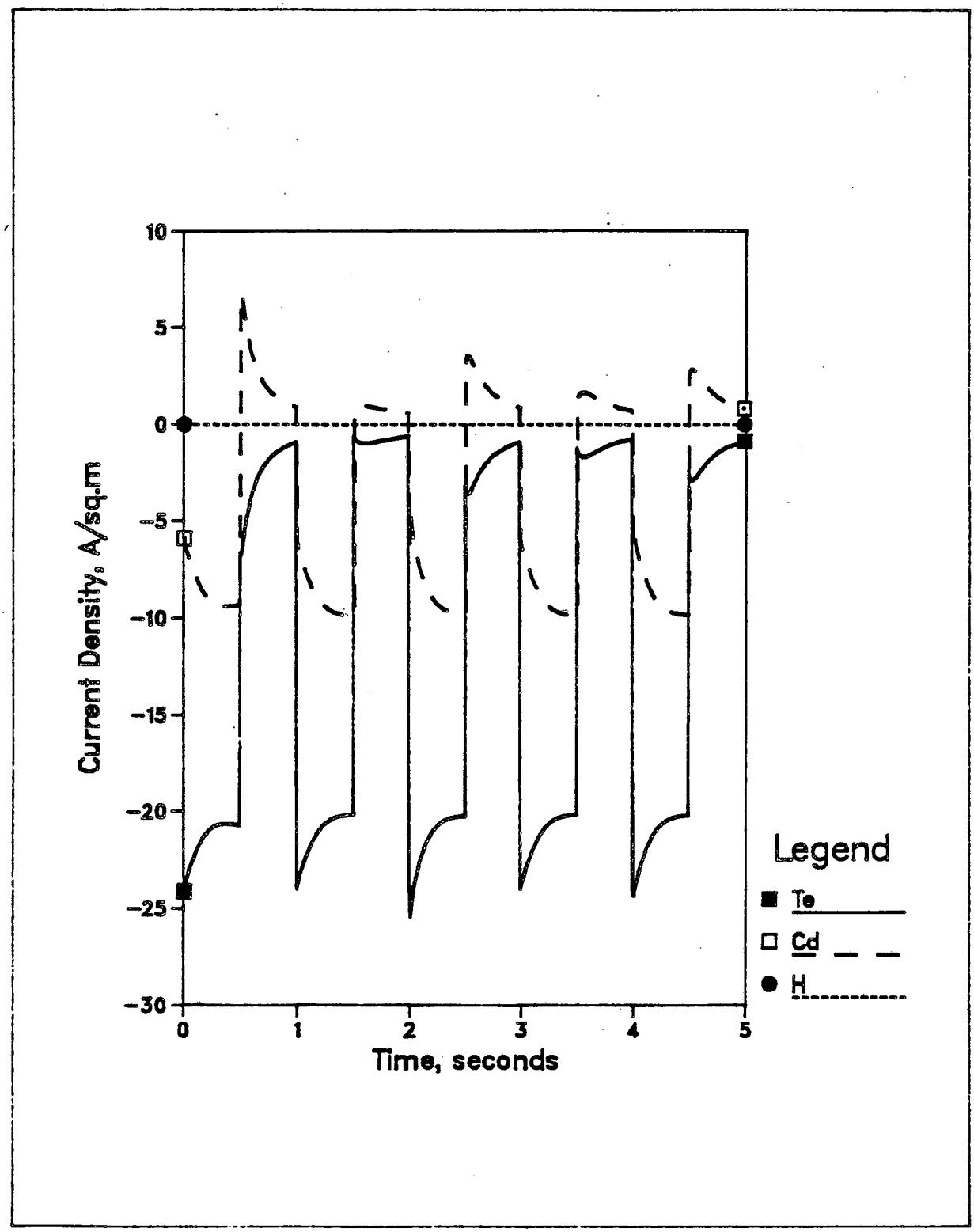

Figure 3-17. Base-case, partial current densities. Under these conditions, reaction ν does not take place.

reach a uniform and sustained periodic state, both experimentally and theoretically. About 1.5 *RSAT* are deposited per cycle. It is the electrodeposit's influence that prolongs the approach to steady state; the surface-concentration profiles reach a periodic state prior to the fifth cycle, as seen in Fig. 3-16. The partial current densities during a particular cycle are dependent on the *RSAT* concentration formed during the previous cycle. It is because of this dependence on the previous cycle that the system oscillates about the uniform periodic state until the fifth cycle.

In Fig. 3-18, the electrodeposit mole fractions are presented for the base conditions. The mole fractions are related to the atomic mole fraction by the following equations:

$$x_{Te} = \frac{\mathcal{X}_{Te} - \mathcal{X}_{Cd} + P}{1 + P} \qquad [3\text{-}22]$$

$$x_{Cd} = \frac{\mathcal{X}_{Cd} - \mathcal{X}_{Te} + P}{1 + P} \qquad [3\text{-}23]$$

$$x_{CdTe} = \frac{1 - P}{1 + P} \qquad [3\text{-}24]$$

As expected, due to the Gibbs free energy of formation of CdTe being large and negative, very little free Cd exists for $\mathcal{X}_{Cd} < 0.5$. Most of the Cd is present in the CdTe. It can also be seen that during the off-times, the free Te present in the deposit increases. During the off-times, Cd dissolves, and free Te is released into the electrodeposit, which increases the Te mole fraction.

The experimental and calculated electrode potential behavior is presented in Figs. 3-19 and 3-20 for the fifth cycle, after the system has reached a periodic state. To construct the theoretical curve in Fig. 3-19 (labeled INITIAL), the measured rate parameters ($k_{a,l}$, $k_{c,l}$, and, β_{act}) for the Te deposition, Cd deposition, and H_2 evolution were used. In an attempt to

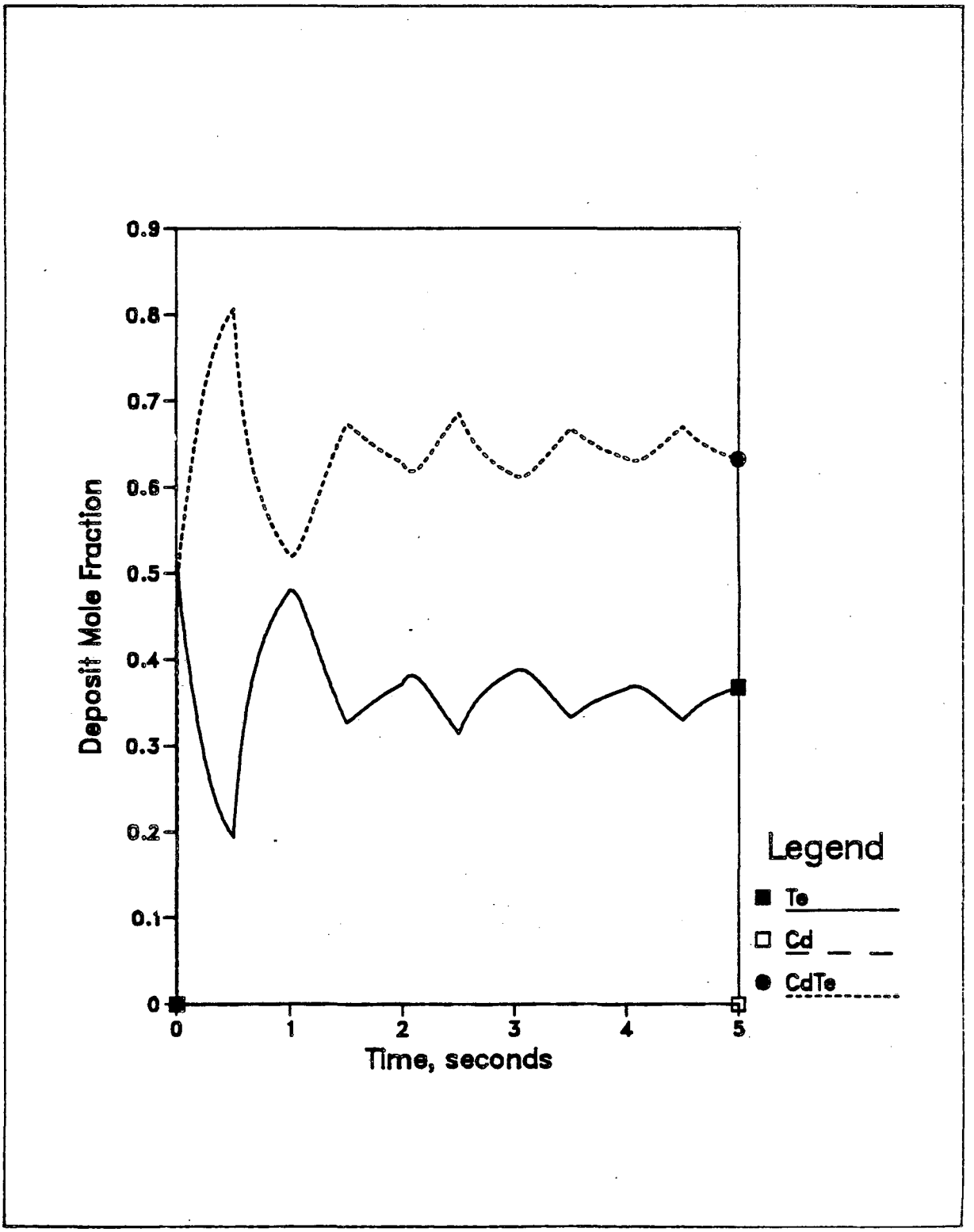

Figure 3-18. Base-case, integrated deposit mole fractions.

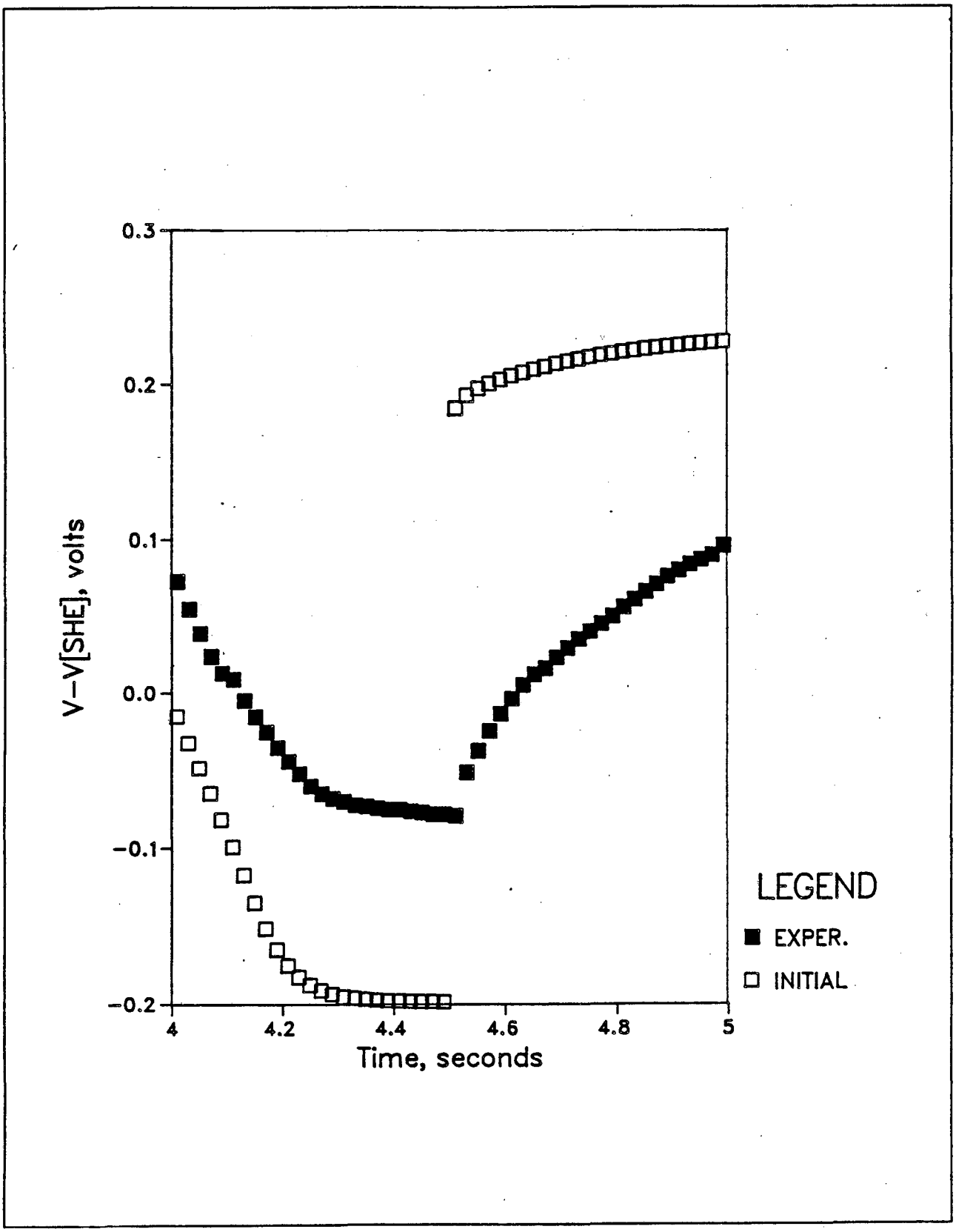

Figure 3-19. Electrode potential for the deposition process. No adjustable parameters were used to construct the theoretical curve labeled INITIAL.

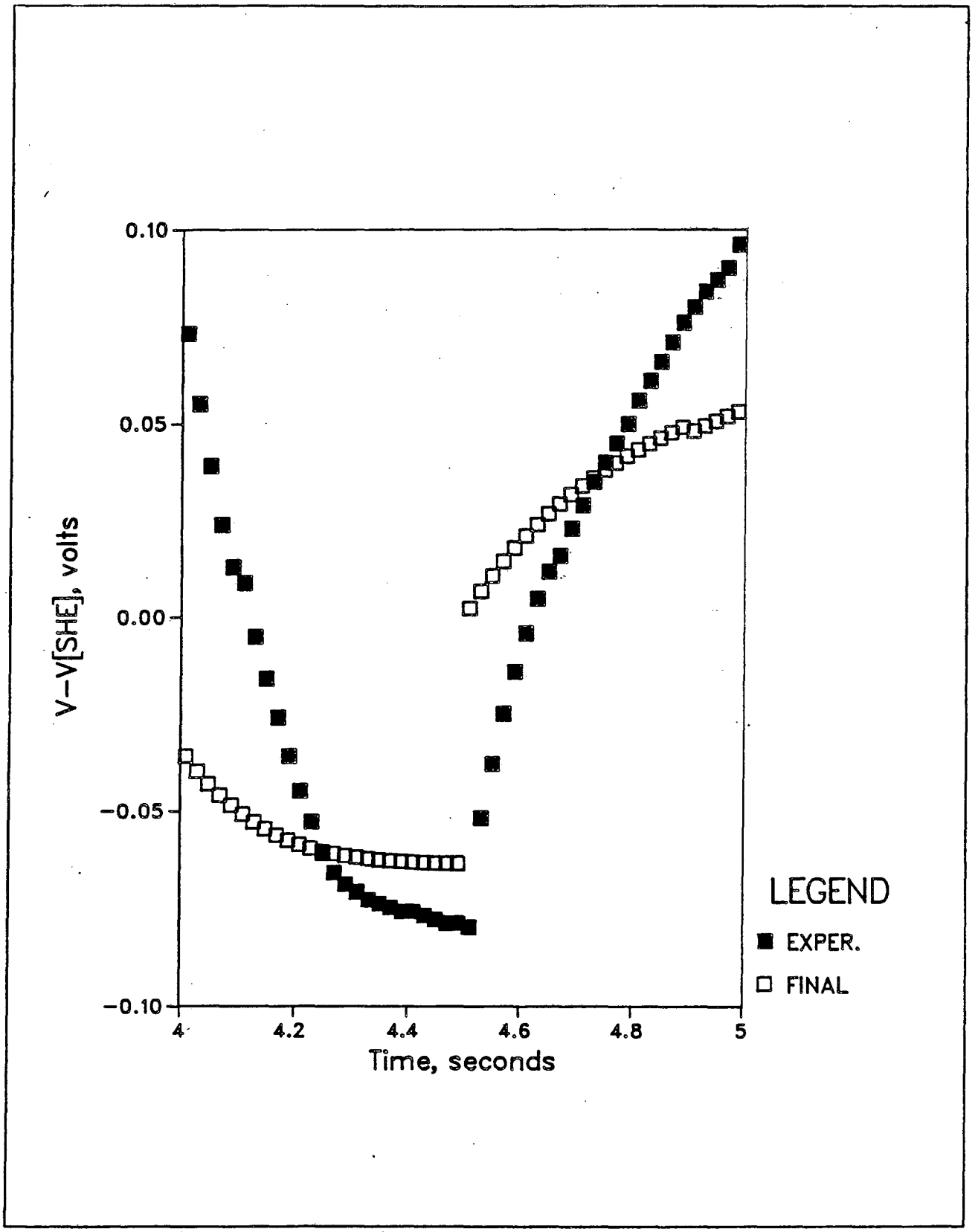

Figure 3-20. Electrode potential for the deposition process. The ordinate is different from Fig. 3-19. An optimization routine was used to fit $k_{c,1}$, β_l, β_{act}.

force reaction v to take place with the current source specified in Fig. 3-15, $D_{Te^{2-}}$ was set to a high value, and the rate constants for reaction v were also set to a high value; the ratio of the rate constants is fixed by the standard electrode potential. To represent better the experimental curve, a multidimensional optimization routine was used to minimize the difference between the calculated and experimental potential response. The optimization routine is discussed in Chapter 4, and the computer program used to calculate the optimized curve, labeled FINAL in Fig. 3-20, is given in Appendix 3. The optimization routine was not sensitive to the kinetic parameters for H_2 evolution or Te dissolution to produce Te^{2-}; these parameters remained unchanged. β_{act} was set equal to 0.055 to construct the INITIAL curve in Fig. 3-19, as this was the value Jordan used in his high temperature experiments. The optimization routine changed this parameter more than any other. The final values of the optimized parameters are listed in Table 3-3. The shape of the INITIAL curve in Fig. 3-19 resembles the experimental curve. After the optimization routine operates on the model, the resultant FINAL curve in Fig. 3-20 is displaced closer to the experimental curve. It should be noted that the ordinate is different in Figs. 3-19 and 3-20. The proposed fit solution in Fig. 3-20 does not represent an entirely satisfactory result, although the theoretical solution does remain in a potential region near the experimental curve. A sensitivity analysis of the optimized parameters is addressed in the following text in order to gain insight into the model's behavior.

The effect of changes in the Te deposition kinetics is depicted in Figs. 3-21 and 3-22. If the rate constants $k_{a,ii}$ and $k_{c,ii}$ are set larger by an order of magnitude, or a larger symmetry factor, more Te is incorporated into the electrodeposit. The periodic state is reached more quickly since Cd

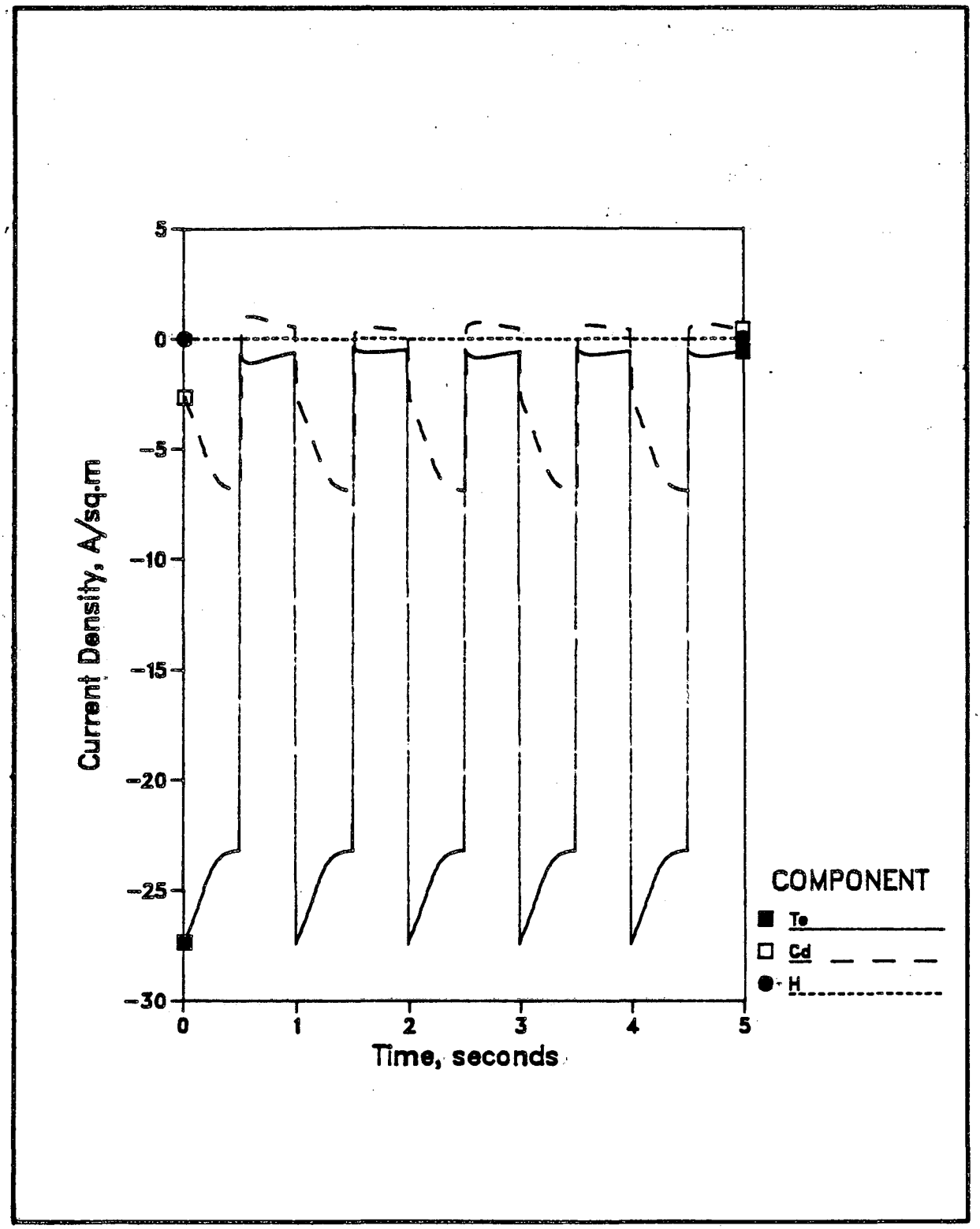

Figure 3-21. Parametric analysis: tellurium-deposition rate constants. $k_{a,ii}$, and $k_{c,ii}$ are increased by an order of magnitude relative to the base conditions.

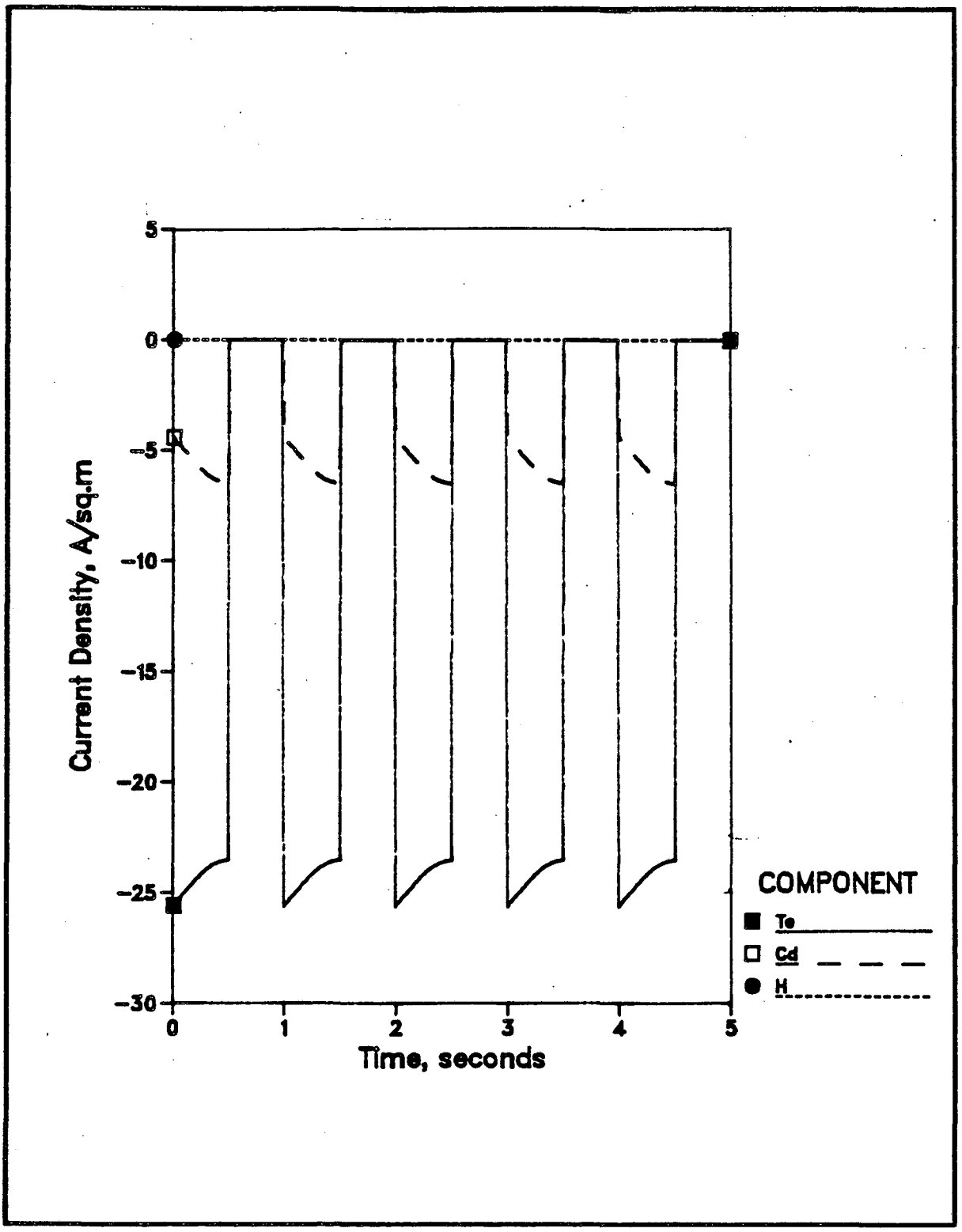

Figure 3-22. Parametric analysis: tellurium-deposition symmetry factor β_{ti} increased to 0.74 from 0.16 for the base conditions.

dissolution from the lower Cd-content deposit is supressed during the off-time. A uniform and sustained periodic state is reached by the third cycle in each case.

If the Cd kinetic constants are reduced by an order of magnitude, the system reaches a steady state after about 2 cycles, as seen in Fig. 3-23, for the same reasons as just discussed. Because the system is more sensitive to the Cd-electrodeposition kinetics, a steady state is reached more quickly in Fig. 3-23 than in Figs. 3-21 and 3-22. The system is less sensitive to Te-electrodeposition kinetics, reaction *ii*, because the major obstacle to Te deposition is the $HTeO_2^+$-mass-transfer resistance.

If the hydrogen rate constants are increased by four orders of magnitude, the partial current densities during the deposition process are represented by Fig. 3-24. For this case, H_2 is evolved during the on-time, slightly reducing the Te and Cd deposition rates, relative to the base-case deposition rates. During the off-time, the low concentration of soluble H_2 is oxidized to H^+, and at the end of the off-time both Cd and Te electrodeposit, in contrast to any of the previous results.

If β_{act} is increased by an order of magnitude, increasing the dissociation of CdTe, the electrodeposit composition history in Fig. 3-25 results. Comparing Fig. 3-25 with the base-case deposit-mole-fraction plot in Fig. 3-18, we can see that a higher concentration of free Te results with the increased CdTe dissociation.

The mole-fraction plot in Fig. 3-26 shows that if the base-case physicochemical parameters are used, the CdTe content in the electrodeposit can be increased by specifying an on-time to off-time ratio of 3:1 for the cell-current source, instead of the 1:1 ratio used in the base conditions.

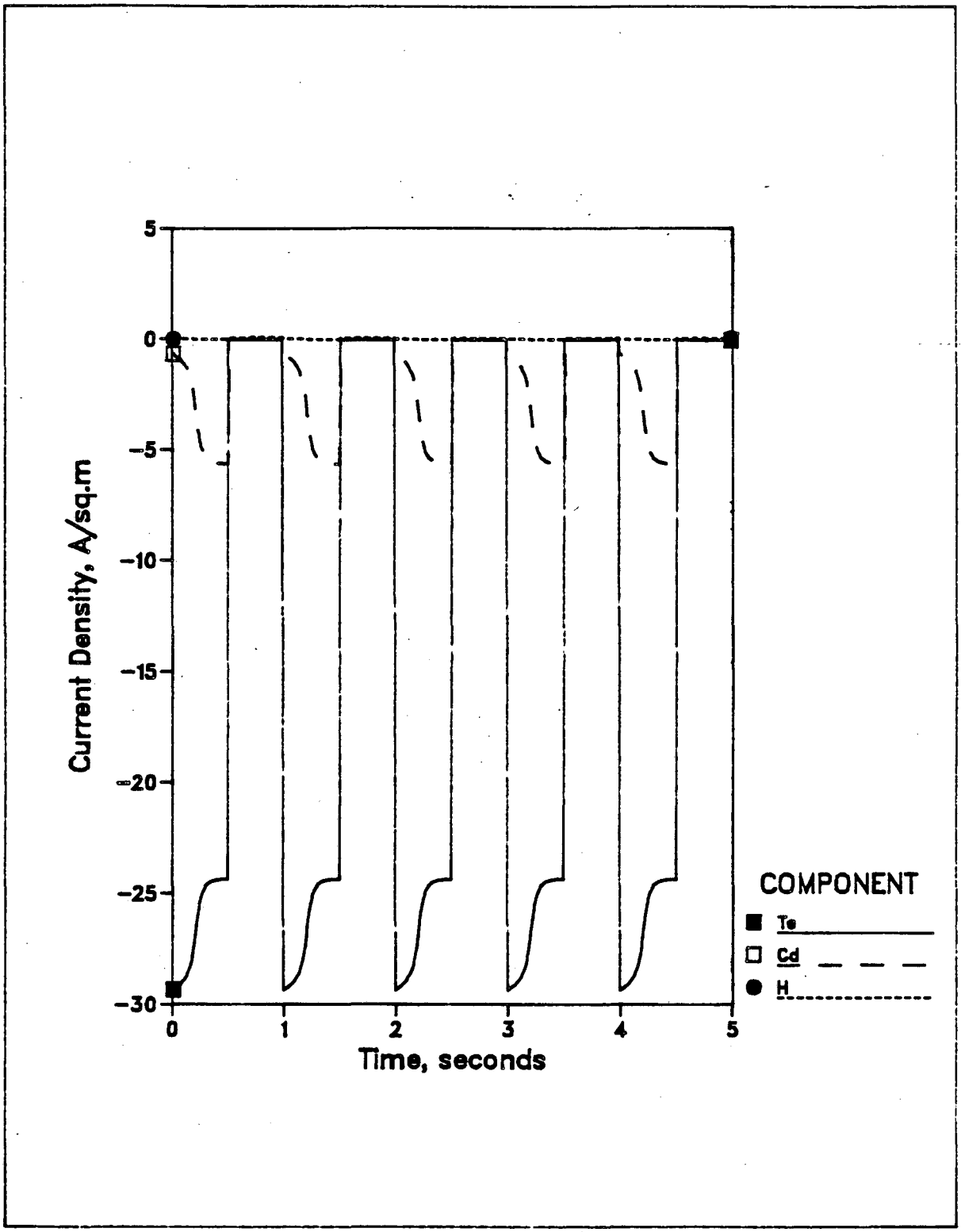

Figure 3-23. Parametric analysis: cadmium-deposition rate constants $k_{a,iv}$ and $k_{c,iv}$ decreased by an order of magnitude relative to the base conditions.

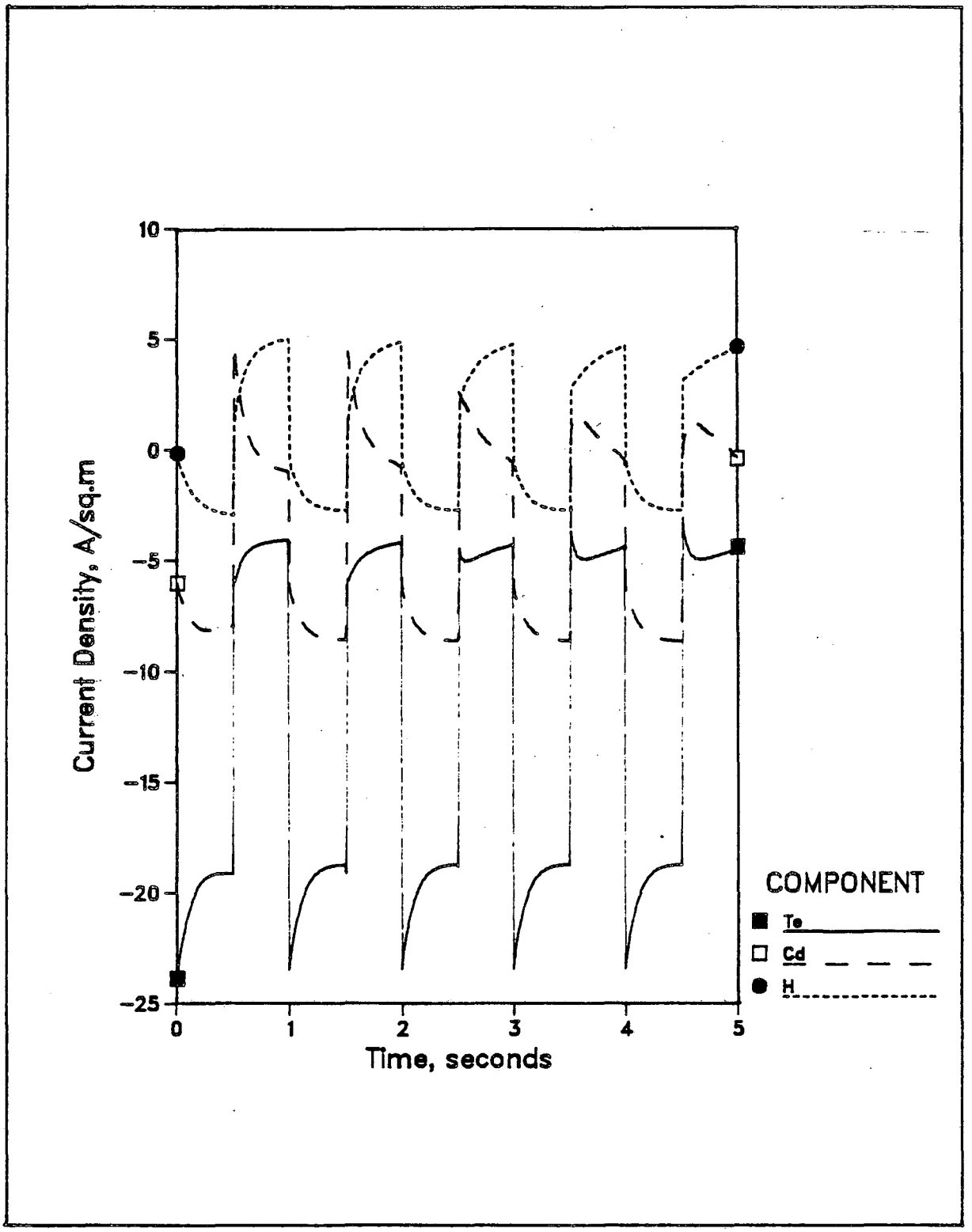

Figure 3-24. Parametric analysis: hydrogen-evolution rate constants $k_{a,iii}$ and $k_{c,iii}$ increased by an order of magnitude relative to the base conditions.

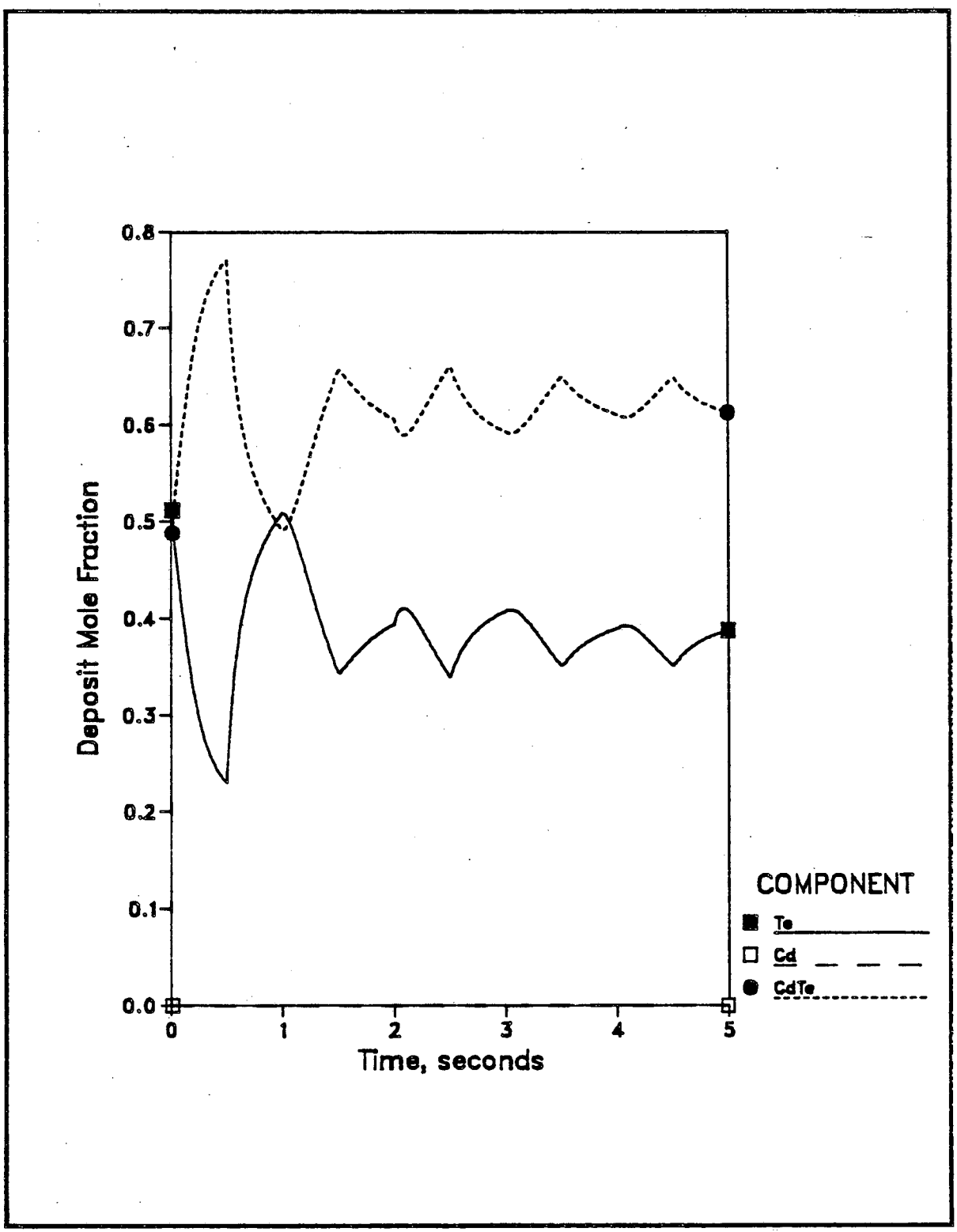

Figure 3-25. Parametric analysis: solid-state dissociation factor β_{act} increased by an order of magnitude relative to the base conditions.

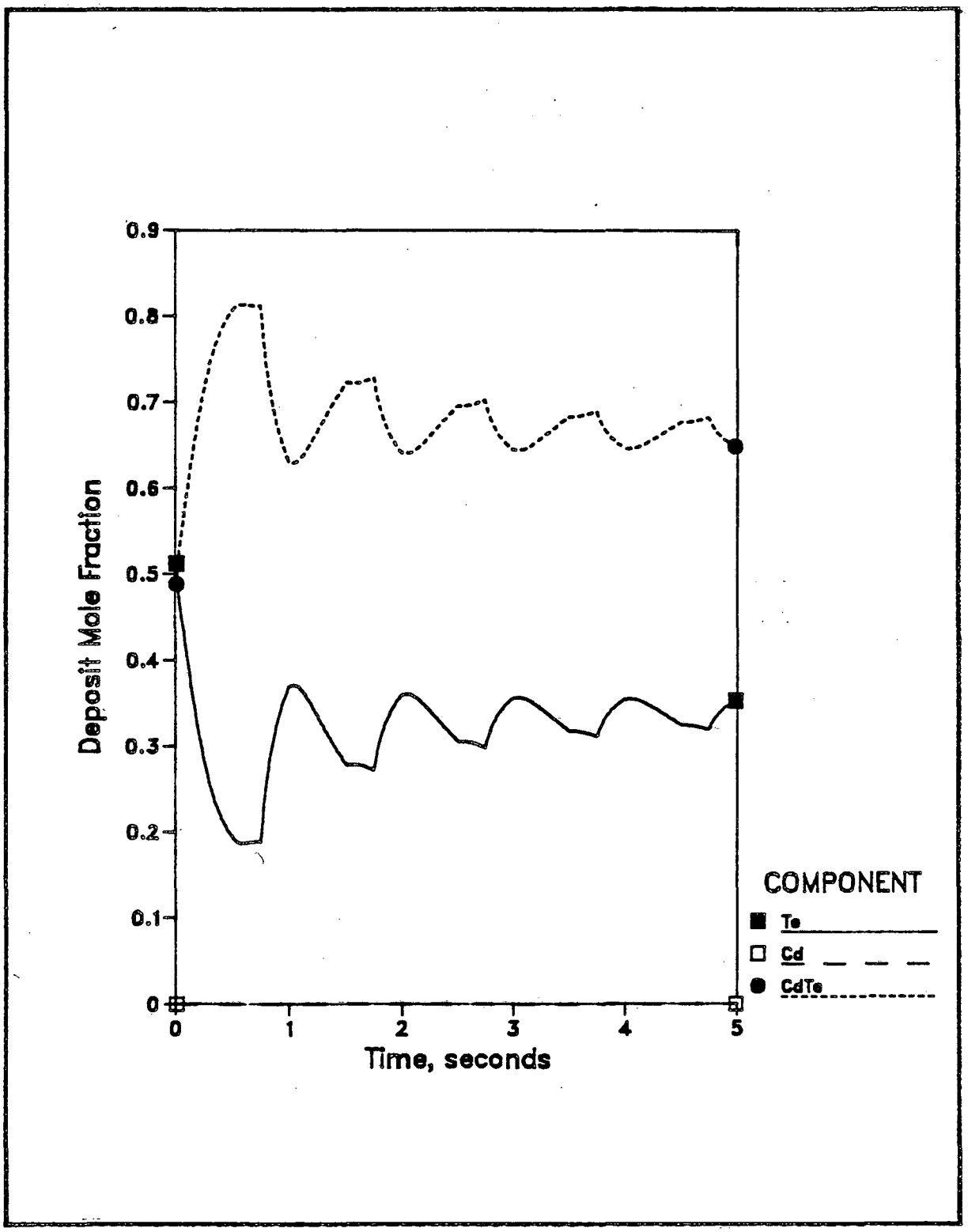

Figure 3-26. Parametric analysis: on-time to off-time ratio for the cell-current density set to 3:1.

Since the $HTeO_2^+$ species is mass-transfer limited during the majority of the on-time, the Cd^{2+} rate of reaction increases throughout the on-time (*eg.* Fig. 3-17). During the extra on-time in the 3:1 mode of operation, more Cd is deposited, which combines with the free Te in the electrodeposit to form CdTe. More cathodic potentials result in the 3:1 mode of operation, and some hydrogen evolution occurs during the last part of the on-time. The CdTe content in the electrodeposit can also be increased by increasing the maximum current during the on-time. The partial currents for a maximum cathodic current density equal to twice that of the base conditions is shown in Fig. 3-27. In this mode of operation, the $HTeO_2^+$ species quickly becomes mass-transfer limited, and the rate of Cd deposition increases during the on-time. With the added amount of Cd in the electrodeposit, a larger Cd corrosion current is observed during the off-time. It can also be seen that H_2 begins to evolve during the on-time. The system reaches a uniform and sustained periodic state after the second cycle since about 3 *RSAT* are deposited during the on-time, the system being nearly driven to a steady state by the end of each on-time.

In this section, a mathematical model has been presented that, when combined with experimentally obtained polarization curves, can aide in the investigation of the periodic electrodeposition of CdTe. The next section of this work will deal with experimental observations useful in the study of the CdTe electrodeposition process and of the deposited material.

Characterization of CdTe Electrodeposits

In this section, we address the atomic composition, phase structure, surface morphology, and photovoltaic properties of CdTe electrodeposits. An

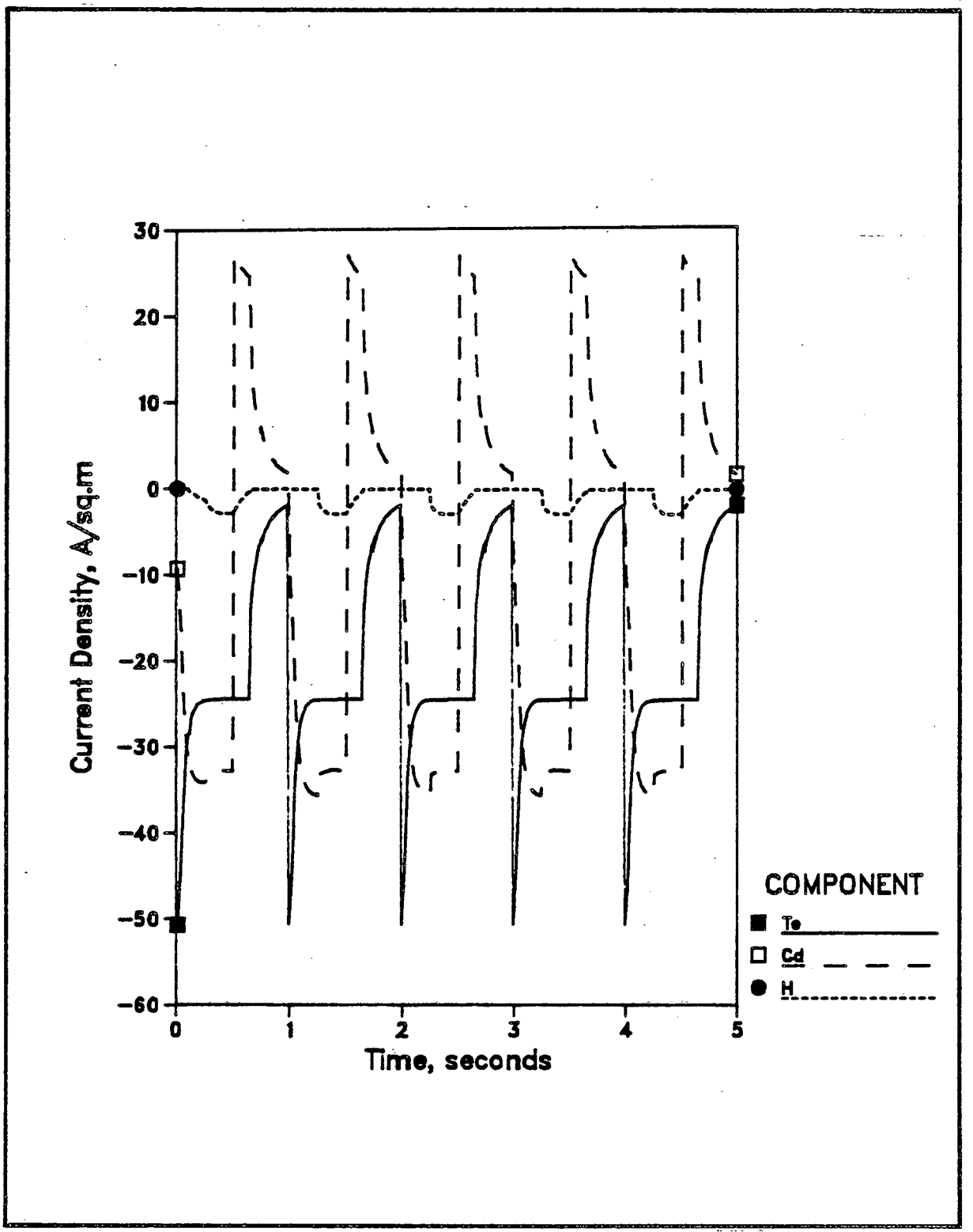

Figure 3-27. Parametric analysis: maximum, cathodic pulse-current density twice that of the base condition.

x-ray analyzer was used to evaluate atomic compositions, and an x-ray diffractometer was employeed to elucidate deposit phase structure. Scanning electron microscopy provided surface morphology information. The photovoltaic properties of the CdTe deposit were investigated by means of steady state and transient photoresponse experiments.

For the model and experimental work presented in the previous section, the electrolyte temperature was 25°C. For the study of CdTe electrodeposited at 25°C, the experiments outlined in Fig. 3-28 were implemented. A cyclic, triangular current source with a minimum cathodic current density of 0 and a maximum cathodic current density of 5.1 $\frac{mA}{cm^2}$ is shown in the upper plot of Fig. 3-28. In the lower illustration of Fig. 3-28, the potential response is given for varying illumination intensities. The deposits were illuminated with a 150 watt, tungsten-halogen, fiber-optic light source (Dolan-Jenner Industries, Inc., Model 510 Fiber-Lite). The potential response labeled dark is obtained for no illumination of the deposit during the electrodeposition process. The two other potential response curves correspond to low illumination intensity and high illumination intensity incident to the forming electrodeposit. It can be seen that the light sources, which generate minority carriers (electrons) in the p-semiconductor, displace the electrode potential to more positive values around the peak cathodic current density. Near zero current, the deposit surface is mostly metallic tellurium, and no longer a semiconductor. It is apparent in Fig. 3-28, however, that the open-circuit potential (at 300, 600, and 900 s) is a function of the illumination intensity. This is due to the different deposit compositions, which have been altered by the light source during the deposition process. For higher illumination intensities, more cadmium is incorporated into the electrodeposit

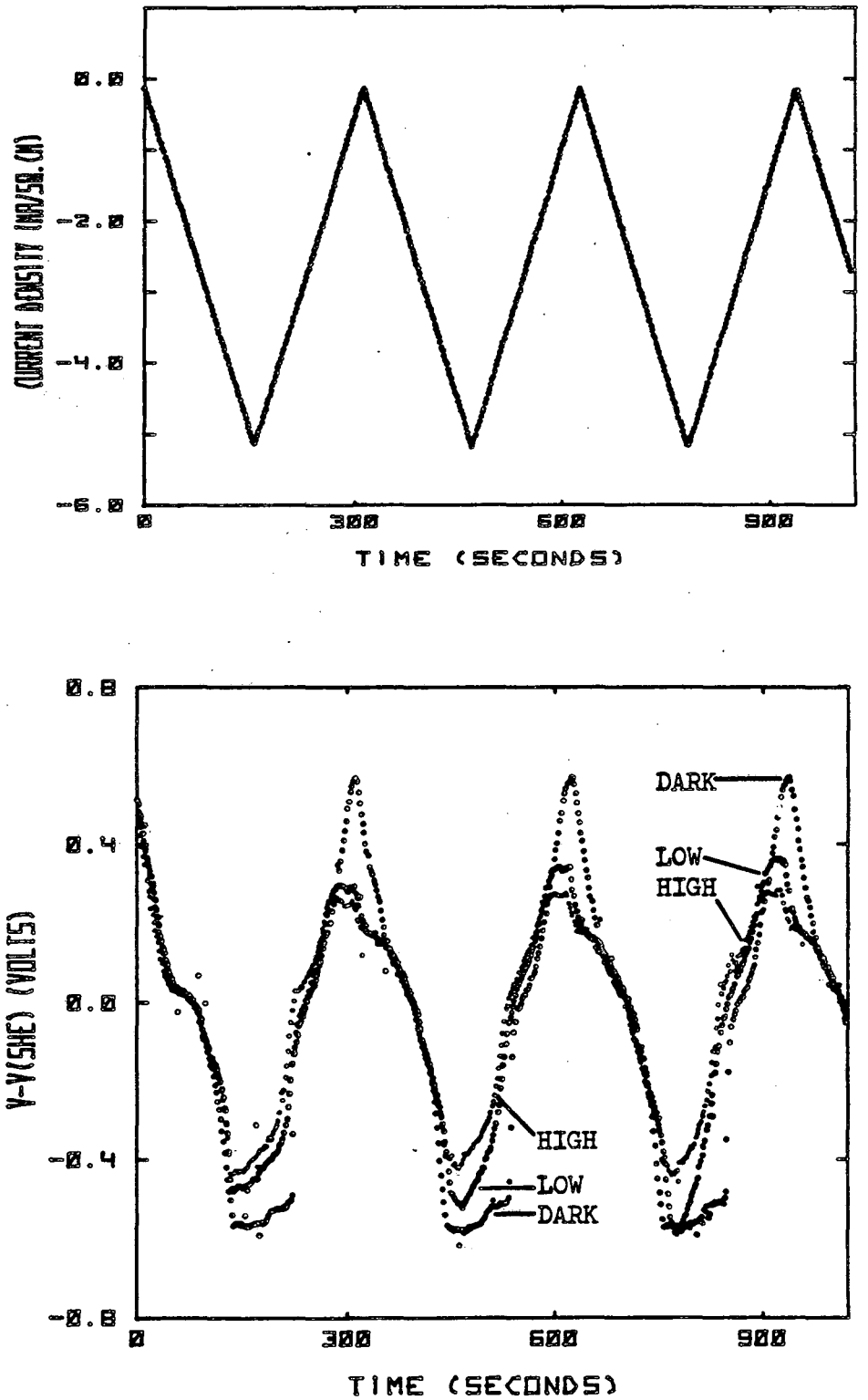

Figure 3-28. Photoresponse of electrodepositing cadmium-telluride material. Upper plot: cell-current density. Lower plot: potential response for varying illumination intensities. The illumination intensities (DARK, LOW, HIGH) are indicated for each curve.

and a more cathodic potential is observed at zero current.

The preceding analysis is supported by the results displayed in Figs. 3-29, 3-30, and 3-31. The experiments outlined in Fig. 3-28 were conducted with an additional variation: the fiber-optic light source was chopped to create a pulse-light source of low duty cycle; the on-time to off-time ratio was near 0.1. For no illumination, the potential response in Fig. 3-29 was recorded, which is identical to the dark-current potential response in Fig. 3-28. For the low intensity, pulse-light source, the potential response of Fig. 3-30 resulted. The high intensity, pulse-light source was used to obtain the potential response displayed in Fig. 3-31. Two key conclusions can be formulated from the analysis of Figs. 3-29, 3-30, and 3-31. First, the pulse-light source of low duty cycle can be used to obtain *in situ* the photoresponse of the forming electrodeposit. During the off-time, a potential response curve similar in form to the nonilluminated potential response in Fig. 3-29 is obtained for both the low and high light-source potential traces in Figs. 3-30 and 3-31. During the on-time, a second potential response curve is obtained within the off-time traces in Figs. 3-30 and 3-31. The difference between the on-time and off-time traces represents the *in situ* photoresponse of the electrodepositing material. Careful comparison of the digitally obtained potential data shows that the high light source data in Fig. 3-31 are displaced to slightly more anodic potentials during the pulse on-time. The second conclusion to be drawn in the analysis of Figs. 3-29, 3-30, and 3-31 concerns the open-circuit behavior of the electrochemical system. Comparison of Figs. 3-29, 3-30, and 3-31 shows that nearly identical open-circuit potentials are obtained for all three experiments, in contrast to the results for the constant-intensity light-source experiments displayed in Fig. 3-28. Because

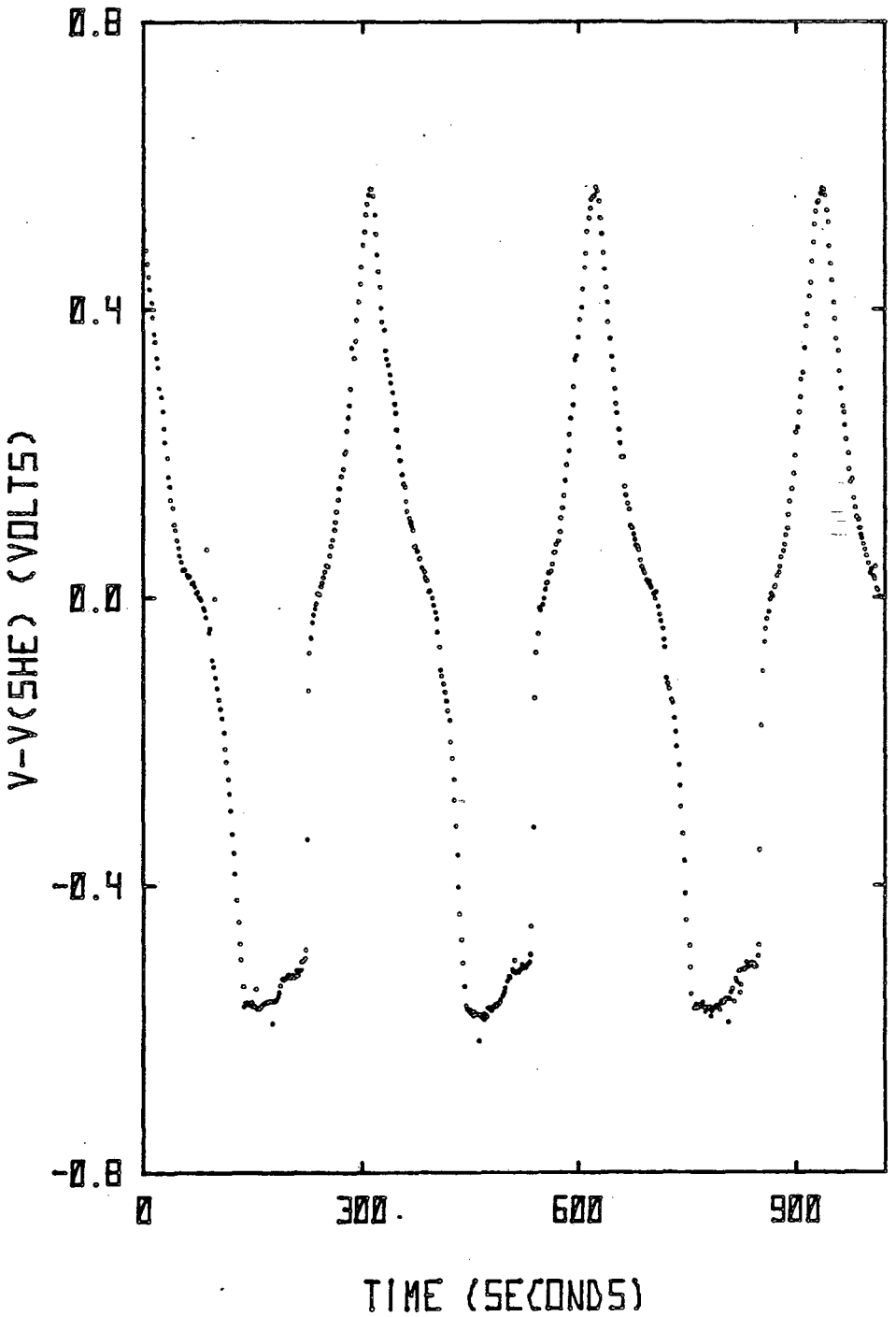

Figure 3-29. Potential response for the current source given in Fig. 3-28 and no light source.

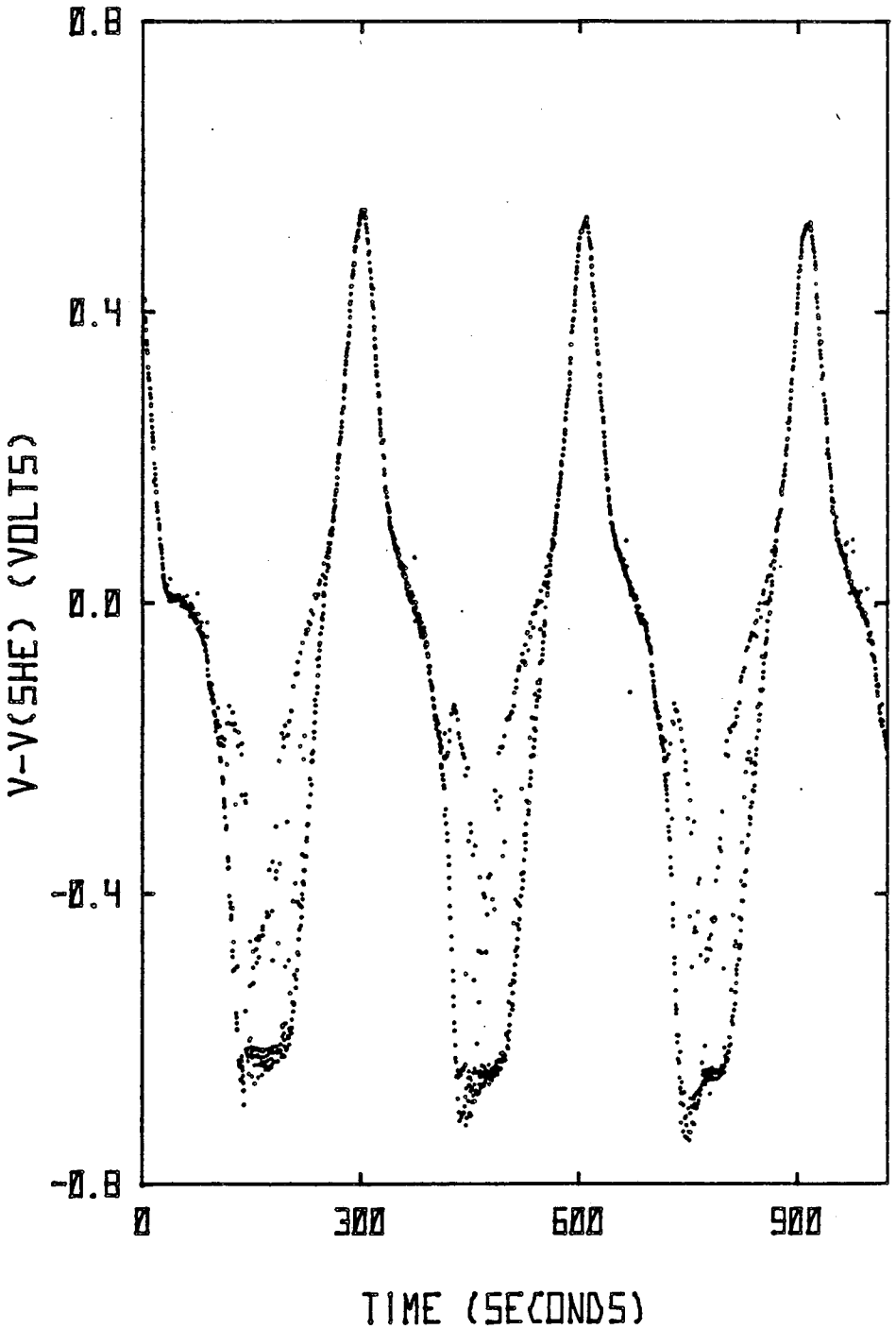

Figure 3-30. Potential response for the current source given in Fig. 3-28. A low intensity, pulse-light source with a 0.1 duty cycle periodically illuminated the electrodepositing cadmium-tellurium material.

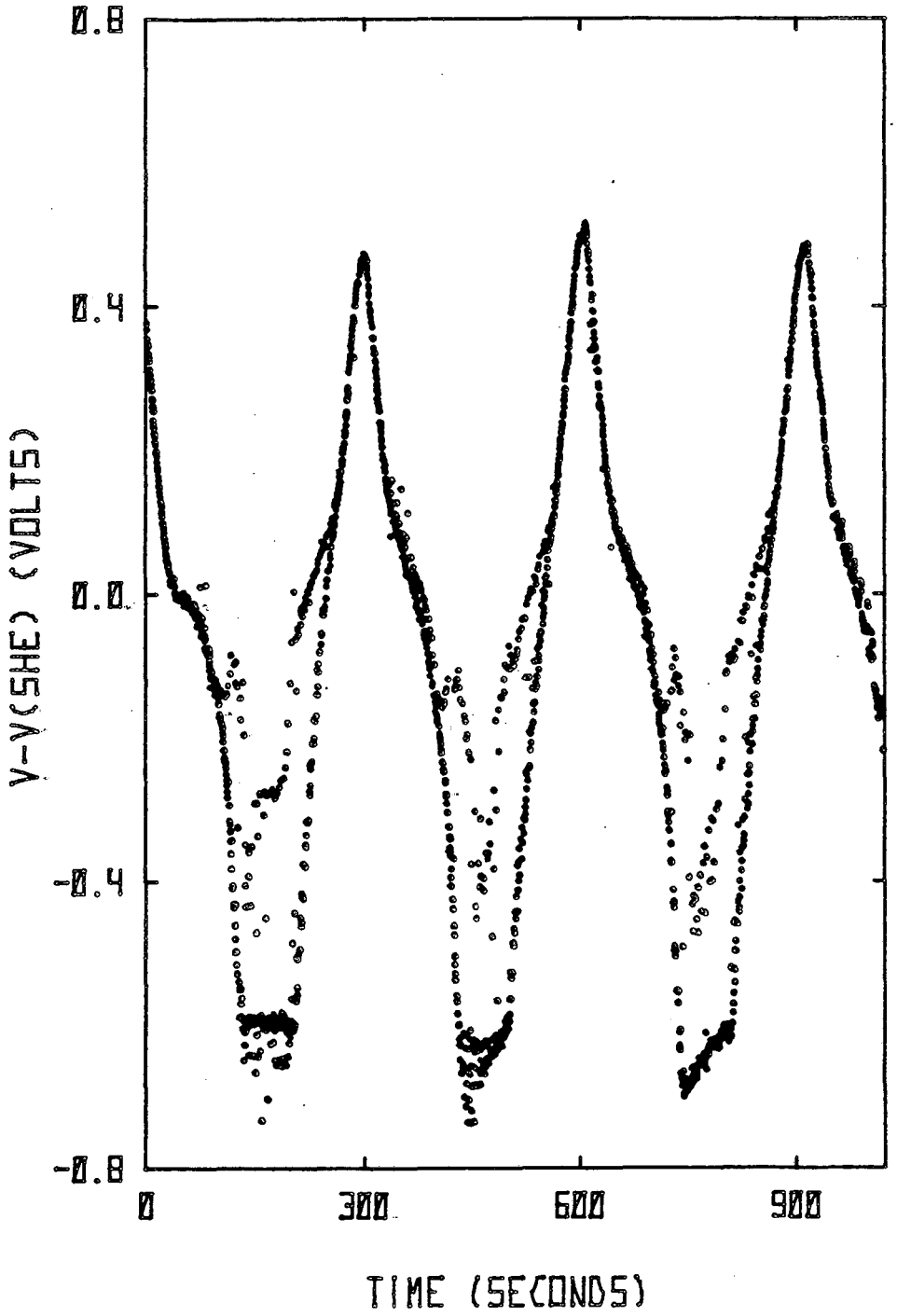

Figure 3-31. Potential response for the current source given in Fig. 3-28. A high intensity, pulse-light source with a 0.1 duty cycle periodically illuminated the electrodepositing cadmium-tellurium material.

the integrated amount of light striking the deposit is very small for the pulse-light source of low duty cycle, the electrodeposit composition is virtually unchanged by the light source, and the electrodeposits are of identical composition at open-circuit. The electrodeposit surface is no longer semiconducting or photovoltaic near zero current, being composed primarily of metallic tellurium. Since the deposits are of identical composition and the surface is not photovoltaic near zero current, identical open-circuit potentials are obtained.

The effect of a pulse-current source on the electrodeposit morphology is investigated in the scanning electron micrographs shown in Figs. 3-32 through 3-36. The electrolyte composition and temperature are listed in the figure captions; these are identical to the conditions used in the modeling work. The electrodeposit compositions were all about 47 atomic percent cadmium (± 2 atomic percent) as measured *ex situ* with a Kevax x-ray analyzer. The deposit in Fig. 3-32 was obtained with a direct current source of $1.5 \times i_{lim,HTeO_2^+}$. The pulse-current source frequencies are listed in the figure captions of Figs. 3-33 through 3-36. The pulse-current sources had off-times of zero current and on-times with a cathodic current density of $1.7 \times i_{lim,HTeO_2^+}$; the factor 1.7 (instead of 1.5) was found to place more cadmium in the deposit (as predicted by the model work and investigated in Fig. 3-27), and make up for the cadmium dissolution during the off-times. The upper micrograph in each of Figs. 3-32 through 3-36 was taken at 2000× and the lower micrograph at 5000× magnification. The electrodeposits were nearly 1 μm thick. Although there is a significant difference between the surface morphology for the direct current deposit versus the pulse-current deposits, the latter electrodeposits all had similar surface morphologies.

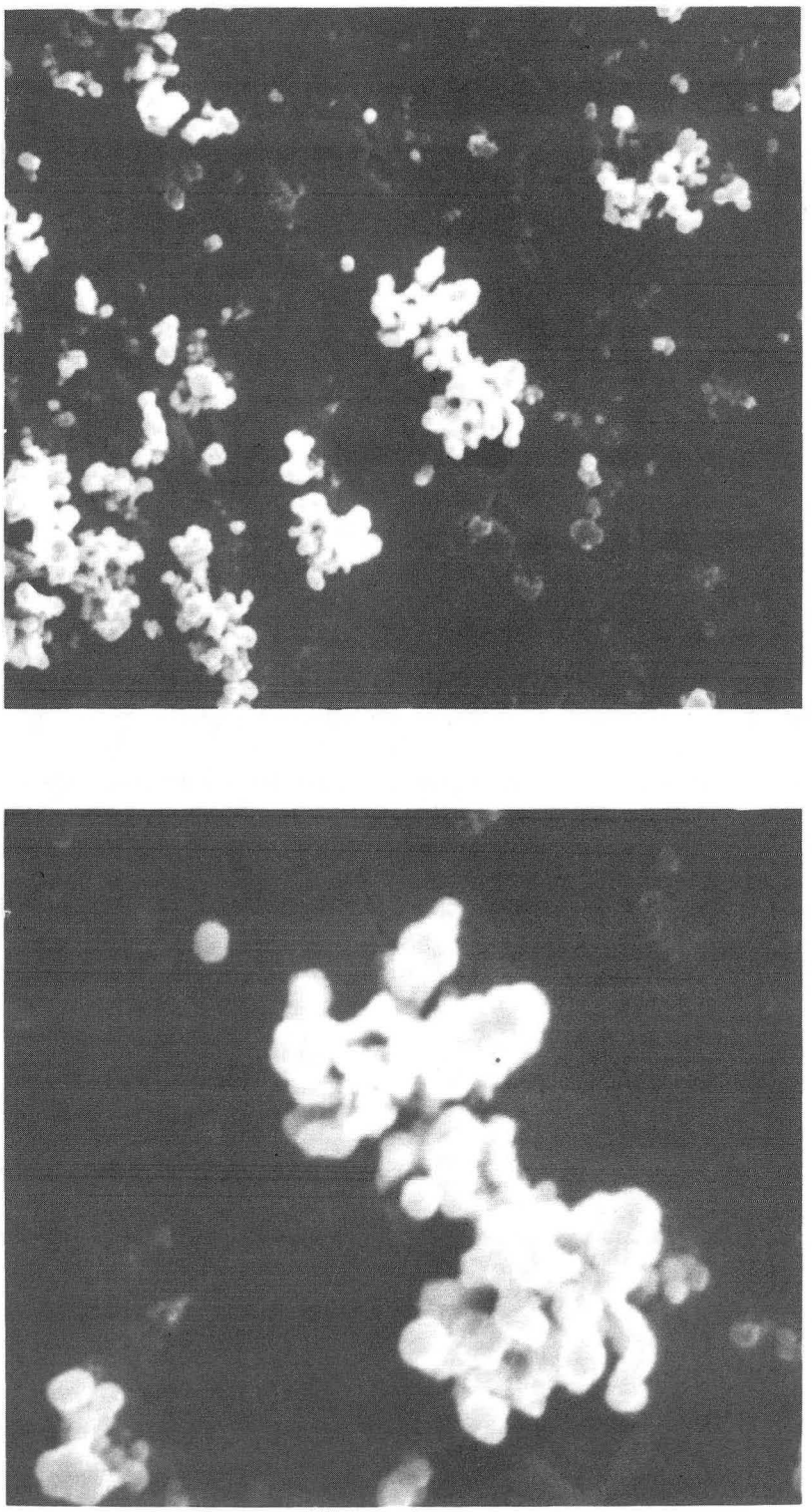

XBB859-7671

Figure 3-32. Scanning electron micrographs of a CdTe electrodeposit created with a direct current source. The width of the upper micrograph is 50 μm, and the lower micrograph width is 20 μm. A 25°C, 0.3-molal-H_2SO_4, 0.001-molal-$HTeO_2^+$, 0.1-molal-Cd^{2+}, aqueous electrolyte was used.

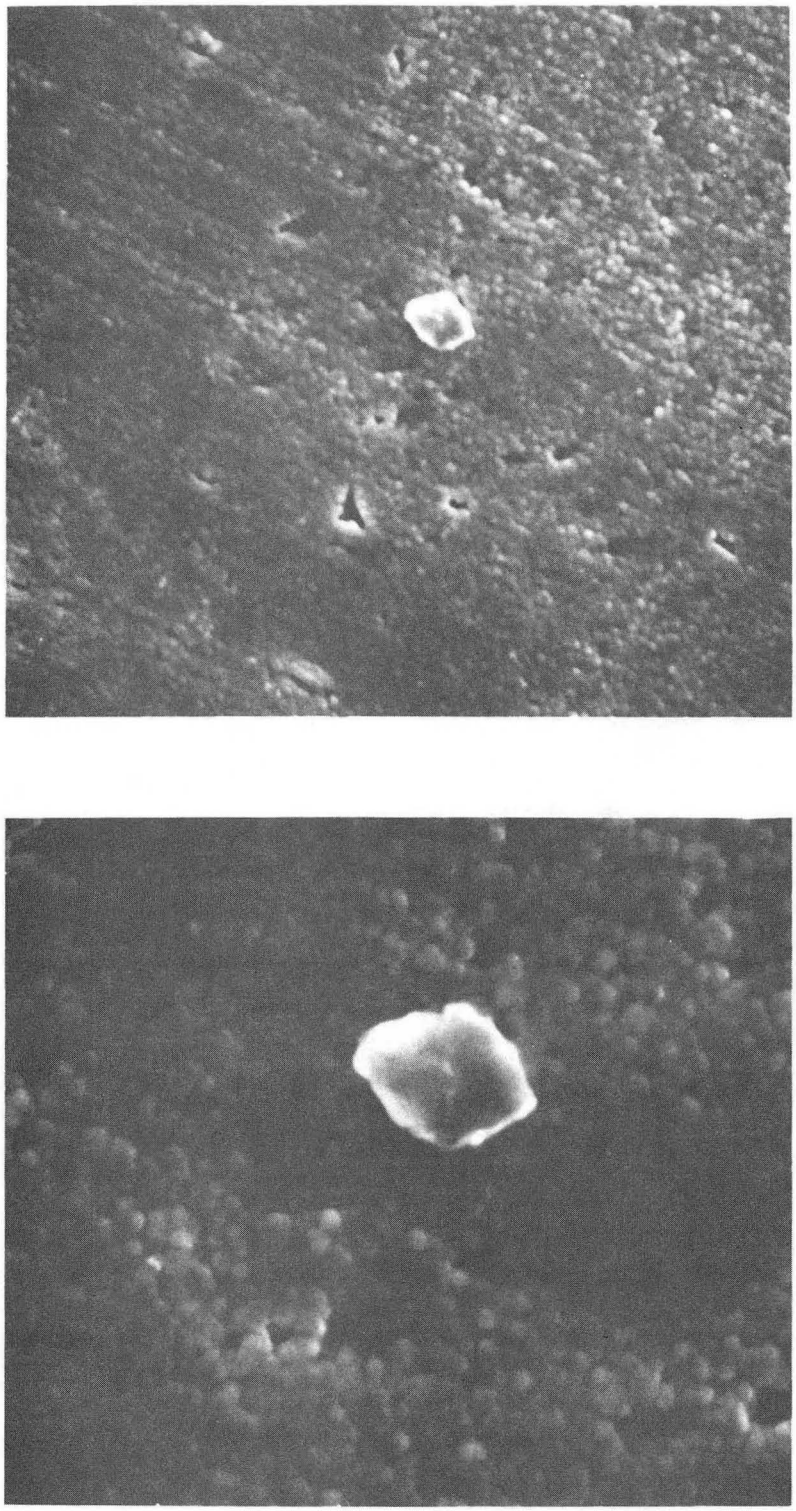

XBB859-7674

Figure 3-33. Scanning electron micrographs of a CdTe electrodeposit created with a 1.00-Hz pulse-current source. The width of the upper micrograph is 50 μm, and the lower micrograph width is 20 μm. A 25°C, 0.3-molal-H_2SO_4, 0.001-molal-$HTeO_2^+$, 0.1-molal-Cd^{2+}, aqueous electrolyte was used.

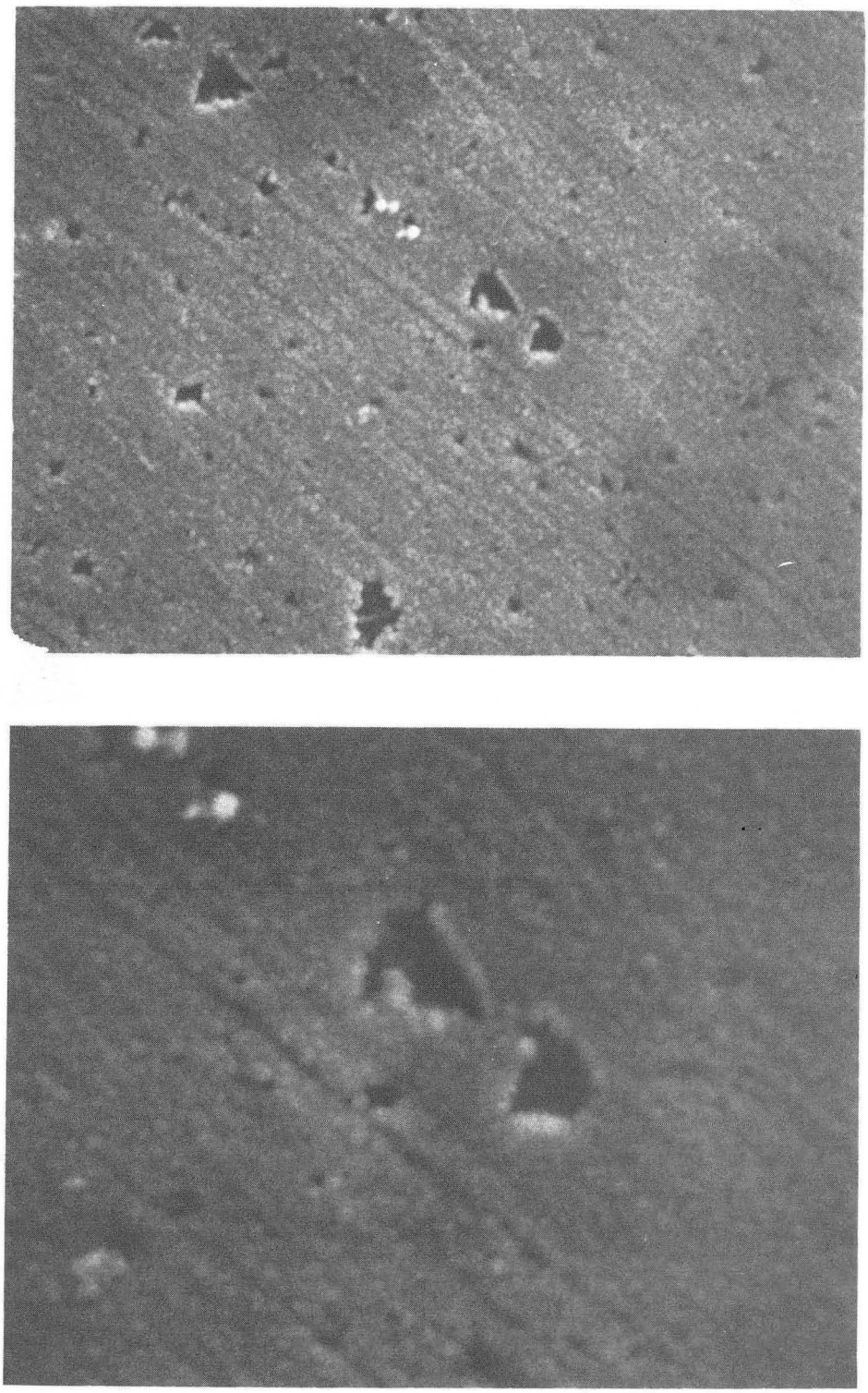

XBB859-7677

Figure 3-34. Scanning electron micrographs of a CdTe electrodeposit created with a 10.0-Hz pulse-current source. The width of the upper micrograph is 50 μm, and the lower micrograph width is 20 μm. A 25°C, 0.3-molal-H_2SO_4, 0.001-molal-$HTeO_2^+$, 0.1-molal-Cd^{2+}, aqueous electrolyte was used.

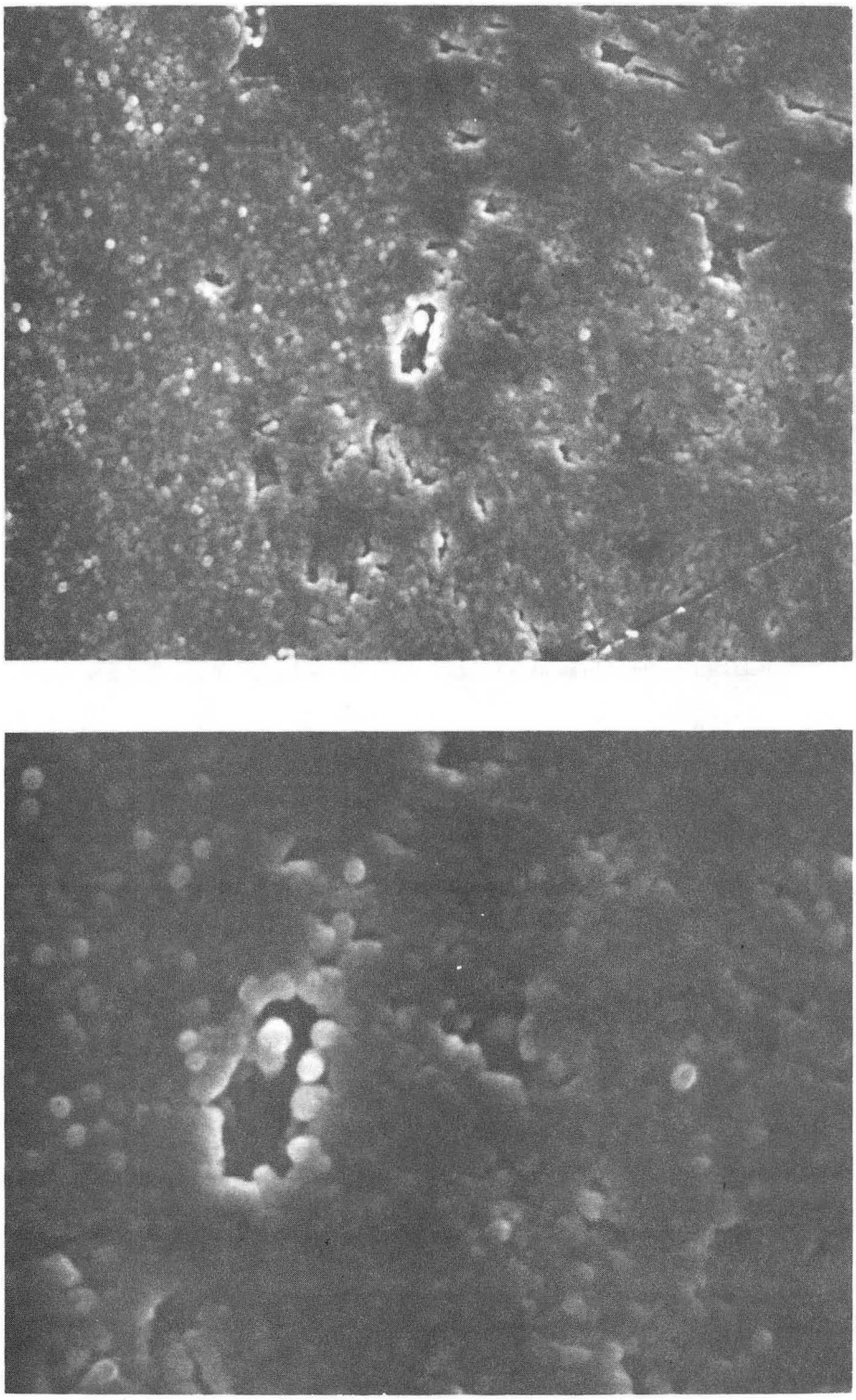

XBB859-7680

Figure 3-35. Scanning electron micrographs of a CdTe electrodeposit created with a 100.-Hz pulse-current source. The width of the upper micrograph is 50 μm, and the lower micrograph width is 20 μm. A 25°C, 0.3-molal-H_2SO_4, 0.001-molal-$HTeO_2^+$, 0.1-molal-Cd^{2+}, aqueous electrolyte was used.

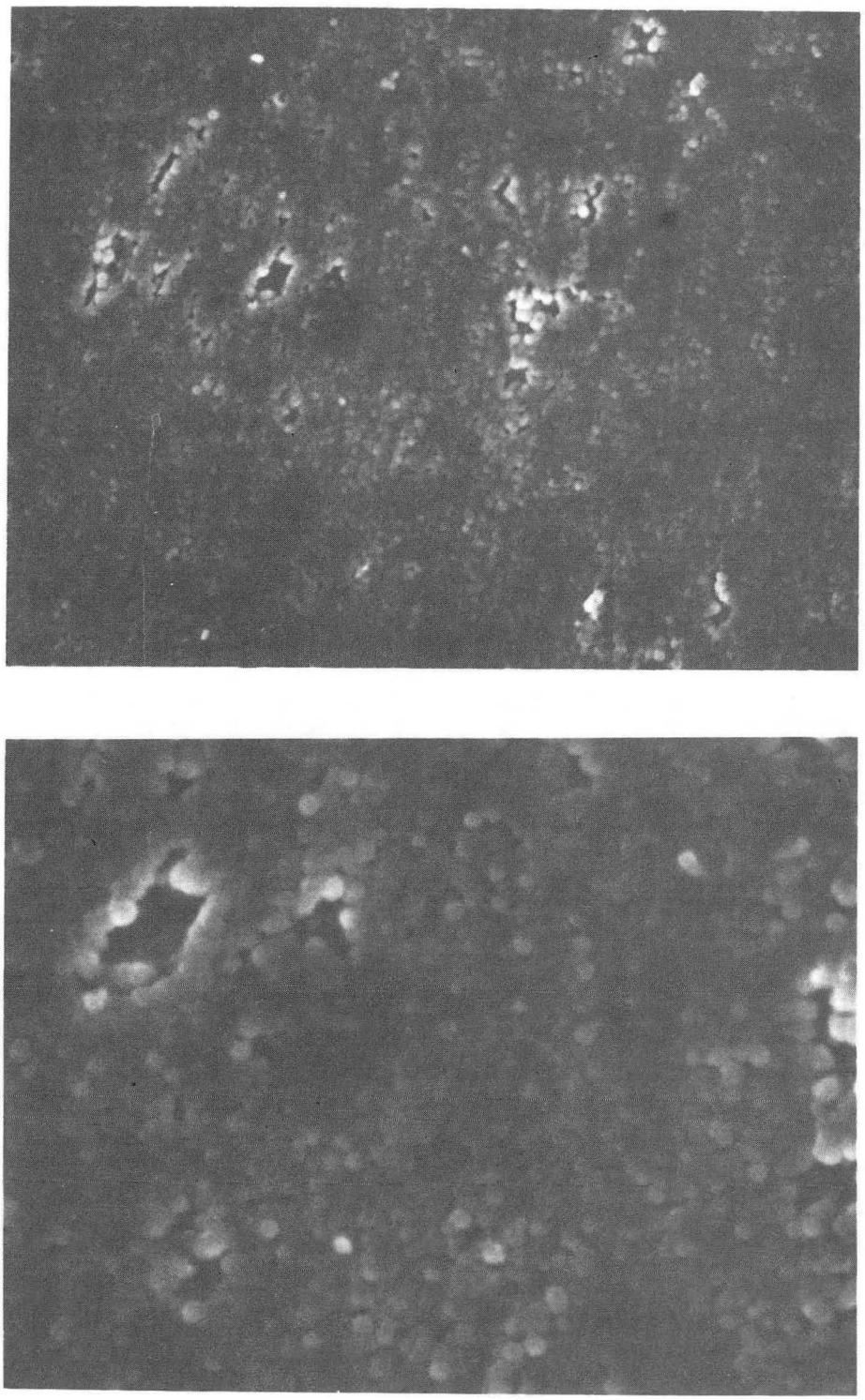

XBB859-7683

Figure 3-36. Scanning electron micrographs of a CdTe electrodeposit created with a 1000-Hz pulse-current source. The width of the upper micrograph is 50 μm, and the lower micrograph width is 20 μm. A 25°C, 0.3-molal-H_2SO_4, 0.001-molal-$HTeO_2^+$, 0.1-molal-Cd^{2+}, aqueous electrolyte was used.

The pulse-current sources produced deposits with amorphous, spherical structures of approximately 0.5 μm in diameter. The direct current source produced a smooth, coherent film covered with distinct crystals approximately 0.7 μm in width. The central nodule in Fig. 3-33 was used to focus the electron microscope and was uncharacteristic of the 1-Hz electrodeposit.

Thus far, we have addressed the electrodeposition of CdTe from an electrolyte maintained near room temperature. Although the results are helpful in the analysis of the CdTe electrodeposition process, solar cell grade CdTe is usually deposited from aqueous, sulfuric acid electrolytes at higher temperatures to promote large grain growth in the electrodeposit. In the investigation described below, the electrolyte temperature was kept at 85°C ± 0.5°C in an effort to produce higher quality, photovoltaic, thin film CdTe.

The high temperature data for $i_{lim,HTeO_2^+}$, shown in Fig. 3-3, can be used as a guideline for the production of 1:1 CdTe. Electrodeposits were formed with a pulse-current source of zero current during the off-time and $1.7 \times i_{lim,HTeO_2^+}$ during the the on-time. The electrodeposit compositions are listed in Table 3-4. The deposits had slightly more tellurium present than cadmium; consequently these deposits were p-semiconductors, since we assume no other impurities affected the photovoltaic properties of the deposits. Trace amounts of lead, plutonium, thallium, and uranium were also detected in some of the electrodeposits. The compositions in Table 3-4 indicate a nearly uniform electrochemical reaction distribution across the disk surface. As expected by potential theory considerations, more cadmium is deposited at the outer edge of the RDE than at the center.

Table 3-4. Compositions of pulse-plated, CdTe electrodeposits.

Sample Number	Frequency of Current Source (Hz)	Atomic % Cd (disk center)	Atomic % Cd (disk edge)
1	0.100	47.5	48.5
2	1.00	45.5	45.8
3	10.0	47.0	47.3
4	100.	46.0	46.0
5	1000	46.7	48.8
Mean Composition:		46.5	47.3

In order to evaluate the photovoltaic properties of the different electrodeposits, the following experiment, illustrated in Fig. 3-37, was completed for each deposit. After approximately a 3 – μm thick electrodeposit had been formed, the deposits were etched in a 50°C, 10-M-NaOH solution for 1 min. During the etching process, the disk rotation rate was maintained at 2000 rpm. The NaOH etch solution has been found to be effective in previous studies of p-CdTe photovoltaic devices (38). Immediately afterwards, the disk electrode was placed in a 1.0-M-NaOH solution at 25°C, and kept stationary. A 0.1-Hz (on-time equal off-time), rectangular square-pulse light source was then employeed, along with the low frequency triangular current-sweep shown in Fig. 3-37. A typical potential response of the etched deposits, with compositions listed in Table 3-4, is shown in Fig. 3-38 for a 100-Hz electrodeposit subject to the experiment outlined in Fig. 3-37. During the photoresponse analysis, the following electrode reaction took place:

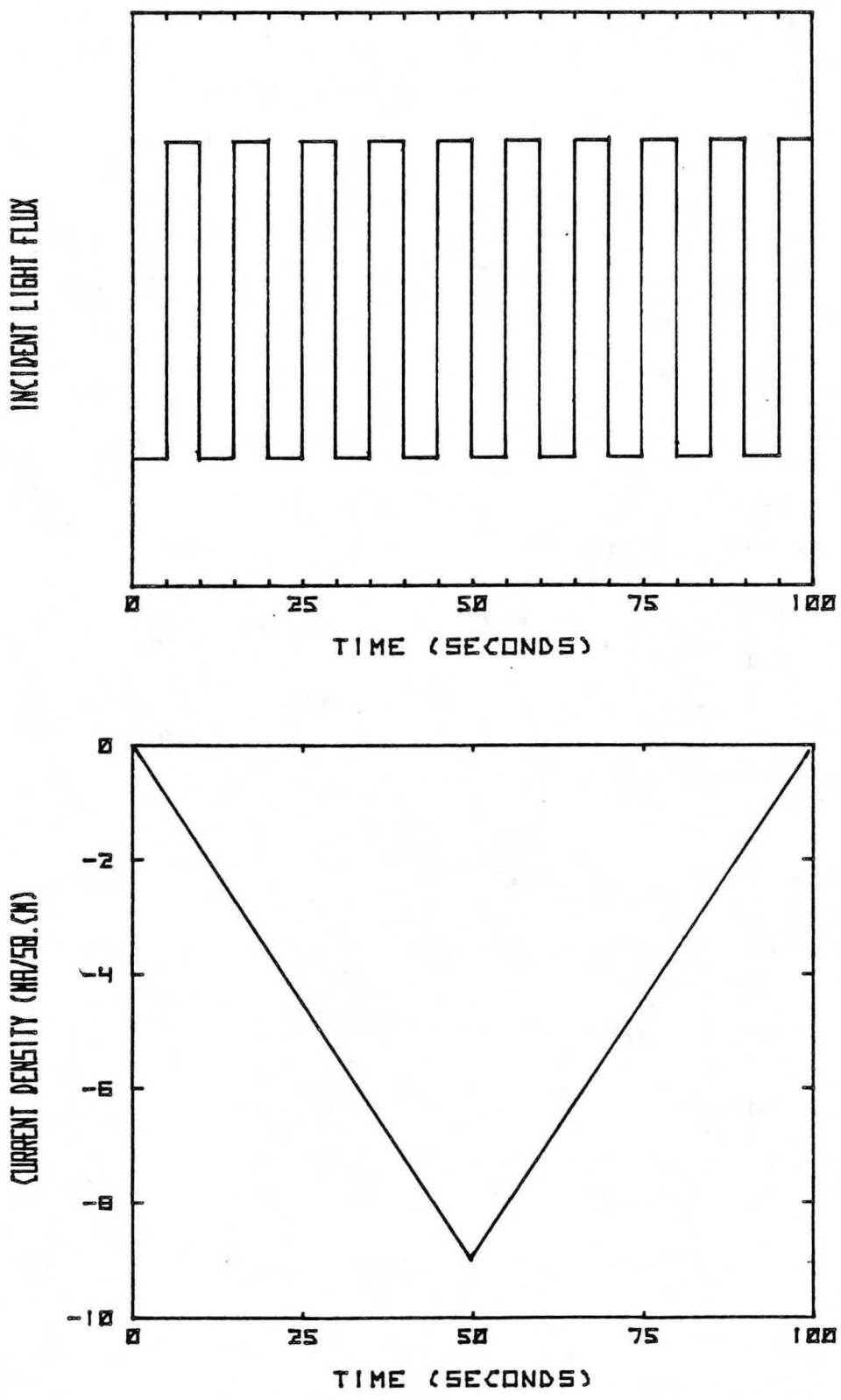

Figure 3-37. Pulse-light source and triangular current-sweep function for electrodeposit characterization.

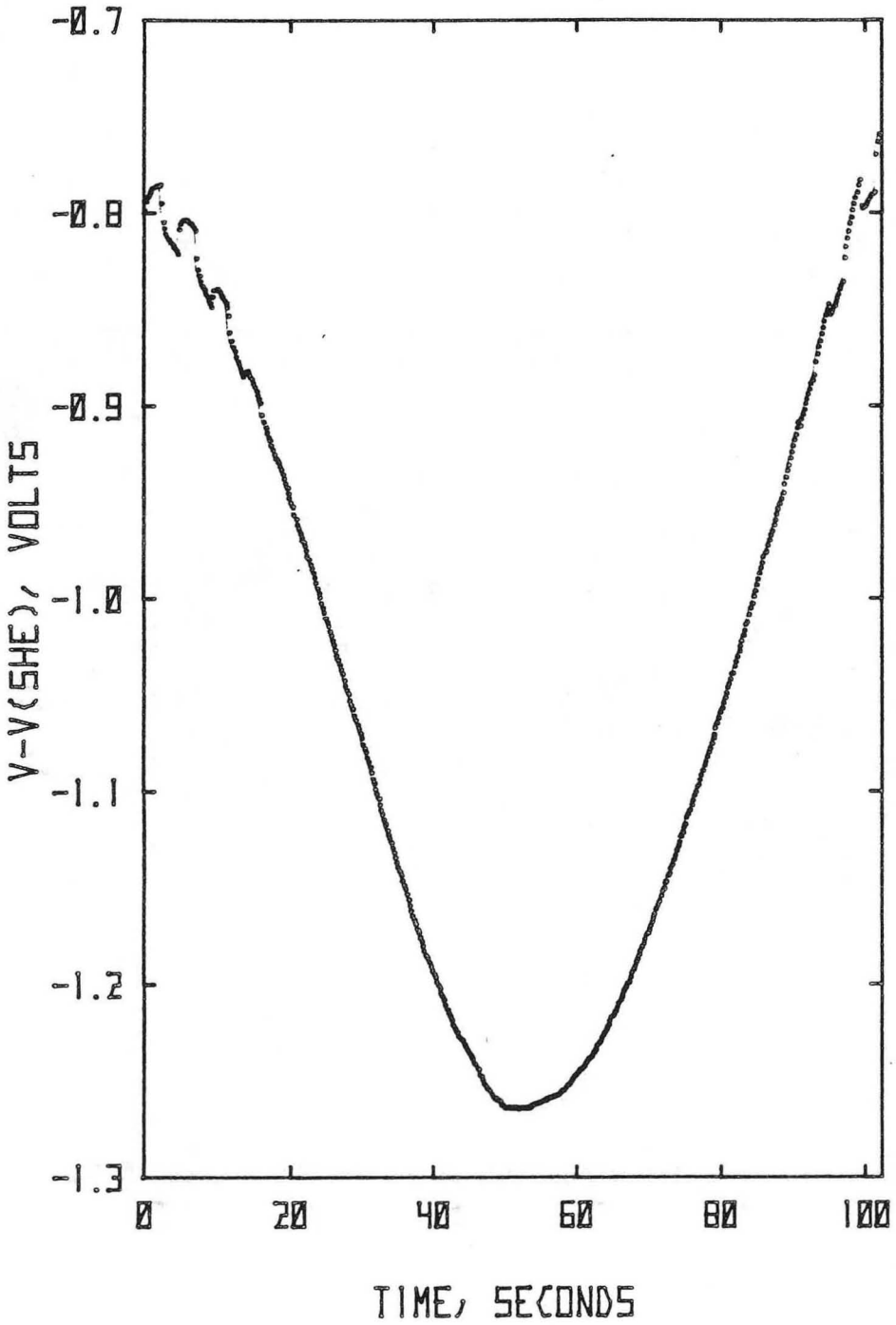

Figure 3-38. Electrode-potential response to the light source and cell-current density displayed in Fig. 3-37. The 1.0-molal-NaOH solution was maintained at 25°C. The electrodeposit was formed with a 100.-Hz current source (sample 4 of Table 3-4).

$$2H_2O + 2e^- \rightarrow 2OH^- + H_2 \ . \qquad [3\text{-}25]$$

For all of the electrodeposits tested, the maximum photoresponse was observed during the first 20 seconds, during which time $|i| < 3.0 \frac{mA}{cm^2}$. In Fig. 3-39, the effect of the etching process on a 100.-Hz electrodeposit is portrayed. In the upper plot, no etching of the 100.-Hz electrodeposit was completed prior to the photoresponse experiment. Consequently, no significant photoresponse resulted. In the lower plot, after 1 minute of the NaOH etching process previously described, the resulting potential response was obtained. The etch process is a very important aspect of semiconductor electrode pretreatment and has been investigated by a number of authors for CdTe devices. Takahashi *et al.* (14) noted a similar relationship between the etching process and the photoresponse for CdTe electrodes. Gaugash and Milnes (39) tested ten different etch solutions for CdTe electrodes. Their results indicated that a tellurium rich surface layer often resulted. This might be explained by the more noble character of tellurium relative to cadmium.

As can be seen in Fig. 3-38, no significant photoresponse results after 20 seconds. In Fig. 3-40, the low current density photoresponse, corresponding to short times in Fig. 3-38, is analyzed. Again, the light source depicted in Fig. 3-37 was used. The current was swept linearly from 0 at -60 $\frac{\mu A}{cm^2 - min}$. The periodic potential response shown in Fig. 3-40 indicated that no electrodeposit corrosion occurred; the surface remained unaltered after the experiment was duplicated 25 times. In an effort to compare the photoresponse of the different electrodeposits listed in Table 3-4, the potential response for the experiment outlined in Fig. 3-37 has been plotted in Fig.

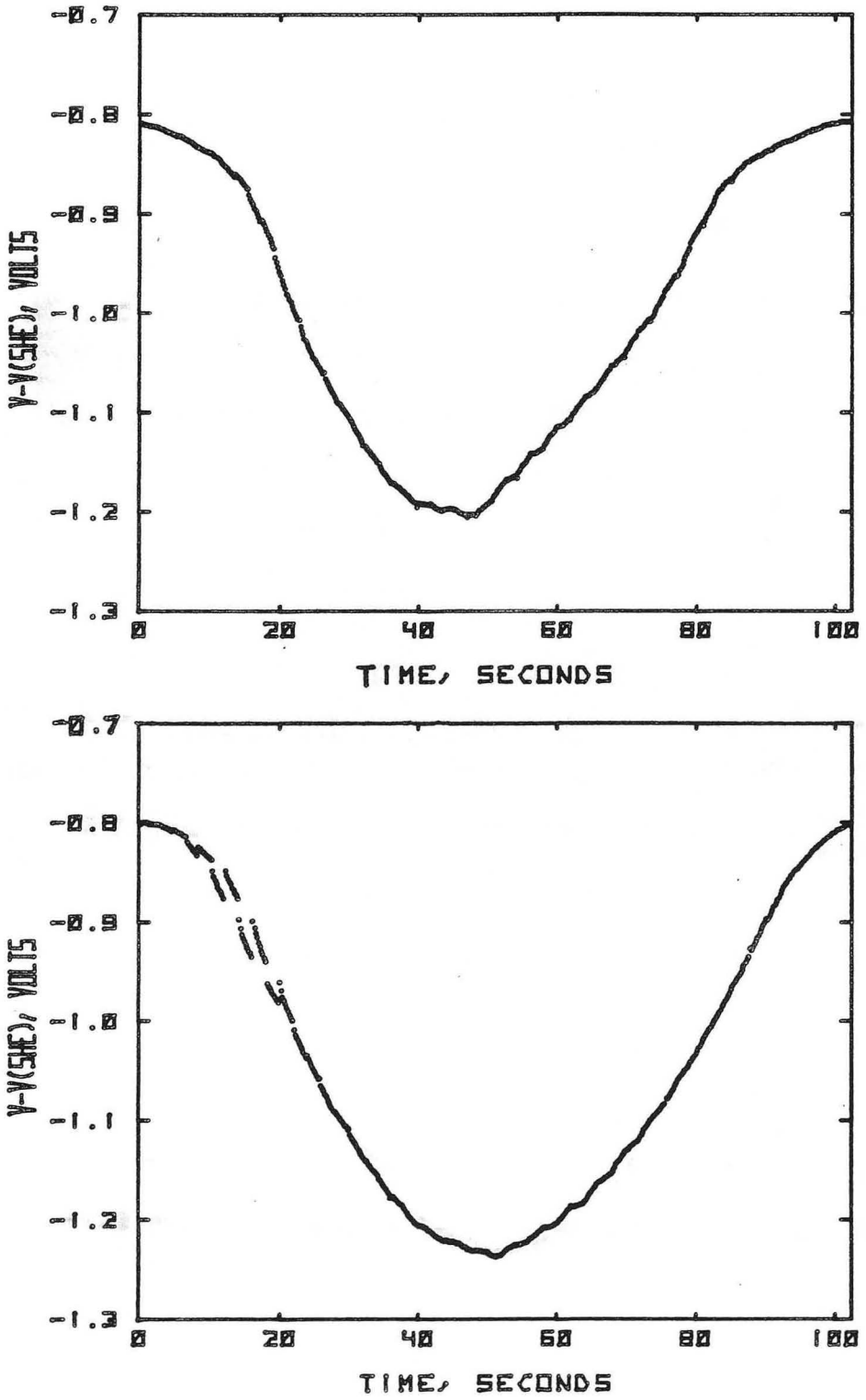

Figure 3-39. Effect of etching process on electrodeposit photoresponse. Upper curve: no etch. Lower curve: 1-min etch in a 50°C, 10-molal-NaOH solution. During the etching process, the RDE rotated at 2000 rpm. For the photoresponse experiment, a 25°C, 1.0-molal-NaOH solution was used.

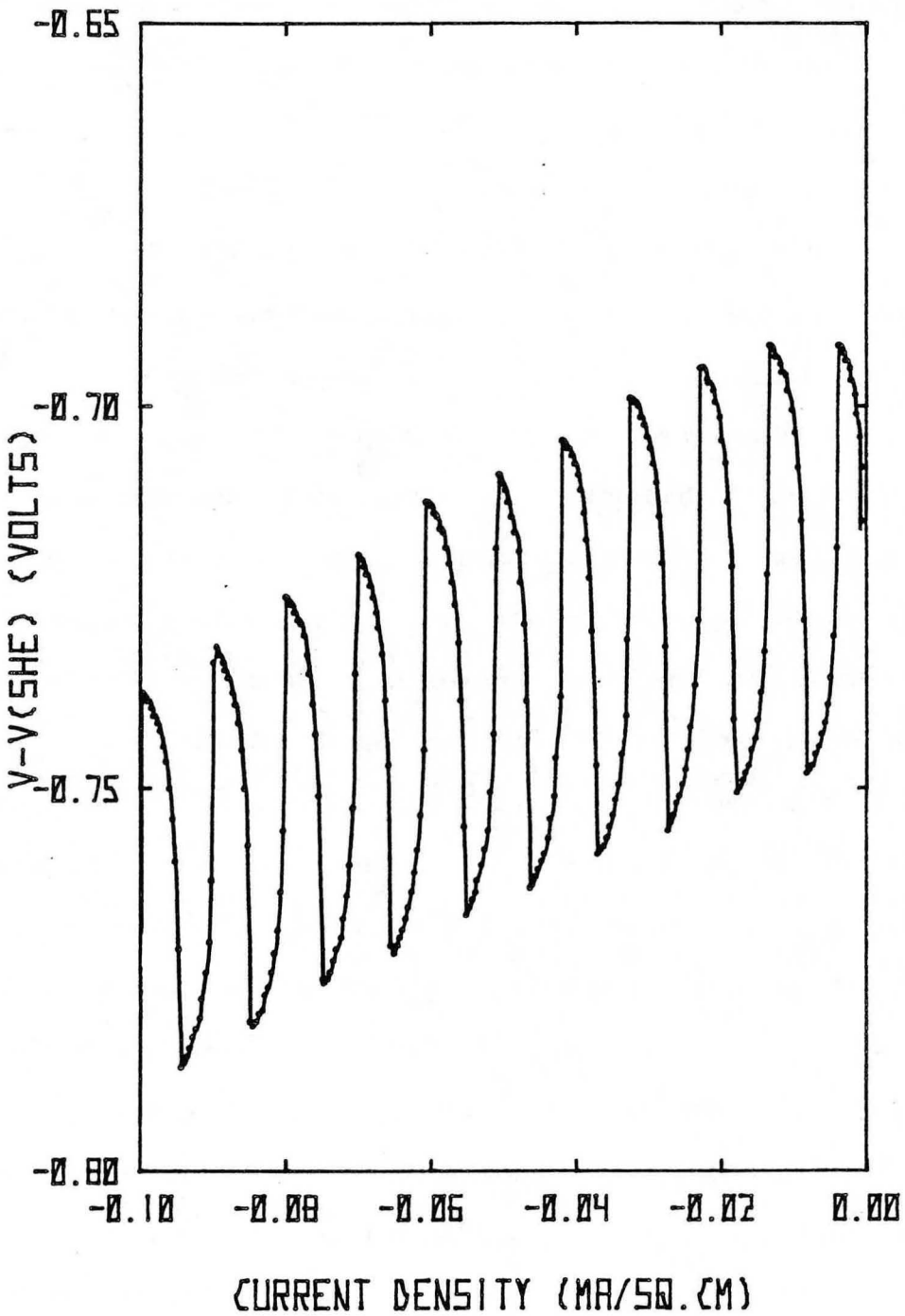

Figure 3-40. Low current-density photoresponse of 100-Hz electrodeposit. The pulse light source is shown in Fig. 3-37. The current was ramped at -60 $\mu A/cm^2$ – min. A 25°C, 1.0-molal-NaOH solution was used.

3-41 for each electrodeposit. It appears that the electrodeposit created with the 100.-Hz cell-current source yielded the largest photoresponse.

The effect of the pulse-current frequency on the electrodeposit morphology in the 85°C experiments is shown in Figs. 3-42 through 3-46. In general, these electron micrographs look very similar to those obtained for the 25°C electrolyte, shown in Figs. 3-32 through 3-36. The diameter of the spherical nodules, however, is larger in the high temperature experiments. The upper micrographs in Figs. 3-42 through 3-46 were obtained at 5000× magnification, as were the lower micrographs in Figs. 3-32 through 3-36; the length scale is the same for each set of micrographs, which allows for direct comparison. The lower micrographs in Figs. 3-42 through 3-46 were obtained at 10,000× magnification, while that in Fig. 3-47 was obtained at 50,000× magnification. The larger diameter of the spheres at the higher temperatures may be due to the fact that approximately 3 times the number of coulombs were passed in the 85°C experiment as in the 25°C experiment. It can also be seen that the spheres are more developed and separate in the 85°C experiments than in the 25 °C experiments. This may be caused by the etching process completed for the electrodeposits formed at 85°C. X-ray diffraction patterns indicated that the deposits were polycrystalline, containing little long range order. Lower pulse-current frequencies and higher electrolyte temperatures yielded sharper x-ray diffraction patterns, indicating more long range order. Due to the polycrystalline, disordered nature of the electrodeposits, quantitative information regarding the amount of each phase present could not obtained from the x-ray diffraction patterns.

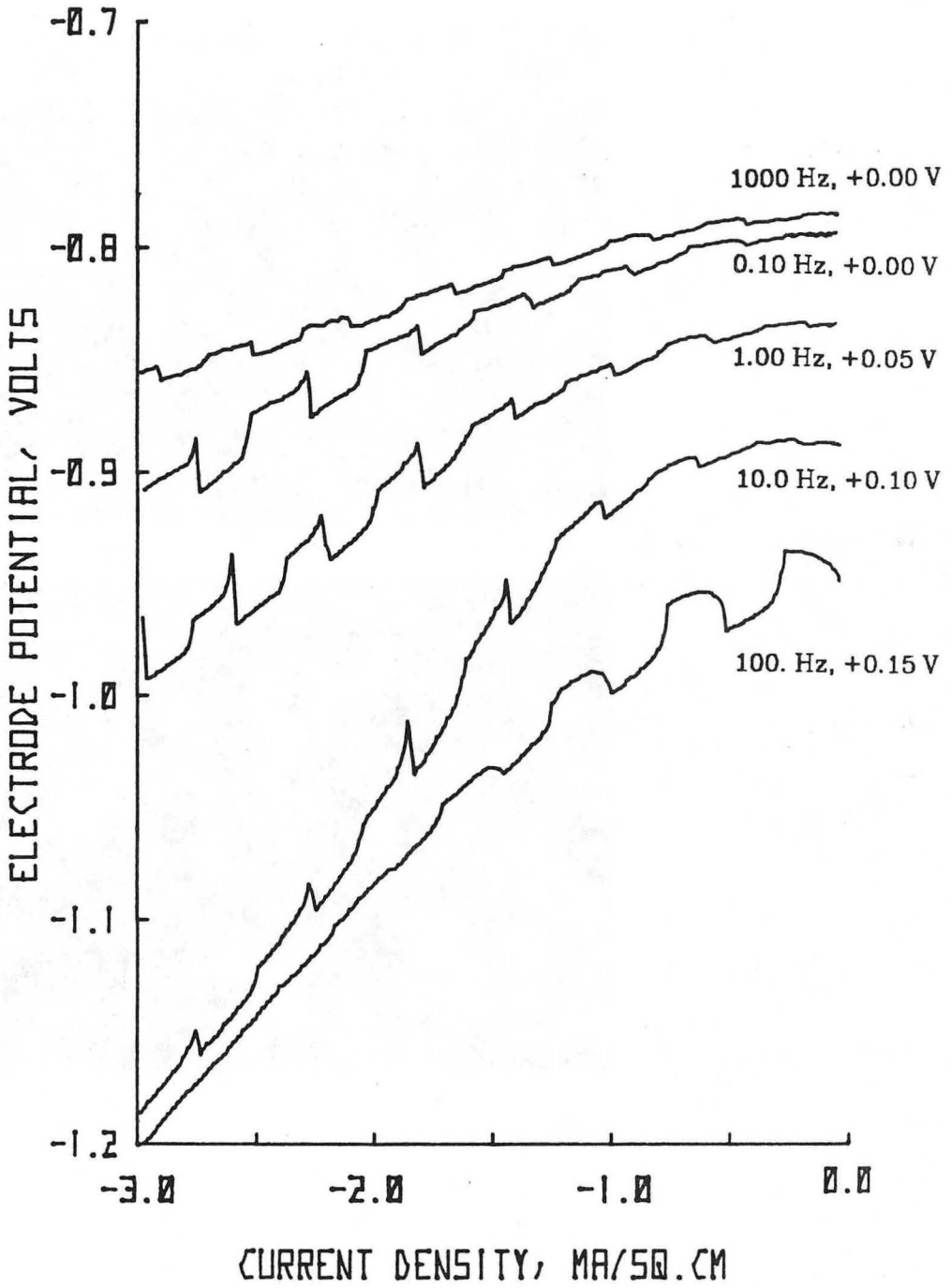

Figure 3-41. Photoresponse of samples 1-5 of Table 3-4. The light source and current density are shown in Fig. 3-37. The first parameter to each curve denotes the current frequency used to electrodeposit the CdTe. The second parameter gives the potential used to shift the curves so that none of the potential traces overlaps. A 25°C, 1.0-molal-NaOH solution was used.

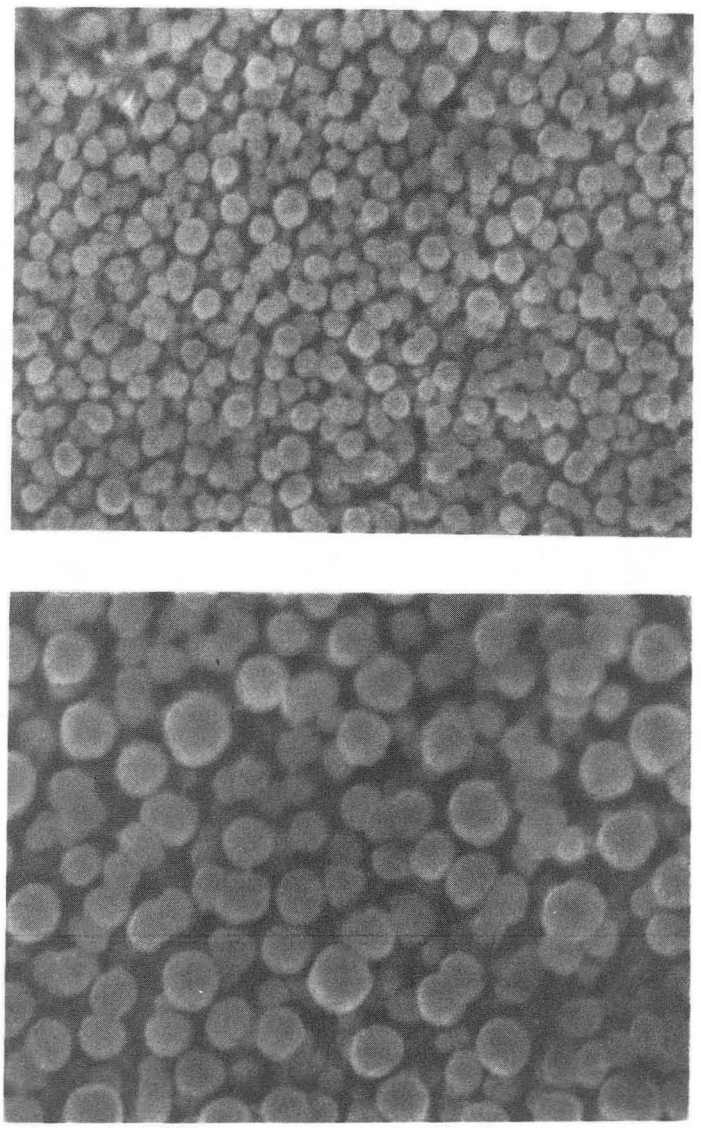

XBB859-7696

Figure 3-42. Scanning electron micrographs of a CdTe electrodeposit created with a 0.100-Hz pulse-current source. The width of the upper micrograph is 18 μm and the lower micrograph width is 9 μm. An 85°C, 0.3-molal-H_2SO_4, 0.001-molal-$HTeO_2^+$ 0.1-molal-Cd^{2+}, aqueous electrolyte was used.

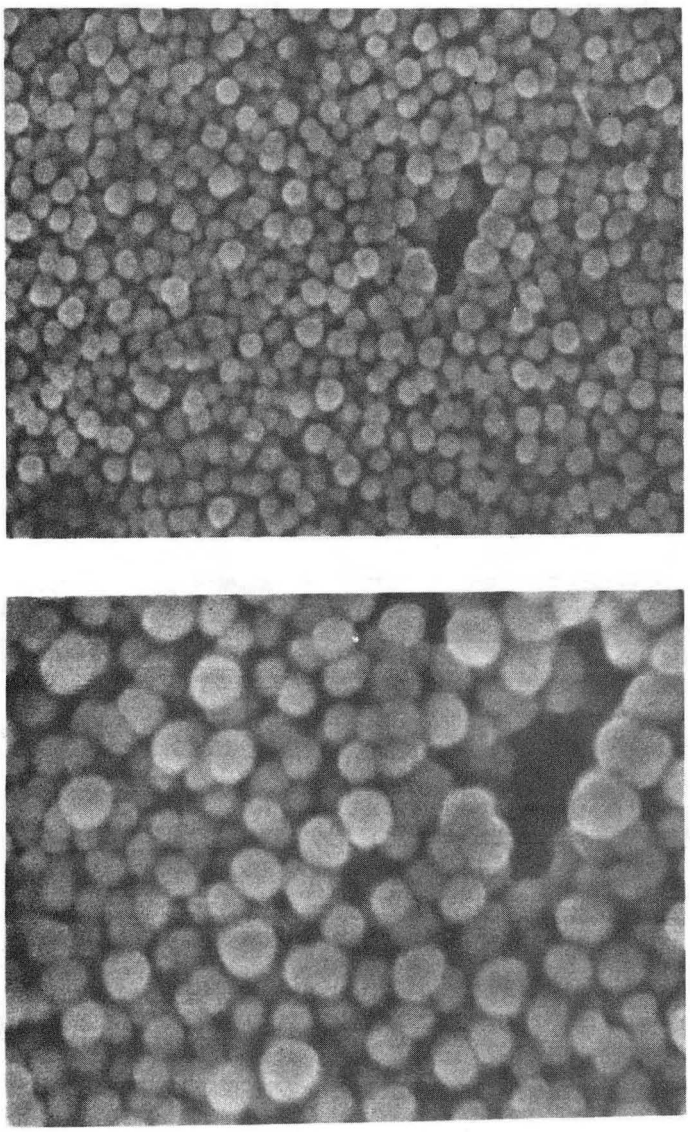

XBB859-7699

Figure 3-43. Scanning electron micrographs of a CdTe electrodeposit created with a 1.00-Hz pulse-current source. The width of the upper micrograph is 18 μm and the lower micrograph width is 9 μm. An 85°C, 0.3-molal-H_2SO_4, 0.001-molal-$HTeO_2^+$, 0.1-molal-Cd^{2+}, aqueous electrolyte was used.

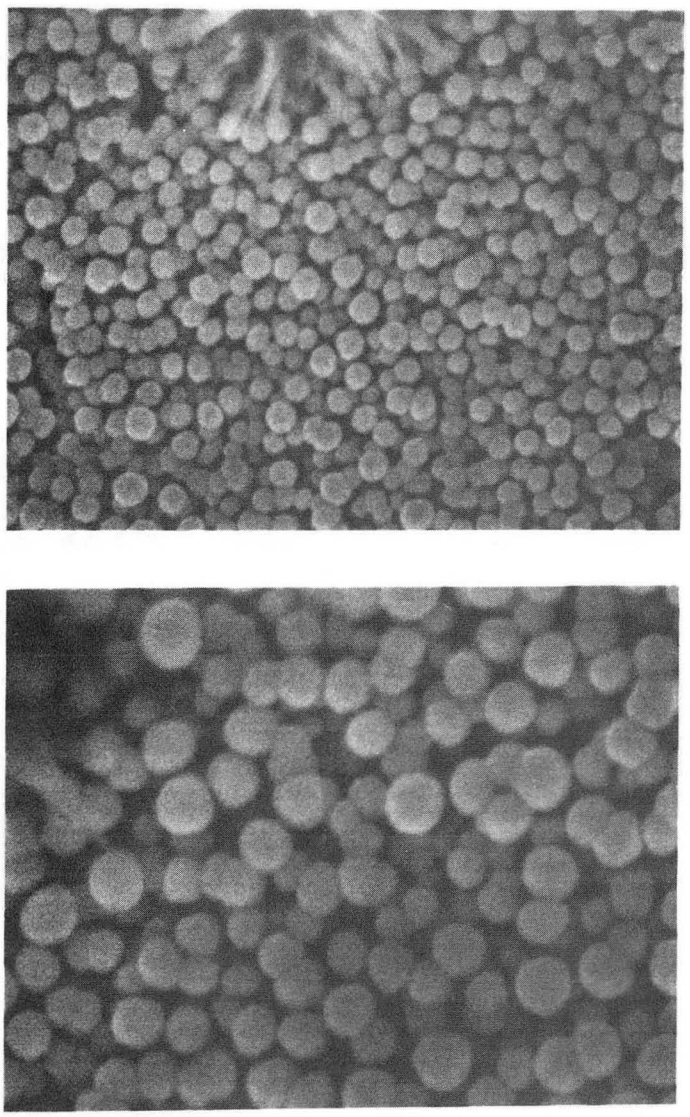

XBB859-7702

Figure 3-44. Scanning electron micrographs of a CdTe electrodeposit created with a 10.0-Hz pulse-current source. The width of the upper micrograph is 18 μm and the lower micrograph width is 9 μm. An 85°C, 0.3-molal-H_2SO_4, 0.001-molal-$HTeO_2^+$, 0.1-molal-Cd^{2+}, aqueous electrolyte was used. A dust particle is shown in the upper center portion of the upper micrograph.

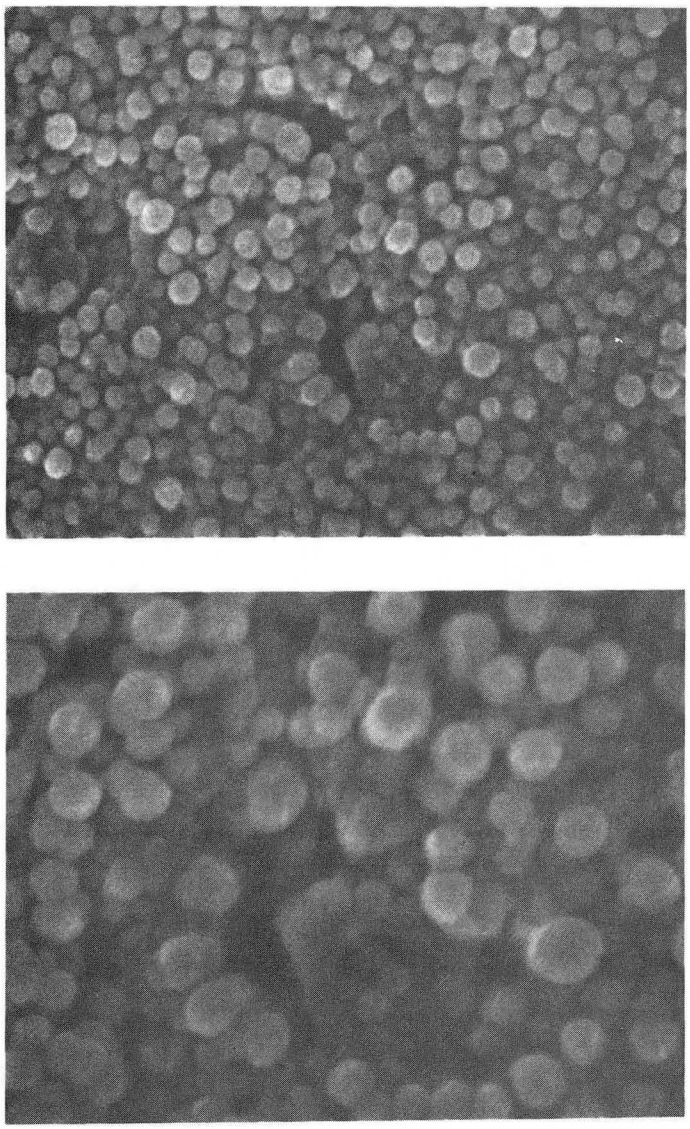

XBB859-7705

Figure 3-45. Scanning electron micrographs of a CdTe electrodeposit created with a 100.-Hz pulse-current source. The width of the upper micrograph is 18 μm and the lower micrograph width is 9 μm. An 85°C, 0.3-molal-H_2SO_4, 0.001-molal-$HTeO_2^+$, 0.1-molal-Cd^{2+}, aqueous electrolyte was used.

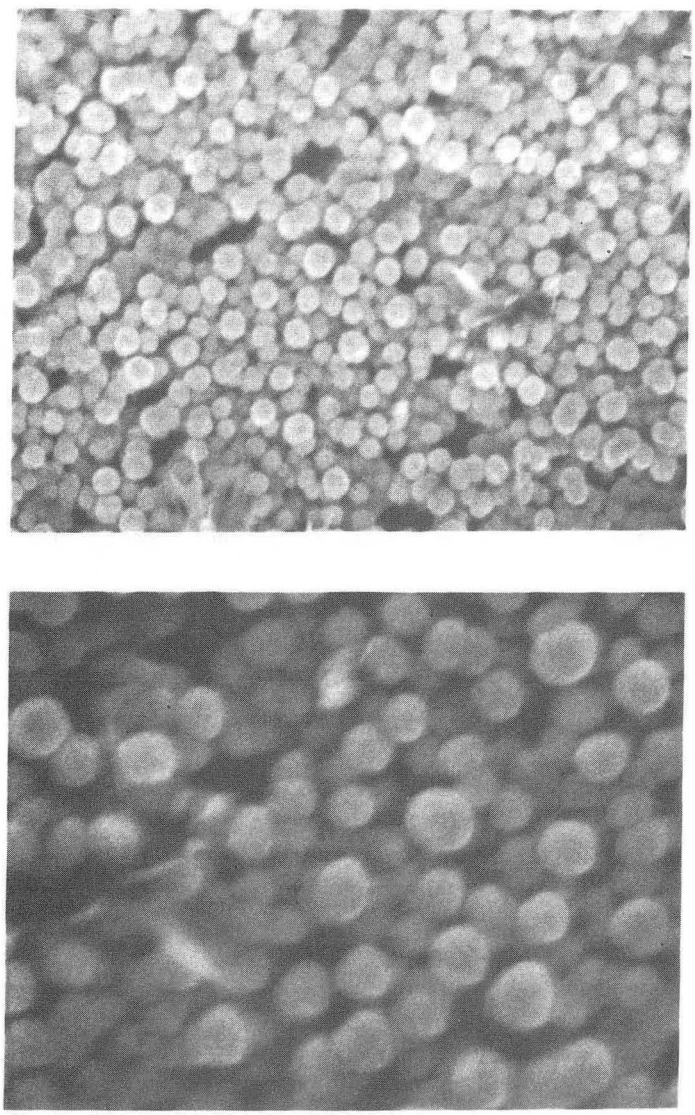

XBB859-7708

Figure 3-46. Scanning electron micrographs of a CdTe electrodeposit created with a 1000-Hz pulse-current source. The width of the upper micrograph is 18 μm and the lower micrograph width is 9 μm. An 85°C, 0.3-molal-H_2SO_4, 0.001-molal-$HTeO_2^+$, 0.1-molal-Cd^{2+}, aqueous electrolyte was used.

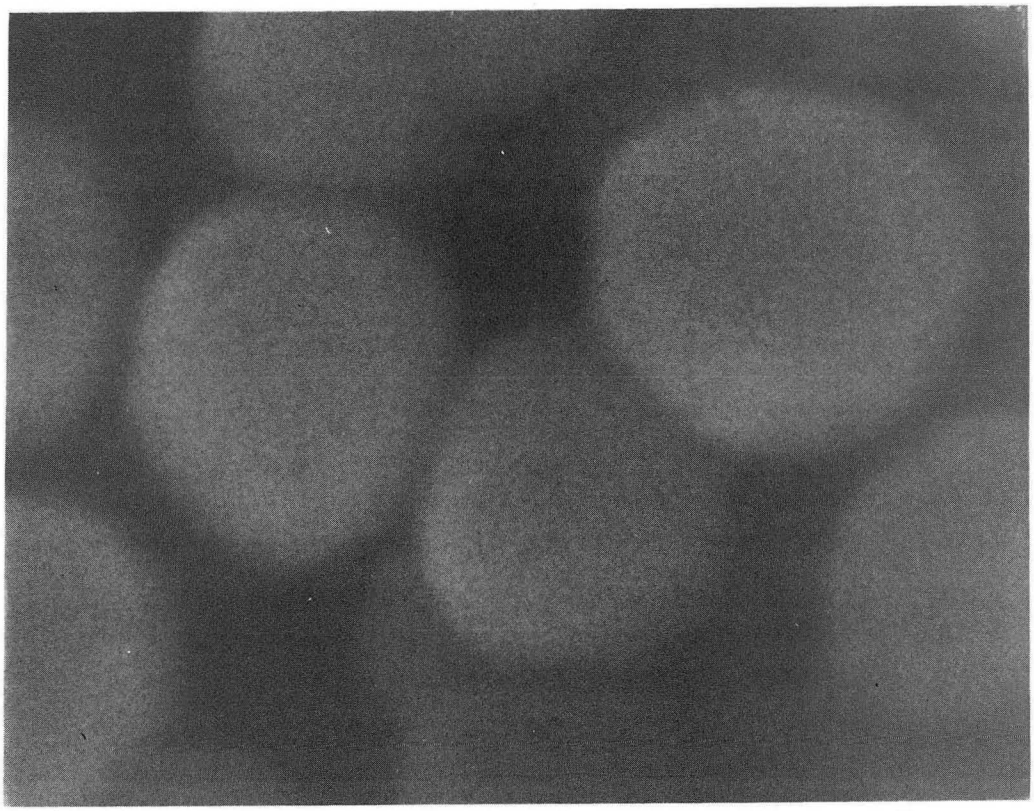

XBB859-7709

Figure 3-47. Scanning electron micrographs of a CdTe electrodeposit created with a 10.0-Hz pulse-current source. The width of the micrograph is 2.3 μm. An 85°C, 0.3-molal-H_2SO_4, 0.001-molal-$HTeO_2^+$, 0.1-molal-Cd^{2+}, aqueous electrolyte was used.

Conclusion

The codeposition of tellurium and cadmium represents an intriguing process problem with unique chemistry. In this work, we have addressed the evaluation of physicochemical parameters for tellurium deposition, cadmium deposition, and the codeposition of tellurium and cadmium. In addition, results are presented for the *in situ* investigation of forming electrodeposits. The influence of the pulse-current-source frequency on the electrodeposit morphology and photovoltaic behavior is clearly illustrated. Perhaps the most important aspect of the characterization study is that pronounced changes in the deposit photovoltaic properties and surface morphology result from changes in the cell-current waveform. Knowledge of the CdTe-electrodeposition physicochemical parameters, and the material properties resulting from the electrodeposition conditions, should prove helpful in the electrochemical fabrication of CdTe devices.

Nomenclature

a_i	surface activity of component i
c_i	concentration of species i, $\frac{\text{mol}}{\text{cm}^3}$
c_i^b	bulk concentration of species i, $\frac{\text{mol}}{\text{cm}^3}$
$c_{i,ref}$	reference electrode compartment concentration of species i, $\frac{\text{mol}}{\text{cm}^3}$
D_i	diffusion coefficient of species i, $\frac{\text{cm}^2}{\text{s}}$
e^-	symbol for an electron
E	electrode potential relative to the reference electrode, V
f	F/RT, V^{-1}
F	Faraday's constant, 96487 $\frac{\text{C}}{\text{equivalent}}$
i	cell-current density, $\frac{\text{mA}}{\text{cm}^2}$
i_l	partial current density for reaction l, $\frac{\text{mA}}{\text{cm}^2}$
$k_{a,l}$	anodic rate constant of reaction l
$k_{c,l}$	cathodic rate constant of reaction l
M_i	symbol for chemical formula of species i
n_l	number of electrons in reaction l
p_{H_2}	hydrogen partial pressure, atm
r	cell ohmic resistance, $\Omega - \text{cm}^2$
R	universal gas constant, 8.314 $\frac{\text{J}}{\text{mol} - \text{K}}$
$RSAT$	relevant surface-activity thickness, cm

s_i stoichiometric coefficient of species i

t time, s

T absolute temperature, K

U_l^θ standard electrode potential for reaction l, V

v_y normal velocity component to a rotating disk electrode, $\frac{cm}{s}$

x_i molecular mole fraction of species i

$\bar{x}_i$ atomic mole fraction of species i

y normal distance from the electrode surface, cm

α interchange energy, $\frac{J}{mol}$

β_{act} degree of CdTe dissociation at $\bar{x}_{Te} = \bar{x}_{Cd} = 0.5$

β_l symmetry factor for reaction l

δ_i Levich diffusion layer thickness of species i, cm

ν kinematic viscosity, $\frac{cm^2}{s}$

ρ_o solvent mass density, $\frac{kg}{cm^3}$

$\hat{\rho}_i$ species i molar density, $\frac{mol}{cm^3}$

ω disk rotation speed, $\frac{radian}{s}$

References

1. C.A. Tibbals, *J. Am. Chem. Soc.*, 31(1909)902.
2. *Physics and Chemistry of II-VI Compounds*, M. Aven and J.S. Prener, editors, Wiley, New York, 1967.
3. K. Zanio, *Cadmium Telluride*, Semiconductors and Semimetals, volume 13, Academic Press, New York, 1978.
4. J.L. Loferski, *J. Appl. Phys.*, 27(777)1956.
5. W.J. Danaher and L.E. Lyons, *Nature*, 271(1978)139.
6. M.P.R. Panicker, M. Knaster, and F.A. Kroger, *J. Electrochem. Soc.*, 125(1978)566.
7. G. Fulop, M. Doty, P. Meyers, J. Betz, and C.H. Liu, *Appl. Phys. Lett.*, 40(1982)327.
8. R.D. Engelken, Ph.D. Thesis, University of Missouri-Rolla, MI, 1983.
9. H.J. Gerritsen, *J. Electrochem. Soc.*, 131(1984)136.
10. M. Takahashi, K. Uosaki, and H. Kita, *J. Appl. Phys.*, 55(1984)3879.
11. K. Uosaki, M. Takahashi, and H. Kita, *Electrochim. Acta*, 29(1984)279.
12. L.E. Lyons, G.C. Morris, D.H. Horton, and J.G. Keyes, *J. Electroanal. Chem.*, 168(1984)101.
13. R.N. Bhattacharya, *J. Electrochem. Soc.*, 131(1984)939.
14. M. Takahashi, K. Uosaki, and H. Kita, *ibid.*, 131(1984)2304.
15. A.S. Baranski and W.R. Fawcett, *ibid.*, 127(1980)766.
16. A.S. Baranski, W.R. Fawcett, A.C. McDonald, R.M. de Nobriga, and J.R. MacDonald, *ibid.*, 128(1981)963.
17. M. Skyllas-Kazacos, *J. Electroanal. Chem.*, 148(1983)233.

18. J.J. Lingane and L.W. Niedrach, *J. Am. Chem. Soc.*, 70(1948)1997.

19. *Ibid.*, 71(1949)196.

20. R.H. Flowers, *J. Inorg. Nucl. Chem.*, 9(1959)155.

21. R. Schuhmann, *J. Am. Chem. Soc.*, 47(1925)356.

22. I.M. Issa and S.A. Awad, *J. Phys. Chem.*, 58(1954)948.

23. K.L. Cheng, *Anal. Chem.*, 33(1961)761.

24. W.A. Dutton and W. Charles Cooper, *Chem. Revs.*, 66(1966)657.

25. W. Charles Cooper, *Tellurium*, Van Nostrand Reinhold, New York, 1971.

26. J.S. Newman, *Electrochemical Systems*, Prentice Hall, Inc., Englewood Cliffs, New Jersey, 1973.

27. N.V. Ngac, O. Vittori, and G. Quarin, *J. Electroanal. Chem.*, 167(1984)227.

28. M.L. Tarng and G.K. Wehner, *J. Appl. Phys.*, 42(1971)2449.

29. M.L. Tarng and G.K. Wehner, *J. Appl. Phys.*, 43(1972)2268.

30. S.H. Overbury, P.A. Bertrand, and G.A. Samorjai, *Chem. Revs.*, 75(1975)547.

31. A. Brenner, *Electrodeposition of Alloys, Principles and Practice*, volume 1, Academic Press, New York, pp. 186-198.

32. S. Swathirajan, General Motors Research Publication, GMR-5006, 1985.

33. A.S. Jordan, *Metal. Trans.*, 1(1970)239.

34. J.L. Lingane and L.W. Niedrach, *J. Am. Chem. Soc.*, 70(1948)4115.

35. R.A. Jamieson and S.P. Perone, *J. Electroanal. Chem.*, 23(1969)441.

36. M. Shinagawa, N. Soramasu, Y. Mori, and T. Okuma, *ibid.*, 75(1977)809.

37. M.J. Barbier, A.M. De Becdelievre, and J. De Becdelievre, *ibid.*, 94(1978)47.

38. J.L. Sculfort, R. Triboulet, and P. Lemasson, *J. Electrochem. Soc.*, 131(1984)209.

39. P. Gaugash and A.G. Milnes, *ibid.*, 128(1981)924.

Appendix 3

HP9825A Data-Acquisition Program

```
0: dsp "GENERAL
 1090A, 9/4/84";
 wait 3000
1: dim G[2],H[2]
 ,S[6],B$[45],
 C$[45],E$[3],
 U$[5]
2: dim A[6],F,L,
 R,Z,A$[30],H$[4
 5],I$[45],J$[45
 ]
3: dsp "MONITOR
 CURRENT ON CHAN
 NEL 1";wait
 3000
4: dsp "MONITOR
 V-V(ref) ON
 CHANNEL 2";wait
  3000
5: ent "# OF
 POINTS? 4096,
 2048, or 1024",
 Z
6: dim Y$[2Z+16]
7: buf "data",
 Y$,2
8: ent "HAS THE
 DATA BEEN STORE
 D?",E$
9: if cap(E$)="Y
 ES";gto "ACCESS
 "
10: enp "TITLE",
 A$;spc
11: fxd 0;enp
 "RUN #",R;spc
12: ent "millise
 conds/pt",L
13: ent "CHANNEL
  1 OFFSET VOLTA
 GE?",A[1]
14: ent "CHANNEL
  2 OFFSET VOLTA
 GE?",A[2]
15: ent "CHANNEL
  1 FULL SCALE
 VOLTS?",A[3]
16: ent "CHANNEL
  2 FULL SCALE
 VOLTS?",A[4]
17: ent "ELECTRO
 DE AREA? sq.cm"
 ,A[5]
18: ent "V(ref)-
 V(SHE)? volts",
 A[6]
19: ent "milliam
 ps/volt",F
20: ent "ENTER
 1st CAPTION",H$
21: ent "ENTER
 2nd CAPTION",I$
22: ent "ENTER
 3rd CAPTION",J$
23: wtc 2,3;wtc
 2,0;wait 75
24: tfr 2,"data"
 ,Z
25: wtc 2,3
26: ent "ARE
 THE DATA TO BE
 STORED?",E$
27: if cap(E$)#"
 YES";gto "PLOT"
28: enp "STORAGE
  TAPE",U$;spc
29: enp "STORAGE
  TRACK",U;spc
30: enp "STORAGE
  FILE",E;spc
31: trk U;fdf E
32: rcf E,A[1],
 A[2],A[3],A[4],
 A[5],A[6],F,L,
 R,Z,A$,H$,I$,
 J$,Y$
```

```
33: dsp "THE
 DATA HAVE BEEN
 STORED";wait
 2000
34: ent "ARE
 THE DATA TO BE
 PLOTTED?",E$
35: if cap(E$)="
 YES";sto "PLOT"
36: stp
37: "ACCESS":
38: ent "TRACK
 THAT DATA ARE
 STORED ON?",U
39: ent "FILE
 THAT DATA ARE
 STORED ON?",E
40: trk U;fdf E
41: ldf E,A[1],
 A[2],A[3],A[4],
 A[5],A[6],F,L,
 R,Z,A$,H$,I$,
 J$,Y$
42: "PLOT":
43: ent "WANT
 MAX-MIN VARIABL
 E PRT OUT?",E$
44: if cap(E$)#"
 YES";sto 51
45: LZ/2000→T
46: fxd 2;prt
 "Tmax, sec. ",
 T;spc
47: prt "Imin,
 mA/sq.cm ",(-
 A[3]-A[1])F/
 A[5];spc
48: prt "Imax,
 mA/sq.cm ",(A[3
 ]-A[1])F/A[5];
 spc
49: prt "Vmin,
 volts ",-A[4]-
 A[2]+A[6];spc
50: prt "Vmax,
 volts ",A[4]-
 A[2]+A[6];spc
51: ent "x-min?"
 ,S[1]
52: ent "x-max?"
 ,S[2]
53: ent "y-min?"
 ,S[3]
54: ent "y-max?"
 ,S[4]
55: ent "x-tic?"
 ,S[5]
56: ent "y-tic?"
 ,S[6]
57: ent "# of
 digits dsp afte
 r x-decimal?",
 G[1]
58: ent "# of
 digits dsp afte
 r y-decimal?",
 G[2]
59: ent "X AXIS
 CAPTION?",B$
60: ent "Y AXIS
 CAPTION?",C$
61: ent "DO YOU
 WANT NEW CAPTIO
 NS?",E$
62: if cap(E$)#"
 YES";sto 67
63: ent "ENTER
 TITLE",A$
64: ent "ENTER
 1st CAPTION",H$
65: ent "ENTER
 2nd CAPTION",I$
66: ent "ENTER
 3rd CAPTION",J$
67: fxd G[1]
68: S[2]-(7/5)(S
 [2]-S[1])+.2(S[
 2]-S[1])→A
69: S[2]+.2(S[2]
 -S[1])→B
70: S[4]-(8.5/
 7)(S[4]-S[3])-
 .05(S[4]-S[3])+
 C
```

```
71: S[4]+(1/7)(S
 [4]-S[3])-.05(S
 [4]-S[3])→D
72: scl A,B,C,D
73: pen
74: plt S[1],
 S[3],-2
75: (1/16/4.5)(S
 [2]-S[1])→H[1]
76: (1/16/7)(S[4
 ]-S[3])→H[2]
77: int((S[2]-
 S[1])/S[5])→M
78: int((S[4]-
 S[3])/S[6])→N
79: for I=1 to M
80: iplt S[5],0,
 0
81: iplt 0,H[2],
 0
82: iplt 0,-H[2]
 ,0
83: next I
84: plt S[2],
 S[3],0
85: for I=1 to N
86: iplt 0,S[6],
 0
87: iplt -H[1],
 0,0
88: iplt H[1],0,
 0
89: next I
90: plt S[2],
 S[4],-1
91: plt S[1],
 S[3],-2
92: for I=1 to N
93: iplt 0,S[6],
 0
94: iplt H[1],0,
 0
95: iplt -H[1],
 0,0
96: next I
97: plt S[1],
 S[4],0
98: for I=1 to M
99: iplt S[5],0,
 0
100: iplt 0,-
 H[2],0
101: iplt 0,H[2]
 ,0
102: next I
103: plt S[2],
 S[4],-1
104: csiz 1.5,2,
 1.357,0
105: for I=0 to
 M
106: S[1]+I*S[5]
 →U
107: -(len(str(U
 ))/2+.3)→V
108: plt U,S[3],
 0
109: cplt V,-
 1.25
110: lbl U
111: next I
112: fxd G[2]
113: for I=0 to
 N
114: S[3]+I*S[6]
 →U
115: -(len(str(U
 ))+1)→V
116: plt S[1],U,
 0
117: cplt V,-.3
118: lbl U
119: next I
120: csiz 1.5,2,
 1.357,0
121: plt A,C,0
122: cplt 0,2
123: lbl H$
124: plt A,C,0:
 cplt 0,1
125: lbl I$
126: plt A,C,0:
 cplt 0,0
```

```
127: lbl J$
128: csiz 1.75,
 2,1.357,0
129: -(len(B$)/
 2+.3)→V
130: (S[2]-S[1])
 /2+S[1]→U
131: plt U,S[3],
 0
132: cplt V,-3
133: lbl B$
134: deg
135: csiz 1.75,
 2,1.357,90
136: -(len(C$)/
 2+.3)→V
137: (S[4]-S[3])
 /2+S[3]→U
138: plt A,U,0
139: cplt V,-1
140: lbl C$
141: csiz 2,2,
 1.357,0
142: -(len(A$)/
 2+.3)→V
143: (S[2]-S[1])
 /2+S[1]→U
144: plt U,D,0
145: cplt V,-1
146: lbl A$
147: fxd 5;0→T;
 0→B;0→Y
148: ent "DO
 YOU WANT A CURR
 ENT-TIME PLOT?"
 ,E$
149: 1→P
150: if cap(E$)=
 "YES";sto "PLOT
 S"
151: ent "WANT
 A POTENTIAL-
 TIME PLOT?",E$
152: 3→P
153: if cap(E$)=
 "YES";sto "PLOT
 S"
154: ent "WANT
 AN INTEGRATED
 CHARGE PLOT?",
 E$
155: 5→P
156: if cap(E$)=
 "YES";sto "PLOT
 S"
157: dsp "POLARI
 ZATION PLOT
 WILL BE MADE";
 wait 2000
158: 9→P
159: "PLOTS":
160: for I=1 to
 Z by 2
161: if I=Z-1;
 sto "ENDPLT"
162: .001(I+1)L/
 2→T
163: (itf(Y$[2I-
 1,2I]).0005A[3]
 -A[1])F/A[5]→C
164: itf(Y$[2I+
 1,2I+2]).0005A[
 4]-A[2]+A[6]→V
165: jmp P
166: if T<S[1]
 or T>S[2];next
 I
167: dsp T,"sec
 ",C,"mA/sq.cm";
 plt T,C,-2;pen;
 next I
168: if T<S[1]
 or T>S[2];next
 I
169: dsp T,"sec
 ",V,"volts";
 plt T,V,-2;pen;
 next I
170: if T<S[1]
 or T>S[2];next
 I
171: dsp T,"sec
 ",W,"mCoul";-
 2T(B+C)/(I+1)→W
```

```
172: C+B→B
173: plt T;W;-2;
 pen;next I
174: if C<S[1]
 or C>S[2];next
 I
175: dsp C;"mA/
 sq.cm ";V;"volt
 s";plt C;V;-2;
 pen;next I
176: "ENDPLT":en
 t "DO YOU WANT
 ANOTHER PLOT?",
 E$
177: if cap(E$)=
 "YES";gto "PLOT
 "
178: stp ;end
*12853
```

Optimization Program for the Codeposition of Cd and Te

```
      program FCT (input,output)
c
c     This program fits the three rate constants, three symetery
c     factors, and the degree of dissociation of CdTe in the
c     deposit for an equimolar composition of Cd and Te.
c     The vector xguess contains the first guesses of
c     these parameters.  The logarithms of the rate constants
c     are used in the optimization routine.
c
c           xguess(1)=rkc(1)
c           xguess(2)=rkc(2)
c           xguess(3)=b(1)
c           xguess(4)=b(2)
c           xguess(5)=bet1=bet2
c           xguess(6)=rkc(3)
c           xguess(7)=b(3)
c
c     The program CT is used to predict the electrode
c     potential.  In this program, CT is used as a
c     subroutine.  The description of CT is given below.
c
c     The library routine LMDIF1 is used to mimimize the sum
c     sum of m nonlinear functions in n variables by a
c     modification of the Levenberg-Marquardt algorithm.
c     A general least-squares solver (LMDIF1) is used.
c     Subroutine fcn calculates the functions.  The Jacobian
c     is calculated by a foward-difference approximation.
c     [Garbow, Hillstrom, and More, Argonne National Laboratory,
c     March 1980]
c
c     subroutine CT
c
c     Nov. 5, 1984
c     This subroutine changes FNGC in order to model the
c     CdTe system.  The changes in FNGC allow for the
c     RAS model to be used instead of the NRTL model.
c     To incorporate these modifications, the following
c     changes are made:
c
c           1. The read statements are changed.
c           2. The print statements are changed.
c           3. The common statements are changed.
c           4. Subroutine act is changed.  The weighting
c              of all monolayers within the RSAT is set
c              equal to unity.  This is equivalent to
c              prop >> 1 in FNGC.
c
      common a(3),ac(3),alph1,alph2,b(3),bet1,bet2
```

```
      common c(3),cf(3),cg(3),csf(3)
      common d(3),den(3),densol,depth,dimcsf(3),e,eq(3),eref
      common fa,fitot(3),fr,ichose,n,ncom,op(3)
      common p,pi2,pi(3,2000),pmax,r,rka(3),rkc(3),rsat
      common s(3),t,tcyc,ts
      common v,x1,x2,x(3),xitot(3)
c
c     The next two common statements are needed only for FCT
c     and fcn.
      common /one/ ncyc,nopt,pmin,t2,t3,tprint
      common /two/ jpr,vexp(50)
      dimension fvec(50),iwa(7),wa(435),xguess(7)
      external fcn
      read 5, ncyc
    5   format(15x,i10)
c
      read 10, densol
      read 10, eref
      read 10, pmax
      read 10, pmin
      read 10, r
      read 10, rsat
      read 10, t2
      read 10, t3
      read 10, tprint
      read 10, ts
   10   format(15x,e10.3)
c
      read 15, (c(i),i=1,ncom)
      read 15, (d(i),i=1,ncom)
      read 15, (den(i),i=1,ncom)
      read 15, (eq(i),i=1,ncom)
      read 15, (s(i),i=1,ncom)
   15   format(15x,e10.3,2x,e10.3,2x,e10.3)
c
c     The optimization parameters are now entered.
c     tol is the error tolerance.
c     m is the number of data points.
c     nparm is the number of parameters to be fit.
c     lwa is (m*nparm + 5*nparm + m) normally.
      read 20, m
      read 20, nparm
      lwa=m*nparm + 5*nparm + m
   20   format(15x,i10)
c
      read 25, tol
      read 25, (xguess(i),i=1,nparm)
c     The logrithms of the rate constants are optimized.
      xguess(1)=alog10(xguess(1))
      xguess(2)=alog10(xguess(2))
      xguess(6)=alog10(xguess(6))
```

```
   25     format(15x,e10.3)
c
       read 30, (vexp(i),i=1,m)
   30     format(15x,f10.3)
c
c      The next statement pertains to the print out.
       jpr=0
c      The variable nopt is a counter for the optimization routine.
       nopt=0
c
c      END OF DATA ENTRIES
c
ccccccccccccccccccccccccccccccccccccccccccccccccccccccccccccccccccccccc
c
c      Call for parameter fit.
       call lmdif1(fcn,m,nparm,xguess,fvec,tol,info,iwa,wa,lwa)
       fnorm=enorm(m,fvec)
c      Print results.
       jpr=1
       call fcn(m,nparm,xguess,fvec,iflag)
       xguess(1)=10.**xguess(1)
       xguess(2)=10.**xguess(2)
       xguess(6)=10.**xguess(6)
       print 1000, fnorm,info,(xguess(i),i=1,nparm)
 1000    format(/5x,#Final L2 norm of the residuals = #,f15.7 //
     *          5x,#Exit parameter = #,2x,i10 //
     *          5x,#Final approximate parameters# //
     *          5x,#xguess(1), rkc(1)     = #,e15.8 /
     *          5x,#xguess(2), rkc(2)     = #,e15.8 /
     *          5x,#xguess(3), b(1)       = #,f15.12 /
     *          5x,#xguess(4), b(2)       = #,f15.12 /
     *          5x,#xguess(5), bet        = #,f15.12 /
     *          5x,#xguess(6), rkc(3)     = #,e15.8 /
     *          5x,#xguess(7), b(3)       = #,f15.12)
c
       stop
       end
c
ccccccccccccccccccccccccccccccccccccccccccccccccccccccccccccccccccccccc
c
       subroutine fcn(m,nparm,xguess,fvec,iflag)
c
       dimension fvec(50),xguess(7)
       common a(3),ac(3),alph1,alph2,b(3),bet1,bet2
       common c(3),cf(3),cg(3),csf(3)
       common d(3),den(3),densol,depth,dimcsf(3),e,eq(3),eref
       common fa,fitot(3),fr,ichose,n,ncom,op(3)
       common p,pi2,pi(3,2000),pmax,r,rka(3),rkc(3),rsat
       common s(3),t,tcyc,ts
       common v,xl,x2,x(3),xitot(3)
       common /one/ ncyc,nopt,pmin,t2,t3,tprint
```

```
      common /two/ jpr,vexp(50)
c
      sumfv=0.
c
c     The constraints (walls) are placed on the problem now.
      if(xguess(1).ge.-100.)2,2010
    2 if(xguess(1).le.100.)3,2010
    3 if(xguess(2).ge.-100.)4,2010
    4 if(xguess(2).le.100.)5,2010
    5 if(xguess(3).ge.0.)6,2010
    6 if(xguess(3).le.1.)7,2010
    7 if(xguess(4).ge.0.)8,2010
    8 if(xguess(4).le.1.)9,2010
    9 if(xguess(5).ge.0.)10,2010
   10 if(xguess(5).le.0.5)11,2010
   11 if(xguess(6).ge.-100.)12,2010
   12 if(xguess(6).le.100.)13,2010
   13 if(xguess(7).ge.0.)14,2010
   14 if(xguess(7).ge.1)go to 2010
c
c     The logarithms of the rate constants were used in the
c     optimization routine.
      xguess(1)=10.**xguess(1)
      xguess(2)=10.**xguess(2)
      xguess(6)=10.**xguess(6)
c
c     Define constants.
      fr=38.9442
      fa=96487.0
      pi2=3.141592654**2
c
c     The program variables are set equal to the vector xguess.
      rkc(1)=xguess(1)
      rka(1)=rkc(1)*exp(-eq(1)*fr*.529)
      rkc(2)=xguess(2)
      rka(2)=rkc(2)*exp(+eq(2)*fr*.403)
      b(1)=xguess(3)
      b(2)=xguess(4)
      bet1=xguess(5)
      bet2=bet1
      rkc(3)=xguess(6)
      rka(3)=rkc(3)
      b(3)=xguess(7)
c
c     The next statement relates alpha, the energy of interaction
c     parameter, with beta, the degree of dissociation parameter.
c     The reference given in suboutine act should be consulted
c     for questions.
c
      alph1=-4963.*alog(bet1**2./(3.57e-18*(1.-bet1**2.)))
      alph2=alph1
```

```
c
c
c       The substrate mole fractions are set and the diffusion
c       parameters are calculated.
        do 20 i=1,ncom
          a(i)=d(i)/(s(i)/.89298)**2
   20     continue
c
c       The total cycle time tl is
        tl=t2+t3
c
c       Initialize counters.
c       iter and kcount are used in order that the number of time
c       steps per cycle need not be equal to m, the number of
c       experimental data points to be optimized per cycle.
        k=0
        iter=int(tl/ts)/m
        kcount=iter-1
c
c       Start the program.....
        n=0
        t=0.0
c
c       Obtain the initial surface activities.
        call act
c
c       Print the output-column headings.
c       print 80
c  80     format(3x,#time#,4x,#tot cur#,4x,#cur 1#,5x,#cur 2#,5x,
c    *            #cur 3#,4x,#rsat x1#,4x,#rsat x2#,4x,#tot x1#,
c    *            4x,#tot x2#,4x,#tot x3#,4x,#depth#/)
c       print 90
c  90     format(3x,#time#,4x,#voltage#,3x,#overpot1#,2x,#overpot2#,
c    *            2x,#overpot3#,2x,#dimcsf1#,3x,#dimcsf2#,3x,#dimcsf3#,
c    *            3x,#gross x1#,2x,#gross x2#,2x,#rsat ac1#,2x,
c    *            #rsat ac2#/)
c
        ntot=ncyc*int(tl/ts)
        do 1000 n=1,ntot
          t=float(n)*ts
c
c         The applied current is now obtained.
          tcyc=amod(t,tl)
c         For linear sweep chronopotentiometry (LSC),   ichose=1
c         For pulsed current chronopotentiometry (PCC), ichose=2
          if(ichose.eq.2)go to 150
c
c         LSC
            if(tcyc.le.t2)go to 120
            p=(pmin-pmax)/t3 *(tl-tcyc) + pmax
            go to 160
```

```
  120       p=(pmin-pmax)/t2 *tcyc + pmax
            go to 160
c
c         PCC
  150       continue
            if(tcyc.le.t2)go to 155
            p=pmin
            go to 160
  155       p=pmax
c
  160     continue
c
c         The current independent functions cf(i) and cg(i)
c         are now obtained for both components.
            call conc
c
c         The electrode potential is now found.
            call genkin
c
c
c         The results are now printed.
c         if(amod(float(n),tprint).ne.0.)go to 900
c         print 200, t,p,pi(1,n),pi(2,n),pi(3,n),x(1),
c    *               x(2),xitot(1),xitot(2),xitot(3),depth
c 200       format(x,f8.4,x,4(f9.4,x),5(f9.6,x),e10.4)
c         print 201, t,v,op(1),op(2),op(3),dimcsf(1),dimcsf(2),dimcsf(3)
c    *               ,x1,x2,ac(1),ac(2)
c 201       format(x,f8.4,x,4(f9.5,x),5(f9.6,x),e9.2,x,e9.2/)
c
c         The relevant surface activities, mole fractions, and
c         the deposit thickness are now found.
c 900     continue
          call act
          if(t.le.float(ncyc-1)*t1)go to 1000
          kcount=kcount+1
          if(kcount.lt.iter)go to 1000
          k=k+1
          fvec(k)=vexp(k)-v
          sumfv=sumfv + sqrt(fvec(k)**2)
          if(jpr.eq.1)print 950, k,t,p,v,vexp(k),fvec(k)
  950       format(x,i3,x,4(f10.5,x),f10.5)
          kcount=0
          if(k.eq.m)nopt=nopt+1
          if(k.eq.m)print 960, (xguess(i),i=1,nparm),sumfv
  960       format(x,2(e15.8,x),2(f12.9,x),e12.6,x,e15.8,x,f12.9,x,f8.5)
          if(k.eq.m)sumfv=0.
ccccccccccccccccccccccccccccccccccccccccc
c         The next three lines can be used to stop the program
c         after one interation.
c         if(nopt.eq.1)print 970, nopt
c 970       format(x,/#STOP, nopt= #,i4)
```

```
c          if(nopt.eq.1)stop
ccccccccccccccccccccccccccccccccccccccccc
 1000      continue
        go to 2030
c
 2010   do 2020 k=1,m
          fvec(k)=10000.
 2020     continue
        go to 2040
c
 2030   xguess(1)=alog10(xguess(1))
        xguess(2)=alog10(xguess(2))
        xguess(6)=alog10(xguess(6))
c
 2040   continue
        return
        end
c
ccccccccccccccccccccccccccccccccccccccccccccccccccccccccccccccccccccccccccccccccc
c
        subroutine conc
c
c       This program calculates the concentration functions
c       cf(i) and cg(i).  The surface concentration can then
c       be obtained by c(surface)=cg(i) + pi(i,n)*cf(i).
c       Nisancioglu and Newman's current-step solution
c       and the Sand equation, are used along with
c       the method of superposition to solve for the
c       transient, convective mass transfer.
c       [Nisancioglu and Newman, J. Electroanal. Chem., 50(1974)23-39]
c
        common a(3),ac(3),alph1,alph2,b(3),bet1,bet2
        common c(3),cf(3),cg(3),csf(3)
        common d(3),den(3),densol,depth,dimcsf(3),e,eq(3),eref
        common fa,fitot(3),fr,ichose,n,ncom,op(3)
        common p,pi2,pi(3,2000),pmax,r,rka(3),rkc(3),rsat
        common s(3),t,tcyc,ts
        common v,x1,x2,x(3),xitot(3)
c
        dimension con(10),eig(10)
c
        pie=3.141592654
c
        con(1)=.663516066
        con(2)=.081564022
        con(3)=.034457046
        con(4)=.01962199
        con(5)=.0128965
        con(6)=.0092267
        con(7)=.0069829
        con(8)=.0055048
```

```
      con(9)=.0044645
      con(10)=.0037089
c
      eig(1)=2.58078493
      eig(2)=12.3099728
      eig(3)=24.4331401
      eig(4)=38.3054830
      eig(5)=53.5740271
      eig(6)=70.0220380
      eig(7)=87.5010784
      eig(8)=105.902059
      eig(9)=125.140833
      eig(10)=145.15016
c
      do 500 i=1,ncom
c       The function cf(i) is now obtained.
        w=a(i)*ts
        if(w.ge.0.01)go to 15
        cf(i)=2.0/(eq(i)*fa) *sqrt(ts/(pie*d(i)))
        go to 20
   15   cf(i)=0.0
        do 16 j=1,10
          cf(i)=cf(i) + con(j)*exp(-eig(j)*w)
   16     continue
        cf(i)=s(i)/(eq(i)*fa*d(i)) *(1.0 - cf(i)/.89298)
   20   continue
c
c       The function cg(i) is obtained here.
        cg(i)=0.0
        if(n.eq.1)go to 110
        do 100 k=1,n-1
          w=a(i)*ts*float(n-k+1)
          if(w.ge.0.01)go to 25
          w=pi2*d(i)/(4*s(i)**2) *ts*float(n-k+1)
          cg1=1.0 - 4.0*sqrt(w)/pie**1.5
          go to 30
   25     cg1=0.0
          do 26 j=1,10
            cg1=cg1 + con(j)*exp(-eig(j)*w)
   26       continue
          cg1=cg1/.89298
   30     w=a(i)*ts*float(n-k)
          if(w.ge.0.01)go to 35
          w=pi2*d(i)/(4*s(i)**2) *ts*float(n-k)
          cg2=1.0 - 4.0*sqrt(w)/pie**1.5
          go to 40
   35     cg2=0.0
          do 36 j=1,10
            cg2=cg2 + con(j)*exp(-eig(j)*w)
   36       continue
          cg2=cg2/.89298
```

```
   40       cgk=pi(i,k)*(cg1 - cg2)
            cg(i)=cgk + cg(i)
  100       continue
  110     cg(i)=c(i) - s(i)*cg(i)/(eq(i)*fa*d(i))
  500     continue
c
        return
        end
c
ccccccccccccccccccccccccccccccccccccccccccccccccccccccccccccccccccccccccccc
c
        subroutine genkin
c
c       This subroutine uses Butler-Volmer kinetics to calculate the
c       electrode potential.  The value of e calculated by this sub-
c       routine is not the electrode potential v.  v=e-eref+p*r
c       where eref is the potential difference between the reference
c       electrode and a SHE and r is the cell resistance.
c
        common a(3),ac(3),alph1,alph2,b(3),bet1,bet2
        common c(3),cf(3),cg(3),csf(3)
        common d(3),den(3),densol,depth,dimcsf(3),e,eq(3),eref
        common fa,fitot(3),fr,ichose,n,ncom,op(3)
        common p,pi2,pi(3,2000),pmax,r,rka(3),rkc(3),rsat
        common s(3),t,tcyc,ts
        common v,x1,x2,x(3),xitot(3)
c
        dimension q(3,3),z(7,3)
c
        do 20 i=1,ncom
          q(1,i)=(1.0-b(i))*eq(i)*fr
          q(2,i)=-b(i)*eq(i)*fr
          q(3,i)=(1.0 - 2.0*b(i))*eq(i)*fr
c
          z(1,i)=rka(i)*ac(i)
          z(2,i)=rkc(i)*cg(i)/densol
          z(3,i)=1.0/(eq(i)*fa)
          z(4,i)=rkc(i)*cf(i)/densol
          z(5,i)=z(1,i)*(1.0 - b(i))*fr/fa
          z(6,i)=z(2,i)*b(i)*fr/fa
          z(7,i)=z(1,i)*z(4,i)*eq(i)*fr
   20     continue
c
c       If n=1 or the Newton-Raphson becomes unstable,
c       the bisection method is used to find a bound
c       on e.  Then the Newton-Raphson is used to obtain e.
        if(n.gt.1)go to 45
   25   e1=2.
        e2=-3.
        do 41 k=1,50
          em=(e1+e2)/2.0
```

```
            hbil=-p
            hbim=-p
            do 30 i=1,ncom
              hbil=hbil + (z(1,i)*exp(q(1,i)*el) - z(2,i)*
     1            exp(q(2,i)*el))/(z(3,i) + z(4,i)*exp(q(2,i)*el))
              hbim=hbim + (z(1,i)*exp(q(1,i)*em) - z(2,i)*
     1            exp(q(2,i)*em))/(z(3,i) + z(4,i)*exp(q(2,i)*em))
     30       continue
            if(hbil*hbim.gt.0.0)go to 35
            e2=em
            go to 40
     35     el=em
     40     enew=(el+e2)/2.0
            change=abs((abs(enew) - abs(em))/enew)
            if(change.le.0.01)go to 44
     41     continue
c       If the next statement is executed, convergence was not achieved.
            print 42,em
     42       format(2x,#No convergence. em=#,e10.4)
            stop
c
c       The Newton-Raphson is now started.
     44     e=enew
     45     do 100 j=1,100
              h=-p
              dh=0.0
              do 50 i=1,ncom
                h=h + (z(1,i)*exp(q(1,i)*e) - z(2,i)*exp(q(2,i)*
     1            e))/(z(3,i) + z(4,i)*exp(q(2,i)*e))
                dh=dh + (z(5,i)*exp(q(1,i)*e) + z(6,i)*exp(q(2,i)*
     1            e) + z(7,i)*exp(q(3,i)*e))/(z(3,i) + z(4,i)*
     2            exp(q(2,i)*e))**2
     50         continue
              enew=e - h/dh
              change=abs((abs(enew) - abs(e))/enew)
              if(change.ge.0.5)go to 25
              e=enew
c             print 99, j,e
c    99         format(1x,i3,2x,f15.10)
              if(change.le.0.0005)go to 110
    100       continue
c
c       If a transfer to 110 was not made, convergence was not
c       achieved.
            print 105, e
    105       format(1x,#No convergence#,2x,f10.5)
            stop
c
c       The individual currents are now obtained.
    110     do 120 i=1,ncom
              pi(i,n)=(z(1,i)*exp(q(1,i)*e) - z(2,i)*exp(q(2,i)*e))/
```

```
     1            (z(3,i) + z(4,i)*exp(q(2,i)*e))
  120     continue
c
c       The surface concentration csf(i), the dimensionless
c       surface concentration dimcsf(i), and the surface
c       overpotential op(i) of each species are now calculated.
        do 130 i=1,ncom
          csf(i)=cg(i) + pi(i,n)*cf(i)
          if(c(i).eq.0.0)go to 130
          dimcsf(i)=csf(i)/c(i)
          if(ac(i).ne.0.0)go to 125
          op(i)=-9.999999
          go to 130
  125     op(i)=e - 1.0/(eq(i)*fr)* alog(rkc(i)*csf(i)/(
     1          densol*rka(i)*ac(i)))
  130     continue
c
c       The eletrode potential relative to a specified reference
c       electrode is now obtained.
        v=e - eref + p*r
c
        return
        end
c
ccccccccccccccccccccccccccccccccccccccccccccccccccccccccccccccccccccccccccc
c
        subroutine act
c
c       This subroutine determines the surface activities
c       of the components in the electrodeposit.  The RAS
c       activity model is used on each thickness of deposit
c       equivalent to the RSAT.  Monolayers below the RSAT
c       have no influence on the surface composition.
c       [Jordan, Metallurgical Transactions, 1(1970)239.]
c
        common a(3),ac(3),alph1,alph2,b(3),bet1,bet2
        common c(3),cf(3),cg(3),csf(3)
        common d(3),den(3),densol,depth,dimcsf(3),e,eq(3),eref
        common fa,fitot(3),fr,ichose,n,ncom,op(3)
        common p,pi2,pi(3,2000),pmax,r,rka(3),rkc(3),rsat
        common s(3),t,tcyc,ts
        common v,x1,x2,x(3),xitot(3)
c
        dimension flux(3)
c
        rgas=8.314
        temp=298
c
        if(n.ge.1)go to 10
c
c       Calculate the initial surface activities if t=0.0
```

```
          depth=0.0
          do 5 i=1,3
            fitot(i)=0.0
            x(i)=0.
            xitot(i)=0.
      5     continue
          xl=0.
          x2=0.
          go to 180
c
c         The variables are initialized.
     10   do 15 i=1,3
            flux(i)=0.0
            x(i)=0.0
     15     continue
          thick=0.0
c
c         Starting with the last time step, the rsat composition
c         is calculated.
          do 100 j=1,n
            k=n+1-j
c
c           The deposit thickness for each time step is now found.
c           Cathodic currents are taken as negative in this
c           work.  The calculation of the thickness for
c           each time step is approximate since it is assumed
c           that the equilibrium constant for Cd + Te = CdTe is
c           far to the right.  This is a valid approximation,
c           especially since we only want an estimate of the thick-
c           ness.  Later, when the depth of the total deposit is
c           calculated, a more rigoress treatment is used.
c           Amagats law is used when calculateing the thickness.
c
            fluxln=pi(1,k)/(eq(1)*fa)
            flux2n=pi(2,k)/(eq(2)*fa)
ccccccccccccccccccccccccccccccc
c
c           print 22, j,fluxln,flux2n
c  22         format(x,#j=       #,i15,/,
c     *             x,#fluxln= #,f15.13,/,
c     *             x,#flux2n= #,f15.13)
c
ccccccccccccccccccccccccccccccc
            if(fluxln.lt.0.)go to 24
            if(flux2n.lt.0.)go to 23
c           Cd and Te dissolved.
            tflux3=0.
            tflux2=flux2n
            tfluxl=fluxln
            go to 261
c           Cd deposited and Te dissolved.
```

```
   23     tflux3=0.
          tflux2=flux2n
          tflux1=flux1n
          go to 261
   24     if(flux2n.lt.0.)go to 25
c         Te deposited and Cd dissolved.
          tflux3=0.
          tflux2=flux2n
          tflux1=flux1n
          go to 261
c         Both Cd and Te deposited.
   25     if(flux2n.lt.flux1n)go to 26
c         More Te deposited than Cd.
          tflux3=flux2n
          tflux1=flux1n-flux2n
          tflux2=0.
          go to 261
c         More Cd deposited than Te.
   26     tflux3=flux1n
          tflux2=flux2n-flux1n
          tflux1=0.
c
c         thickn is the thickness per time step n.  If thickn
c         is greater than the rsat, the program is halted.
  261     thickn=-ts*(tflux1/den(1) + tflux2/den(2) +
     *           tflux3/den(3))
          if(thickn.le.rsat)go to 28
          print 27, n,t,thickn
   27       format(x,#The time step is too large.#,/,
     *           x,#n=      #,i15,/,
     *           x,#t=      #,f15.9,/,
     *           x,#thickn= #,e15.8)
          stop
   28     thick=thick + thickn
          flux(1)=flux(1) + flux1n
          flux(2)=flux(2) + flux2n
          ftot=flux(1) + flux(2)
ccccccccccccccccccccccccccccccc
c
c         print 29, tflux1,tflux2,tflux3,flux(1),flux(2),
c    *              thickn,thick
c  29      format(x,#tflux1 = #,f15.13,/,
c    *           x,#tflux2 = #,f15.13,/,
c    *           x,#tflux3 = #,f15.13,/,
c    *           x,#flux(1)= #,f15.13,/,
c    *           x,#flux(2)= #,f15.13,/,
c    *           x,#thickn = #,e15.8,/,
c    *           x,#thick  = #,e15.8)
c
ccccccccccccccccccccccccccccccc
c
```

```
c         The rsat composition is calculated if thick => rsat
c         or if j=n and we have scanned down to the electrode
c         substrate.
          if(j.eq.n)go to 36
          if(thick.lt.rsat)go to 100
   36     x(1)=flux(1)/ftot
          x(2)=flux(2)/ftot
c         Due to the numerical solution of this problem,
c         sometimes a very small, negative mole fraction
c         or a mole fraction slightly in excess or unity
c         can result.  This is corrected below.
          if(x(1).gt.1.)x(1)=1.
          if(x(1).lt.0.)x(1)=0.
          if(x(2).gt.1.)x(2)=1.
          if(x(2).lt.0.)x(2)=0.
ccccccccccccccccccccccccccccccc
c
c         print 37, x(1),x(2)
c  37       format(x,#x(1)= #,f15.10,/,
c    *             x,#x(2)= #,f15.10)
c
ccccccccccccccccccccccccccccccc
          go to 120
  100     continue
c
c       The relevant surface composition has now been obtained.  The
c       total deposit mole fractions and the deposit depth are now
c       obtained.  It is assumed that Amagat's law applys. The three
c       phases present are Te (1), Cd (2), and CdTe (3).
  120   ftotal=0.0
        do 170 i=1,2
          fitot(i)=fitot(i) + ts*pi(i,n)/(eq(i)*fa)
c         Because of the finite time steps, sometimes a very small
c         postive value of fitot(i) can result.  This is physically
c         unrealistic as it implys the original substrate dissolved.
          if(fitot(i).gt.0.0)fitot(i)=0.0
          ftotal=ftotal + fitot(i)
  170     continue
        do 175 i=1,2
          xitot(i)=fitot(i)/ftotal
  175     continue
        if(xitot(1).gt.0.5)alph=alph1
        if(xitot(1).gt.0.5)bet=bet1
        if(xitot(1).lt.0.5)alph=alph2
        if(xitot(1).lt.0.5)bet=bet2
        alph=alph/(rgas*temp)
        pact=sqrt(1. - 4.*xitot(1)*xitot(2)*(1. - bet**2.))
        x1=xitot(1)
        x2=xitot(2)
        xitot(1)=(x1-x2+pact)/(1.+pact)
        xitot(2)=(x2-x1+pact)/(1.+pact)
```

```
      xitot(3)=1.-xitot(1)-xitot(2)
      if(x1.le.0.)xitot(1)=0.
      if(x2.le.0.)xitot(2)=0.
      if(xitot(3).eq.1.)xitot(3)=0.
      depth=-ftotal*(xitot(1)/den(1) + xitot(2)/den(2) +
     *               xitot(3)/den(3))
c
c     The activities are now obtained.
  180 if(x(1).gt.0.5)alph=alph1 $ bet=bet1
      if(x(1).le.0.5)alph=alph2 $ bet=bet2
      alph=alph/(rgas*temp)
      pact=sqrt(1. - 4.*x(1)*x(2)*(1. - bet**2.))
      ac(1)=(x(1) - x(2) + pact)/(1. + pact)*exp(alph*x(2)**2.)
      ac(2)=(x(2) - x(1) + pact)/(1. + pact)*exp(alph*x(1)**2.)
c
c     Due to round-off errors, sometime a very small, negative value
c     of activity can result.  This is corrected below.
      if(ac(1).lt.0.)ac(1)=0.
      if(ac(2).lt.0.)ac(2)=0.
      if(x(1).le.0.)ac(1)=0.
      if(x(2).le.0.)ac(2)=0.
c
c     The next line would be used to calculate the activity of
c     CdTe.  For this program, ac(3) is the activity of hydrogen.
c     ac(3)=(1. - pact)/(1. + pact)*exp(alph/2.*(1. - 4.*x(1)*x(2)))
      ac(3)=1.
c
ccccccccccccccccccccccccccccccc
c
c     print 181, ac(1),ac(2),ac(3)
c 181 format(x,#ac(1)= #,e15.8,/,
c    *       x,#ac(2)= #,e15.8,/,
c    *       x,#ac(3)= #,e15.8,/)
c     if(n.eq.10)stop
c
ccccccccccccccccccccccccccccccc
c
      return
      end
c
ccccccccccccccccccccccccccccccccccccccccccccccccccccccccccccccccccccccccccccc
```

Data File for Cd-Te Optimization Program

ichose	2		
ncom	3		
ncyc	2		
densol	1.020e+03		
eref	0.000e+00		
pmax	-3.000e+01		
pmin	0.000e+00		
r	0.000e+00		
rsat	1.000e-09		
t2	5.000e-01		
t3	5.000e-01		
tprint	1.000e+00		
ts	1.000e-02		
c(i)	1.040e+00	1.060e+02	3.160e+02
d(i)	9.600e-10	3.600e-10	9.312e-09
den(i)	4.900e+04	7.690e+04	2.580e+04
eq(i)	4.000e+00	2.000e+00	1.000e+00
s(i)	1.580e-05	1.130e-05	3.359e-05 [2500 rpm]
m	50		
nparm	7		
tol	1.000e-10		
xguess(1)	1.000e-01	[rkc(1)]	
xguess(2)	3.000e-05	[rkc(2)]	
xguess(3)	1.000e-01	[b(1)]	
xguess(4)	1.500e-01	[b(2)]	
xguess(5)	5.500e-02	[beta]	
xguess(6)	1.500e-07	[rkc(3)]	
xguess(7)	5.000e-01	[b(3)]	
101	.073	The next 50 points are for run	
102	.055	#9218412. (2500 rpm)	
103	.039		
104	.024		
105	.013		
106	.009		
107	-.005		
108	-.016		
109	-.026		
110	-.036		
111	-.045		
112	-.053		
113	-.061		
114	-.066		
115	-.069		
116	-.071		
117	-.073		
118	-.074		
119	-.075		
120	-.076		

121	-.076
122	-.077
123	-.078
124	-.079
125	-.079
126	-.080
127	-.052
128	-.038
129	-.025
130	-.014
131	-.004
132	.005
133	.012
134	.016
135	.023
136	.029
137	.035
138	.040
139	.045
140	.050
141	.056
142	.061
143	.066
144	.071
145	.076
146	.080
147	.084
148	.087
149	.090
150	.096

Chapter 4.

Triangular Current-Sweep Chronopotentiometry at Rotating Disk and Stationary, Planar Electrodes

Cyclic chronopotentiometric and chronoamperometric techniques have been shown to be particulary useful in the study of electrode reactions. (1) In the study of these electrochemical methods, the question arises: Can one more conveniently obtain kinetic, thermodynamic, and transport information by controlling the potential or the current? In chronoamperometric experiments, the potential is a programmed function, and the current is a dependent variable. This method has the advantage of using the reversible cell potential, an easily calculated value, as a reference point. In chronopotentiometric experiments, the current is a programmed function, and the potential is a dependent variable. The relevant diffusion-limited current and zero current represent two references.

Potential-controlled processes are usually more difficult to describe mathematically. In this case, a kinetic expression relating the cell current, electrode potential, and ionic surface concentrations of the reactant and product species must be introduced as a boundary condition to link the controlled potential to the mass-transport problem. For current-controlled processes, on the other hand, the mass-transport problem avoids kinetic considerations, provided only one electrochemical reaction takes place and the rate of reaction is uniform along the electrode surface.

In this work, we develop the required mass-transfer solutions for triangular current-sweep chronopotentiometry at a rotating disk electrode (RDE) and at a stationary, planar electrode (SPE). The solutions are shown to

converge rapidly and are easily implemented. Analogous solutions for triangular potential-sweep chronoamperometry (cyclic voltammetry) do not exist for electrode processes with kinetic resistance. Andricacos and Ross have published solutions for triangular potential-sweep chronoamperometry at an RDE (2) and at an SPE (3), in the absence of kinetic resistance. Their elegant mathematics yielded solutions more cumbersome than those presented in this work. In a later publication (4) they compared their models with experimental results for the electrodeposition of silver, a reversible system. In the present work, the kinetic processes are easily addressed; because of this, we are able to use a multidimensional optimization routine to fit experimental data by adjusting appropriate physicochemical constants.

The effects of double-layer charging, migration, and a non-uniform potential field are neglected in this treatment. The experiments reported in this work were designed to minimize these effects, to demonstrate the applicability of the theoretical results, and to study the technologically important cadmium deposition process.

Triangular Current-Sweep Chronopotentiometry at an SPE

Fick's second law, the diffusion equation, is used to describe the transport of reactants and products:

$$\frac{\partial c_i}{\partial t} = D_i \frac{\partial^2 c_i}{\partial y^2} \quad . \qquad [4\text{-}1]$$

The initial condition is uniform concentration,

$$c_i(0,y) = c_i^{\infty} \quad , \qquad [4\text{-}2]$$

and the two boundary conditions are bulk concentration of species far from

the electrode,

$$c_i(t,\infty) = c_i^{\infty} \quad , \qquad [4\text{-}3]$$

and Faraday's law relating the concentration gradient at the electrode surface to the programmed current function

$$\frac{\partial c_i(t,0)}{\partial y} = \frac{s_i i(t)}{nFD_i} \quad . \qquad [4\text{-}4]$$

The electrode reaction is written as

$$ne^- \underset{k_a}{\overset{k_c}{\rightleftarrows}} \sum_i s_i M_i^{z_i} \quad . \qquad [4\text{-}5]$$

For $s_i > 0$, the species is an anodic reactant. For $s_i < 0$, the species is a cathodic reactant.

The triangular-sweep function $i(t)$ can be expressed by a Fourier series (5)

$$i(t) = i_I + (i_{II} - i_I)\left(\frac{1}{2} - \frac{4}{\pi^2}\sum_{j=1,3,\ldots}^{j=\infty} \frac{1}{j^2}\cos\frac{j\pi t}{L}\right) . \qquad [4\text{-}6]$$

This programmed current density is depicted in Fig. 4-1.

Using Duhamel's theorem, Eqs. [4-1] - [4-4] can be replaced by

$$c_i^{surf} - c_i^{\infty} = -\frac{s_i}{nF\sqrt{\pi D_i}}\int_0^t i(\lambda)(t-\lambda)^{-\frac{1}{2}} d\lambda \quad . \qquad [4\text{-}7]$$

This equation, derived in Appendix 4, has appeared numerous times in the SPE chronopotentiometry literature. (6-11) Two reviews (12,13) also cover the SPE literature.

After Eq. [4-6] is substituted into Eq. [4-7] and the required integration

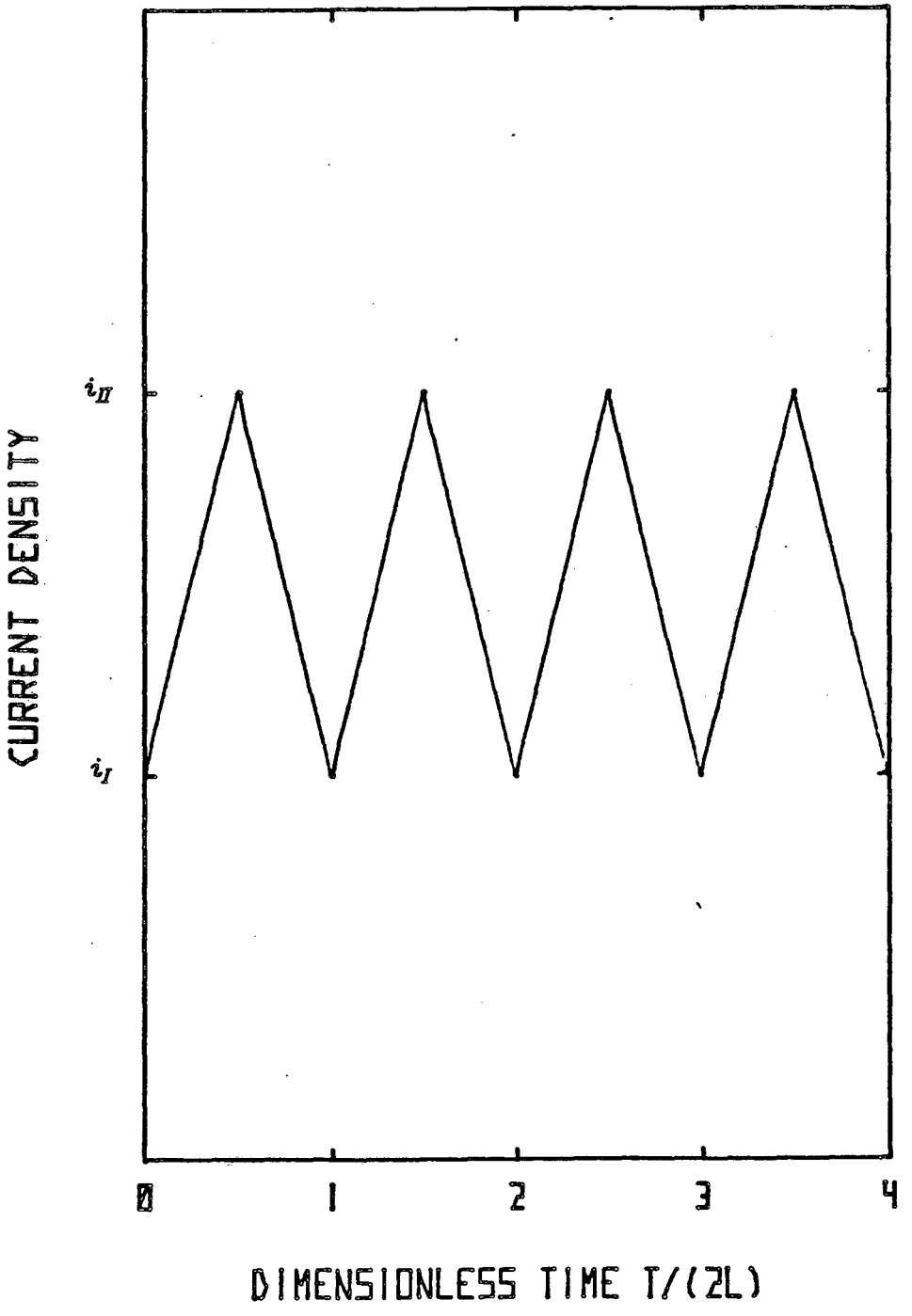

Figure 4-1. Periodic current source. For the experiments in this work, $i_I = 0$ and $i_{II} = -1.53\ \mathrm{mA/cm^2}$.

is performed, the following solution is obtained:

$$\frac{c_i^{surf}}{c_i^{\infty}} = 1 - \frac{s_i(i_{II} - i_I)}{nFc_i^{\infty}}\left(\frac{L}{\pi D_i}\right)^{\frac{1}{2}}\left\{\left[1 + \frac{i_I}{2(i_{II} - i_I)}\right]\left(\frac{t}{L}\right)^{\frac{1}{2}} - \frac{8}{\pi^2}\sum_{j=1,3,\ldots}^{j=\infty}\frac{1}{\sqrt{2j^5}} \times \right.$$

$$\left.\left[\cos\left(\frac{j\pi t}{L}\right)C_F\left(\sqrt{2jt/L}\right) + \sin\left(\frac{j\pi t}{L}\right)S_F\left(\sqrt{2jt/L}\right)\right]\right\} \qquad [4\text{-}8]$$

The functions C_F and S_F are Fresnel integrals. They are tabulated, and the following expressions can be used to evaluate them: (14)

$$C_F(x) = \frac{1}{2} + f(x)\sin\left(\frac{\pi}{2}x^2\right) - g(x)\cos\left(\frac{\pi}{2}x^2\right) \qquad [4\text{-}9]$$

$$S_F(x) = \frac{1}{2} - f(x)\cos\left(\frac{\pi}{2}x^2\right) - g(x)\sin\left(\frac{\pi}{2}x^2\right) \qquad [4\text{-}10]$$

$$f(x) = \frac{1 + 0.926x}{2 + 1.792x + 3.104x^2} + \epsilon(x) \qquad [4\text{-}11]$$

$$g(x) = \frac{1}{2 + 4.142x + 3.492x^2 + 6.670x^3} + \epsilon(x) \qquad [4\text{-}12]$$

$$|\epsilon(x)| \leq 0.002$$

For values of t greater than L, C_F and S_F rapidly approach $\frac{1}{2}$. The concentration expression can be further simplified since a relatively accurate answer is obtained if only the $j = 1$ term is kept in the series. This is shown in Fig. 4-2, where a plot of the surface concentration is given. With these approximations, and for $i_I = 0$, the concentration expression simplifies to

$$\frac{(c_i^{\infty} - c_i^{surf})nF}{s_i i_{II}}\left(\frac{\pi D_i}{L}\right)^{\frac{1}{2}} = \left(\frac{t}{L}\right)^{\frac{1}{2}} - \frac{2\sqrt{2}}{\pi^2}\left[\cos\left(\frac{\pi t}{L}\right) + \sin\left(\frac{\pi t}{L}\right)\right]. \qquad [4\text{-}14]$$

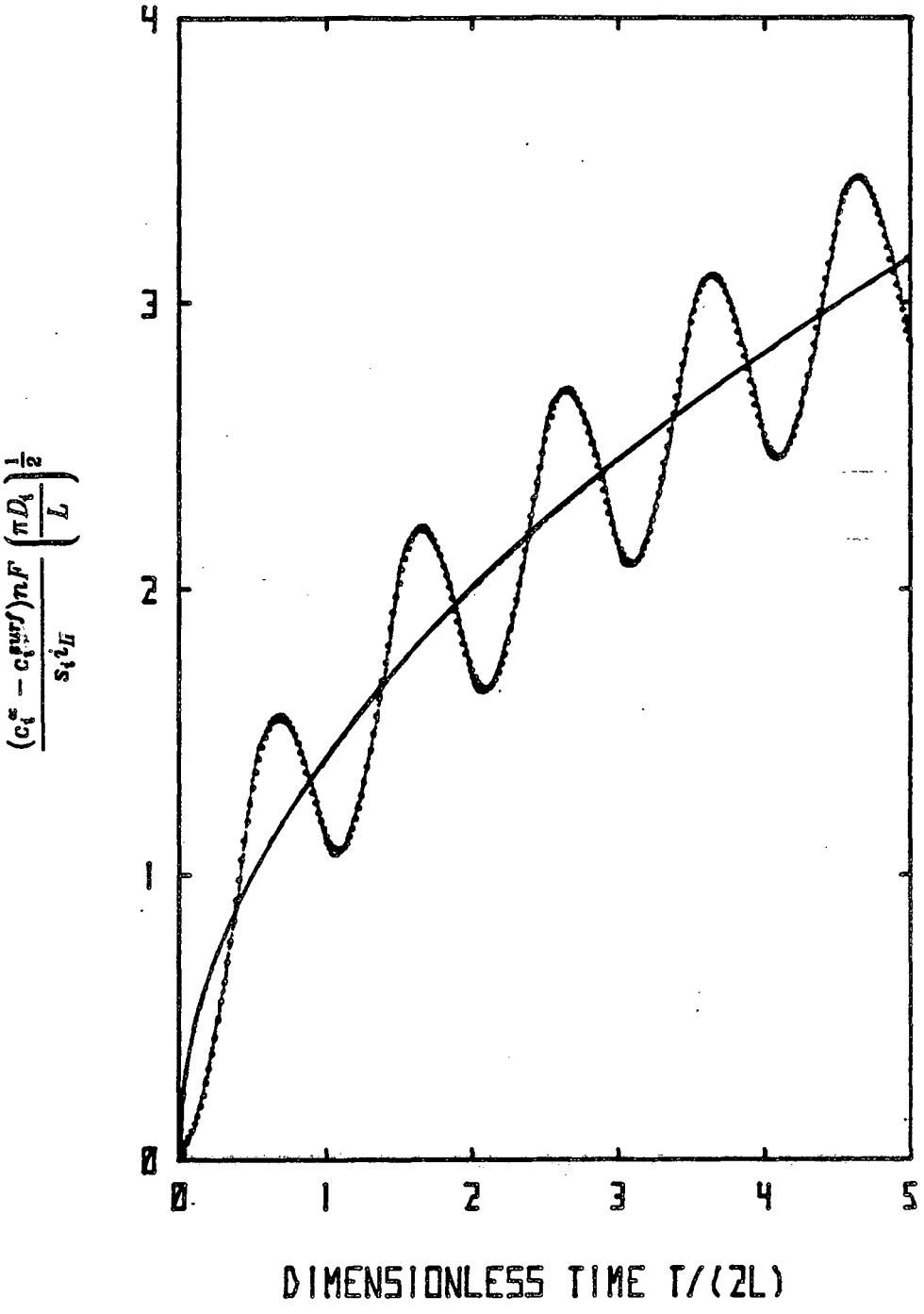

Figure 4-2. The dimensionless concentration for the SPE. The periodic solution is represented by the wavy, solid curve. The dotted curve results if only the $j = 1$ term is retained in the series. The solid, monotonic curve represents the SPE solution if the current were stepped to $i_{II}/2$. For this plot, $i_I = 0$.

Equation [4-14] represents a satisfying result of this work. The relatively cumbersome mathematical description of the SPE system has been simplified to yield a compact and accurate solution for the surface concentrations. It is evident that the concentration oscillates about the value corresponding to a current step to $\frac{i_{II}}{2}$, the average current density for the process.

Triangular Current-Sweep Chronopotentiometry at an RDE

Current-controlled electrolysis at an RDE has received a great deal of attention. (15-24) In a general treatment for the RDE system incorporating both radial and axial variations in concentration and potential, dimensionless groups arise which contain the disk radius, rotation rate, current density, and other transport and kinetic parameters. (17) Experiments can be easily constructed to remove radial effects (18), as can be seen by an analysis of the appropriate dimensionless groups. For experimental conditions consisting of a small disk, low reactant and product concentrations, and a well supported electrolyte, a one-dimensional treatment (excluding radial variations) can be used to analyze rigorously the RDE system. In the present work, a one-dimensional convective-diffusion equation is used to model the transport of the reactants and products:

$$\frac{\partial c_i}{\partial t} + v_y \frac{\partial c_i}{\partial y} = D_i \frac{\partial^2 c_i}{\partial y^2} \qquad [4\text{-}15]$$

The velocity normal to the disk surface is given by (21,22)

$$v_y = -0.51023\,\omega^{\frac{3}{2}} \nu^{-\frac{1}{2}} y^2 \ . \qquad [4\text{-}16]$$

The initial and boundary conditions are given by Eqs. [4-2], [4-3], and [4-4].

The electrode reaction is given by Eq. [4-5], and the current density is expressed in Eq. [4-6].

To obtain a solution, an integral analogous to Eq. [4-7] is required. In their classic treatment, Rosebrugh and Lash Miller (15) obtained such an integral for the case of pure diffusion, which can be modeled by Eqs. [4-1] (the diffusion equation), [4-2], [4-4], and the boundary condition

$$c_i(y,\delta_i) = c_i^{\infty} \quad . \tag{4-17}$$

where δ_i represents the thickness of a stagnant diffusion layer. Pesco and Cheh have made use of this approach to model periodic-current chronopotentiometry at an RDE. (20)

The convective-diffusion equation, Eq. [4-15], subject to the conditions given by Eqs. [4-2], [4-3], and [4-4] can be replaced by the following superposition integral. (19,27)

$$c_i(\theta_i,\zeta_i) - c_i^{\infty} = \int_0^{\theta_i} \frac{\partial c_i(\lambda,0)}{\partial \zeta_i} \frac{\partial}{\partial \lambda} \Theta_{F,i}(\theta_i - \lambda,\zeta_i) d\lambda \quad . \tag{4-18}$$

The new variables are

$$\theta_i = \frac{D_i t}{\delta_i^2} \quad , \tag{4-19}$$

$$\delta_i = \left(\frac{3D_i}{0.51023\nu}\right)^{\frac{1}{3}} \left(\frac{\nu}{\omega}\right)^{\frac{1}{2}} \quad , \tag{4-20}$$

$$\zeta_i = \frac{y}{\delta_i} \quad , \text{and} \tag{4-21}$$

$$\Theta_{F,i} = \frac{c_i}{\left[\frac{\partial c_i(\theta,0)}{\partial \zeta_i}\right]} \quad . \tag{4-22}$$

In contrast to the SPE system, the RDE system has a characteristic length δ_i, which is representative of the the region where the concentration differs from c_i^∞; however, the convective-diffusion equation is used to model the transport, and δ_i is used only to nondimensionalize the problem. Since the SPE system has no characteristic length, the complete mass-transfer solution can be displayed in Fig. 4-2 by a single curve. Such a convenient plot for the RDE system cannot be constructed.

The dimensionless concentration function $\Theta_{F,i}$ results from the flux-step problem, described by the convective-diffusion equation, along with conditions [4-2], [4-3], and a flux-step for the last boundary condition. The solution for the flux-step problem is

$$\Theta_{F,i} = \int_{\zeta_i}^{\infty} e^{-x^3}\,dx - \sum_{k=0}^{k=\infty} B_k Z_k(\zeta_i) e^{-b_k \theta_i} \quad . \qquad [4\text{-}23]$$

Equations [4-18] and [4-23] result from the work of Nisancioglu and Newman. The values of B_k and b_k are given in Appendix 4. At the electrode surface, the eigenfunction Z_k is equal to unity. Using Fick's law, the normal gradient $\frac{\partial c_i}{\partial \zeta_i}$ in Eq. [4-18] can be related to the current density $i(t)$. After combining Eqs. [4-6], [4-18], and [4-23] and integrating, the following expression can be obtained for the concentrations

$$\frac{(c_i^{\infty} - c_i)nFD_i}{s_i(i_{II} - i_I)} = \left(\frac{1}{2} + \frac{i_I}{i_{II} - i_I}\right)\sum_{k=0}^{k=\infty} B_k Z_k(1 - e^{-b_k\theta_i}) - \frac{4}{\pi^2}\sum_{k=0}^{k=\infty} b_k B_k Z_k \sum_{j=1,3,\ldots}^{j=\infty} \quad [4\text{-}24]$$

$$\frac{1}{j^2\left[b_k^2 + \left(\frac{j\pi}{\theta_{L,i}}\right)^2\right]}\left\{b_k\cos\left(\frac{j\pi\theta_i}{\theta_{L,i}}\right)\left[1 + e^{-b_k\theta_i}\left\{\left(\frac{j\pi}{b_k\theta_{L,i}}\right)\sin\left(\frac{j\pi\theta_i}{\theta_{L,i}}\right) - \cos\left(\frac{j\pi\theta_i}{\theta_{L,i}}\right)\right\}\right]\right.$$

$$\left. + \left(\frac{j\pi}{\theta_{L,i}}\right)\sin\left(\frac{j\pi\theta_i}{\theta_{L,i}}\right)\left[1 - e^{-b_k\theta_i}\left\{\left(\frac{b_k\theta_{L,i}}{j\pi}\right)\sin\left(\frac{j\pi\theta_i}{\theta_{L,i}}\right) + \cos\left(\frac{j\pi\theta_i}{\theta_{L,i}}\right)\right\}\right]\right\}$$

where $\theta_{L,i} = \dfrac{D_i L}{\delta_i^2}$.

This solution can be considerably simplified. At the electrode surface, $Z_k = 1$. For $i_I = 0$ and long times, the solution can be further reduced to

$$\frac{(c_i^{\infty} - c_i^{surf})nFD_i}{s_i i_{II}} = \frac{1}{2}\Gamma\left(\frac{4}{3}\right) - \frac{4}{\pi^2}\sum_{k=0}^{k=\infty} b_k B_k \sum_{j=1,3,\ldots}^{j=\infty} \frac{1}{j^2\left[b_k^2 + \left(\frac{j\pi}{\theta_{L,i}}\right)^2\right]} \times \quad [4\text{-}25]$$

$$\left[b_k\cos\left(\frac{j\pi\theta_i}{\theta_{L,i}}\right) + \left(\frac{j\pi}{\theta_{L,i}}\right)\sin\left(\frac{j\pi\theta_i}{\theta_{L,i}}\right)\right].$$

As was observed for the SPE system, this solution oscillates about the solution for a current step to $\dfrac{i_{II}}{2}$, the average current density during the process.

The Current-Potential Expression

The most accessible experimental variables are the total cell current and the potential of the working electrode with respect to a suitable reference. We shall therefore relate the predicted concentrations to the programmed current density and the measured potential by a Butler-Volmer kinetic expression

$$\frac{i}{nF} = k_a e^{(1-\beta)nfV} \prod_i a_i^{s_i} - k_c e^{-\beta nfV} \prod_i a_i^{-s_i} \quad , \qquad [4\text{-}26]$$

where $f = \frac{F}{RT}$, a_i represents the activity of species i, and

$$V = E + \left[U^0_{ref} - \frac{1}{n_{ref} f} \sum_i s_{i,ref} \ln a_{i,ref} \right] - ir \quad . \qquad [4\text{-}27]$$

The bracketed term in Eq. [4-27] represents the open-circuit potential difference between the reference electrode and a standard hydrogen electrode (SHE). E is the measured potential between the working electrode and the reference electrode. The last term in Eq. [4-27] accounts for the ohmic drop between the working electrode and the reference electrode. Therefore, the potential difference between the working electrode and a SHE, corrected for ohmic drop, is represented by V.

For dilute solutions, the activities in Eq. [4-26] can be replaced by concentrations. For the discharge of a metal ion ($a_{solid} = 1$) in a dilute system with negligible ohmic drop, Eqs. [4-26] and [4-27] can be combined to yield

$$\frac{i}{nF} = k_a e^{(1-\beta)nfE} - k_c e^{-\beta nfE} \left(\frac{c_i^{surf}}{\rho_o} \right) . \qquad [4\text{-}28]$$

The SHE has been taken as a reference, and a first-order reaction has been assumed. Since a SHE has been assumed, the bracketed term in Eq. [4-27] is

zero. It should be noted that the concentration overpotential is included in this treatment since the surface concentration of the discharging metal ion is used. Equation [4-28] contains two independent kinetic parameters, β and the magnitude of either k_c or k_a . The Gibbs free energy of reaction fixes the ratio $\frac{k_c}{k_a}$.

In this work, the electrodeposition of cadmium from dilute, aqueous, $CdSO_4 - K_2SO_4$ solutions has been chosen to test the viability of the theoretical model. The deposition of cadmium from a well supported, aqueous electrolyte, a technologically important process, has been the subject of a number of fundamental studies. (28-39) Furthermore, since cadmium alloys are also commonly electrodeposited, understanding the Cd^{2+} discharge behavior is desirable for these processes as well.

Burstein (39) describes the present state of understanding of the kinetics of the cadmium electrode as follows: "Even in acid-sulfate and perchlorate solutions in which the metal does not equilibrate with the oxides, there is no agreement regarding its mechanism of dissolution." It is not clear whether a one-step mechanism,

$$Cd^{2+} + 2e^- \underset{k_a}{\overset{k_c}{\rightleftharpoons}} Cd \qquad [4\text{-}29]$$

described by Eq. [4-28], or a two-step mechanism, involving a Cd^+ species, should be used to capture the salient features of the kinetic behavior. (29,30,31,32,35,36,37,38)

Since the Cd^+ species has never been shown to exist as a stable ion in solution, it is postulated that Cd^+ is adsorbed at the electrode surface. The

proposed mechanism is:

$$Cd^{2+} + e^- \underset{k_{a,1}}{\overset{k_{c,1}}{\rightleftharpoons}} Cd^{+}_{ads} \qquad [4\text{-}30]$$

$$Cd^{+}_{ads} + e^- \underset{k_{a,2}}{\overset{k_{c,2}}{\rightleftharpoons}} Cd \qquad [4\text{-}31]$$

This mechanism appears in the metal-deposition literature for cadmium (30) and other metal/metal-ion systems. (26,32) With our nomenclature, the current-potential expression for the two-step process, given by Eqs. [4-30] and [4-31], (referred to with subscripts 1 and 2, respectively) is

$$\frac{i}{2F} = \frac{k_{a1}k_{a2}e^{(2-\beta_1-\beta_2)fE} - k_{c1}k_{c2}e^{-(\beta_1+\beta_2)fE}\left(\frac{C^{surf}_{Cd^{2+}}}{\rho_o}\right)}{k_{c2}e^{-\beta_2 fE} + k_{a1}e^{(1-\beta_1)fE}} \qquad [4\text{-}32]$$

In writing Eq. [4-32], it is assumed that the time rate of change of the current is slow enough to allow reactions 1 and 2 to occur at the same rate ($i_1 = i_2 = \frac{i}{2}$), since the Cd^{+}_{ads} ions do not diffuse away from the electrode surface. For this reason, our experiments were conducted at relatively low frequencies. It should be noted that for $k_{c2} \gg k_{a1}$ or $k_{c2} \ll k_{a1}$, an apparent one-step current-potential expression results. We also have

$$\Delta G^{\circ}_1 = FU^{\circ}_1 = RT \ln \frac{k_{c1}}{k_{a1}} \text{, and} \qquad [4\text{-}33]$$

$$\Delta G^{\circ}_2 = FU^{\circ}_2 = RT \ln \frac{k_{c2}}{k_{a2}} ; \qquad [4\text{-}34]$$

and hence

$$U_1^\theta + U_2^\theta = -0.806 \text{ V}, \qquad [4\text{-}35]$$

the standard electrode potential for the reduction of Cd^{2+} to Cd. In Eqs. [4-33] and [4-34], the rate constants need not have the same units since the standard state activities of the products and reactants are also included in these expressions.

Equation [4-32] has five independent parameters: β_1, β_2, k_{c1}, k_{c2}, and U_1^θ. The ratios of the rate constants are fixed by Eqs. [4-33] and [4-34]. The sum $U_1^\theta + U_2^\theta$ is fixed by Eq. [4-35].

Neither Eq. [4-28] nor Eq. [4-32] can be solved explicitly for E. A Newton-Raphson routine which converges rapidly for each equation is outlined in Appendix 4.

Experimental

The experiments described below were designed to illustrate the utility of triangular current-sweep chronopotentiometry. We have chosen the deposition of cadmium because of its technological importance and because it offered two key advantages: the hydrogen overvoltage is very high on this metal, and cadmium ions are not complexed in the aqueous, potassium-sulfate electrolyte employed in this study.

A 5-mm-diameter, glassy-carbon disk electrode was employed in our experiments. Standard metallographic polishing techniques were used to remove all projections greater than one micron in height. The potential of the working electrode was measured against a mercury-mercurous sulfate reference electrode. For the RDE experiments, a Pine Instruments ASRP2 rotator was used. The Princeton Applied Research model 173 potentiostat/galvanostat controlled the operation of the cell. An Interstate

F77 function generator was used with the potentiostat/galvanostat. The data were stored on a Nicolet 1090A digital oscilloscope and later transferred to an HP9825 computer.

The electrolyte, a $0.0058-M-CdSO_4 / 0.25-M-K_2SO_4$ solution, was prepared from analytical reagent grade chemicals and distilled water which was passed through a Culligan water purification unit consisting of an organic trap, a deionizer, and a microfilter. The specific conductance of the treated water was 15 Mohm-cm. Nitrogen, first equilibrated with a similar electrolyte, was bubbled through the cell solution for 1 hour prior to experiments. A nitrogen atmosphere was maintained above the electrolyte during the experiment. The temperature was maintained at 25°C. Handbook values were used for the solvent density ρ_o ($0.001 \frac{kg}{cm^3}$) and the kinematic viscosity ν ($0.01 \frac{cm^2}{s}$).

The diffusion coefficient of Cd^{2+}, $3.6 \times 10^{-6} \frac{cm^2}{s}$, was calculated from the limiting current curves depicted in Fig. 4-3. The resulting Levich plot is shown in Fig. 4-4. The line drawn through the points in Fig. 4 was obtained by the method of least squares; the origin was not included in the linear regression.

Discussion

We have chosen a Levenberg-Marquardt algorithm to compare and contrast the theoretically predicted electrode potentials with the experimentally measured results. One basic algorithm for finding a minimum is the method of steepest descent, which goes back to Cauchy and his attempts to solve the problem of finding a minimum of a real-valued, multivariable func-

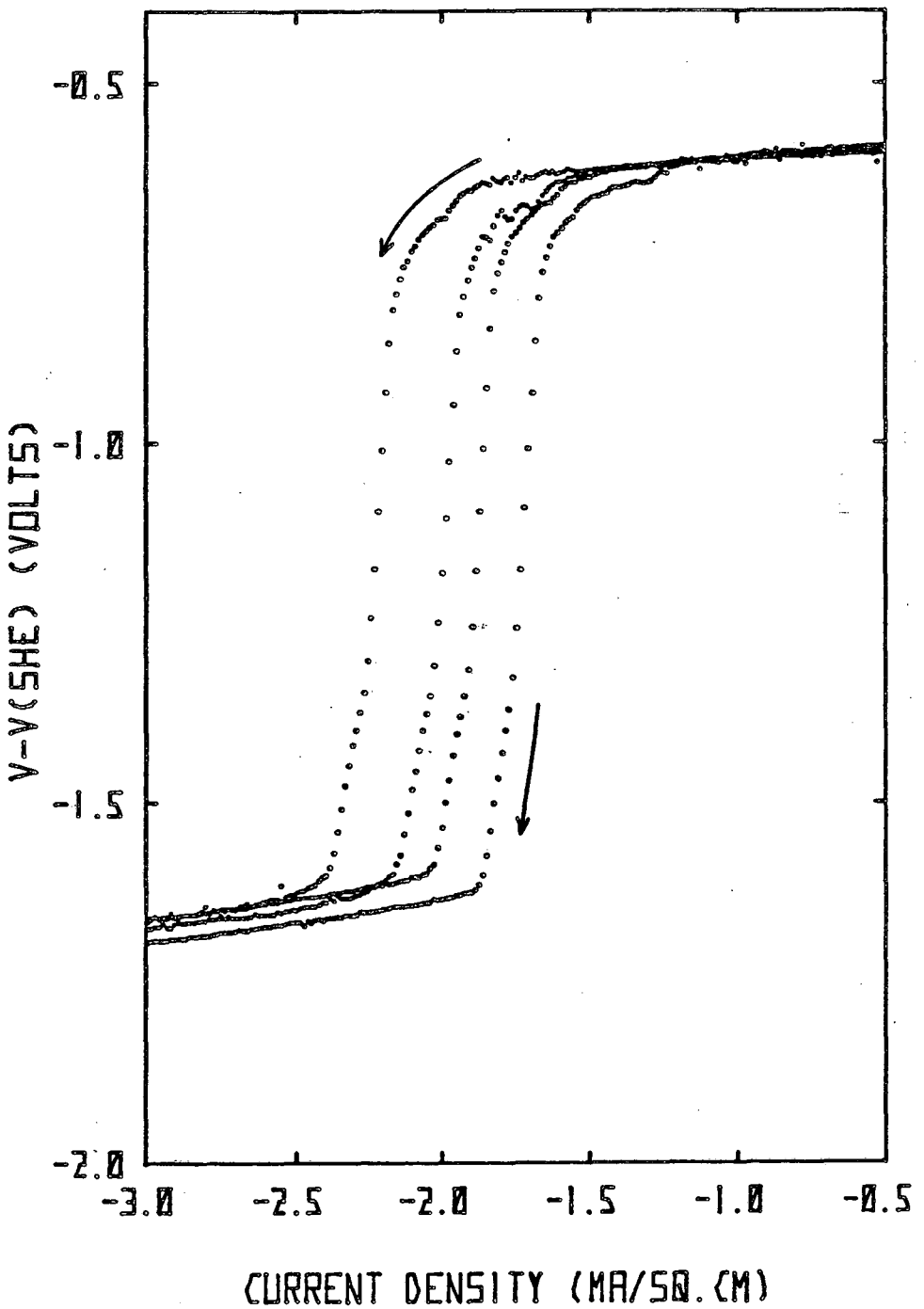

Figure 4-3. Limiting current curves for Cd^{2+}. The current is swept from 0 mA/cm^2 at a rate of $-0.75\ mA/min\text{-}cm^2$. From right to left, the curves represent 235, 275, 314, and 392 rpm.

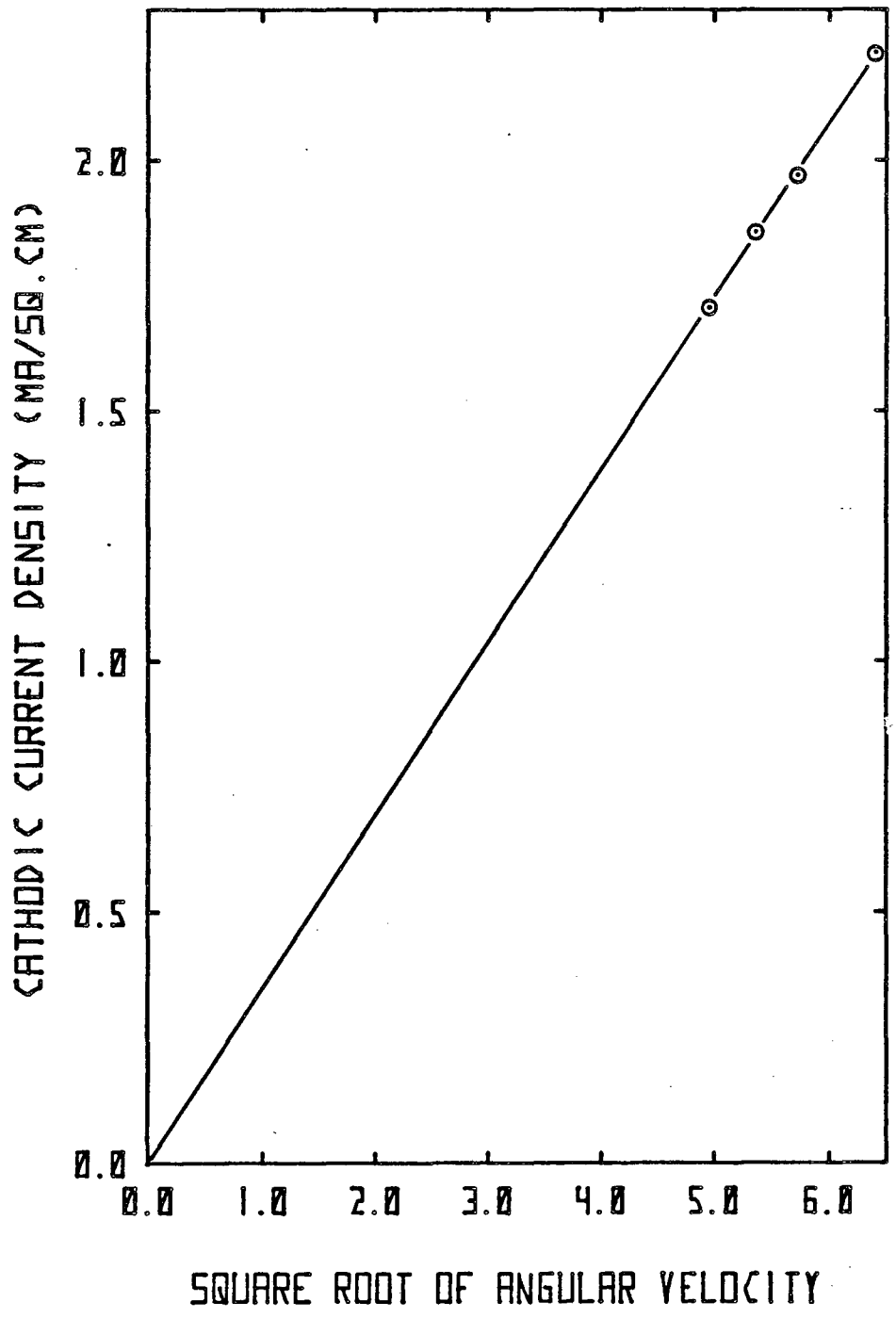

Figure 4-4. Levich plot for Cd^{2+}. These data yield $D_{Cd^{2+}} = 3.6 \times 10^{-6}$ cm^2/s.

tion by repeatedly finding minima of a function of one variable. Alternatively, the Newton-Raphson algorithm can be used to vary the parameters until the partial derivatives of the objective function $\sum_k (E_{k,theory} - E_{k,experiment})^2$ with respect to the parameters to be optimized are sufficiently close to zero. The Newton-Raphson method is often seen to diverge from the solution, while the method of steepest descent converges in an agonizingly slow and computationally expensive fashion. Levenberg (32) proposed a method to estimate intelligently a damping factor for the Newton-Raphson routine, while preserving the symmetry of the problem in order that simplified methods for the solution of linear, simultaneous equations could still be employed. Marquardt (33) proposed another modification which allowed a proper scaling of the problem by making use of the standard deviations of the partial derivatives in the Jacobian. Marquardt used a *maximum neighborhood* method which performs an optimum interpolation between the Newton-Raphson method and the method of steepest descent. The Levenberg-Marquardt routine we used was written by Garbow, Hillstrom, and More. (34) Another more recent method, the Simplex algorithm (35,36) is appealing; however, it does not converge as quickly as a Levenberg-Marquardt algorithm, which avoids the divergence problems of the Newton-Raphson without incurring unacceptable losses in speed. Three experiments, each with fifty data points, were used as data bases in the optimization program. Typically, the program used less than 500 CP seconds on a CDC 7600 computer. The computer program for the one-step mechanism is listed at the end of Appendix 4.

Results obtained from the RDE system were used to compare experiment and theory. With this system, natural convection, spherical diffusion,

and one-micron surface roughness will not be important considerations. This is less often the case for the SPE system.

After optimizing the two parameters for Eq. [4-28] and the five parameters for Eq. [4-32], we found that the two-step mechanism could not be used to represent the data better than the one-step mechanism. A number of initial guesses were attempted to ensure that the fit solution was indeed a global minimum. It is unfortunate that we could not prove or disprove the validity of the two-step mechanism; instead, it is shown that over a broad cathodic potential range the two-step mechanism cannot be used to represent the data better.

We originally introduced the two-step mechanism to ascertain whether it could better represent the cusp in the potential-time data shown at $\frac{t}{2L} = 0.25$ in Fig. 4-7. Since the data could not be better represented by the two-step mechanism, and since there is no physical evidence for the presence of Cd^+, we prefer the use of Eq. [4-28], representing the single-step charge transfer, for the current-potential relation. The optimized results, however, cannot be used to refute the two-step mechanism because it is possible that the kinetic constants for the one-step process represent lumped parameters.

The optimized parameters are:

$$\beta = 0.5707$$

$$k_c = 6.991 \times 10^{-17} \ \frac{\text{kg}}{\text{cm}^2 - \text{s}}$$

These parameters can be used to calculate an exchange-current density:

$$i_o = nFk_a^{\beta}k_c^{1-\beta}a_{Cd}^{\beta}(c_{Cd^{2+}}^{\infty})^{1-\beta} .$$

For the pure cadmium electrode, $a_{Cd} = 1$. The above equation can be used to calculate $i_o = 0.0897 \frac{mA}{cm^2}$. Vetter has cited (37) values of $\beta = 0.55$ and $i_o = 1.5 \frac{mA}{cm^2}$ for a similar $0.005-M-CdSO_4/0.8-M-K_2SO_4$ electrolyte, cadmium-electrode system at $20\,^{o}C$. The exchange-current densities differ by an order of magnitude, although the symmetry factors show close agreement.

The kinetic parameters can be used to calculate the appropriate dimensionless groups to verify the one-dimensional nature of the mass transport in the experiments. These calculations were made, and we conclude that the one-dimensional analysis, stated explicitly by Eq. [4-15], is a correct representation for this experimental system.

Calculated potential-time curves for the single-step, two-parameter mechanism are compared with experiment in Figs. 4-5, 4-6 and 4-7. Figure 4-8 displays the surface concentration during the high frequency experiment. The results for the five-parameter model could not be distinguished from the results for the two-parameter model. The uppermost curve in each figure represents the potential response which would result in the absence of kinetic resistance. These results represent the uniform and sustained periodic state; hence, Eq. [4-25] can be used to obtain the surface concentrations. When $\frac{t}{2L} = 0$, the current density is i_I. For $\frac{t}{2L} = 0.5$, the current density is i_{II}. In these experiments, $i_I = 0$ and $i_{II} = -1.53 \frac{mA}{cm^2}$. The low-frequency results are shown in Figs. 4-5 and 4-6. Both the model and experimental results display a pseudosteady state. For the low frequency cases,

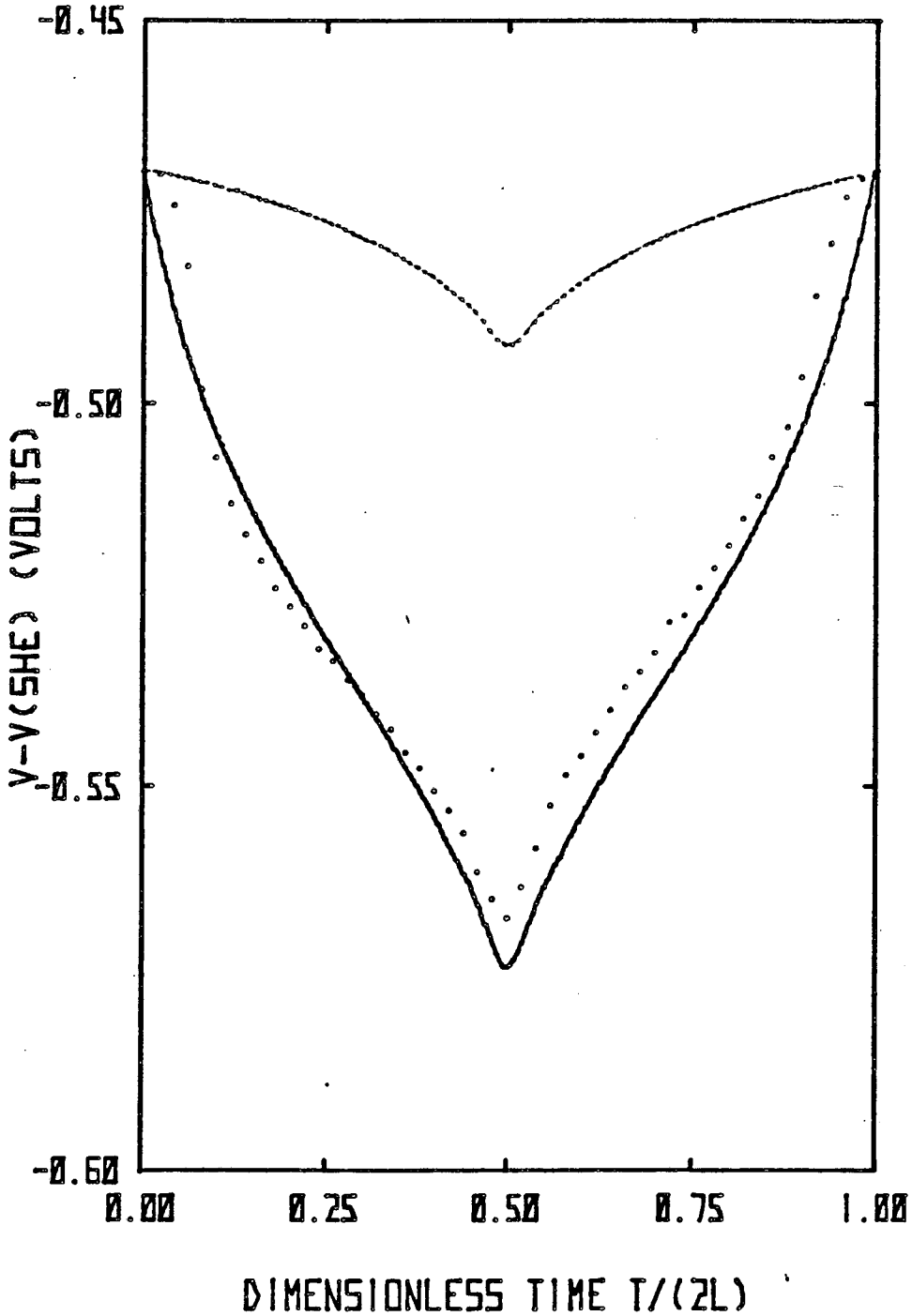

Figure 4-5. Electrode potential. Dotted curve: experimental data. (235 rpm, 0.01 Hz) Lower, solid curve: optimized model prediction. Upper, solid curve: theoretically calculated potential for no kinetic resistance.

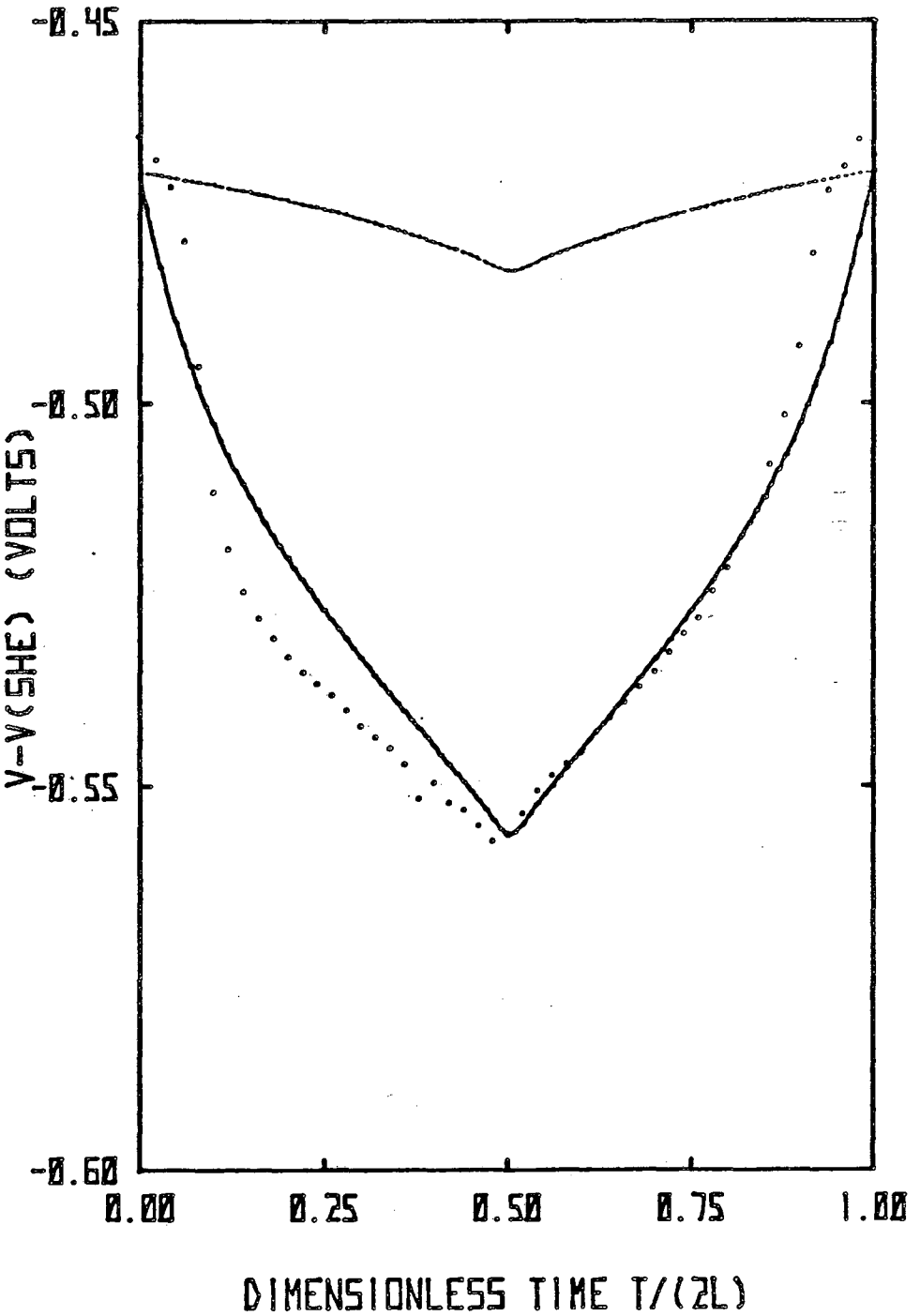

Figure 4-6. Electrode potential. Dotted curve: experimental data. (392 rpm, 0.01 Hz) Lower, solid curve: optimized model prediction. Upper, solid curve: theoretically calculated potential for no kinetic resistance.

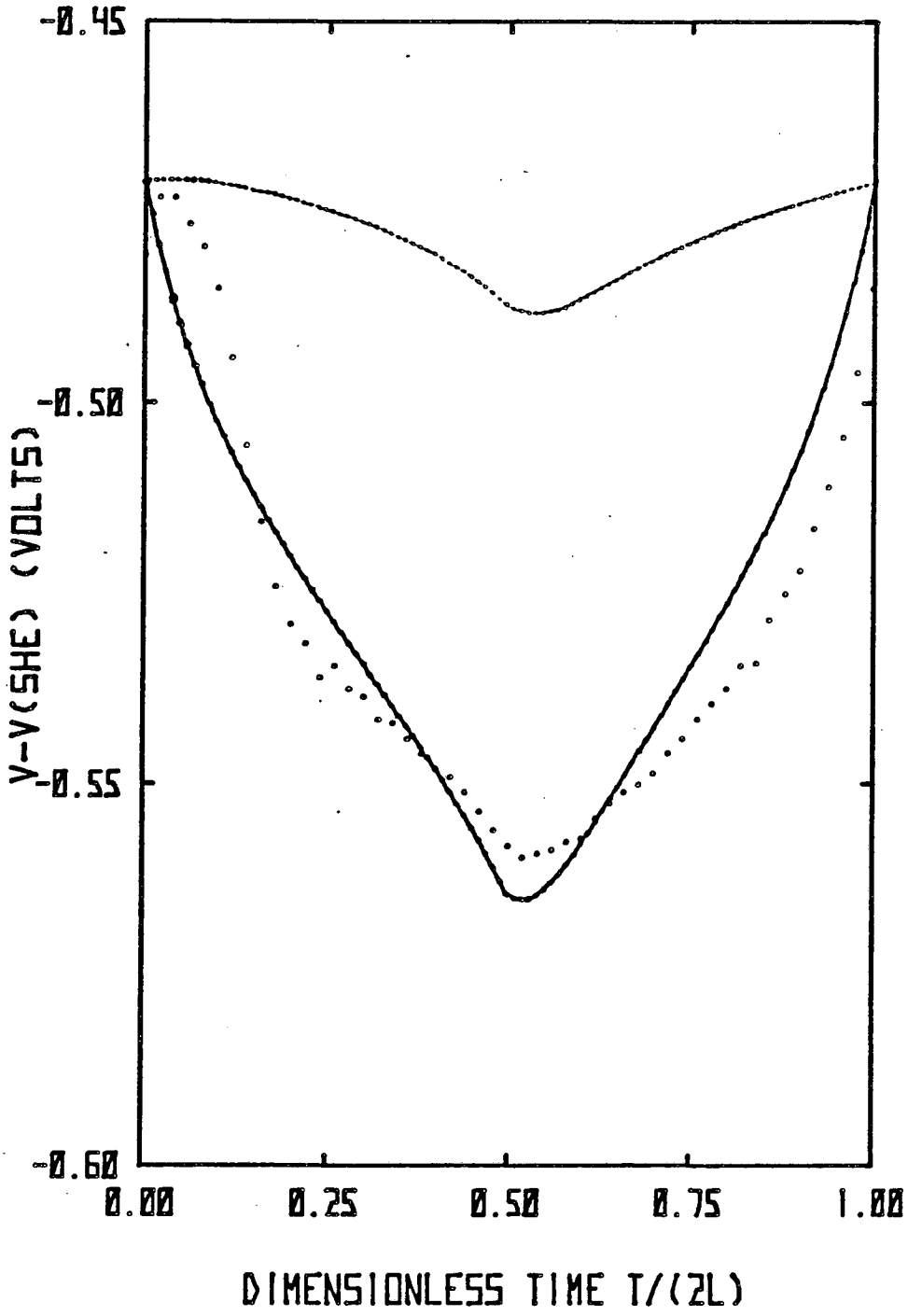

Figure 4-7. Electrode potential. Dotted curve: experimental data. (235 rpm, 0.1 Hz) Lower, solid curve: optimized model prediction. Upper, solid curve: theoretically calculated potential for no kinetic resistance. concentration during the higher frequency experiment.

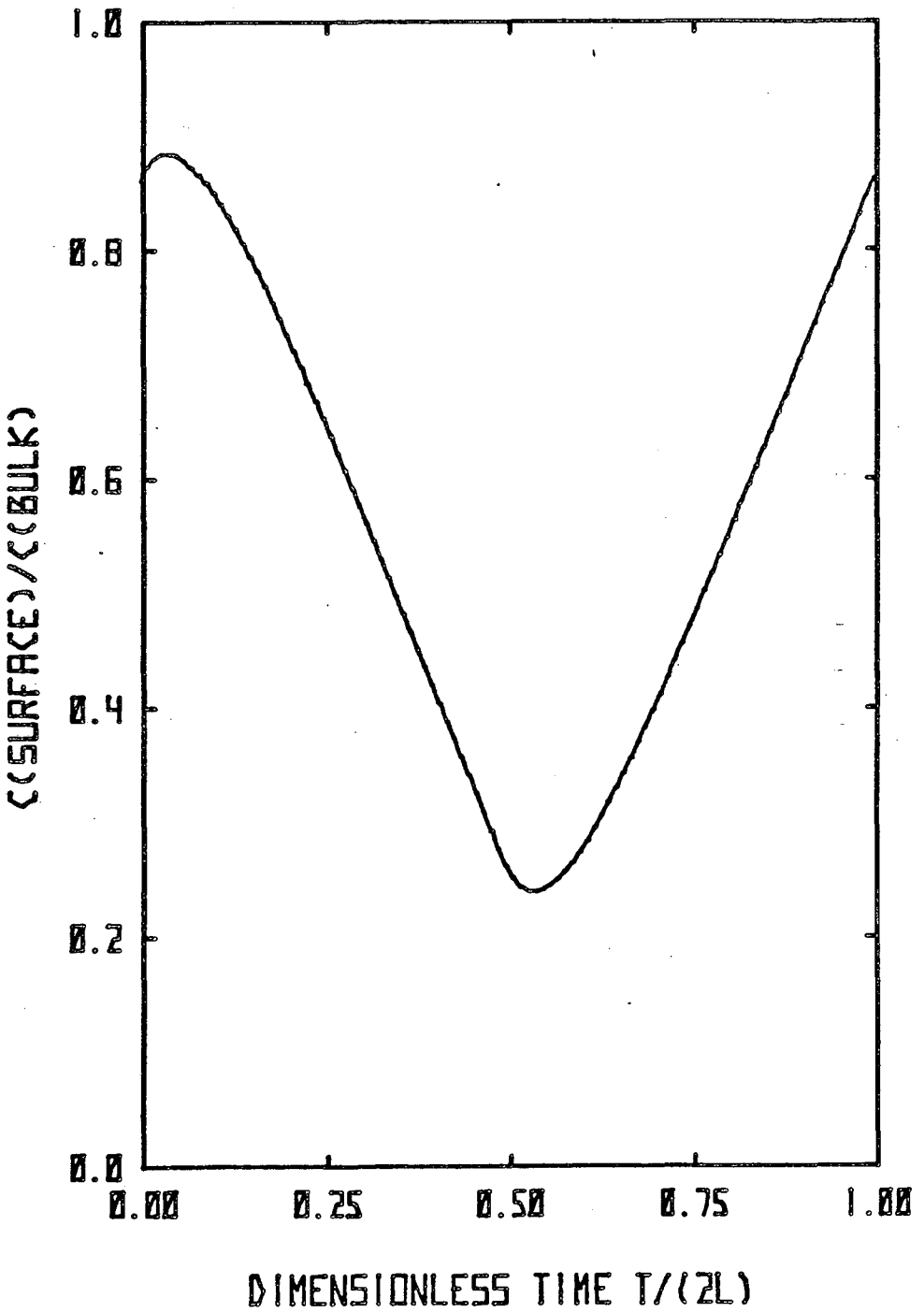

Figure 4-8. Surface concentration. The $c_{Cd^{2+}}^{surf}$ history during the uniform and sustained periodic state for the conditions of Fig. 7.

the concentration $c_{Cd^{2+}}^{surf}$ is lowest halfway through the cycle, when $i = i_{II}$. Correspondingly, the concentration overpotential has its largest magnitude at midcycle. This is particularly apparent in Fig. 4-5.

The slightly higher frequency results are shown in Figs. 4-7 and 4-8. Fig. 4-7 has a an asymmetric nature relative to Figs. 4-5 and 4-6 because the characteristic time L for the current sweep is of the same order of magnitude as the characteristic time $\frac{\delta_i^2}{D_i}$ for the mass transport. The corresponding concentration profile shown in Fig. 4-8 is asymmetric as well.

Conclusions

Convenient mass-transfer solutions have been obtained for triangular current-sweep chronopotentiometry at rotating disk and stationary, planar electrodes in the absence of free convection. Because the solutions can be evaluated efficiently, a numerical multidimensional-optimization routine, which requires a large number of functional evaluations, was used to compare and contrast the ability of various discharge mechanisms to match experimental data. Using the rotating disk system, we have examined the cadmium electrodeposition process. For a single-step, two-electron transfer mechanism, the optimized exchange-current density (based on the bulk concentration of Cd^{2+}) and the symmetry factor are 0.0897 $\frac{mA}{cm^2}$ and 0.571, respectively.

Nomenclature

a	activity
c	concentration, $\frac{\text{mol}}{\text{cm}^3}$
D	diffusion coefficient, $\frac{\text{cm}^2}{\text{s}}$
E	measured electrode potential, V
e^-	symbol for the electron
F	Farraday's constant, $\frac{\text{C}}{\text{equivalent}}$
i	current density, $\frac{\text{A}}{\text{cm}^2}$
i_o	exchange-current density, $\frac{\text{A}}{\text{cm}^2}$
i_I, i_{II}	current densities defined in Fig. 4-1, $\frac{\text{A}}{\text{cm}^2}$
G^θ	standard free energy of reaction, $\frac{\text{J}}{\text{mol}}$
k_a, k_c	anodic and cathodic rate constants
L	one-half the cycle period, s
M_i	symbol for the chemical formula of species i
n	number of electrons in a reaction
r	cell resistance multiplied by the disk area, Ω–cm^2
R	universal gas constant, 8.314 $\frac{\text{J}}{\text{mol}-\text{K}}$
s	stoichiometric coefficient
T	absolute temperature, K
t	time, s

U^0	standard electrode potential, V
V	electrode potential defined by Eq. 4-27, V
v_y	velocity normal to the electrode surface, $\frac{cm}{s}$
y	distance normal to the electrode surface, cm
z	charge number

Greek letters

β	symmetry factor
δ	characteristic length, cm
ζ	dimensionless distance
Θ_F	dimensionless concentration
θ	dimensionless time
θ_L	dimensionless half-cycle time
$\Gamma(4/3)$	the gamma function of 4/3
λ	dummy variable of integration, s
ν	kinematic viscosity, $\frac{cm^2}{s}$
π	3.1415...
ρ_o	solvent density, $\frac{kg}{cm^3}$
ω	angular rotation of the disk, $\frac{radian}{s}$

Subscripts

i	species i
ref	reference electrode compartment
1,2	reactions 1 and 2

Superscripts

surf	electrode surface
∞	far away from the electrode surface

References

1. A.J. Bard and L.R. Faulkner, *Electrochemical Methods*, Wiley, New York, 1980, p. 434.
2. P.C. Andricacos and P.N. Ross Jr., . Electrochem. Soc., 130(1983)1340.
3. *Ibid.*, 130(1983)1353.
4. *Ibid.*, 131(1984)1531.
5. *Standard Math Tables*, W.H. Beyer, Editor, CRC Press, Cleveland, Ohio, 1973, p. 406.
6. A.C. Testa and W.H. Reinmuth, *Anal. Chem.*, 33(1961)1325.
7. R.W. Murray and C.N. Reilley, *J. Electroanal. Chem.*, 3(1962)64.
8. R.W. Murray and C.N. Reilley, *ibid.*, 3(1962)182.
9. W.H. Reinmuth, *Anal. Chem.*, 34(1962)1446.
10. H.B. Herman and A.J. Bard, *ibid.*, 35(1963)1121.
11. H.B. Herman and A.J. Bard, *ibid.*, 36(1964)510.
12. M. Paunovic, *J. Electroanal. Chem.*, 14(1967)447.
13. R.K. Jain, H.C. Gaur, and B.J. Welch, *ibid.*, 79(1977)211.
14. *Handbook of Mathematical Functions*, M. Abramowitz and I.A. Stegun, Editors, Dover Publications, Inc., New York, 1972, pp. 300-302.
15. T.R. Rosebrugh and W. Lash Miller, *J. Phys. Chem.*, 14(1910)816.
16. V.S. Krylov and V.N. Babak, *Sov. Electrochem.*, 7(1971)626; (*Elektrokhimiya*, 7(1971)649).
17. J.S. Newman, *J. Electrochem. Soc.*,113(1966)1235.
18. B. Miller and S. Bruckenstein, *ibid.*,117(1970)1032.
19. K.M. Nisancioglu and J.S. Newman, *J. Electroanal. Chem.*, 50(1974)23.

20. K. Viswanathan, M.A. Farrel Epstein, and H.Y. Cheh, *J. Electrochem. Soc.*, 125(1978)1772.

21. D.A. Scherson, P.F. Marconi, and J.S. Newman, *ibid.*, 127(1980)2603.

22. P.C. Andricacos and H.Y. Cheh, *J. Electroanal. Chem.*, 121(1981)133.

23. D-T. Chin, *J. Electrochem. Soc.*, 130(1983)1657.

24. A.M. Pesco and H.Y. Cheh, *ibid.*, 131(1984)2259.

25. W.G. Cochran, *Proceedings of the Cambridge Philosophical Society*, 30(1934)365.

26. J.S. Newman, *Electrochemical Systems*, Prentice-Hall, Inc., Englewood Cliffs, NJ, 1973.

27. K.M. Nisancioglu, *Ph.D. Thesis*, University of California, Berkeley, 1973.

28. K.J. Vetter, *Electrochemical Kinetics*, S. Bruckenstein and B. Howard, Translation Editors, Academic Press, New York, 1967.

29. A.R. Despic, D.R. Jovanovic, and S.P. Bingulac, *Electrochim. Acta*, 15(1970)459.

30. K.E. Heusler and L. Gaiser, *J. Electrochem. Soc.*, 117(1970)762.

31. N.A. Hampson and R.J. Latham, *J. Electroanal. Chem.*, 32(1971)175.

32 V.V. Losev, *Modern Aspects of Electrochemistry*, volume 7, B.E. Conway and J.O'M. Bockris, editors, Plenum Press, New York, 1972, pp. 314-398.

33. J.N. Jovicevic, A.R. Despic, and D.M. Drazic, *Electrochim. Acta*, 22(1977)577.

34. J.A. Harrison and D.R. Sandbach, *J. Electroanal. Chem.*, 85(1977)125.

35. L. Kisova, M. Goledzinowski, and J. Lipkowski, *ibid.*, 95(1979)29.

36. C.P.M. Bongenaar, A.G. Remijnse, M. Sluyters-Rehbach and J.H. Sluyters, *ibid.*, 111(1980)139.

37. C.P.M. Bongenaar, A.G. Remijnse, E. Temmerman, M. Sluyters-Rehbach, and J.H. Sluyters, *ibid.*, 111(1980)155.

38. H.P. Agarwal and P. Jain, *Electrochim. Acta*, 26(1981)621.

39. G.T. Burstein, *J. Electrochem. Soc.*, 130(1983)2133.

40. K. Levenberg, *Quart. Appl. Math.*, 2(1944)164.

41. D.W. Marquardt, *J. Soc. Indust. Appl. Math.*, 11(1963)431.

42. B.S. Garbow, K.E. Hillstrom, and J.J. More, Argonne National Laboratory, March 1980.

43. J.A. Nelder and R. Mead, *The Computer Journal*, 7(1965)308.

44. M.S. Caceci and P. Cacheris, *BYTE*, May 1984, p.340.

45. W. Lorenz, *Z. Electrochem.*, 58(1954)912.

Appendix 4

Duhamel's Integral for the SPE

The flux-step (or current-step) problem is given by the diffusion equation,

$$\frac{\partial c_i}{\partial t} = D_i \frac{\partial^2 c_i}{\partial y^2} \ , \qquad [4A\text{-}1]$$

subject to an initial condition representing initially uniform concentration,

$$c_i(0,y) = c_i^{\infty} \ , \qquad [4A\text{-}2]$$

a boundary condition for bulk concentration of species far from the electrode,

$$c_i(t,\infty) = c_i^{\infty} \ , \qquad [4A\text{-}3]$$

and a second boundary condition relating the current density to the concentration gradient at the electrode surface by Farraday's law,

$$\frac{\partial c_i(t,0)}{\partial y} = \frac{s_i i}{nFD_i} \ . \qquad [4A\text{-}4]$$

The solution, often referred to as the Sand equation, is

$$c_i^{surf} - c_i^{\infty} = -\frac{2s_i i}{nF}\left(\frac{t}{\pi D_i}\right)^{\frac{1}{2}} \ . \qquad [4A\text{-}5]$$

Using equation [A-5], Duhamel's integral can be written for the SPE system with a time-varying current source:

$$c_i^{surf} - c_i^{\infty} = -\int_0^t i(\lambda)\frac{d}{d\lambda}\left[-\frac{2s_i}{nF}\left(\frac{t-\lambda}{\pi D_i}\right)^{\frac{1}{2}}\right]d\lambda \qquad [4A\text{-}6]$$

or

$$c_i^{surf} - c_i^{\infty} = -\frac{s_i}{nF\sqrt{\pi D_i}} \int_0^t i(\lambda)(t-\lambda)^{-\frac{1}{2}} \, , \qquad [4A\text{-}7]$$

which is Eq. [4-7] of the text. The development of an integral analogous to Eq. [4A-7] for the RDE system is easily accomplished by a similar derivation.

The Coefficients and Eigenvalues for Eq. [4-23]

The following table gives the first ten eigenvalues b_k and coefficients B_k. Reference 15 or 23 should be consulted for the eigenfunctions $Z_k(\zeta)$.

Table 4A-1. Coefficients and Eigenvalues for Eq. [4-23]

k	B_k	b_k
0	0.663516066	2.58078493
1	0.081564022	12.3099728
2	0.034457046	24.4331401
3	0.01962199	38.3054830
4	0.0128965	53.5740271
5	0.0092267	70.0220380
6	0.0069829	87.5010784
7	0.0055048	105.902059
8	0.0044654	125.140833
9	0.0037089	145.15016

The Newton-Raphson Algorithms

For both current-potential expressions, E is solved for by a Newton-Raphson algorithm.

The One-Step Reaction Scheme

The function $H(E)$ is defined by

$$H = i(t) - i(E) \, . \qquad [4A\text{-}8]$$

The cell-current density $i(t)$ is known. The second term $i(E)$ is given

by the right side of Eq. [4-28]. For the correct value of E, H will be zero. The potential E (equal to V in Eq. [4-27] since a SHE reference is assumed and the ohmic drop is neglected) can be found by iteration:

$$E_{new} = E_{old} - \left.\frac{H}{\left(\frac{dH}{dE}\right)}\right|_{old} \qquad [4A\text{-}9]$$

The derivative $\frac{dH}{dE}$ is

$$\frac{dH}{dE} = k_a(1-\beta)nfe^{(1-\beta)nfE} + k_c\beta nfe^{-\beta nfE}\frac{c_{Cd^{2+}}^{surf}}{\rho_o} \qquad [4A\text{-}10]$$

The Two-Step Reaction Scheme

Making use of Eq. [4-32], the function H is defined as

$$H = w_1e^{w_2E} + w_3e^{w_4E} + w_5e^{w_6E} + w_7e^{w_8E} \qquad [4A\text{-}11]$$

The new variables are:

$$w_1 = k_{c1}k_{c2}exp(-2fU^\theta)$$

$$w_2 = (2-\beta_1-\beta_2)f$$

$$w_3 = k_{c1}k_{c2}\frac{c_{Cd^{2+}}^{surf}}{\rho_o}$$

$$w_4 = -(\beta_1+\beta_2)$$

$$w_5 = -\frac{i}{2F}k_{c2}$$

$$w_6 = -\beta_2 f$$

$$w_7 = -\frac{i}{2F}k_{c1}exp(-fU_1^\theta)$$

$$w_8 = (1-\beta_1)f$$

The value of U^θ is -0.403 volts for this system. The derivative $\frac{dH}{dE}$ is

$$\frac{dH}{dE} = w_1 w_2 e^{w_2 E} + w_3 w_4 e^{w_4 E} + w_5 w_6 e^{w_6 E} + w_7 w_8 e^{w_8 E} \quad . \qquad [4A\text{-}12]$$

Equations [4A-9],[4A-11], and [4A-12] can be used to solve for E.

Optimization Program for the One-Step Mechanism

```
      program RDE1 (input,output)
c
c     December 1,1984
c     This program models the electrodeposition of cadmium
c     from an aqueous solution of potassium sulfate.  The
c     solution is well supported.  A one-step reaction scheme
c     is assumed valid.
c
c     INPUTS
c     bulk concentration Cd(+2), mol/l ..................... c
c     most anodic current, A/sq.cm ......................... curl
c     most cathodic current, A/sq.cm ....................... cur2
c     diffusion coefficient, sq.cm/sec ..................... d
c     electrons per reaction ............................... eq
c     rotation rate, 1/sec ................................. omega
c     cycle period, sec .................................... tl
c     standard electrode potential, volts .................. utheta
c     viscosity, sq.cm/sec ................................. vis
c     ---------------- Initial guesses ---------------------
c     cathodic rate constant Cd(+2) to Cd, cm/sec ........... x(1)
c     symmetry factor Cd(+2) to Cd ......................... x(2)
c
      dimension fvec(150),iwa(2),wa(460),x(2)
      common b(10),c,curl,cur2,d,e(10),eq,fa,fr
      common omeg(3),pie,pr,s,tone(3),utheta,v(150),vis,vth
      external fcn
c
c     The next line pertains to the print out of results.
      pr=0.
c
c     Optimization parameters
c     tol is the erorr tolerance.
c     m is the number of data points.
c     n is the number of parameters to be fit.
c     lwa is (m*n + 5*n + m) normally.
c     The vector x contains the initial guesses.
      read 4,m
      read 4,n
      lwa=m*n + 5*n + m
    4   format(10x,i10)
      read 5, tol
      read 5, (x(i),i=1,n)
    5   format(10x,5e10.4)
c
c     Inputs for the evaluation of v-v(ref)
      read 10, c
      read 10, curl
      read 10, cur2
```

```
      read 10, d
      read 10, eq
      read 10, omeg(1)
      read 10, omeg(2)
      read 10, omeg(3)
      read 10, tone(1)
      read 10, tone(2)
      read 10, tone(3)
      read 10, utheta
      read 10, vis
10      format(10x,f15.10)
      read 15, (v(i),i=1,m)
15        format(10x,f15.10)
c
c     The first guess at v-v(ref) is now made.
      vth=-.45
c
c
c     Constants
      fa=96487.
      fr=38.9442
      pie=3.14159
      b(1)=.663516066
      b(2)=.081564022
      b(3)=.034457046
      b(4)=.01962199
      b(5)=.0128965
      b(6)=.0092267
      b(7)=.0069829
      b(8)=.0055048
      b(9)=.0044645
      b(10)=.0037089
      e(1)=2.58078493
      e(2)=12.3099728
      e(3)=24.4331401
      e(4)=38.3054830
      e(5)=53.5740271
      e(6)=70.0220380
      e(7)=87.5010784
      e(8)=105.902059
      e(9)=125.140833
      e(10)=145.15016
c     END OF INPUTS
c
ccccccccccccccccccccccccccccccccccccccccccccccccccccccccccccccccc
c
c     Call for parameter fit.
      call lmdif1(fcn,m,n,x,fvec,tol,info,iwa,wa,lwa)
      fnorm=enorm(m,fvec)
c     Print results.
      pr=1.
```

```
      call fcn(m,n,x,fvec,iflag)
      print 1000, fnorm,info,(x(j),j=1,n)
 1000   format(5x,#Final L2 norm of the residuals = #,f15.7 //
     *         5x,#Exit parameter = #,2x,i10 //
     *         5x,#Final, approximate parameters# //
     *         10x,#x(1) (rate constant)     = #,e15.7 /
     *         10x,#x(2) (symmetry factor)   = #,f15.7 /)
c
      end
c
ccccccccccccccccccccccccccccccccccccccccccccccccccccccccccccccccccc
c
      subroutine fcn(m,n,x,fvec,iflag)
      dimension fvec(150),x(2)
      common b(10),c,curl,cur2,d,e(10),eq,fa,fr
      common omeg(3),pie,pr,s,tone(3),utheta,v(150),vis,vth
c
c     The constraints are put on the problem now.
      if(x(2).ge.0.)5,110
    5 if(x(2).le.1.)10,110
   10 if(x(1).lt.0.)go to 110
c
      dc 100 j=1,m
c
c       The values of variables for the different runs are
c       now obtained.
        if(j.gt.m/3)go to 20
        jtime=0
        tl=tone(1)
        omega=omeg(1)
        go to 40
   20   if(j.gt.2*m/3)go to 30
        jtime=m/3
        omega=omeg(2)
        tl=tone(2)
        go to 40
   30   jtime=2*m/3
        omega=omeg(3)
        tl=tone(3)
c
   40   s=1.8049*d**(1./3.)*vis**(1./6.)*sqrt(1./omega)
        dimtl=tl*d/s**2.
        diml=0.5*dimtl
        ti=float(j-jtime)/float(m/3)*tl
        t=ti*d/s**2.
        concl=0.
        do 90 k=1,10
          conc2=0.
          do 80 l=1,15,2
            rl=float(l)
            conc2=conc2 + (e(k)*cos(rl*pie*t/diml) +
```

```
     *              (rl*pie/diml)*sin(rl*pie*t/diml))/
     *              (rl**2*(e(k)**2 + (rl*pie/diml)**2))
  80         continue
           concl=concl + e(k)*b(k)*conc2
  90       continue
c
           y=(.5 + curl/(cur2-curl))*.89298 -
     *       4.*concl/pie**2
           y=1. + 1000.*(cur2-curl)*s*y/(2.*fa*d*c)
           c2=y*c
c
c       c2 is the surface concentration of Cd(+2).  The
c       next portion of this program calculates the potential
c       difference between the working electrode and the
c       reference electrode, which is a directly measureable
c       quantity.
c
           if(t.le.diml)cur=(cur2-curl)*t/diml + curl
           if(t.gt.diml)cur=(curl-cur2)*t/diml + 2*cur2 - curl
           do 95 i=1,100
c
c            The next two lines are for debugging.
c
c            print 951, vth
c 951        format(2x,#vth= #,f15.7)
c
             if(vth.gt.-0.4)vth=-.4
             if(vth.lt.-4.)vth=-4.
             hzero=cur/(eq*fa) - x(1)*(exp(-eq*fr*utheta)*exp((
     *            1.-x(2))*eq*fr*vth) - c2*exp(-x(2)*eq*fr*vth))
             dhzero=-x(1)*(exp(-eq*fr*utheta)*(1.-x(2))*eq*fr*
     *             exp((1.-x(2))*eq*fr*vth) + c2*x(2)*eq*fr*
     *             exp(-x(2)*eq*fr*vth))

             vthnew=vth - hzero/dhzero
             if(abs((vthnew-vth)/vthnew).le.0.0005)go to 97
             vth=vthnew
  95         continue
           print 96, c2,vth
  96         format(2x,#NO CONVERGENCE c2= #,e15.7,# vth= #,e15.7)
c
           stop
  97       fvec(j)=v(j)-vthnew
           if(pr.eq.1.)print 98, j,ti,cur,y,vth,v(j),fvec(j)
  98         format(2x,i3,2x,5(e10.3,2x),e10.3)
           if(j.eq.m)print 99, (x(i),i=1,n)
  99         format(x,e20.12,x,f20.12)
 100       continue
         go to 130
c
c       In case a constraint was hit, the following 3 lines
```

```
c        are used.
  110    do 120 i=1,m
           fvec(i)=100.
  120      continue
c
  130    continue
         return
c
c        Last line of subroutine fcn.
c
         end
ccccccccccccccccccccccccccccccccccccccccccccccccccccccccccc
```

Data File for Optimization Program

```
m                150
n                  2
tol           1.e-15
x(i)      1.0000e-10 .5000e+00
c          .0058
curl       .0
cur2      -.00153
d          .0000036
eq         2.0
omega(1)   24.7
omega(2)   41.1
omega(3)   24.7
tl(1)      100.
tl(2)      100.
tl(3)      10.
utheta    -.4030
vis        .01
v(1)      -.4680      [run #7188401]
2         -.4700
3         -.4740
4         -.4820
5         -.4980
6         -.5070
7         -.5130
8         -.5170
9         -.5205
10        -.5240
11        -.5265
12        -.5290
13        -.5320
14        -.5335
15        -.5360
16        -.5380
17        -.5405
18        -.5425
19        -.5455
20        -.5475
21        -.5505
22        -.5530
23        -.5560
24        -.5610
25        -.5645
26        -.5670
27        -.5630
28        -.5580
29        -.5525
30        -.5485
31        -.5460
```

32	-.5430	
33	-.5400	
34	-.5370	
35	-.5350	
36	-.5325	
38	-.5275	
39	-.5240	
40	-.5215	
41	-.5185	
42	-.5150	
43	-.5120	
44	-.5070	
45	-.5030	
46	-.4965	
47	-.4860	
48	-.4790	
49	-.4730	
50	-.4705	
51	-.4650	[run #7188402]
52	-.4680	
53	-.4715	
54	-.4785	
55	-.4950	
56	-.5115	
57	-.5190	
58	-.5245	
59	-.5280	
60	-.5305	
61	-.5330	
62	-.5350	
63	-.5365	
64	-.5380	
65	-.5400	
66	-.5420	
67	-.5435	
68	-.5450	
69	-.5470	
70	-.5515	
71	-.5495	
72	-.5520	
73	-.5530	
74	-.5550	
75	-.5570	
76	-.5560	
77	-.5535	
78	-.5505	
79	-.5485	
80	-.5470	
81	-.5455	
82	-.5430	
83	-.5410	

84	-.5390	
85	-.5370	
86	-.5350	
87	-.5325	
88	-.5300	
89	-.5280	
90	-.5245	
91	-.5215	
92	-.5175	
93	-.5140	
94	-.5080	
95	-.5015	
96	-.4925	
97	-.4805	
98	-.4720	
99	-.4690	
100	-.4655	
101	-.4805	[run #7188403]
102	-.4730	
103	-.4730	
104	-.4765	
105	-.4795	
106	-.4850	
107	-.4940	
108	-.5055	
109	-.5155	
110	-.5240	
111	-.5290	
112	-.5315	
113	-.5360	
114	-.5345	
115	-.5375	
116	-.5385	
117	-.5415	
118	-.5420	
119	-.5440	
120	-.5460	
121	-.5480	
122	-.5490	
123	-.5510	
124	-.5535	
125	-.5560	
126	-.5580	
127	-.5595	
128	-.5590	
129	-.5585	
130	-.5575	
131	-.5570	
132	-.5545	
133	-.5525	
134	-.5510	

135	-.5500
136	-.5485
137	-.5460
138	-.5440
139	-.5415
140	-.5395
141	-.5375
142	-.5345
143	-.5340
144	-.5285
145	-.5250
146	-.5220
147	-.5165
148	-.5110
149	-.5045
150	-.4960

Chapter 5.

The Transient and Periodic Illumination of a Semiconductor-Electrolyte Interface

Since Brattain and Garett's fundamental study of the semiconductor-electrolyte interface (1), there has been a large research effort directed towards understanding and characterizing semiconductor-liquid junctions. Promising photoelectrolysis and solar cell schemes exist based on such an interface. (2) Bard (3) and Heller (4) have recently reviewed efficient photoelectrochemical (PEC) systems, elucidating problems and progress.

A useful technique in the characterization of PEC cells is to analyze the system's response to a varying light source. (5,6,7) This is analogous to varying the current or potential (chronopotentiometry or chronoamperometry, respectively) in order to study traditional electrochemical systems. In this work, we present analytic solutions for minority-carrier transport equations that allow for the description of a PEC cell subject to pulse, step, sinusoidal, and periodic square-pulse illumination. This treatment is an extension of existing steady-state models by Gartner (8) and Dewald (9). These models have been shown by a number of authors to predict very accurately the behavior of wide band gap PEC systems. (10,11,12,13,14)

The response of a photoactive system to a varying light intensity has been the subject of many studies. van Roosbroeck examined injected current-carrier transport in a semiconductor as a means to determine carrier lifetimes and surface recombination velocities. (15) Since van Roosevroeck's study, numerous researchers have addressed the response of PEC systems under varying illumination intensities. (*ie.* 16,17,18,19,20) In

addition, Laser and Bard implemented a more general digital-simulation model to study transient charge injection in a PEC cell. (21)

The major emphasis of this treatment deals with the solution to the equations describing minority-carrier transport in the semiconductor; this is because semiconductor-electrolyte interfaces are often analogous to *Schottky barriers* in metal-semiconductor contacts, and the electrolyte-species transport usually plays a minor role in the determining the PEC system behavior. (1,22) For the description of many PEC systems, it is necessary to incorporate kinetic resistances at the interface. (23) The next section of this work addresses the proper use of a semiconductor-electrode kinetic expression. Following this section, the minority carrier transport equations are solved.

The Interfacial Kinetic Expression

A number of treatments for the analysis of semiconductor-electrolyte systems state that a Butler-Volmer type equation is probably the best expression available to describe the cell current-potential relationship. In most of these analyses (though not all, for example, ref. 24), the irreversibilities associated with electrochemical reactions are neglected; hence, it is not made clear how to relate specifically the measured cell potential to the cell current. It is the purpose of this section to illustrate clearly how to apply the current-potential equation to experimental data.

The following discussion will treat the reaction of semiconductor electrons with electrolyte species. An analogous treatment can be used to describe reactions with semiconductor holes. We will not address activity coefficient corrections in this work. For the electrochemical reaction

$$O + ne^- \underset{k_{c,i}}{\overset{k_{a,i}}{\rightleftharpoons}} R \qquad [5\text{-}1]$$

the current-potential relationship is

$$\frac{i}{nF} = k_a \exp[(1-\beta)nfV]\frac{c_R}{\rho_o} - k_c \exp(-\beta nfV)\frac{c_O}{\rho_o} c_{e^-} \qquad [5\text{-}2]$$

where surface concentrations are used, $f = \frac{F}{RT}$, and

$$V = E + \left[U^{\theta}_{ref} - \frac{1}{n_{ref} f}\sum_i s_{i,ref} \ln\left(\frac{c_{i,ref}}{\rho_o}\right)\right] - \Delta\Phi_{IR} - \Delta\Phi_{SE} - \Delta\Phi_{MS} \; . \qquad [5\text{-}3]$$

The potential of a platinum wire, intimately contacted to the semiconductor, with respect to a reference electrode is the measured cell potential E. The bracketed term in Eq. [5-3] represents a Nernst expression for the reference electrode, denoted henceforth as U^{eq}_{ref}. The cell ohmic potential drop is represented by $\Delta\Phi_{IR}$. The potential differences across the space-charge regions in the semiconductor near the metal-semiconductor and semiconductor-electrolyte interfaces are denoted by $\Delta\Phi_{MS}$ and $\Delta\Phi_{SE}$, respectively. The symbol Δ proceeding Φ_{MS} and Φ_{SE} refers to spatial differences; hence $\Delta\Phi_{MS}$ is the value of the electric potential at the metal side of the metal-semiconductor space-charge region less the value of the electric potential at the semiconductor side of the space-charge region. Similarly, $\Delta\Phi_{SE}$ is the value of the electric potential at the semiconductor side of the semiconductor-electrolyte space-charge region less the value of the electric potential at the electrolyte side of the space-charge region. Therefore, the potential difference between a platinum wire contacted to the semiconductor and a SHE, corrected for ohmic drop and potential differences across the

space-charge regions, is represented by V. The potential difference across the diffuse portion of the semiconductor-electrolyte double layer in the electrolyte is usually very small and is neglected in this work. (2)

At equilibrium, $i = 0$, and Eq. [5-2] reduces to

$$V^{eq} = \frac{1}{nf}\ln\frac{k_c}{k_a} + \frac{1}{nf}\ln\frac{c_O c_{e^-}^n}{c_R} \qquad [5\text{-}4]$$

or

$$FV^{eq} = \frac{1}{n}(\mu_O^\theta + n\mu_{e^-}^{o,Pt} - \mu_R^\theta) + \frac{RT}{n}\ln\frac{c_O c_{e^-}^n}{c_R} \; . \qquad [5\text{-}5]$$

In Eq. [5-5], we have made use of the following dilute-solution expression for the electrochemical potential (25,26)

$$\mu_i = \mu_i^{ref} + RT\ln c_i + z_i F\Phi \; . \qquad [5\text{-}6]$$

The first two terms on the right side of Eq. [5-6] represent purely chemical contributions. The superscript θ denotes a reference state of infinite dilution in an aqueous phase. Since the rate constants are related to the standard hydrogen electrode, the superscript o,Pt is required to denote the standard state electrochemical potential of the electrons in platinum, the electrode material used in the SHE. Equation [5-5] can be combined with Eq. [5-3] to yield the measured equilibrium cell voltage

$$FE^{eq} = \frac{1}{n}(\mu_O^\theta + n\mu_{e^-}^{o,s} - \mu_R^\theta) + \frac{RT}{n}\ln\frac{c_O}{c_R} + \mu_{e^-}^{o,Pt} - \mu_{e^-}^{o,s} + RT\ln c_{e^-} \qquad [5\text{-}7]$$

$$+ F(\Delta\Phi_{MS} + \Delta\Phi_{SE} - U_{ref}^{eq})$$

where $\mu_{e^-}^{o,s}$ represents the standard-state electrochemical potential of

electrons in the semiconductor.

Under most equilibrium conditions, a Boltzmann expression can be used to relate ionic concentrations to potential differences within a conducting phase: (27)

$$c_{e^-} = c_{e^-}^{b,s} \exp(-f\,\Delta\Phi_{SE}) \qquad [5\text{-}8]$$

$$c_{e^-}^{b,s} = c_{e^-}^{Pt} \exp(-f\,\Delta\Phi_{MS}) \qquad [5\text{-}9]$$

where the superscript b,s denotes the bulk semiconductor. When Eqs. [5-8] and [5-9] are inserted into Eq. [5-7], $\Delta\Phi_{SE}$ and $\Delta\Phi_{MS}$ cancel. The cell voltage can then be represented by

$$FE^{eq} = (\mu_{e^-}^{o,Pt} + RT\ln c_{e^-}^{Pt}) - (\mu_{e^-}^{o,s} + RT\ln c_{e^-}^{b,s}) \qquad [5\text{-}10]$$

$$+ \frac{1}{n}(\mu_O^0 + n\mu_{e^-}^{o,s} - \mu_R^0) + \frac{RT}{n}\ln\frac{c_O c_{e^-}^{b,s}}{c_R}$$

$$+ \left(\frac{1}{2}\mu_{H_2}^0 - \mu_{H^+}^0 - \mu_{e^-}^{o,Pt}\right) + RT\ln\frac{(c_{H_2})^{\frac{1}{2}}}{c_{H^+}c_{e^-}^{o,Pt}} .$$

The first line on the right side of Eq. [5-10] represents the potential difference between the platinum contact and the bulk semiconductor. The second line represents the potential difference across the semiconductor-electrolyte interface. The last line indicates that a hydrogen reference electrode has been assumed. This is the same expression that is obtained if the cell potential is expressed by summing the potential differences between the various phases at equilibrium. (28) Equation [5-10] can be further simplified by canceling the semiconductor terms (denoted with superscript s) and pla-

tinum terms (denoted with superscript *Pt*). As is expected, the open-circuit cell potential is independent of the semiconductor phase.

It is important to note that the potential difference across the space-charge region near the metal-semiconductor contact, $\Delta\Phi_{MS}$, had to be included in order to develop rigorously the cell-potential expression. This term is often neglected in semiconductor-electrode analyses. $\Delta\Phi_{MS}$ is also a function of cell polarization; for a uniformly doped semiconductor, a Schottky barrier analysis may suffice. It is also possible to alter the dopant concentration to minimize $\Delta\Phi_{MS}$. (29) In general, the theory is well developed for metal-semiconductor contacts, and we will only address the semiconductor-electrolyte contact.

Evaluation of the Minority-Carrier Concentration

Although the treatment we present in this section for the solution to the minority-carrier transport is approximate, its steady-state counterpart has proved to be a valuable tool for the description of many PEC systems. More complete discussions of the full equations governing electron, hole, and ionic transport can be found elsewhere. (24,30) In order to develop the full cell current-potential relationship, the relation between the cell current and $\Delta\Phi_{MS}$ is required, and Gauss' law must be incorporated to solve for $\Delta\Phi_{SE}$ and for the surface overpotential associated with the charge-transfer reaction across the Helmholtz layer. With extrinsic semiconductors, usually the *depletion approximation* can be used to simplify the evaluation of $\Delta\Phi_{SE}$, resulting in a parabolic potential distribution across the space-charge region. (*cf.* ref. 2, Eq. [5-23]) The potential drop across the Helmholtz layer is usually assumed to vary linearly. (*cf.* ref 23, Eqs. [5-29] and [5-30])

The three regions of interest in this analysis, the electrolyte, the semiconductor space-charge layer, and the neutral semiconductor are shown in Fig. 5-1. The semiconductor is represented by a space-charge region for $0 < x < w$ and an electrically neutral region for $x > w$.

The space-charge region is modeled as an equilibrated reservoir of minority carriers (electrons in a p-semiconductor, holes in an n-semiconductor). Since small concentration and potential variations across the thin space-charge region give rise to large gradients in concentration and potential and large, opposing diffusion and migration fluxes, the equilibrium assumption is invoked. A flux balance on the region yields

$$-\frac{i}{z_i F} + \int_0^w I(t)\alpha e^{-\alpha x} dx = N\Big|_{x=w} + v_s(c^w - c^b) \quad . \qquad [5\text{-}11]$$

The first term is related to the flux of minority carriers into the region by electrochemical reaction. For holes, $z_i = 1$ and for electrons, $z_i = -1$. Anodic currents are taken as positive in this work. The second term represents generation by illumination. The flux of minority carriers out of the region, $N\Big|_{x=w}$, is obtained by solving the continuity equation for the minority carrier in the semiconductor. The last term in Eq. [5-11] represents a very approximate treatment for surface recombination. The surface-recombination term is similar to a Shockley, Hall, Read surface-recombination model (31,32) if the energies of the trap sites are located near midgap, the hole and electron *capture cross sections* are identical and the charge carriers are at low concentration.

In Gartner's treatment, surface recombination is neglected, and the minority-carrier concentration is set to zero at $x = w$. The Gartner model begins to fail for systems with negligible space-charge widths, or small

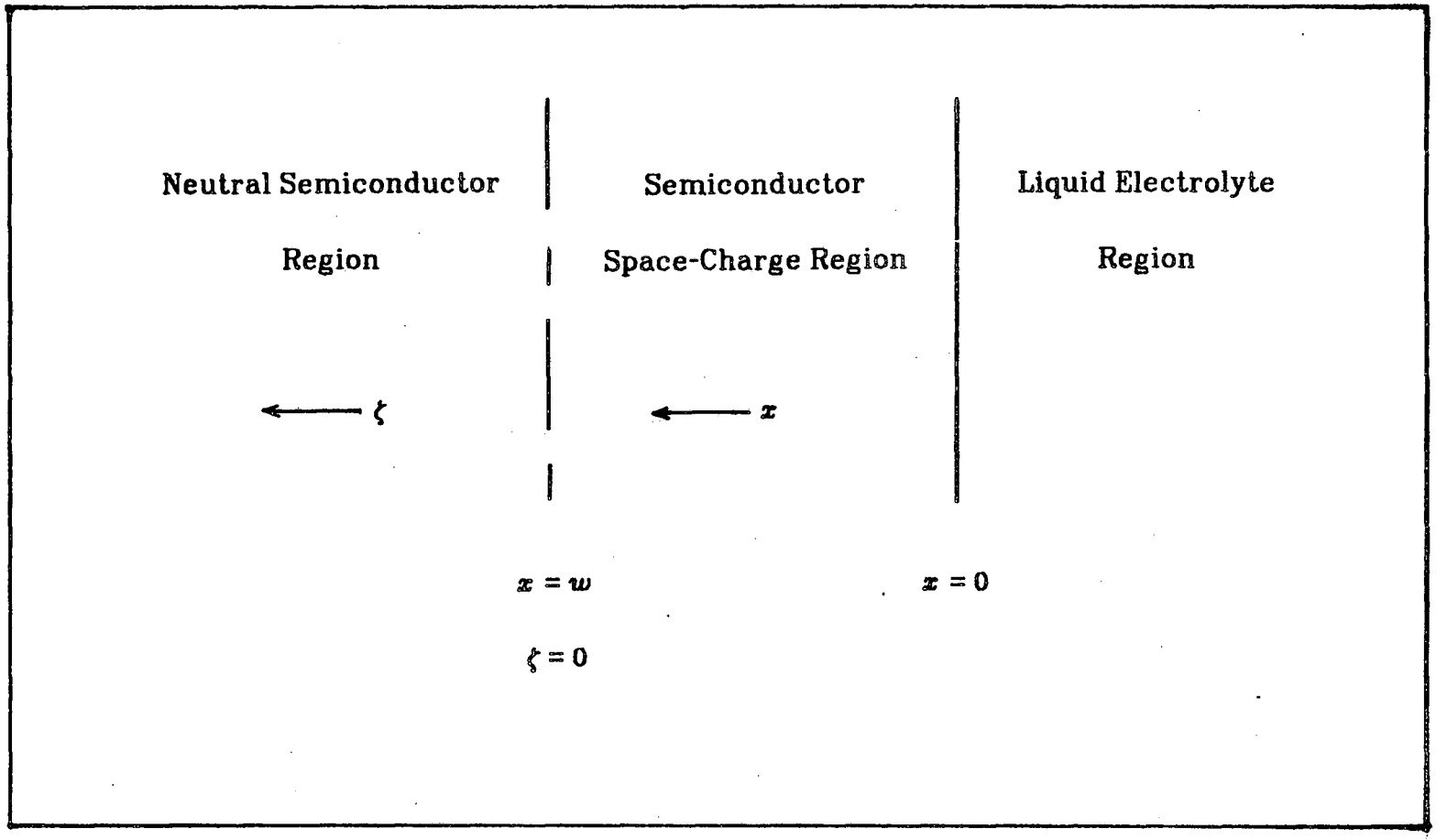

Figure 5-1. Schematic illustration of semiconductor-electrolyte interface.

potential drops across the space-charge region. Including the recombination term and a non-zero minority-carrier concentration at $x = w$ represents additions to the Gartner model which appear in Dewald's work and improve the analysis of PEC cells. (13)

The one-dimensional equation of continuity for the description of the minority-carrier transport within the bulk semiconductor is

$$\frac{\partial c}{\partial t} = D \frac{\partial^2 c}{\partial x^2} - \frac{c - c^b}{\tau} + I(t)\alpha e^{-\alpha x} \qquad [5\text{-}12]$$

Migration terms are not included in the continuity expression since the majority-carrier concentration is assumed large and invariant, thus acting as a supporting electrolyte and reducing the effect of the electric field on minority-carrier transport. This is usually a good assumption for extrinsic semiconductors. The simple bulk recombination model, which makes use of the *carrier lifetime* τ is analogous to the simple surface-recombination model used in Eq. [5-11] and embodies the same assumptions. The exclusion of the electric field effects and the use of a simple recombination model are more valid for *low level injection* situations. In general, the treatment we present is analogous to the *ideal-diode analysis*, in which both of these assumptions are made. (33,34,35)

The boundary conditions and initial condition are

$$c(t,\infty) = c^b \,, \qquad [5\text{-}13]$$

$$c(t,w) = c^w \qquad [5\text{-}14]$$

$$c(0,x) = c^{init}(x) \,. \qquad [5\text{-}15]$$

The first boundary condition states that the minority-carrier concentration

reaches its bulk value for large distances from the interface. This boundary condition is valid for semiconductor thicknesses substantially greater $\sqrt{\tau D}$, the characteristic length for this transport problem, also denoted by L, the ***diffusion length.*** The second boundary condition sets the concentration at $x = w$. In the last condition, the initial concentration profile is set equal to the steady-state value for constant illumination. The full steady-state solution, with constant illumination intensity I, is:

$$c(x) = c^b - \frac{\frac{i}{z_i F} - I\left(1 - \frac{e^{-\alpha w}}{\alpha L + 1}\right)}{v_s + \frac{L}{\tau}} e^{-\frac{x-w}{L}} \qquad [5\text{-}16]$$

$$- \frac{I\alpha\tau e^{-w\alpha}}{(\alpha L)^2 - 1}\left[e^{-\alpha(x-w)} - e^{-\frac{x-w}{L}}\right]$$

At zero current ($i = 0$) and no illumination ($I = 0$), the minority-carrier concentration is equal to its bulk value for all $x \geq w$. For the problems solved in this work, the interface was initially not illuminated.

The solution to the system of equations [5-12]-[5-15] can be combined with Eq. [5-11] to yield c^w. If the ***quasi-equilibrium assumption*** is invoked, the charge carriers are assumed to be in translational equilibrium across the space-charge region (9), and the surface concentration can be related to c^w by a Boltzmann factor $c^{surf} = c^w \exp(z_i f \Delta\Phi_{SE})$.

Equations [5-12]-[5-15] can be non-dimensionalized with the following definitions:

$$\zeta = \frac{x - w}{L} \qquad [5\text{-}17]$$

$$\theta = \frac{t}{\tau} \qquad [5\text{-}18]$$

$$\Theta = \frac{c - c^b}{c^b} \qquad [5\text{-}19]$$

$$\alpha = \alpha L \qquad [5\text{-}20]$$

$$\lambda = -\frac{i}{z_i F(v_s + \frac{L}{\tau})c^b} \qquad [5\text{-}21]$$

$$\phi = \frac{I(t)a\tau e^{-wa}}{c^b} \qquad [5\text{-}22]$$

with these definitions, the problem can be restated as

$$\frac{\partial \Theta}{\partial \theta} = \frac{\partial^2 \Theta}{\partial \zeta^2} - \Theta + \phi(\theta)e^{-a\zeta} \qquad [5\text{-}23]$$

$$\Theta(\theta,\infty) = 0 \qquad [5\text{-}24]$$

$$\Theta(\theta,0) = \Theta^w \qquad [5\text{-}25]$$

$$\Theta(0,\zeta) = \lambda e^{-\zeta} \qquad [5\text{-}26]$$

Equation [5-23] is a linear partial differential equation with constant coefficients, and Eq. [5-26] prescribes the nonlinear initial condition. The Laplace transform technique can be used to reduce Eq. [5-23] to an ordinary differential equation:

$$\frac{d^2\overline{\Theta}}{d\zeta^2} - \overline{\Theta}(s + 1) = -\lambda e^{-\zeta} - \phi(s)e^{-a\zeta}\ , \qquad [5\text{-}27]$$

where s is the Laplace transform variable and an overbar indicates a transformed variable. The transformed boundary conditions are

$$\overline{\Theta}(\infty) = 0 \text{ , and} \qquad [5\text{-}28]$$

$$\overline{\Theta}(0) = \frac{\Theta^w}{s} \text{ .} \qquad [5\text{-}29]$$

The solution to the system of equations [5-27]-[5-29] is

$$\overline{\Theta} = \left[\frac{(\Theta^w - \lambda)}{s} - \frac{\phi(s)}{s + 1 - \alpha^2}\right] e^{-\sqrt{s+1}\zeta} + \frac{\lambda}{s} e^{-\zeta} + \frac{\phi(s) e^{-\alpha\zeta}}{s + 1 - \alpha^2} \text{ .} \qquad [5\text{-}30]$$

The flux of the minority carrier at $x = w$, in Laplace space, is

$$\overline{N}\Big|_{x=w} = -c^b \frac{D}{L} \frac{d\overline{\Theta}}{d\zeta}\Big|_{\zeta=0} \qquad [5\text{-}31]$$

where

$$\frac{d\overline{\Theta}}{d\zeta}\Big|_{\zeta=0} = -\left[\frac{(\Theta^w - \lambda)}{s} - \frac{\phi(s)}{s + 1 - \alpha^2}\right]\sqrt{s+1} - \frac{\lambda}{s} - \frac{\phi(s)\alpha}{s + 1 - \alpha^2} \text{ .} \qquad [5\text{-}32]$$

The inversion of Eq. [5-31] yields $N\Big|_{x=w}$, which can be used in Eq. [5-11] to obtain the minority-carrier concentration c^w , Θ^w in dimensionless terms. Combining the inverted expression for Eq. [5-31] with Eq. [5-11] yields

$$\Theta^w - \sigma_1 \frac{d\Theta}{d\zeta}\Big|_{\zeta=0} = \sigma_2 \qquad [5\text{-}33]$$

where σ_1 and σ_2 are dimensionless groups introduced for convenience:

$$\sigma_1 = \frac{L}{\tau v_s} \qquad [5\text{-}34]$$

$$\sigma_2(t) = -\frac{1}{v_s c^b}\left[\frac{i}{z_i F} + I(t)(e^{-\alpha w} - 1)\right] \qquad [5\text{-}35]$$

The next portion of this work addresses the evaluation of $\frac{d\Theta}{d\zeta}\Big|_{\zeta=0}$ and Θ^w.

Light impulse - The light flux function is shown in Fig. 5-2. In the limit of vanishingly small pulse width Δt, the Laplace transform of the light impulse with area I_o is $\phi(s) = \phi_o$ in dimensionless form. (ref 36, p. 65) Substituting this value of $\phi(s)$ into Eq. [5-32], and inverting yields

$$\left.\frac{d\Theta}{d\zeta}\right|_{\zeta=0} = (\lambda - \Theta^w)e^{-\theta}\left[\frac{1}{\sqrt{\pi\theta}} + e^{\theta}\mathrm{erf}\,(\theta^{\frac{1}{2}})\right] \qquad [5\text{-}36]$$

$$+ \phi_o e^{-\theta}\left[\frac{1}{\sqrt{\pi\theta}} + \alpha e^{\alpha^2\theta}\mathrm{erf}\,(\alpha\theta^{\frac{1}{2}})\right] - \lambda - \phi_o \alpha e^{(\alpha^2-1)\theta} \,.$$

The inversions required to obtain Eq. [5-36] can be found in most Laplace transform tables (*ie.* 37,38,39) after the translation properties of Laplace transform (ref. 36, pp. 60-61) are used on the function $\left.\frac{d\overline{\Theta}}{d\zeta}\right|_{\zeta=0}$.

The concentration Θ^w can be found by substituting Eq. [5-36] into Eq. [5-33]:

$$\Theta^w = \frac{1}{1 + \sigma_1 e^{-\theta}\left[\frac{1}{\sqrt{\pi\theta}} + e^{\theta}\mathrm{erf}\,(\theta^{\frac{1}{2}})\right]}\left[\sigma_2 + \sigma_1\left\{\lambda e^{-\theta}\left[\frac{1}{\sqrt{\pi\theta}} + e^{\theta}\mathrm{erf}\,(\theta^{\frac{1}{2}}) - e^{\theta}\right]\right.\right.$$

$$\left.\left. + \phi_o e^{-\theta}\left[\frac{1}{\sqrt{\pi\theta}} + \alpha e^{\alpha^2\theta}\left(\mathrm{erf}\,(\alpha\theta^{\frac{1}{2}}) - 1\right)\right]\right\}\right] \qquad [5\text{-}37]$$

For long times, $\Theta^w = \frac{\sigma_2(\theta)}{(1 + \sigma_1)}$, or

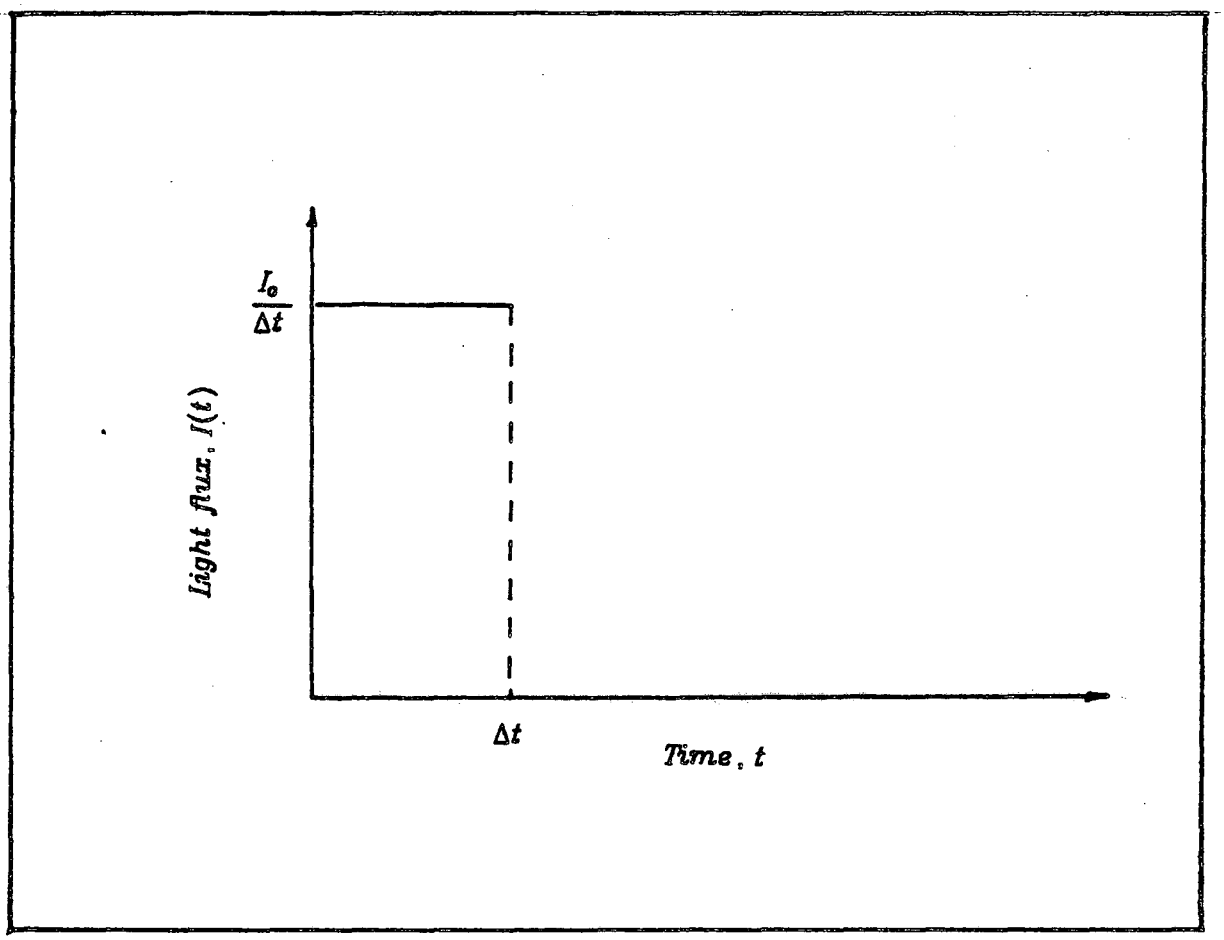

Figure 5-2. Impulse light-flux function.

$$\Theta^w = -\frac{i}{z_i F C^b (v_s + \frac{L}{\tau})} \qquad [5\text{-}38]$$

which is the expected result in view of Eq. [5-16].

Light step - The light-step function is shown in Fig. 5-3. For this step function, $\phi(s) = \frac{\phi_o}{s}$. Substituting this value of $\phi(s)$ into Eq. [5-32] gives the following expression for $\left.\frac{d\overline{\Theta}}{d\zeta}\right|_{\zeta=0}$:

$$\left.\frac{d\overline{\Theta}}{d\zeta}\right|_{\zeta=0} = -\left[\frac{\Theta^w - \lambda}{s} - \frac{\phi_o}{s(s+1-\alpha^2)}\right]\sqrt{s+1} - \frac{\lambda}{s} - \frac{\phi_o \alpha}{s(s+1-\alpha^2)} \qquad [5\text{-}39]$$

The inversion of $\frac{\sqrt{s+1}}{s(s+1-\alpha^2)}$ is presented in the Appendix 5. The complete inversion of Eq. [5-39] gives

$$\left.\frac{d\Theta}{d\zeta}\right|_{\zeta=0} = (\lambda - \Theta^w)e^{-\theta}\left[\frac{1}{\sqrt{\pi\theta}} + e^{\theta}\mathrm{erf}\,(\theta^{\frac{1}{2}})\right] \qquad [5\text{-}40]$$

$$+ \frac{\phi_o}{\alpha^2-1}\left[\alpha\,\mathrm{erf}\,(\alpha\theta^{\frac{1}{2}})e^{(\alpha^2-1)\theta} - \mathrm{erf}\,(\theta^{\frac{1}{2}})\right] - \lambda - \frac{\phi_o \alpha}{\alpha^2-1}\left(e^{(\alpha^2-1)\theta} - 1\right).$$

Combining Eqs. [5-33] and [5-40] yields

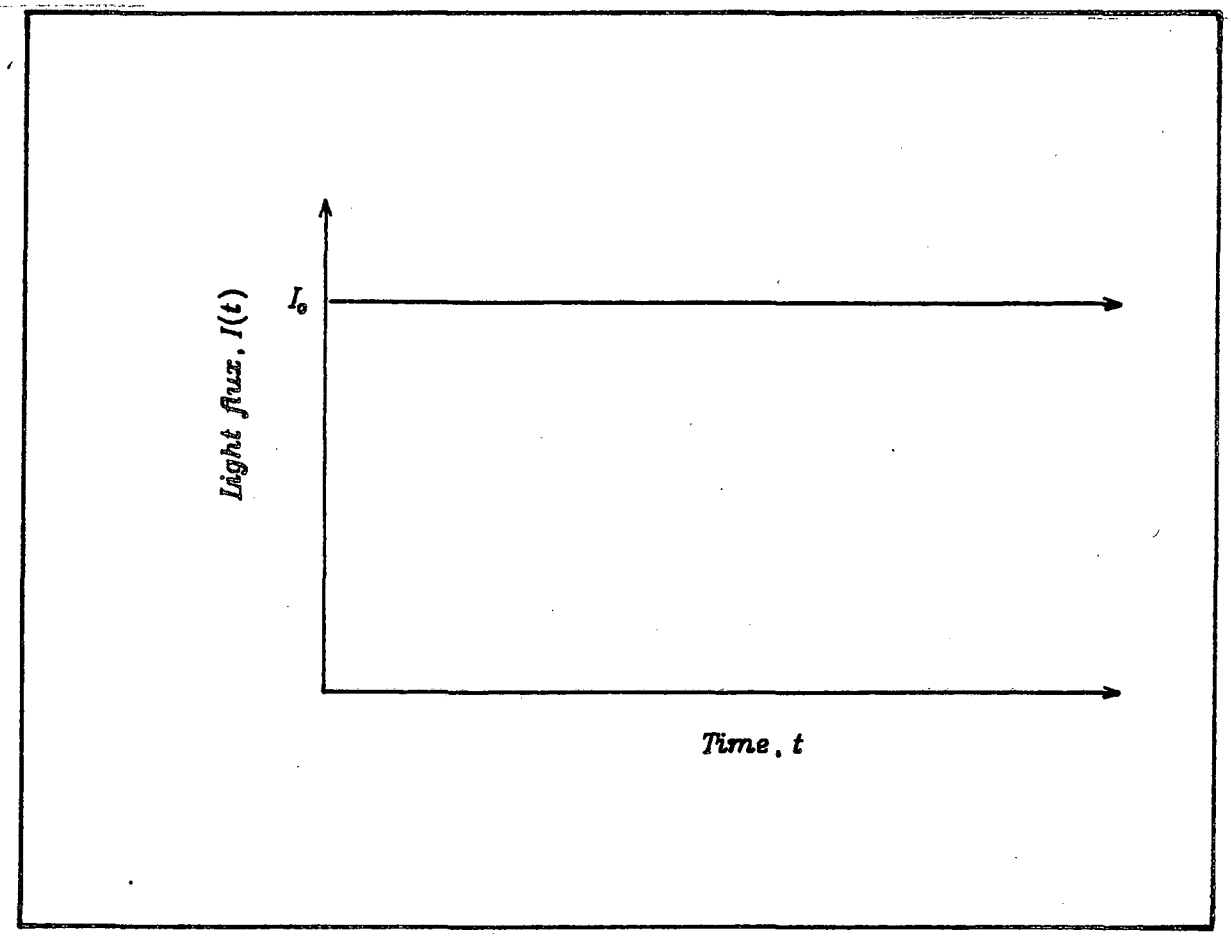

Figure 5-3. Step light-flux function.

$$\Theta^w = \frac{1}{1 + \sigma_1 e^{-\theta}\left[\frac{1}{\sqrt{\pi\theta}} + e^{\theta}\mathrm{erf}\left(\theta^{\frac{1}{2}}\right)\right]}\left\{\sigma_2 + \sigma_1\left\{\lambda e^{-\theta}\left[\frac{1}{\sqrt{\pi\theta}} + e^{\theta}\mathrm{erf}\left(\theta^{\frac{1}{2}}\right) - e^{\theta}\right]\right.\right.$$

$$\left.\left. + \frac{\phi_o}{\alpha^2 - 1}\left[\alpha\mathrm{erf}\left(\alpha\theta^{\frac{1}{2}}\right)e^{(\alpha^2-1)\theta} - \mathrm{erf}\left(\theta^{\frac{1}{2}}\right) + \alpha\left(1 - e^{(\alpha^2-1)\theta}\right)\right]\right\}\right\}. \qquad [5\text{-}41]$$

For long times,

$$\Theta^w = \frac{\sigma_2 + \frac{\phi_o}{\alpha + 1}\sigma_1}{1 + \sigma_1} \qquad [5\text{-}42]$$

or

$$\Theta^w = -\frac{\frac{i}{z_i F} - I_o\left[1 - \frac{e^{-w\alpha}}{1 + \alpha L}\right]}{c^b\left(v_s + \frac{L}{\tau}\right)}. \qquad [5\text{-}43]$$

This agrees with Eq. [5-16] evaluated at $x = w$.

Periodic square-pulse illumination - The light source is depicted in Fig. 5-4. The light source can be expressed by a Fourier series (40)

$$I(t) = I_o + \frac{4}{\pi}(J_o - I_o)\sum_{i = 1,3,5,\cdots}^{\infty}\frac{1}{i}\sin\left(\frac{i\pi\theta}{\theta_T}\right) \qquad [5\text{-}44]$$

where the dimensionless half-cycle period is $\theta_T = \frac{T}{\tau}$. If only the $i = 1$ term is kept in the summation, we can obtain a solution for sinusoidal illumination. Inverting and substituting Eq. [5-44] into Eq. [5-32] yields:

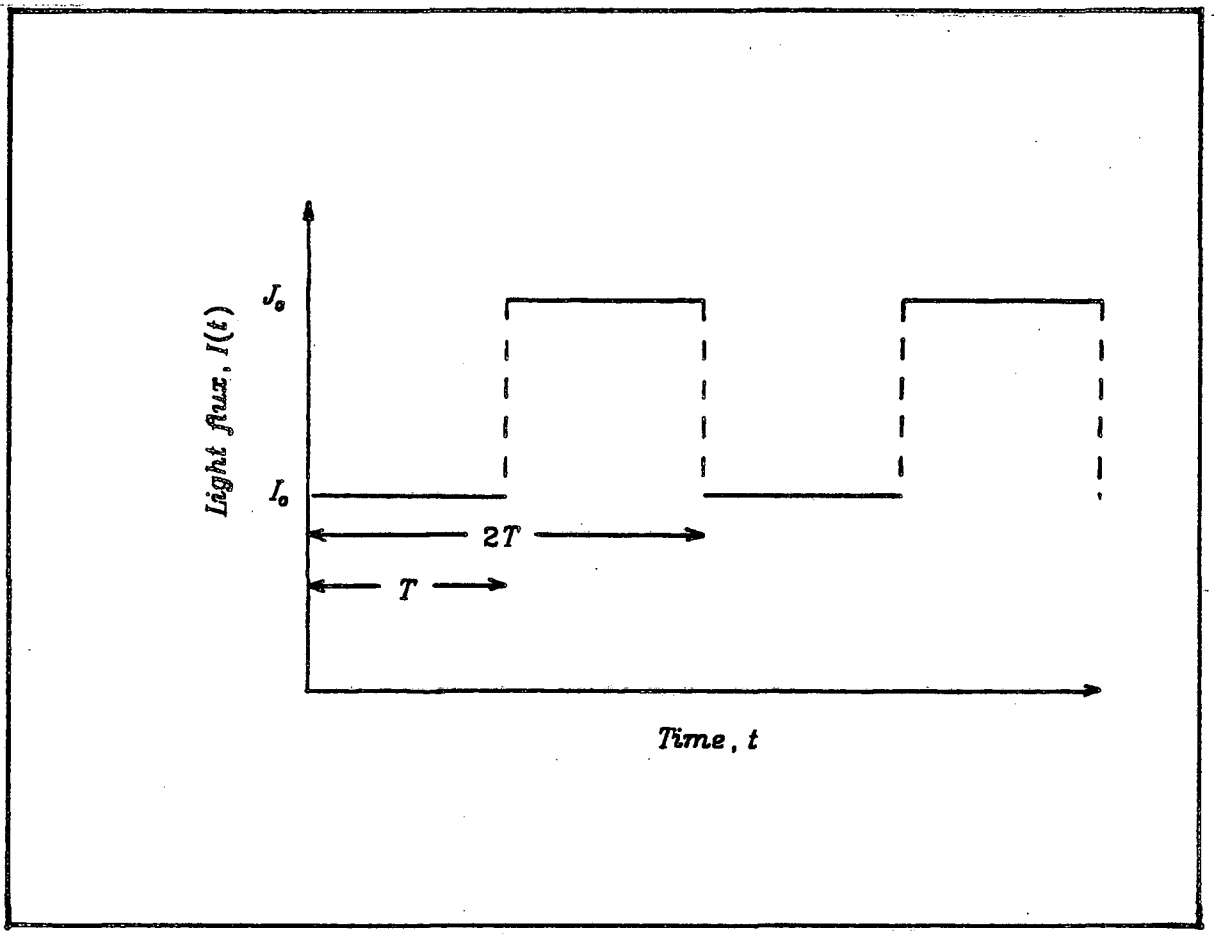

Figure 5-4. Periodic light-flux function

$$\left.\frac{d\overline{\Theta}}{d\zeta}\right|_{\zeta=0} = \left(\left.\frac{d\overline{\Theta}}{d\zeta}\right|_{\zeta=0}\right)_{step} \qquad [5\text{-}45]$$

$$-\Psi_i\left[\frac{\alpha}{(s^2+\gamma_i^2)(s+1-\alpha^2)} - \frac{\sqrt{s+1}}{(s^2+\gamma_i^2)(s+1-\alpha^2)}\right]$$

where $\gamma_i = \frac{i\pi}{\theta_T}$ and Ψ_i is the operator

$$\Psi_i = \frac{4(J_o - I_o)\alpha\tau e^{-w\alpha}}{c^b\theta_T} \sum_{i=1,3,5,\cdots}^{\infty} . \qquad [5\text{-}46]$$

The term $\left(\left.\frac{d\overline{\Theta}}{d\zeta}\right|_{\zeta=0}\right)_{step}$ represents a light step to I_o, given in Eq. [5-39]. The inversion of Eq. [5-45] is outlined in Appendix 5. The result is

$$\left.\frac{d\Theta}{d\zeta}\right|_{\zeta=0} = \left(\left.\frac{d\Theta}{d\zeta}\right|_{\zeta=0}\right)_{step} - \Psi_i\left(\left[\frac{X_1}{\gamma_i}\cos(\gamma_i\theta) - \frac{X_2}{\gamma_i}\sin(\gamma_i\theta)\right]\right. \qquad [5\text{-}47]$$

$$+ \frac{\alpha}{(\alpha^2-1)^2+\gamma_i^2}\left\{\frac{1-\alpha^2}{\gamma_i}\sin(\gamma_i\theta) - \cos(\gamma_i\theta) + e^{(\alpha^2-1)\theta} - \mathrm{erf}\,(\alpha\theta^{\frac{1}{2}})e^{(\alpha^2-1)\theta}\right.$$

$$\left.\left. + \frac{\alpha(1-\alpha^2)}{\gamma_i}\left[X_1\cos(\gamma_i\theta) - X_2\sin(\gamma_i\theta)\right] + \alpha\left[X_1\sin(\gamma_i\theta) + X_2\cos(\gamma_i\theta)\right]\right\}\right)$$

The step solution, $\left(\left.\frac{d\Theta}{d\zeta}\right|_{\zeta=0}\right)_{step}$, is expressed in Eq. [5-40]. The functions X_1 and X_2 are

$$X_1 = \frac{1}{\sqrt{\pi}} \sum_{j=0}^{\infty} \sum_{k=0}^{\infty} \frac{(-1)^{j+k} \gamma_i^{2k+1} \theta^{j+2k+\frac{3}{2}}}{j!(2k+1)!(j+2k+\frac{3}{2})} \qquad [5\text{-}48]$$

and

$$X_2 = \frac{1}{\sqrt{\pi}} \sum_{j=0}^{\infty} \sum_{k=0}^{\infty} \frac{(-1)^{j+k} \gamma_i^{2k} \theta^{j+2k+\frac{1}{2}}}{j!(2k)!(j+2k+\frac{1}{2})} . \qquad [5\text{-}49]$$

For long times, the exponential terms in Eq. [5-47] vanish, and the functions X_1 and X_2 reach limiting values (see Appendix 5):

$$X_1 = \left(\frac{\sqrt{1+\gamma_i^2} - 1}{2(\gamma_i^2 + 1)} \right)^{\frac{1}{2}} \qquad (\theta \to \infty) \qquad [5\text{-}50]$$

$$X_2 = \left(\frac{\sqrt{1+\gamma_i^2} + 1}{2(\gamma_i^2 + 1)} \right)^{\frac{1}{2}} \qquad (\theta \to \infty) \qquad [5\text{-}51]$$

Inserting Eq. [5-47] into Eq. [5-33] yields Θ^w :

$$\Theta^w - \Theta^{w,step} = \frac{-\sigma_1 \Psi_i}{1 + \sigma_1 e^{-\theta} \left[\frac{1}{\sqrt{\pi\theta}} + e^{\theta} \mathrm{erf}\,(\theta^{\frac{1}{2}}) \right]} \left(\left[\frac{X_1}{\gamma_i} \cos(\gamma_i \theta) - \frac{X_2}{\gamma_i} \sin(\gamma_i \theta) \right] \right.$$

$$+ \frac{\alpha}{(\alpha^2-1)^2 + \gamma_i^2} \left\{ \frac{1-\alpha^2}{\gamma_i} \sin(\gamma_i \theta) - \cos(\gamma_i \theta) + e^{(\alpha^2-1)\theta} - \mathrm{erf}\,(\alpha\theta^{\frac{1}{2}}) e^{(\alpha^2-1)\theta} \right.$$

$$\left. \left. + \frac{\alpha(1-\alpha^2)}{\gamma_i} \left[X_1 \cos(\gamma_i \theta) - X_2 \sin(\gamma_i \theta) \right] + \alpha \left[X_1 \sin(\gamma_i \theta) + X_2 \cos(\gamma_i \theta) \right] \right\} \right) \qquad [5\text{-}52]$$

where $\Theta^{w,step}$ is represented by the mathematical expression of Eq. [5-41]. It should be noted, however, that σ_2 is a function of time. Hence, $\Theta^{w,step}$, which

contains $\sigma_2(\theta)$, will vary since $I(t)$ changes periodically from I_o to J_o. For long times, $\Theta^{w,step} = \dfrac{\sigma_2(\theta) + \dfrac{\phi_o}{\alpha+1}\sigma_1}{1+\sigma_1}$, and the exponential terms in Eq. [5-52] vanish leaving the following long-time solution:

$$\Theta^w = \frac{\sigma_2(\theta) + \dfrac{\phi_o}{\alpha+1}}{1+\sigma_1} - \frac{\sigma_1\Psi_i}{1+\sigma_1}\left(\left[\frac{X_1}{\gamma_i}\cos(\gamma_i\theta) - \frac{X_2}{\gamma_i}\sin(\gamma_i\theta)\right]\right. \qquad [5\text{-}53]$$

$$+ \frac{\alpha}{(\alpha^2-1)^2+\gamma_i^2}\left\{\frac{1-\alpha^2}{\gamma_i}\sin(\gamma_i\theta) - \cos(\gamma_i\theta)\right.$$

$$\left.\left. + \frac{\alpha(1-\alpha^2)}{\gamma_i}\left[X_1\cos(\gamma_i\theta) - X_2\sin(\gamma_i\theta)\right] + \alpha\left[X_1\sin(\gamma_i\theta) + X_2\cos(\gamma_i\theta)\right]\right\}\right)$$

To implement Eq. [5-53], the long-time representations for X_1 and X_2, which are given in Eqs. [5-50] and [5-51], should be used. The function Θ^w attains a uniform and sustained periodic state. Since the system reaches a periodic state, and the mathematical description is analytic and straightforward, this technique is promising as a convenient analytical tool.

Conclusion

Analytic solutions have been obtained for minority-carrier concentrations at the semiconductor surface during pulse (Eq. [5-37]), step (Eq. [5-41]), sinusoidal and periodic square-pulse (Eq. [5-52]) illumination of a semiconductor-electrolyte interface. The analytical solutions can serve as useful comparisons for more general modeling of the unsteady-state illumination of a semiconductor-electrolyte interface. In addition, the analytic

solutions can be used to describe accurately the *low level injection* behavior of wide band gap semiconductors commonly used in photoelectrolysis cells and other photoelectrochemical systems. For these systems, since the periodic illumination of a photoelectrochemical cell results in a periodic photoresponse, the analytic solutions are useful for the evaluation of system physicochemical parameters. The periodic-illumination technique is analogous to the traditional cyclic chronopotentiometry and chronoamperometry electrochemical techniques. In particular, the cycle period of the varying light source can easily be adjusted to match the time constants of the photoelectrochemical cell processes, which makes this technique a valuable analytical tool for the investigation of semiconductor-electrolyte interfaces.

Nomenclature

α	light absorption coefficient, $\frac{1}{\text{cm}}$
c	concentration, $\frac{\text{mol}}{\text{cm}^3}$
D	diffusion coefficient, $\frac{\text{cm}^2}{\text{s}}$
e^-	symbol for the electron
E	measured electrode potential, V
f	$\frac{F}{RT}$, V^{-1}
F	Farraday's constant, $\frac{\text{C}}{\text{equivalent}}$
i	current density, $\frac{\text{A}}{\text{cm}^2}$
I	incident light flux, $\frac{\text{mol}}{\text{cm}^2-\text{s}}$
k_a, k_c	anodic and cathodic rate constants, $\frac{\text{kg}}{\text{cm}^2-\text{s}}$
L	diffusion length, cm
L^{-1}	symbol for the inverse Laplace transform
n	number of electrons in a reaction
R	universal gas constant, 8.314 $\frac{\text{J}}{\text{mol}-\text{K}}$
s	Laplace transform variable, $\frac{1}{\text{s}}$
s_i	stoichiometric coefficient of species i
t	time, s
T	absolute temperature, K

U^{θ} standard electrode potential, V

v_s surface recombination velocity, $\frac{cm}{s}$

V electrode potential defined by Eq. [5-3], V

w space-charge thickness in the semiconductor near the semiconductor-electrolyte interface, cm

x distance variable, cm

z_i charge number of species i

α dimensionless light absorption coefficient

β symmetry factor

ζ dimensionless distance variable

θ dimensionless time

Θ^w dimensionless concentration

λ dimensionless current density

μ_i symbol for the electrochemical potential of species i

ρ_o solvent density, $\frac{kg}{cm^3}$

σ_1 dimensionless constant defined in Eq. [5-34]

σ_2 dimensionless group defined in Eq. [5-35]

τ carrier lifetime , s

ϕ dimensionless incident light flux

Φ electrical potential, V

Subscripts

IR	ohmic
MS	metal-semiconductor interface
SE	semiconductor-electrolyte interface
ref	reference electrode compartment

Superscripts

b,s	bulk semiconductor
eq	equilibrium
init	initial
o,Pt	reference state in the platinum phase
o,s	reference state in the semiconductor phase
surf	surface

References

1. W.H. Brattain and C.G.B. Garett, *Bell Syst. Tech. J.*, 34(1955)129.
2. H. Reiss, *J. Electrochem. Soc.*, 125(1978)937.
3. A.J. Bard, *J. Electroanal. Chem.*, 168(1984)5.
4. A. Heller, *Science*, 223(1984)1141.
5. R.G. Shulman, *Semiconductors*, N.B. Hannay, editor, Reinhold, New York, 1959, pp. 493-496.
6. R.H. Bube, *Photoconductivity of Solids*, John Wiley and Sons, New York, 1960, p. 425.
7. G.M. Martin and D. Bois, *Semiconductor Characterization Techniques* , P.A. Barnes and G.A. Rozgonyi, editors, The Electrochemical Society, New York, 1978, pp. 32-42.
8. W.W. Gartner, *Phys. Rev.*, 116(1959)84.
9. J.F. Dewald, *Semiconductors*, N.B. Hannay, editor, Reinhold, New York, 1959, pp. 737-739.
10. Y.G. Chai and W.W. Anderson, *J. Appl. Phys.*, 27(1975)183.
11. M.A. Butler, *J. Appl. Phys.*, 48(1977)1914.
12. W. Kautek, H. Gerisher, and H. Tributsch, *J. Electrochem. Soc.*, 127(1980)2471.
13. W.L. Ahlgren, *J. Electrochem. Soc.*, 128(1981)2123.
14. P. Lemasson, A. Etcheberry, and J. Gautron, *Electrochim. Acta.*, 27(1982)607.
15. W. vanRoosbroeck, *J. Appl. Phys.*, 26(1955)380.
16. G.C. Barker, A.W. Gardner, and D.C. Sammon, *J. Electrochem. Soc.*, 113(1966)1182.

17. J. O'M. Bockris and K. Uosaki, *ibid.*, 124(1977)1348.

18. F. Decker and M. Fracastoro-Decker, *J. Electroanal. Chem.*, 126(1981)241.

19. S. Gottesfeld and S.W. Feldberg, *ibid.*, 146(1983)47.

20. L.M. Peter, J. Li, and R. Peat, *ibid.*, 165(1984)29.

21. D. Laser and A.J. Bard, *J. Electrochem. Soc.*, 123(1976)1828, 1833, and 1837.

22. H. Gerisher, *J. Electroanal. Chem.*, 58(1975)263.

23. H. Gerisher, *Physical Chemistry, an Advanced Treatise*, volume IXA, H. Eyring, editor, Academic Press, New York, 1970, pp. 463-542.

24. M.E. Orazem and J. Newman, *J. Electrochem. Soc.*, 131(1984)2569, 2574, and 2582.

25. A.J. Bard and L.R. Faulkner, *Electrochemical Methods*, John Wiley and Sons, New York, 1980, p. 60.

26. M.E. Orazem and J. Newman, *J. Electrochem. Soc.*, 131(1984)2715.

27. T.B. Grimley, *Proc. Roy. Soc. London, ser. A*, 201(1950)40.

28. M. Green, *Modern Aspects of Electrochemistry*, volume 2, J. O'M Bockris, editor, Academic Press, 1959, pp. 370-372.

29. *Ohmic Contacts to Semiconductors*, Bertram Schwartz, editor, The Electrochemistry Society, New York, 1968.

30. J. Newman, *Electrochemical Systems*, Prentice-Hall, Englewood Cliffs, New Jersey, 1973.

31. W. Shockley and W.T. Read, *Phys. Rev.*, 87(1952)835.

32. R.N. Hall, *ibid.*, 87(1952)387.

33. A.S. Grove, *Physics and Technology of Semiconductor Devices*, John Wiley and Sons, New York, 1967, pp. 183-186.

34. R.S. Muller and T.I. Kamis, *Device Electronics for Integrated Circuits*, John Wiley and Sons, New York, 1977, pp. 165-179.

35. S.M. Sze, *Semiconductor Devices, Physics and Technology*, John Wiley and Sons, New York, 1985, pp. 87-92.

36. F.B. Hildebrand, *Advanced Calculus for Applications*, second edition, Prentice-Hall, Englewood Cliffs, New Jersey, 1976.

37. *Handbook of Mathematical Functions*, M. Abramowitz and I.A. Stegun, editors, Dover Publications, New York, 1972.

38. G.E. Roberts, *Table of Laplace Transforms*, W.B. Saunders Company, Philadelphia, Pennsylvania, 1966.

39. F. Oberhettinger and L. Badii, *Tables of Laplace Transforms*, Springer-Verlag, New York, 1973.

40. *Standard Math Tables*, S.M. Selby, editor, CRC Press, Cleveland, Ohio, 1972, p. 480.

41. I.S. Gradshteyn and I.M. Rhzhik, *Tables of Integrals, Series, and Products*, fourth edition prepared by Yu. V. Geronimus and M. Yu. Tseytlin, translation editor A. Jeffrey, Academic Press, New York, 1965, p. 484.

Appendix 5

Inversion of Equation [5-40]

The only inversion needed to obtain Eq. [5-40] from Eq. [5-39] that is not tabulated is presented below. Using the convolution theorem, (ref. 36, p.63)

$$L_I^{-1} = L^{-1}\left[\frac{\sqrt{s+1}}{s(s+1-\alpha^2)}\right] = \int_0^\theta L^{-1}\left(\frac{1}{s}\right)\Big|_{\theta-\tilde{\theta}} L^{-1}\left(\frac{\sqrt{s+1}}{(s+1-\alpha^2)}\right)\Big|_{\tilde{\theta}} d\tilde{\theta} \qquad [5A\text{-}1]$$

Making use of the translation property, the product of the inversions within the integral can be evaluated:

$$L_I^{-1} = \int_0^\theta \frac{e^{-\tilde{\theta}}}{\sqrt{\pi\tilde{\theta}}} d\tilde{\theta} + \int_0^\theta \alpha e^{(\alpha^2-1)\tilde{\theta}} \mathrm{erf}\,(\alpha\tilde{\theta}^{\frac{1}{2}}) d\tilde{\theta} \qquad [5A\text{-}2]$$

The first integral is $\mathrm{erf}\,(\theta^{\frac{1}{2}})$. The second integral can be evaluated by the ***integration by parts*** technique. The final answer is

$$L_I^{-1} = \frac{1}{\alpha^2-1}\left[-\mathrm{erf}\,(\theta^{\frac{1}{2}}) + \alpha\,\mathrm{erf}\,(\alpha\theta^{\frac{1}{2}}) e^{(\alpha^2-1)\theta}\right] \qquad [5A\text{-}3]$$

Inversion of Equation [5-45]

In order to invert Eq. [5-45], ***partial fraction expansion*** is used:

$$L_{II}^{-1} = L^{-1}\left[\frac{\alpha}{(s^2+\gamma_i^2)(s+1-\alpha^2)}\right] \qquad [5A\text{-}4]$$

$$= L^{-1}\left\{\frac{\alpha}{(1-\alpha^2)^2+\gamma_i^2}\left[\frac{1-\alpha^2-s}{(s^2+\gamma_i^2)} + \frac{1}{(s+1-\alpha^2)}\right]\right\}$$

In the expanded form, the inversion of L_{II}^{-1} can be evaluated to yield

$$L_{\bar{II}}^{-1} = \frac{\alpha}{(1-\alpha^2)^2 + \gamma_i^2}\left[\frac{(1-\alpha^2)}{\gamma_i}\sin(\gamma_i\theta) - \cos(\gamma_i\theta) + e^{(\alpha^2-1)\theta}\right] \qquad [5A\text{-}5]$$

The remaining term that requires inversion in Eq. [5-45] is

$$L_{\bar{III}}^{-1} = L^{-1}\left[\frac{\sqrt{s+1}}{(s^2+\gamma_i^2)(s+1-\alpha^2)}\right] \qquad [5A\text{-}6]$$

Using the convolution theorem, $L_{\bar{III}}^{-1}$ can be expressed as

$$L_{\bar{III}}^{-1} = \int_0^\theta L^{-1}\left[\frac{\sqrt{s+1}}{(s+1-\alpha^2)}\right]\Bigg|_{\tilde{\theta}} L^{-1}\left[\frac{1}{(s^2+\gamma_i^2)}\right]\Bigg|_{\theta-\tilde{\theta}} d\tilde{\theta} \ . \qquad [5A\text{-}7]$$

The inversion of the first factor in Eq. [5A-7] was completed in the development of Eq. [5A-2]. The inversion of the second bracketed term in Eq. [5A-7] is $\frac{1}{\gamma_i}\sin\left[\gamma_i(\theta-\tilde{\theta})\right]$, which can be expanded in order to express $L_{\bar{III}}^{-1}$ as

$$L_{\bar{III}}^{-1} = -\frac{1}{\gamma_i}\left[X_1\cos(\gamma_i\theta) - X_2\sin(\gamma_i\theta)\right] - \frac{\alpha}{\gamma_i}\left[X_3\cos(\gamma_i\theta) - X_4\sin(\gamma_i\theta)\right] \qquad [5A\text{-}8]$$

where

$$X_1 = \int_0^\theta \sin(\gamma_i\tilde{\theta})\frac{e^{-\tilde{\theta}}}{\sqrt{\pi\tilde{\theta}}}d\tilde{\theta}\ , \qquad [5A\text{-}9]$$

$$X_2 = \int_0^\theta \cos(\gamma_i\tilde{\theta})\frac{e^{-\tilde{\theta}}}{\sqrt{\pi\tilde{\theta}}}d\tilde{\theta}\ , \qquad [5A\text{-}10]$$

$$X_3 = \int_0^\theta \sin(\gamma_i\tilde{\theta})\, e^{(\alpha^2-1)\tilde{\theta}}\mathrm{erf}\,(\alpha\tilde{\theta}^{\frac{1}{2}})d\tilde{\theta}\ , \text{ and} \qquad [5A\text{-}11]$$

$$X_4 = \int_0^\theta \cos(\gamma_i\tilde{\theta})\, e^{(\alpha^2-1)\tilde{\theta}}\mathrm{erf}\,(\alpha\tilde{\theta}^{\frac{1}{2}})d\tilde{\theta}\ . \qquad [5A\text{-}12]$$

The functions X_3 and X_4 can be integrated by making use of the *integration by parts* technique. The task is somewhat arduous, and we will only outline the treatment of X_3. The function X_4 can be dealt with in an analogous

fashion.

To integrate X_3 by parts, define

$$u = \sin(\gamma_i\tilde{\theta})\mathrm{erf}\,(\alpha\tilde{\theta}^{\frac{1}{2}}), \text{ then} \qquad [5A\text{-}13]$$

$$du = \left[\gamma_i\cos(\gamma_i\tilde{\theta})\mathrm{erf}\,(\alpha\tilde{\theta}^{\frac{1}{2}}) + \sin(\gamma_i\tilde{\theta})\frac{\alpha}{\sqrt{\pi\tilde{\theta}}}e^{-\alpha^2\tilde{\theta}}\right]d\tilde{\theta}\ . \qquad [5A\text{-}14]$$

Also define

$$dv = e^{(\alpha^2-1)\tilde{\theta}}d\tilde{\theta}\ , \text{ then} \qquad [5A\text{-}15]$$

$$v = \frac{e^{(\alpha^2-1)\tilde{\theta}}}{\alpha^2-1}\ . \qquad [5A\text{-}16]$$

X_3 can be then be written as $X_3 = uv - \int v\,du\Big|_0^{\tilde{\theta}}$, or

$$X_3 = \frac{e^{(\alpha^2-1)\tilde{\theta}}}{\alpha^2-1}\sin(\gamma_i\tilde{\theta})\mathrm{erf}\,(\alpha\tilde{\theta}^{\frac{1}{2}}) - \frac{\alpha^2}{\alpha^2-1}X_1 \qquad [5A\text{-}17]$$

$$- \frac{\gamma_i}{\alpha^2-1}\int \cos(\gamma_i\tilde{\theta})\mathrm{erf}\,(\alpha\tilde{\theta}^{\frac{1}{2}})e^{(\alpha^2-1)\tilde{\theta}}d\tilde{\theta}\Big|_0^{\tilde{\theta}}\ .$$

The last term in Eq. [5A-17] can be integrated by parts again. For this integration, $\sin(\gamma_i\tilde{\theta})$ in Eq. [5A-13] is replaced with $\cos(\gamma_i\tilde{\theta})$, and Eq. [5A-15] is used again for the definition of v. Performing the integration, Eq. [5A-17] becomes

$$X_3 = \frac{e^{(\alpha^2-1)\tilde{\theta}}}{\alpha^2-1}\sin(\gamma_i\tilde{\theta})\mathrm{erf}\,(\alpha\tilde{\theta}^{\frac{1}{2}}) - \frac{\alpha}{\alpha^2-1}X_1 \qquad [5A\text{-}18]$$

$$- \frac{\gamma_i}{\alpha^2-1}\left[\frac{e^{(\alpha^2-1)\tilde{\theta}}}{\alpha^2-1}\cos(\gamma_i\tilde{\theta})\mathrm{erf}\,(\alpha\tilde{\theta}^{\frac{1}{2}}) + \frac{\gamma_i}{\alpha^2-1}X_3 - \frac{\alpha}{\alpha^2-1}X_2\right]\Bigg|_0^{\tilde{\theta}}\ .$$

Equation [5A-18] can be solved algebraically for X_3. The resulting expres-

sions for X_3 and the function X_4 are:

$$X_3 = \frac{1}{1 + \frac{\gamma_i^2}{(\alpha^2-1)^2}} \times \left[\frac{e^{(\alpha^2-1)\theta}}{\alpha^2-1} \sin(\gamma_i\theta) \operatorname{erf}(\alpha\theta^{\frac{1}{2}}) \right. \qquad [5A\text{-}19]$$

$$\left. - \frac{\gamma_i}{(\alpha^2-1)^2} e^{(\alpha^2-1)\theta} \cos(\gamma_i\theta) \operatorname{erf}(\alpha\theta^{\frac{1}{2}}) - \frac{\alpha}{\alpha^2-1} X_1 + \frac{\alpha\gamma_i}{(\alpha^2-1)^2} X_2 \right],$$

and

$$X_4 = \frac{1}{1 + \frac{\gamma_i^2}{(\alpha^2-1)^2}} \times \left[\frac{e^{(\alpha^2-1)\theta}}{\alpha^2-1} \cos(\gamma_i\theta) \operatorname{erf}(\alpha\theta^{\frac{1}{2}}) \right. \qquad [5A\text{-}20]$$

$$\left. + \frac{\gamma_i}{(\alpha^2-1)^2} e^{(\alpha^2-1)\theta} \sin(\gamma_i\theta) \operatorname{erf}(\alpha\theta^{\frac{1}{2}}) - \frac{\alpha}{\alpha^2-1} X_2 - \frac{\alpha\gamma_i}{(\alpha^2-1)^2} X_1 \right].$$

The functions X_3 and X_4 can be placed into Eq. [5A-8] to yield $L_{\bar{III}}^{-1}$. $L_{\bar{II}}^{-1}$ and $L_{\bar{III}}^{-1}$ (Eqs. [5A-8] and [5A-4], respectively) can then be combined with Eq. [5-45] to obtain $\left.\frac{d\Theta}{d\zeta}\right|_{\zeta=0}$.

A straightforward integration of X_1 and X_2 does not appear possible. The integrands of these functions, however, can be expressed in a power series, which can be integrated to yield the expressions given in Eqs. [5-48] and [5-49]. For long times, the integral expressions for X_1 and X_2, Eqs. [5A-9] and [5A-10], reach limiting values listed in Eqs. [5-50] and [5-51]. (41)

This report was done with support from the Department of Energy. Any conclusions or opinions expressed in this report represent solely those of the author(s) and not necessarily those of The Regents of the University of California, the Lawrence Berkeley Laboratory or the Department of Energy.

Reference to a company or product name does not imply approval or recommendation of the product by the University of California or the U.S. Department of Energy to the exclusion of others that may be suitable.

LAWRENCE BERKELEY LABORATORY
TECHNICAL INFORMATION DEPARTMENT
UNIVERSITY OF CALIFORNIA
BERKELEY, CALIFORNIA 94720